Thermal characterization of GeSbTe alloys by Raman thermometry for Phase-Change Memories

Caractérisation thermique des alliages GeSbTe par thermométrie Raman pour les mémoires à changement de phase

Thèse

présentée à l'Université de Lille, faculté des Sciences et Technologies Institut d'Electronique, de Microélectronique et de Nanotechnologies (IEMN) UMR CNRS 8520 par

Akash Rajendra PATIL

pour obtenir le titre de

DOCTEUR DE L'UNIVERSITE

Spécialité : Electronique, microélectronique, nanoélectronique et micro-ondes, Ecole Doctorale Sciences de l'Ingénierie et des Systèmes (ENGSYS-632)

Soutenue le **27 novembre 2023** devant le jury composé de :

Olivier THOMAS Professeur, IM2NP CNRS – Aix-Marseille Université, France	Rapporteur
llaria ZARDO Professor, University of Basel, Switzerland	Rapporteure
Valentina GIORDANO Chargé de Recherche, Institut Lumière Matière, CNRS, Lyon, France	Examinatrice
Damien DELERUYELLE Professeur des Universités, INSA Lyon, France	Président
Gabriele NAVARRO Ingénieur Docteur, CEA-LETI, Grenoble, France	Examinateur
Emmanuel DUBOIS Directeur de recherche, IEMN, CNRS, Lille, France	Examinateur
Jean-François ROBILLARD Enseignant-Chercheur, Junia, Lille, France	Directeur de Thèse
Simon JEANNOT Ingénieur Docteur, STMicroelectronics, Crolles, France	Co-encadrant de Thèse
Philippe BOIVIN Ingénieur Docteur, STMicroelectronics, Rousset, France	Invité

Contents

PREFACE AND ACKNOWLEDGEMENTS ..... **V**

ABSTRACT – RÉSUMÉ ..... **VII**

GLOSSARY ..... **IX**

INTRODUCTION **1**

Chapter 1 Phase Change Memory – from Device to Material **9**

1.1 Phase change memory **11**
1.1.1 Device functionality 15
1.1.2 PCM device architecture 18
1.1.3 Thermal engineering of PCM 22
1.1.4 Current PCM standpoint 24

1.2 Phase Change Materials **25**
1.2.1 Meta-stable and stable crystalline phase 26
1.2.2 Amorphous phase 28
1.2.3 Phase transition from amorphous to crystalline 29
1.2.4 Evolution of GST 30
1.2.5 Doping of GST-225 32
1.2.6 Ge-rich doped GST 32

1.3 Chapter summary **35**

Chapter 2 Thermal Characterization of Phase Change Materials **37**

2.1 Thermal conductivity of GeSbTe based Phase Change Materials **39**
2.1.1 Transport properties and structural origin 40
2.1.2 Electronic and lattice contribution to thermal conductivity – general theory 42
2.1.3 Understanding the evolution of thermal conductivity on phase transition 44
2.1.4 Thermal conductivity reports for GST-225 46
2.1.5 Pseudo-binary alloys and effect of doping 48

2.2 Thermal characterization techniques 50
2.2.1 3-omega Technique 51
2.2.2 Thermoreflectance 53
2.2.2 Photo thermal radiometry 55
2.2.3 Current perspective of thermal characterization for chalcogenides 56

2.3 Conclusion 57

Chapter 3 Raman Thermometry for GeSbTe Alloys 59

3.1 From Raman spectroscopy to thermometry 61
3.1.1 Raman spectroscopy 61
3.1.2 Raman selection rules 62
3.1.3 Raman thermometry 66

3.2 Experimental development of Raman thermometry for chalcogenides 70
3.2.1 Experimental setup 70
3.2.2 Material and thickness considerations 75
3.2.3 Example of Raman thermometry 77

3.3 Conclusion 83

Chapter 4 Structural Investigation of Ge-Rich GST And GeTe 85

4.1 Vibrational modes of GeSbTe based alloys: context 87
4.1.1 Elemental Ge, Sb and Te: 87
4.1.2 GeTe- Sb_2Te_3 pseudo binary line 88

4.2 Structural investigation of Ge-rich GeSbTe alloys 90
4.2.1 Raman spectrum of amorphous GGST and GGSTN 91
4.2.2 Transition from amorphous to crystalline: Ex-situ Raman analysis 93
4.2.3 In-situ XRD characterization of GGST and GGSTN 95

4.3 Crystallization story: Ge-rich GST 98

4.4 Structural investigation of GeTe 101
4.4.1 Raman spectrum of amorphous phase 102
4.4.2 Transition from amorphous to crystalline: Raman analysis 103
4.4.3 In-situ XRD characterization 105

4.5 Conclusion 107

Chapter 5 Thermal Conductivity – Raman Thermometry 109

5.1 Raman thermometry 111
5.1.1 Materials under study 111
5.1.2 Influence of peak fitting 112

5.1.3 Reliability of the technique ... 113
5.1.4 Amorphous phase stability ... 113
5.1.5 High temperature measurement – crystalline phase ... 115
5.1.6 Revisiting input parameters and modelling assumptions ... 117

5.2 Thermal conductivity measurements ... 118
5.2.1 GGST and GGSTN ... 119
5.2.2 GGSTN as a function of annealing temperature ... 123
5.2.3 Discussion – Thermal conductivity of GST-225 and Ge-rich GST alloys ... 125
5.2.4 GeTe ... 126

5.3 Conclusion ... 128

Conclusions And Perspectives ... 131

References ... 137

Preface and Acknowledgements

Welcome to my doctoral thesis! I am delighted to reach this point of culmination when I can write my personal memoir. It has been a great learning experience, from both scientific and personal development perspective. I have been fortunate to be surrounded by wonderful people who helped me through this exciting, rollercoaster of a journey.

I would like to begin by thanking my supervisors for giving me this opportunity and believing in me. Jean-François has been the biggest motivator and supporter throughout. From kindly accepting me for an internship in 2015 to this PhD journey, I wouldn't have made it so far without his encouragement. His depth of knowledge, leadership, simplicity and positive attitude are commendable. I have learnt a ton of things from him and, I cannot thank him enough.

I am indebted to Philippe Boivin for his guidance and enlightening me with his vast experience. He always had the right questions to ask every time and solutions which improved the research quality. I would like to thank Roberto Simola and Jury Sandrini for their support and helpful discussion with simulations and materials. To end, a big thank you to Simon Jeannot for his encouragement at the end of the thesis and future prospects. A special mention and gratitude to Yannick Le-Friec for providing me with the samples, supporting various requirements, and critical discussions for understating the material.

I would like to thank Emmanuel Dubois for being the backbone of the group, his critical insights, and supporting every activity. The smooth functioning of these 3 years would not have been possible without the efficient organization of Florence Alberti. I am very grateful for your support. I would like to thank Dominique Vignaud for his guidance, quick experimental solutions and key discussions.

The project wouldn't have been complete due to key collaborations. A big thank you to Pascal Roussel and Marielle Huvé at Insitut Chevreul for providing extensive support with in-situ XRD and EDX-TEM characterization for structural understanding the material.

The thesis was carried out in a dynamic and inquisitive environment at IEMN. I would like to thank the direction, CMNF and administrative teams for their support and smooth functioning of all the activities.

This project was a part of the IEMN-STMicroelectronics common laboratory framework. It was initiated towards research and development of phase change memory technology at STMicroelectronics. I would like to thank all the funding agencies and ePCM group involved in making this project possible.

I would like to thank the members of the jury members for accepting to evaluate my thesis, their valuable time and critical inputs.

I am lucky to have made many close friendships at IEMN that made my time here smooth, less stressful and fun. I would like to begin by thanking my group members – Melanie, Jon, Daniel, Hafsa, Maya and Corentin. My extended lab family – a big thank you to Giuseppe, Jash, Sarah, Carlos and Chiara for motivating me and being my weekend support system. My Lille family – Damien, Lucien, Pauline, Guillaume, Maxime, Chloe and Auberie, thank you for making me feel at home and for all the good times.

This thesis wouldn't have been possible without long-distance friendships who were always just a call away – Ganesh, Akanksha, Rahul, Aditi, Prasad, Pranav, Kaustubh, Mayank, Mister Logic, Saranath, Roger, Sergi, Rimsha, Ananya and Urvi. Thank you for being there with me in different stages on my life, supporting me when things got tough and for all the wonderful trips and memories we made together. A big thank you to Esha for dealing with me through the writing phase, my mood swings and making my worse days better.

Lastly, the most important people in my life. I cannot thank my parents enough for supporting me throughout my up brining, being there during every step of my life, for their advice, values and care for me. Me doing a PhD or even moving away from home wouldn't have been possible without them. A big thank you to Snehal and Maarif for always being there for me and ensuring I make the right decisions. My sister has been my biggest cheerleader throughout, responsible for me enjoying every moment and reaching this wonderful stage of my life.

Hope I made everyone proud, enjoy reading the thesis!

I would like to end by stating quotes which motivated me through different phases in these 3 years,

"To do is to be"
- Kant

"To be is to do"
- Socrates

"Do be do be do"
- Scooby-Doo

Cheers,

Akash

Abstract – Résumé

Title: Thermal characterization of GeSbTe alloys by Raman thermometry for Phase-Change Memories

Abstract: Phase change Materials have been the basis of memory storage beginning from its application for optical data storage in 1987. Fast forward to 2010s, phase change memories developed were 1000 times faster with greater endurance than NAND; and 10 times denser than DRAM. PMs based on chalcogenides provide flexibility of faster speed, higher endurance or better thermal stability depending on stoichiometry. Materials engineering of GeSbTe (GST) alloys led to realization of stoichiometry's with high temperature stability suitable for embedded Phase-Change Memories (PCMs) in automotive MCU applications. Alloys like doped Ge-rich GeSbTe presented high temperature data retention owing to high crystallization temperature. In PCM, the reversible switching between phases is thermally initiated. Studies report that < 1% energy is utilized for phase change, whereas most of the energy is lost *via* other heat dissipation pathways in the PCM cell. So, knowledge of the thermal properties of these materials over the entire operation temperature range of PCM cell is crucial for better operation of the memory. The flag-ship GST-225 alloy has been extensively characterized but the current state-of-art falls short on thermal characterization of the newly engineered stoichiometries.

Methods like 3ω, thermo-reflectance and photo-thermal radiometry have been implemented for thermal characterization of GST. These tools come with certain drawbacks such as: additional microfabrication of heaters or transducers, high setup costs or complex post-processing of data. Raman thermometry is an optical characterization technique which requires no microfabrication and can provide an advantage of simultaneous structural investigation. In this work, we investigated PMs like GeTe, Ge-rich GeSbTe and N-doped Ge-rich GeSbTe using Raman thermometry. This was possible by studying the temperature evolution of vibrational modes present in GeSbTe based alloys. We demonstrate successful extraction of temperature and phase dependent thermal properties of these materials to higher temperature (~350°C) by Raman thermometry for the first time. Increasing the Ge content and further N-doping decreased the thermal conductivity which is beneficial for PCM efficiency. Main contribution to thermal conductivity arises from phonons, with negligible electronic contribution. It provides a better understanding of the behavior of these materials at higher temperature and effect of nitrogen content. These results prove Raman thermometry as a rich, quantitative and reliable thermal and structural characterization technique for phase change materials.

Key words: Phase-Change Memory, Phase change materials, Ge-rich GST alloys, Nitrogen doping, thermal conductivity, Raman spectroscopy, Raman thermometry, X-ray diffraction

Titre : Caractérisation thermique des alliages GeSbTe par thermométrie Raman pour les mémoires à changement de phase

Résumé : Les matériaux à changement de phase sont à la base du stockage des mémoires depuis leur application au stockage optique des données en 1987. Dans les années 2010, les mémoires à changement de phase développées étaient 1000 fois plus rapides et plus endurantes que les mémoires NAND, et 10 fois plus denses que les mémoires DRAM. Les mémoires à changement de phase basées sur des chalcogénures offrent la flexibilité d'une vitesse plus rapide, d'une plus grande endurance ou d'une meilleure stabilité thermique en fonction de la stœchiométrie. L'ingénierie des matériaux des alliages GeSbTe (GST) a permis de réaliser des stœchiométries avec une stabilité à haute température convenant aux mémoires à changement de phase (PCM) intégrées dans les applications MCU automobiles. Les alliages tels que le GeSbTe dopé riche en Ge présentent une rétention des données à haute température en raison de la température de cristallisation élevée. Dans les PCM, la commutation réversible entre les phases est initiée thermiquement. Les études indiquent que moins de 1 % de l'énergie est utilisée pour le changement de phase, alors que la plus grande partie de l'énergie est perdue par d'autres voies de dissipation de la chaleur dans la cellule PCM. La connaissance des propriétés thermiques de ces matériaux sur l'ensemble de la plage de température de fonctionnement de la cellule PCM est donc cruciale pour un meilleur fonctionnement de la mémoire. L'alliage phare GST-225 a été largement caractérisé, mais l'état actuel des connaissances ne permet pas de caractériser thermiquement les stœchiométries nouvellement conçues.

Des méthodes telles que 3ω, la thermo-réflectance et la radiométrie photo-thermique ont été mises en œuvre pour la caractérisation thermique des GST. Ces outils présentent certains inconvénients, tels que la microfabrication supplémentaire d'éléments chauffants ou de transducteurs, des coûts d'installation élevés ou un post-traitement complexe des données. La thermométrie Raman est une technique de caractérisation optique qui ne nécessite pas de microfabrication et peut offrir l'avantage d'une étude structurelle simultanée. Dans ce travail, nous avons étudié des particules comme le GeTe, le GeSbTe riche en Ge et le GeSbTe riche en N dopé à l'aide de la thermométrie Raman. Cela a été possible en étudiant l'évolution de la température des modes vibrationnels présents dans les alliages à base de GeSbTe. Nous démontrons pour la première fois l'extraction réussie des propriétés thermiques dépendantes de la température et de la phase de ces matériaux à des températures plus élevées (~350°C) par thermométrie Raman. L'augmentation de la teneur en Ge et le dopage N supplémentaire ont diminué la conductivité thermique, ce qui est bénéfique pour l'efficacité de la PCM. La principale contribution à la conductivité thermique provient des phonons, la contribution électronique étant négligeable. Ces résultats permettent de mieux comprendre le comportement de ces matériaux à des températures plus élevées et l'effet de la teneur en azote Ces résultats prouvent que la thermométrie Raman est une technique de caractérisation thermique et structurelle riche, quantitative et fiable pour les matériaux à changement de phase.

Key words : Mémoire à changement de phase, matériaux à changement de phase, alliages GST riches en Ge, dopage à l'azote, conductivité thermique, spectroscopie Raman, thermométrie Raman, diffraction des rayons X.

Glossary

AD	As-Deposited
BEOL	Back-End-Of-Line
BJT	Bipolar Junction Transistors
CMOS	Complementary Metal-Oxide-Semiconductor
DRAM	Dynamic Random-Access Memory
EXAFS	Extended X-ray Absorption Fine Structure
FCC	Face-Centered Cubic crystalline structure
FDSOI	Fully Depleted Silicon on Insulator
FDTR	Frequency Domain Thermo Reflectance
FEM	Finite Element Method
FeRAM	Ferroelectric Random-Access Memory
FWHM	Full width in Half Maximum
GST	GeSbTe alloys
GGST	Ge-rich GeSbTe
GGSTN	Ge-rich GeSbTe alloy with N-doping
HDD	Hard Disk Drive
ICT	Information and communication technology
IoT	Internet-of-things
ITRS	International Technology Roadmap for Semiconductor
IV	Current vs Voltage curve
LA	Longitudinal Acoustic mode
LO	Longitudinal Optic mode
MCU	Micro-Controller Unit
MEMS	Micro-Electro Mechanical System
MOSFET	Metal–Oxide–Semiconductor Field Effect Transistors
MPTR	

MRAM	Modulated Photo-Thermal Radiometry
MTJ	Magnetic Random-Access Memory
	Magnetic Tunneling Junction
n-TTR	
NVM	Nanosecond Transient Thermo Reflectance
	Non-Volatile Memory
OTS	
PCM	Ovonic Threshold Switch
PM	Phase-Change Memory
PPTR	Phase-Change Material
PTR	Pulsed Photo-Thermal Radiometry
	Photo Thermal Radiometry
RF	
RRAM	Radio Frequency
RT	Resistive Random-Access Memory
	Room Temperature
SCM	
SRAM	Storage Class Memory
STT-RAM	Static Random-Access Memory
SThM	Spin-Transfer Torque Magnetic Random-Access Memory
	Scanning Thermal Microscopy
TA	
TBR	Transverse Acoustic mode
TCR	Thermal Boundary Resistance
TDTR	Thermal Co-efficient of Resistance
TEM	Time Domain Thermo Reflectance
TEM_{00}	Transmission Electron Microscopy
TR	Transverse Electromagnetic Mode – lowest order
	Thermoreflectance
TO	
XANES	Transverse Optic mode
XRD	X-ray absorption of near-edge structure
	X-ray Diffraction

Introduction

"Cramming more components onto integrated circuits", Electronics, Volume 38, 1965, Dr. Gordon Moore predicted that number of components on a chip would double every year [1]. This was based on his observation of a mere few years, when they could fit 60 components on a chip in 1965, and extrapolated it to predict 60000 in 1975. Amazingly enough, it doubled 9 times in those 10 years and the prediction eventually got dubbed as "Moore's law". Since 1970, the number of components have doubled every two years with a few tweaks in the recent decades. This prediction of integration density on a chip was conceptualized in terms of performance by R. Dennard in the constant field scaling theory [2]. Where, dimensional scaling with constant electric field resulted in increased speed and lower power consumption of CMOS (complementary metal-oxide-semiconductor) components[1]. Based on these 2 governing pillars, evolution of smaller, cheaper and faster semiconductor components led to an aggressive cycle of investments and market growth in multitude of technological avenues. To put forth the economics in perspective, the average selling price of the cost of a transistor has plummeted from 5.24 $ per byte in 1954 to mere ***two nano*** $ per byte due to the ability to pack 5.3 trillion transistors per chip in 2023 [3]–[5]. The persistence of the scientific community to have achieved this feat is commendable.

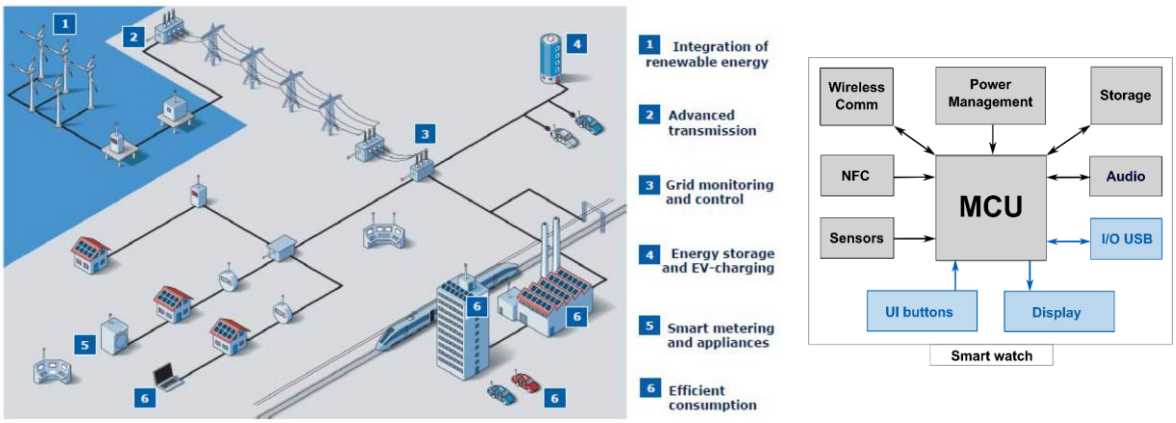

Fig. 1. (left) Entire energy "food chain" from generation via distribution to consumption, in all segments semiconductor power technology devices are required (source: Infineon), Fig. 2. (right) Block diagram of a smart watch illustrating the Micro-Controller Unit (MCU) communicating with various components on its periphery

1 Semiconductor element – transistor - used to store memory

Since then, in over 70 years, technology has traversed multiple facets of daily human life, by engaging in every aspect of our functioning. We are surrounded by intricate microelectronic components like microprocessors, microcontrollers, memory chips, integrated circuits which are the building blocks of every electronic gadget. At every step of our basic necessity – the energy "food chain", these integrated circuits are crucial in efficient production, transmission, storage, regulation and consumption of energy, Fig. 1 [6]. The last two generations have witnessed this evolution, and the devices have matured to be extremely sophisticated. For example, a simple smart watch available for 100€, comprises of an array of different types of integrated circuits as illustrated in Fig. 2 [7]. They perform different intricate functions which are available to us, just by the touch of a finger. The simplicity of user interface with cheap devices and easy access to internet has led to the Internet of Thing (IoT) era enabled by the foundation of information and communication technology (ICT). Information and communications technology (ICT) is an extensional term for information technology (IT) that stresses the role of unified communications and the integration of telecommunications (telephone lines and wireless signals) and computers, as well as necessary enterprise software, middleware, storage and audiovisual, that enable users to access, store, transmit, understand and manipulate information [8]. To support this era, there has been an ever-increasing flow of data. The amount of data generated is exponentially increasing with a predicted rise from 33 Zettabytes in 2018 to a staggering 175 Zettabytes[2] by 2025. To sustain an efficient ecosystem, the endpoint[3] data generators are supported by a core system[4] of designated computing data centers for transfer and storage of data. The scenario of supporting billions of devices in the coming few years, require power efficient and smaller semiconductor memory systems. So far, the development was guided by Moore's laws and Dennard's scaling, which now face a bottleneck. As we reach practical limits of physics, it becomes challenging to shrink the transistor size. Similarly, the power consumption has increased in the recent technology nodes rather than decreasing [9]. To remedy this and be able to store large amounts of data in a small space at a very high speed, new architectural solutions and novel technologies are put forth in the International Technology Roadmap for Semiconductor (ITRS) [10], [11].

- **Existing Memory Hierarchy**

The semiconductor components implemented in ICT constitute a memory hierarchy represented as a pyramid in Fig. 3. The basic components are: logic (on chip - volatile), main memory (off chip - volatile) and storage memory (off chip – non-volatile) based on the Von Neumann architecture. As we move from top to bottom in this pyramid, the operating speed and cost decreases with increasing memory density. This hierarchy functions in the following way:

1. Core – Central processing unit – consists of a logic unit, control unit and registers. Logic unit performs logical operations when called upon by the control unit which reads and interprets instruction from the memory. Registers are high speed storage areas which holds these instructions. (KBs)

[2] 1 Zettabyte = 10^{21} byte = 10^{9} Terabyte = 10^{12} Gigabyte

[3] End point data generators - include all devices on the edge of the network, including PCs, phones, industrial sensors, connected cars, and wearables – low power consumption

[4] Core system - consists of designated computing data centers in the enterprise and cloud providers – high power consumption

2. SRAM/ Cache memory – It is an on-chip memory accessed by the core to find data/ instructions and perform the next operations rather than accessing the off-chip main memory. (size - KBs to MBs)
3. DRAM/ Main memory – Off-chip memory which stores data or program code required by the core to function (size - GBs)
4. Storage memory – it stores virtually all the applications, operating software and programs required for a system to function which is accessed at the end (size – GBs to TBs)

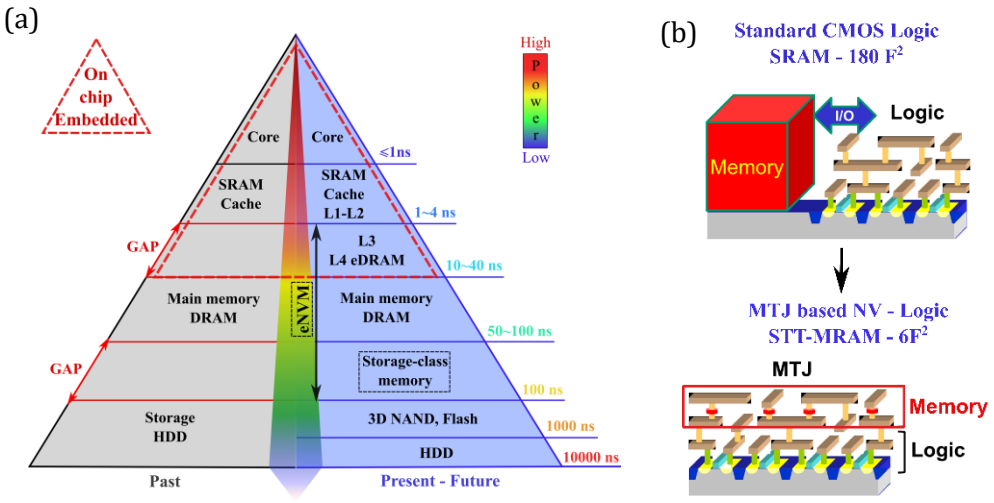

Fig. 3. (a) Comparison of past and present (also, future) of the memory hierarchy in an ICT system, logic components are embedded on the same chip, whereas memory elements are off-chip (standalone), Fig.4. (b) Advantage of emerging non-volatile memory which can be embedded on chip with logic rather than off-chip illustrated by an example of Spin Torque Transfer – Magnetic Random-Access Memory (STT-RAM), which improves the memory size with increased speed.

Depending on the application, be it high-performance computing (eg. data centres) or mobile computing (eg. electronic gadgets), this hierarchy remains the same with some modifications. The first three levels of hierarchy – Core, SRAM and DRAM are volatile memories, which means they must be powered to hold data, and are very fast with high endurance as they are accessed frequently. Whereas the storage memory is non-volatile in nature, and are slow with high memory capacity. All these techniques are based on charge storage mechanism (except hard disk drive – HDD). Over years, the logic components headed towards improvement in performance and on the contrary, main memory and storage memory towards increased density which has created performance gaps in the pyramid. This led to 2 issues in the hierarchy [12]:

1) *speed gap between different levels* – Core-SRAM (~1ns) to DRAM (~100 ns) to storage (~10000ns) present 2 significant speed gaps. SRAM, DRAM and storage memory have different underlying device structures due to their functionality which cause these performance bottlenecks.

2) *rapid increase in the power consumption due to increased density* – increase in the capacity of main memory to boost performance increased the power consumption. This is due to the volatile nature of DRAM as they require continuous stand-by power to function.

Progressively over years, to bridge the performance gaps to core, on-chip cache levels like L2, L3 were introduced and recently, L4 (embedded DRAM, on-chip) is speculated. Different DRAM variations were introduced to bridge the performance gap to the cache levels. Next, for storage, implementation of Flash memories (two types - NAND and NOR) improved the speed gap by 1 order of magnitude compared to HDD. As 2D scaling of device has its physical limitations, vertical integration of transistor was implemented to increase the memory density of 2D Flash. The technology progressed from 32 layers in 2012 to 232 layers in 3D NAND Flash (by Micron), introduced in 2022. This Flash memory is concerned with 2 problems – firstly, 2D scaling has reached its physical limits due to which very few charges are stored which affects data retention and reliability of the cell. And, secondly, an ultimate unknown of how many layers can be stacked for 3D integration. So, solutions are required to move away from the existing hierarchy, address performance gaps and new storage mechanisms for the sustenance of scaling.

- **Storage-class memory**

For modern computing systems, computing efficiency and power consumption benefit from keeping more data in the main working memory without the need of frequently accessing the information from storage memory. Addressing the area of DRAM to Flash, the charge-based memories come with a glass ceiling in terms of scalability in the future and might not provide enhanced performance with low power consumption at low cost, as stated. A solution to this problem is a group of innovative memories, commonly termed as storage class memories (emerging non-volatile memories - eNVM). They are developed to address the drawbacks and potentially replace major parts of the memory hierarchy. Storage class memory (SCM) is a concept which performs like a main working memory (DRAM) but with the capacity and non-volatility of storage memory (Flash), providing best of both worlds. Firstly, non-volatility means that SCM does not require continuous power supply to keep data, which saves power compared to DRAM. Secondly, SCM have Flash like memory density with faster access times like DRAM. This reduces the performance gaps for core to access DRAM and then Flash as SCM provides both functionalities. They can be implemented in both embedded and stand-alone applications. Embedded means that it can be fabricated directly above logic circuitry which enables drastic area and power reduction with improvement in data speed transfer, as illustrated in Fig. 4. They are resistive in nature, where the information is stored in the resistance of a material sandwiched between two electrodes. The resistive nature of the memory offers better scalability. Table 1 presents a comparison of the performance parameters of the typical memories and the new memory technologies., highlighting the advantages.

Following are the typical performance parameters of importance:

Speed (read/ write time) – this is related to the time required to access or save information in a memory cell/ transistor.

Energy (write power) - this represents the energy required to save information in a memory cell/ transistor.

Endurance – this refers to the number of saving / erasing operations a memory cell/ transistor can sustain before degrading.

Parameters	Typical memory technology			New memory technology				
	SRAM	DRAM	Flash (NAND)	FeRAM	ReRAM	PCRAM	STT-MRAM	SOT-MRAM
Non-volatility	No	No	Yes	Yes	Yes	Yes	Yes	Yes
Cell size (F^2)	50-120	6-10	5	15-34	6-10	4-19	6-20	6-20
Read time (ns)	≤2	30	10^3	≈5	1-20	≈2	1-20	≤10
Write time (ns)	≤2	50	10^6	≈10	50	10^2	≈10	≤10
Write power	Low	Low	High	Low	Medium	Low	Low	Low
Endurance (cycles)	10^{16}	10^{16}	10^5	10^{12}	10^6	10^{10}	10^{15}	10^{15}
Future scalability	Good	Limited	Limited	Limited	Medium	Limited	Good	Good

Table 1. Benchmark table of the performance of emerging memories and their comparison with typical memories. The filled green, yellow and red color indicate the desirable, intermediate and undesirable properties of corresponding technologies, respectively. To high-light, the future scalability of PCRAM is tagged as limited due to the fact that the technology is quite mature and already scaled down ($4F^2$) to the current scaling trends. F^2 represents the smallest 2D feature possible to manufacture [13]

The different types of these emerging non-volatile memories (eNVMs) listed in Table 1 are:

1. Ferroelectric memories (FeRAM) - Based on switching and sensing the polarization state of a ferroelectric capacitor to store data
2. Magnetic memories (MRAM)- Memory is stored in magnetization state of a material.
3. Resistive memories (RRAM) - Operates by changing the resistance across a dielectric by generating defects in it.
4. Phase change memories (PCM) - Based on resistivity differences between the amorphous and crystalline phase of a chalcogenide material.

For any of these technologies to replace the existing memories, it has to present a superior combination of scalability, cost per bit, endurance and performance. Development of these emerging NVMs have shown potential to replace different levels of hierarchy, as is evident from the comparison. Cost and ease of fabrication aspect becomes crucial in replacing the existing hierarchy. In the future, eNVMs could not only function as a storage class memory but also replace DRAM and SRAM [12].

Amongst these eNVMs, PCM appears to be the most mature candidate owing to its excellent cycling endurance, good scalability and low power consumption. PCM has been commercially realized for both, stand-alone and embedded applications. In 2015, Intel commercialized 3D XPoint memory product of 128 Gb capacity based on PCM. This technology is up to 1000 times faster and has 100 times greater endurance than NAND-Flash, and is 10 times denser than DRAM [14]. Recently, SK Hynix demonstrated a 256 Gb device based on PCM [15]. For embedded applications, PCM fairs better than its competitors due to a better cost point and high temperature stability. For example, PCM fairs better in ease of fabrication as the number of steps required are far less than its closed competitor MRAM, which helps gain a significant advantage from a cost perspective. For operation in automotive microcontrollers, the memory requires a robust high temperature operation and radiation tolerance which is offered by PCMs.

STMicroelectronics have developed a high density embedded PCM cell based on a 28nm FDSOI[5] technology for Automotive Micro-Controller Applications [16]. Progress of PCM shows it to be a promising candidate to change the memory hierarchy for both high end computation and embedded applications.

Objective of the thesis

Materials engineering has played a crucial role in realization of PCM as a viable technology. The principle behind PCM was discovered more than 50 years back and the first device was fabricated in 1970, coincidentally Dr. Moore was one of the co-authors. The idea did not pick its pace due to poor performance of the device. In 1990s, discovery of GeSbTe based chalcogenide phase change materials (PM) showed fast crystallization kinetics which paved the way for this mechanism to be implemented in optical storage media. Then in early 2000s, PMs were prototyped on CMOS structures as a simple two-terminal structure to be the next generation memory technology. Over these last twenty years, most of the ternary Ge-Sb-Te system has been examined to find the right material which can suffice the demand of a low-cost, high performance and higher endurance memory for SCM applications. Even though PCM consumes lesser power than Flash, it's still higher than its counterparts. This being said, the efficiency of a PCM cell is 1-2%, so there's a large room for improvement.

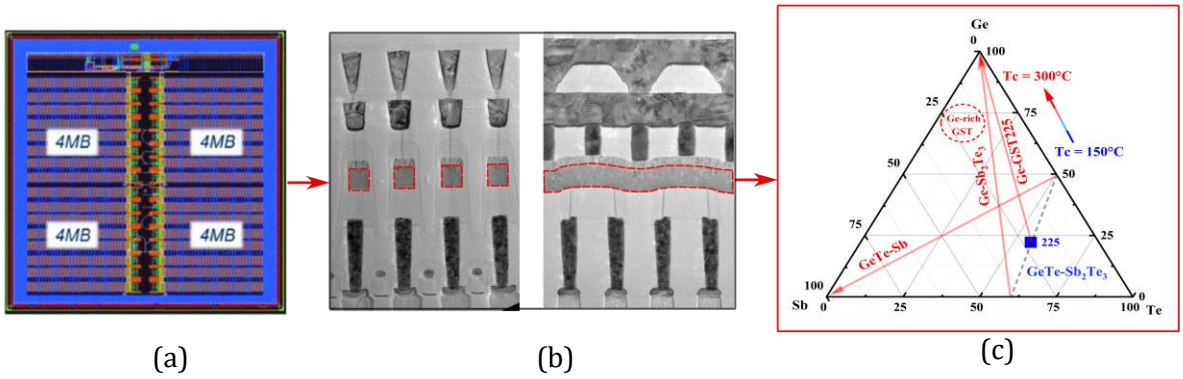

(a) (b) (c)

Fig. 5 Represents the outlook of the thesis from PCM cell to cell structure to the most crucial aspect – materials engineering. a). 16 MC PCM array layout , b). PCM bit cell TEM cross-section along word line and bit line with PM highlighted in red, c). Ge-Sb-Te ternary plot with the red arrows highlighting the direction for investigation of new compositions along various pseudo-binary lines. Enrichment of Ge in GST-225 increased the crystallization temperature from 150 to 300°C, crucial for high temperature stability of the material.

In PCM, the information is stored in the resistivity of the material. The basic mechanism for data storage is thermally assisted transitions from amorphous to crystalline, and vice-versa. The material is sandwiched between two electrodes to achieve the phase transitions. The flag-ship chalcogenide alloy – $Ge_2Sb_2Te_5$ (GST-225) paved the way for early development for PCM as it showed nanosecond switching times between the two material phases. The promising properties of GST-225 were not sufficient for its application due to issues regarding material reliability. Further investigation of alloys in the Ge-Sb-Te ternary family showed promising results

5 Fully depleted Silicon on insulator (FDSOI) – A planar process technology which provides solution to the limitations of bulk CMOS technology at reduced Silicon geometries and smaller nodes, while actually simplifying manufacturing process.

concerning the endurance and high-temperature reliability of the material, as highlighted in Fig. 5. For embedded applications, a combination of Ge-rich GST-225 with N doping demonstrated impressive performance at higher temperatures and has been extensively investigated in the past decade. The promising nature of this newly developed alloys has found application in the devices introduced but persists from ambiguity concerning its structural evolution with temperature and a big-unknown regarding its thermal properties.

- GeSbTe phase change materials undergo 2-3 phase transitions, initially upon crystallization and then a change in crystalline structure at higher temperature. It is key to know the underlying mechanism and temperature of these transitions, as they reflect a change in the transport properties of materials.

- Thermal properties of PM are important in the understanding and optimization of PCMs. Also, in the case of PCM, as it scales down, the neighboring cells come in closer proximity. The local temperature in a PCM cell is very high (>800°C) which can affect the memory stored in the neighboring cell. This phenomena of cross-talk can be tackled by thermal engineering of the material and interfaces as at nanoscale thermal boundary resistance becomes significant.

Investigation of thermal properties of PMs did not keep up pace with the constantly evolving material compositions. Also, it is advantageous to have a characterization technique which can provide simultaneous thermal and structural characterization of the material.

In this context, the objective of the thesis is towards development Raman thermometry for simultaneous structural and thermal characterization of PMs.

- Chapter 1 presents the working principle of PCM, key parameters concerning its operation, connection between device performance and material properties and a detail review of evolving phase change materials.

- Chapter 2 gives the current state-of-art of the thermal properties of phase change materials which is abundant with the analysis of the flag-ship material GST-225 but lacks information about the newly developed alloys. It elaborates on the critical parameters regarding thermal characterization of phase change materials and existing thermal characterization techniques available with their pros and cons. The key requirement for thermal characterization of phase change materials is availability of a technique which gives simultaneous structural and thermal characterization of the material.
- Chapter 3 introduces the technique of Raman thermometry coupled with finite-element simulations for thermal characterization and its implementation for phase change materials.

- Chapter 4 gives an in-depth analysis of the structural investigation of Ge-rich GST alloys and GeTe with Raman thermometry and in-situ XRD. Correlating the results of both techniques, a crystallization story is discussed which helps understand the high temperature behavior of these materials. The goal is to present Raman spectroscopy/ thermometry as a reliable structural investigation tool by correlating the results with XRD.

- Lastly, Chapter 5 reports the thermal properties of Ge-rich GST and Ge-rich GST N-doped alloys as a function of temperature supported with XRD and TEM results. It provides a key insight into the behavior of thermal properties of these newly developed materials which is not similar to the observations for other GST based materials. The effect of the decreasing nature of thermal conductivity of Ge-rich GST could be beneficial to reduce the thermal cross talk between PCM cells.

- Finally, conclusion of the thesis is presented with some future insights for the development of Raman thermometry and material characterization.

Chapter 1

Phase Change Memory – From device to material

The idea of storage systems based on phase change materials and its conception, dates back to the same period as that of the metal oxide silicon field effect transistor (MOSFET) system. The development had been static for a long time until its realization as an optical storage system in the 90's. Over the span of the last 3 decades, phase change materials-based system has evolved from being an optical based rewritable storage to being realized as a storage class memory with potential of replacing NAND Flash and dynamic random-access memory (DRAM).

To elaborate on this development and its realization as a memory in production, this chapter presents an overview of phase change memory cell, with key focus on materials evolution and thermal optimization. The first section presents a general idea of the phase change memory cell, its device operation and performance parameters. Building on this context, the link between the memory cell performance parameters and material properties is elaborated. A detailed evolution of PCM cell structure is presented with focus on thermal engineering. Then, the novel structural basis behind the phase transitions and evolution of phase change materials with stoichiometries tuned to its applicability as a memory device is elaborated. Finally, the chapter will focus on phase change materials integrated for embedded memory application.

1.1 Phase change memory

The principle of phase change memories (PCMs) was realized when the phenomenon of reversible electrical switching in disordered structures was measured by Ovshinsky [17]. Also, known as ovonic threshold switching (OTS), the mechanism causes a rapid and reversible transition in material when subjected to an external voltage. This effect is profoundly found in amorphous glassy semiconductors of group VI-A, especially chalcogenides, referred commonly to sulfides, tellurides, selenides and polonides. These alloys show 2 unique behaviors, the switching effect and the memory effect.

PCMs are based on the memory effect where the phase transition memorized in the material is not altered after cutting off the voltage source. This transition is between a high resistive state (amorphous) and a low resistive state (crystalline). These 2 resistive states denote the capability of material to store data in contrast phases of the material. This unique property of phase change materials has been exploited for its realization as a non-volatile solid state memory technology. The technology is primarily based on chalcogenide alloys, a ternary system of $Ge_xSb_yTe_z$ (GST-XYZ) alloys [18].

For perspective, the first evidence of this memory dates back to 1970, when a 256-bit read mostly memory (RMM) was fabricated [19]. The phase change material was sandwiched between molybdenum electrodes and the current was provided by a p-n diode to induce phase change with the cell size in order of μm (Fig. 1.1). Beginning from 1990's, massive developments on the materials and device structure front led to PCM being realized as one of the most mature non-volatile memory (NVM) candidate [20]. Fast forward to recent years, its capability has been commercialized as a storage class by Intel's 128 Gb 3D XPoint™ chip [21] and embedded-class non-volatile memory integrated in the sub-20nm node as reported in Fig. 1.2 [22].

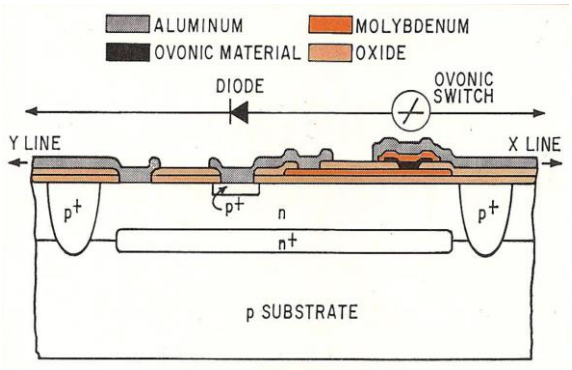

Fig. 1.1: A PCM device fabricated with amorphous film between 2 molybdenum electrodes with a silicon diode in series [19]

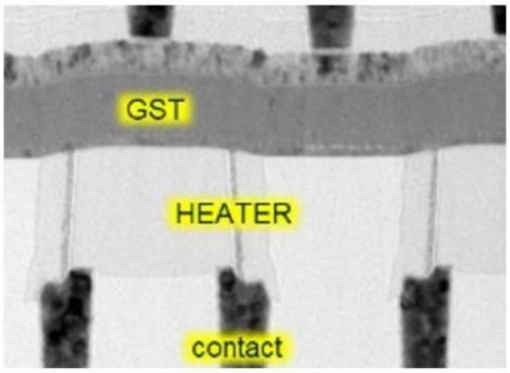

Fig. 1.2: PCM bit-cell of 0.019μm² embedded in 18 nm FDSOI [22]

Device principle:

As stated, phase change memories exploit the unique behavior of chalcogenide materials by reversible switching of the material between amorphous and crystalline phase, with high resistance contrast. The resistance in amorphous state is 3 to 4 magnitudes higher than the

crystalline state enabling the possibility of storing memory in form of "0" bit (low resistance – amorphous state) and "1" bit (high resistance – crystalline state).

The memory device is a two-terminal device with the phase change material sandwiched between 2 electrodes as presented in Fig. 1.3. The commercialized device can be broken down into 2 parts, the access device and the memory device-PCM cell. The access device acts as a selector of the PCM cell and provides current to it. Here, we present a common schematic of a PCM cell. The PCM cell consists of bottom electrode connected to the access device, heater, phase change material and top electrode. The phase change material, as fabricated is in crystalline phase. An electric pulse is applied via the heater and the Joule heating induced at the heater-phase change material interface leads phase transition in GST (dome - α).

By applying different amplitude of voltage pulses the material can be reversibly switched between amorphous and crystalline as illustrated in Fig. 1.4. Different types of electric pulses are applied to write, erase and read the bit stored in the cell. Types of electric pulses, to program the cell are:

1. RESET programming

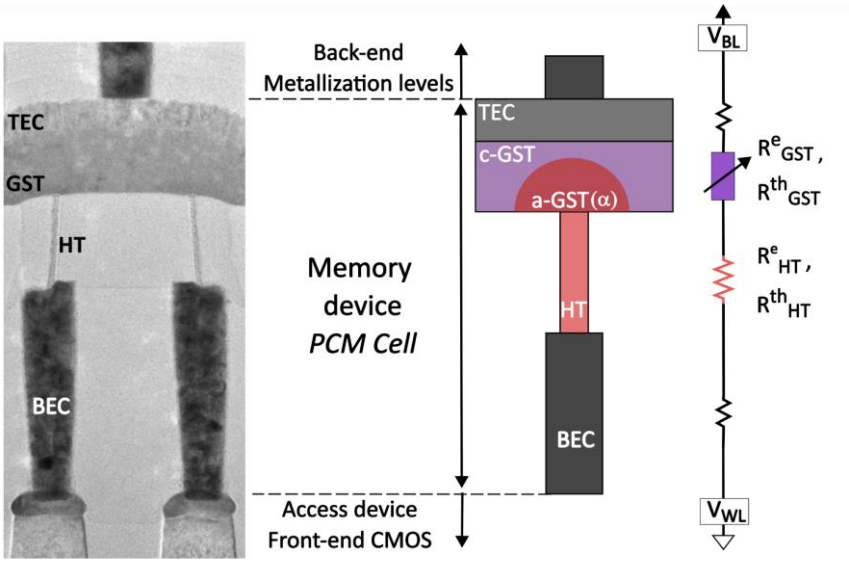

Fig. 1.3 Transmission electron microscopy (TEM) image[6] of PCM cells and an illustration of the PCM cell with GST and heater (HT) sandwiched between top electrode contact (TEC) and bottom contact electrode (BEC) controlled by word line (WL) and bit line (BL). A resistor scheme is presented alongside – GST acts as a variable resistor depending on the phase of the material. α – fraction of material switched

A short duration - large electric current pulse heats the crystalline state material to above melting temperature. Cutting off the pulse leads to immediate quenching of the material, and a dome shaped highly resistive amorphous state is obtained. This process is a power hungry as temperature above 600°C needs to be reached, which is the melting point of GeTe-Sb_2Te_3 alloys [23].

[6] Source - STMicroelectronics

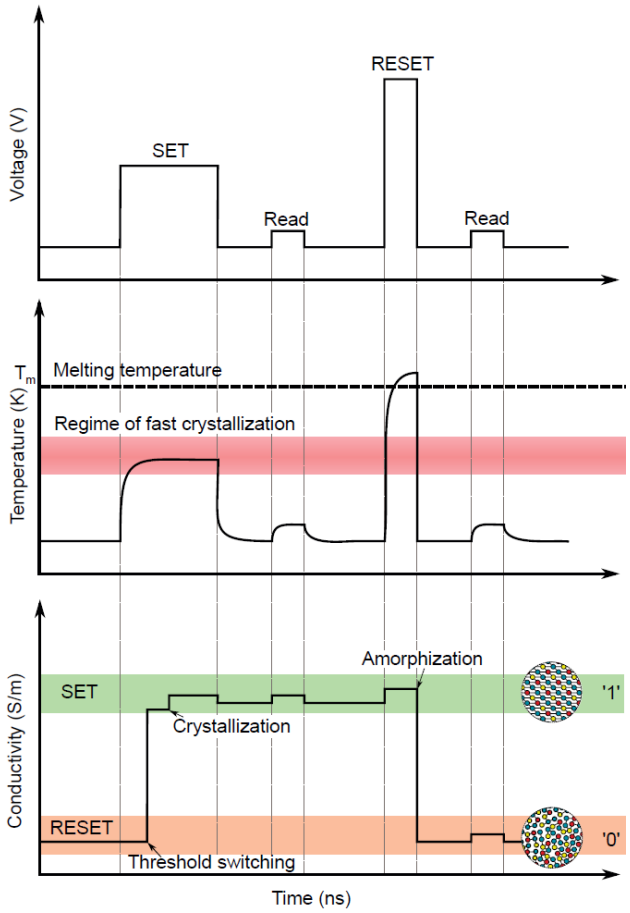

Fig. 1.4 Applied voltage pulse induced change in temperature and conductivity of GST. Programming of the PCM cell - SET programming (green – high conductivity region) heats the material in its crystallization regime to achieve amorphous to crystalline transition, RESET (orange – low conductivity region)a strong pulse melts the crystalline material and immediately quenched to achieve disordered amorphous phase. [24]

2. SET programming

A long duration - medium electric current pulse is applied to anneal the amorphous RESET programmed region (a-GST dome, Fig. 1.3). This increases the temperature of the material above the crystallization temperature and below the melting temperature. In this fast crystallization regime, the amorphous dome is annealed, the material reorganizes and switches the material back to crystalline state. The SET pulse and duration depends on the crystallization kinetics of the material. Hence, this crystallization speed dictates the write speed performance of the PCM

cell. In some present devices, a larger SET pulse is applied enough to melt the material (this SET pulse is still lower than the RESET pulse). This larger SET pulse has a slower down ramp which affects the cooling of the material and gives enough time for the material to crystallize.

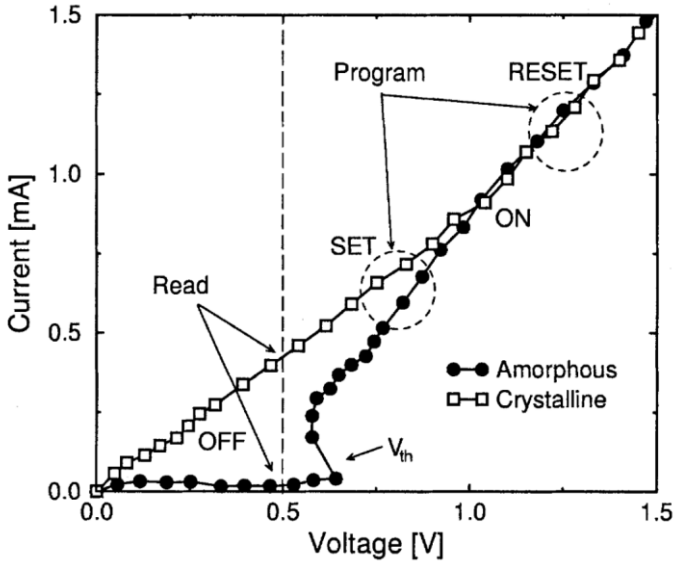

Fig. 1.5: Current as a function of voltage for operation of a PCM device [25]

3. Read

To read the state of the cell, a small current is passed to measure the resistance. The current is small enough to not alter the phase of the programmed region and sense the resistance state. The resistance of the two memory states ranges from few kΩ's (ON or SET state) to some MΩ's (OFF or RESET state).

Electrical behavior of the cell:

I-V curve of this operation is represented in Fig. 1.5. The "OFF" state represents the amorphous state of the material. In this state, the material follows a non-Ohmic behavior. Above a certain voltage (V_{th}), the electronic threshold switching effect occurs, inducing a snapback effect represented by negative differential resistance. The current density increases due to huge thermal generation of electric carriers. Threshold switching – snapback is an important characteristic of this PCM. Due to the high resistance of the heater, the temperature of the GST increases as the leakage from the heater increases, caused by Joule heating. After sufficient increase in temperature, the GST crystallizes - either by reaching the melting point and reorganizing during the cooling ramp, or by having enough time above its crystallization temperature, depending on the SET pulse applied.

Now, the structure of the material is ordered and cell achieves the low resistance crystalline "SET" state, signified by "ON" resistance. In this state, the material shows Ohmic behavior. For RESET, when the material is in crystalline phase, a high voltage bias induces Joule heating inside the heater and local temperature rises above the melting point of GST. The falling edge of the pulse cools the molten material and re-sets it into amorphous phase. The prompt quenching does not let the bonds rearrange and a disordered phase is formed. This bias point is denoted as RESET in the curve and a 50-100 ns current pulse is sufficient to form an amorphous plug. Whereas for SET, a relatively longer pulse is required and depends on the crystallization kinetics of the material. For reading, the operation is performed by biasing the cell with a few mV to sense the current flowing through it and reading the current. The biasing read voltage should be lower than

the threshold voltage in order to not affect the state of the PCM cell. This summarizes the basic working principle of a PCM cell.

1.1.1 Device functionality – Link between material properties and cell performance parameters

The device operation of a PCM cell can be further understood by describing an electro-thermal model. The electrical model is represented by current continuity equation:

$$\nabla \cdot J = -\nabla \cdot (\sigma(T,E)\nabla V) = 0 \qquad \textit{Eq 1-1}$$

In both programming cycles, different pulses are applied and the electrical model gives the spatial electric potential distribution in the memory cell. In this model, the electrical conductivity of GST is described by Poole-Frenkel conduction model which captures the nonlinear dependence of current on applied voltage in both phases of material [26]. The device during operation exhibits threshold switching where the conductivity of the material snaps from a low to high value associated with the electric field inside the material. The electrical conductivity is modelled as a combination of electric breakdown component and temperature dependent component [27]. The input current causes local heating in the material due to leakage from the heater and power is dissipated across the active region (GST). This leads to a temperature rise in the material, induced by Joule heating, where the temperature distribution can be evaluated by the heat diffusion equation:

$$\rho C_p(T)\frac{\partial T}{\partial t} - \nabla(\kappa(T)\nabla T) = \left(\frac{J^2}{\sigma(T,E)}\right) \qquad \textit{Eq 1-2}$$

Here, thermal diffusivity of the material accounts for the rate of increase of temperature in the material. Heat capacity for GST is constant with temperature (except liquid phase) but thermal conductivity is both, phase and temperature dependent. The peak temperature location is defined as the "Hotspot" of the device. The temperature at the hotspot and location plays an important role in defining the efficiency of the device depending on the topology of the device [28]. For stationary conditions it can be predicted by:

$$\nabla^2 T = -\left(\frac{J^2}{\kappa(T)\sigma(T,E)}\right) \qquad \textit{Eq 1-3}$$

Further, heat dissipation pathways can be understood based on the temperature distribution in the PCM cell. To sum up, thermal and electrical properties of material, their temperature and field dependence and the geometry of the cell play an important in understanding the operation of the cell and its optimization.

Performance metrics:

RESET and SET programming cycles are the basis of storing information in PCM device by switching the phase of the material. Characteristics of the pulse required to program the cell, and the threshold voltage are key metrics to define the performance of a PCM cell. These performance metrics are influenced by the material properties and the device geometry. Table 1.1 summarizes the influence of different material properties on the characteristics of PCM device performance.

Phase change material parameter	Influence on PCM device performance
Crystallization temperature and thermal stability of the amorphous phase	Data retention and archival lifetime SET power
Melting temperature	RESET power
Resistivity in amorphous and crystalline phases	ON/OFF ratio SET and RESET current
Threshold voltage	SET voltage and reading voltage SET and RESET power
Thermal conductivity of both phases	SET and RESET power
Crystallization speed	SET pulse duration ,Data rate
Melt quenching speed	RESET pulse duration

Table 1.1: Link between phase change material properties and PCM device performance parameters [29]

The programming cycles are correlated with the material properties as follows:

1. RESET Programming

RESET is a power-hungry process which requires a strong current pulse to melt the crystalline material in its "ON" state and quench it to amorphous phase. In the planar device geometry (PCM cell illustrated in Fig. 1.3), the cell can be viewed as a combination of the heater resistance and a variable GST resistor. The correlation between power generated (P_{gen}) to increase the hotspot temperature (T_{HS}) to melting temperature can be given by,

$$\Delta T = T_{HS} - T_{ambient} = \alpha P_{gen} R^{th}, \qquad \textit{Eq 1-4}$$

$$where\ \frac{1}{R^{th}} = \frac{1}{R^{th}_{HT}} + \frac{1}{R^{th}_{GST}}, \left(R^{th}_{HT} = \frac{1}{k_{HT}} \frac{l_{HT}}{A}, R^{th}_{GST} = \frac{1}{k_{GST}} \frac{l_{GST}}{A} \right)$$

The power generated (P_{gen}) across the cell for an applied melting current is dependent on R_{ON}, which is the cumulative electrical resistance of the cell in ON (crystalline) state,

$$P_{gen} = R_{ON} \cdot I^2_{melt} \qquad \textit{Eq 1-5}$$

Melting current can be modeled by combining equations (1-4) and (1-5) as,

$$I_{melt} = \sqrt{\frac{\Delta T}{\alpha R_{ON}} \left[\frac{1}{R^{th}_{HT}} + \frac{1}{R^{th}_{GST}} \right]} \qquad \textit{Eq 1-6}$$

So, to optimize the metrics of melting current, material properties and device dimensions have to be tuned. I_{melt} can be decreased by scaling the PCM cell and increasing the thermal resistivity of the materials. But it leads to an increase in R_{ON} as illustrated in Fig. 1.6. This can degrade the readout resistivity window and SET operation, as increase in the R_{ON} would make the SET process requiring more power. So a tradeoff between I_{melt} and R_{ON} is essential.

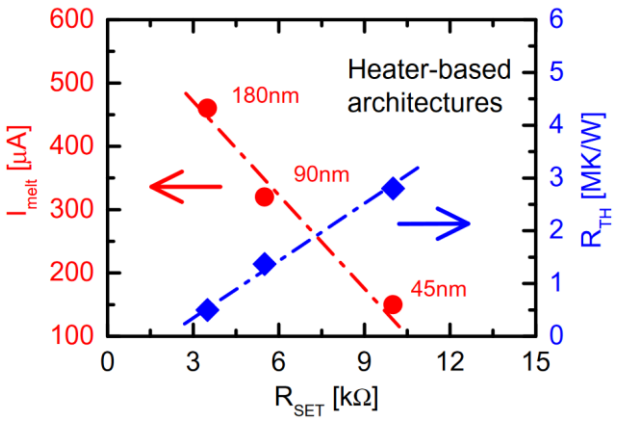

Fig. 1.6: Influence of scaling on melting current (I_{melt}), thermal resistance (R_{TH}) and SET resistance (R_{SET}) [30]

Concerning the speed, heating and the quenching transient are dependent on the thermal diffusivity of the material. The quenching transient during RESET cycle is given by,

$$\tau_{th} = \frac{C_p}{\pi^2 k_{GST}} r^2 \qquad \textit{Eq 1-7}$$

where r is the radius of spherical hot region (α), C_p is heat capacity of the material and k_{GST} is the thermal conductivity of GST. A cooling rate of 10^{11} K/s can be achieved to freeze the liquid phase in a disordered state and electric pulses as short 400 ps have been reported for RESET pulse [31]. With regards to scaling the device, as the cooling transient scales with the square of the cell dimensions the thermal delays are not expected to pose any limitation to the PCM speed.

2. SET Programming

SET pulse is comparatively slower and defines the speed of the device. The crystallization temperature and kinetics of the material dictates the SET cycle operation. During the crystallization of an amorphous phase, small and unstable clusters are created which upon reaching a critical size become a stable nuclei and grow. The time required to reach the critical size is the incubation period which retards crystallization. Depending on the pre-treatment of the PCM cell, the crystallization can be growth dominated or nucleation dominated. Generally, the as-fabricated device is in crystalline state and the RESET programming defines the amorphous mushroom-type dome. During SET cycle, the crystal nucleation can take place from inside the mushroom and crystal growth from crystalline-amorphous interface. Crystallization kinetics of the material plays an important role in determining the SET pulse and hence the speed of PCMs. The crystallization time (or failure time) follows an Arrhenius dependence:

$$\tau_{crys} = \tau_0 e^{\frac{E_A}{kT}} \qquad \textit{Eq 1-5}$$

The activation energy largely depends on stoichiometry and for a 10 years data retention above 85°C, E_A is reported to be in the range of 2. 5-4.0 eV [32]. Failure time of the PCM cell can be defined as the time required for the resistance to decrease to half of its initial value. This value occurs at a specific temperature, which defines the standard 10-year data retention for the cell

following the Arrhenius law. The temperature criteria for data retention can be improved for high temperature applications by improving the crystallization temperature and thermal stability of the phases. The crystalline phase is thermodynamically favorable but its kinetics are slower compared to the speed of formation of amorphous phase. The thermal stability of the material relies on its activation energy, which results from a combination of nucleation and growth phenomena, which also influence the programming speed [33]. So, the specifics of the crystallization process and hence the SET speed, defines the data rate of PCM technology.

3. Material properties and reliability

Crystallization temperature and amorphous phase thermal stability are key to the PCM cell reliability. The melt quenched amorphous phase evolves over time as the memory is continuously switched back and forth. The region which transitions back and forth can change which causes a drift in resistance of the amorphous phase affecting the resistance window. The RESET resistance falls and the phases are no longer distinguishable, affecting ability of the memory to retain data over a period of time.

Continuous cycling of memory over its lifetime tests the reliability of material. Switching of the material leads to a change in density as crystalline density is higher than amorphous can introduce voids in the material. For some stoichiometries, atomic migration, phase segregation and voids formation were observed which leads to failure of device.

Materials are engineered to have high crystallization temperature to achieve high thermal stability of the amorphous phase. This is to avoid accidental crystallization due to high working temperatures. Stand-alone memories qualify with a low temperature requirement, but embedded memory application need thermal stability above 165°C. Extensive materials engineering performed for realization of PCMs are presented in the next part of the chapter.

1.1.2 PCM device architecture

The PCM cell consists of the memory device and an access device. The fabrication process integrates the PCM cells in the back-end-of-line (BEOL) on the top of existing Complementary Metal-Oxide-Semiconductor (CMOS) circuitry. So, the size of the existing access devices largely dictates the size of the memory cell. The access device provides the means to write and read the individual memory cells. They should be capable of supplying high currents required for RESET operation in excess of $1MA/cm^2$ [34], maintain a high ON/OFF ratio and an adequate signal-to-noise margin. Various access devices like Metal-oxide-semiconductor field-effect transistors (MOSFETs), bipolar junction transistors (BJTs), diodes have been implemented.

Comparing the access devices according to minimum feature size (F) for a programming density of $10MA/cm^2$, diodes can have a minimum $4F^2$ layout area, for BJT the footprint ranges from 5.5 to $8F^2$ whereas for MOSFETs can be $8\text{-}10F^2$ [34]. For MOSFETs, the footprint increases for increase in requirement for programming current unlike the vertical structure of diode or BJTs. Scaling rules also suggest that constant voltage drop with scaling could be an issue for MOSFEET devices but BJTs should sustain [35]. The pace of scaling of both the devices is crucial for the PCM cell to evolve parallel with progressing technology nodes as summarized in Table 1.2.

The key to scaling and optimizing the performance of cell was targeted towards minimizing power consumption or the large programming current required by the PCM cell. This would reduce the stringent current requirements posed on the access device. In the conventional PCM

cell, the current is passed through an aperture which increases current density and maximizes thermal power generation due to Joule heating. Two different approaches were followed to minimize the power requirements.

	Parameters	Factor (k>1)
PCM	GST-heater contact area	$1/k^2$
	GST thickness	$1/k$
	Heater height/ thickness	$1/k$
	SET/ RESET resistance	k
	Thermal resistance	k
	Threshold voltage	$log(k)$
	Programming voltage	1
	Programming current	$1/k$
BJT	Emitter area	$1/k^2$
	Base thickness	$1/k$
	Emitter current	$1/k$
MOS	Gate length	$1/k$
	Width	$1/k$
	Saturation current	$1/k$

Table 1.2: Scaling rules expected for PCM also known as Ovonic Unified Memory (OUM), MOS and BJT if each geometric dimension is scaled by a factor of k>1 [35]

The first approach can be termed as "contact minimized". Here, the way to reduce the large RESET current required would be to increase the heater resistance by minimizing the aperture contact area. Different back electrode contact or heater configurations like mushroom, edge, wall, μtrench, and ring shaped heaters connected to a planar phase change layer were studied. The other approach is termed as "volume minimized". Here, the goal is to reduce the size of the programmable volume where the heater and phase change material is confined defining the critical dimensions. Cell configurations are illustrated in Fig. 1.7.

Here, we illustrate the progress of PCM device geometries with scaling and performance parameters. The first state of art device demonstrated feasibility of PCM for stand-alone and embedded applications at 180nm node [20]. The mushroom bottom contact-based device showed fast switching speed of 50ns for SET and 30ns for RESET pulse with high endurance of 10^{12} cycles but programming current in the range of 1mA. The first edge contact device (Fig. 1.7 (e)) at 240nm node presented way to form smaller contacts easily, showcasing the possibility of lowering the reset current to 200μA [36]. The drawback with edge contact being a lateral structure is larger layout area. The primary requirements for commercialization for PCM are high density of cells with lower power consumption, fast programming cycles and high endurance.

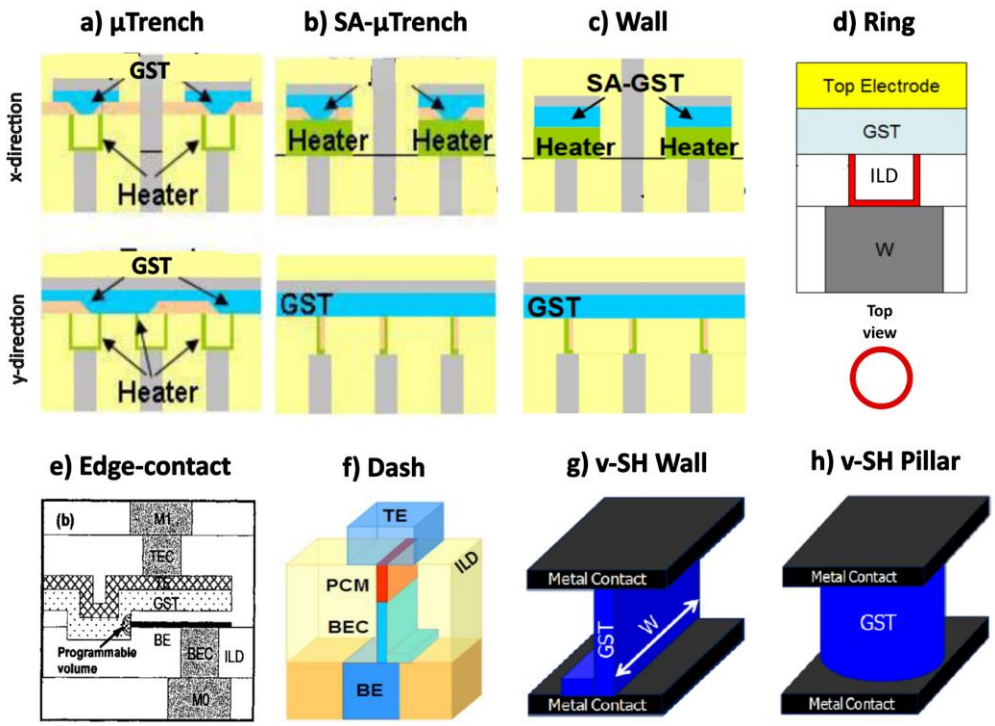

Fig. 1.7 Schematic of cell structure evolution: X and Y direction view for a) µTrench, b) Self-aligned (SA) µtrench [37], c) Wall [38], d) Ring type with top view of heater cross-section [39], e) edge-contact [36], f) Dash (volume minimized) [40], g) vertical-self heating wall and h) vertical-self heating pillar architectures [41]

In 2003, scaling studies showed possibility of reducing the basic memory element in bottom contact devices to 22nm leading to an increase in heater resistance and hence current reduction to 35µA [18]. The challenge would be showcase high density, volume manufacturability and reliability of cells. So further, heater geometries like µTrench and mushroom cell were experimented and integrated at 90nm with a $12F^2$ BJT selector [42]. µTrench with a contact area of $400nm^2$ functioned with 400µA programming current and mushroom cell with a contact area of $3000nm^2$ required 700µA. It was possible to achieve such low contact for the µ-trench heater by sub lithographic techniques. Further, a self-aligned µ-trench solution was introduced which simplified the etch and lithographic requirements by reducing the number of fabrication steps [37]. This simplified the integration at 90nm, reduced the programming current requirement to 300µA. Wall based architecture was next fabricated by reduction of 1 mask step compared to SA-µtrench. This was integrated at 45nm using an innovative double shallow trench isolation for defining BJT access device [38]. This device showed further reduction in I_{RESET} to 200µA with an effective cell size of 0.015µm2 for a 1Gb product. Other ways implemented were ring type heater [39], where the current flows through the contact hole instead of the entire heater minimizing the contact area and hence, I_{RESET}.

Over years, wall-based architecture was found out to be the easiest solution from a technology standpoint due to better lithographic alignment tolerances and programming current controllability for embedded applications [43]. Studies for wall architecture focused on minimizing the power consumption (R_{SET}*I_{RESET}) as power consumption is crucial for

optimization of PCM cell [41]. The scaling of width of the heater that is the aperture, I_{RESET} is lowered but an increase in R_{SET} and R_{TH} leads to insignificant shift in power consumption. It was observed that scaling the heater length down to 50nm, does not affect the power consumption, whereas decreasing the thickness of GST lowers R_{SET}*I_{RESET}. This indicates that the preferential heat dissipation path is towards the top electrode and not towards the bottom electrode. But further scaling of heater length, increases power consumption abruptly as heat dissipates towards the bottom electrode leading to inefficient programming. A possible optimization region is depicted in Fig. 1.8 to find the right balance.

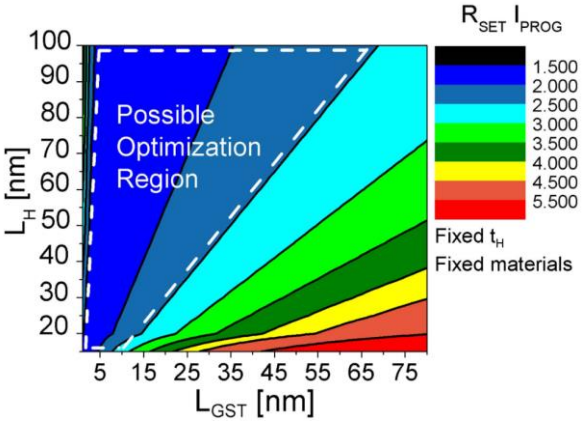

Fig. 1.8 Contour plot of R_{SET} .I_{PROG} as a function of heater height (LH) and GST thickness (LGST) with the dash defined area highlighting the optimization area for lower power consumption [41]

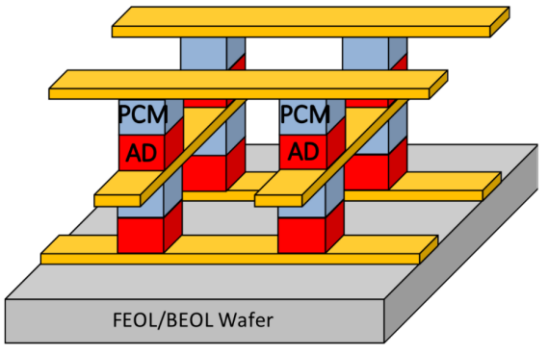

Fig. 1.9 3D cross-point memory structure of a PCM storage element in series with a generic access device (AD) [14]

For the other approach of confining the phase change material and the heater, the current localization and thermal isolation significantly reduced the programming current. The dash-type confined cell presented for a sub-20nm node showed exceptional results for a 7.5 wide cell [40]. The I_{RESET} of 160µA and SET speed of 50ns with similar Vth compared to the conventional planar cell. It can be easily scaled down because the minimum size of the cell is not defined by conventional photolithography but by film thickness which can be well controlled down to few nanometers [44]. For confined cells, it was possible to achieve $4F^2$ size and 10^{15} endurance cycle which is on par with DRAM application requirements without having the DRAM scaling limitations. The dash-confined approach evolved further by using a metallic liner surfactant around GST to provide an alternate path for multi-level computing [45]. The cross-point structure as illustrated in Fig. 1.9, further presented the capability of 3D stacking of memory cells. This cell was prototyped with the feasibility of a 4-deck structure [15].

The main challenges to find the right combination of I_{RESET} and R_{SET} to decrease the power consumption along with scaling were progressively achieved. Scaling results and state of art devices for both wall-based heater and confined architecture, present possibility of scaling under 20nm node. Innovative selector devices like BJT [46], poly-Si or selective epitaxial growth diodes and ovonic threshold switches can be scaled as they are based on a vertical structure. The wall heater based structures are currently commercialized for embedded application and cross-point for storage applications.

1.1.3 Thermal engineering of PCM

In PCM, during the programming cycles heat conducts via the bottom electrode, heater and then the phase transitions occur in the phase change material. This thermal conduction via the interfaces to electrodes, dielectrics or phase change material defines the programming time, current and power consumption. It is crucial to understand the heat dissipation mechanisms of the PCM cell to further optimize its heating efficiency. The heat loss pathways for the RESET operation for both planar and confined cell geometries suggest that less than 1% energy is utilized in phase transitions Fig. 1.10 [47], [48]. Whereas, most of the energy is lost via the metal and dielectrics. 61% of heat is lost via the heater in case of planar cell as it is the most thermally conductive path and 89% laterally via dielectrics in case of confined cell geometry as the dielectric contact area is much larger. Lowering of programming current can be achieved by strong confinement of heat in the electrodes and dielectric.

Studies presenting engineering of heater - TiN material and configuration leads to reduction of the thermal conductivity and so the programming current, significantly. Deriving from the ring shape PCM cell, configuration with a TaN thermal barrier encapsulating the TiN heater forming a ring shape was proposed. It avoids ohmic contact with the bottom electrode blocking heat dissipation paths [49]. This configuration showed a 75% reduction in programming current. TiN/TaN super-lattice configuration has higher carrier scattering sources which lowers the thermal conductivity to 1.5-2 $Wm^{-1}K^{-1}$ instead of 19 $Wm^{-1}K^{-1}$ for bulk TiN [50]. Further engineering of the TiN/TaN heater geometry presented more ways to optimize the RESET characteristics [51].

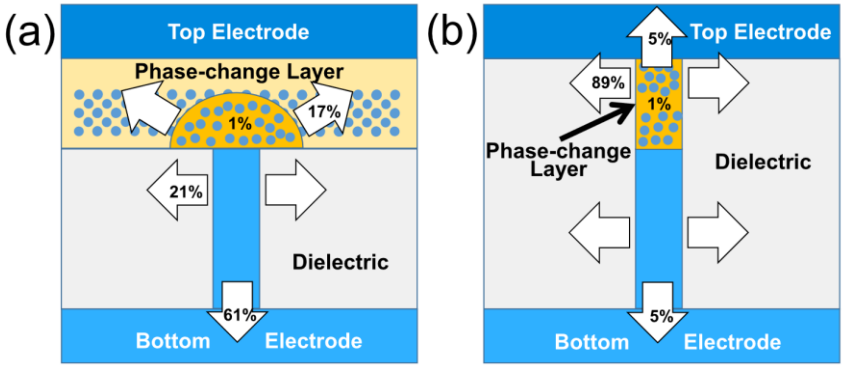

Fig. 1.10: Schematic of a) typical planar heater-based cell and b) confined cell. Arrows highlighting the heat loss paths and energy stored in the phase change layer during RESET operation of the cells [48]

Thermal confinement via dielectric engineering also influences the energy required for RESET operation. Studies have shown that implementing a lower thermal conductivity dielectric encapsulating the phase change layer and the heater can reduce the programming energy requirements Comparison between a dual-layer dielectric stack of Al_2O_3-SiO_2 with SiO_2 showed a 60% reduction in RESET energy [52]. Recent study for a wall-based architecture, showed a decrease in energy requirements by surrounding the heater by SiC instead of SiN decreasing the thermal conductivity of dielectric from 1.4 to 0.4 $Wm^{-1}K^{-1}$ [53].

Now, we move to the interfaces between the GST, inter layer dielectrics and heater via which most of the heat is dissipated. Thermal boundary resistance (TBR) plays an important role in enhancing heat confinement. Scaling of the devices makes TBR more significant as it is comparable to bulk thermal resistances. By engineering thermal anisotropy at the interfaces, without degrading the electrical properties can reduce the programming current significantly. Introduction of fullerenes between GST and the bottom electrode reduced the reset current by a factor of 4 [54]. Another study for a confined cell, introduced TiO_2 at both GST-electrode interfaces showed a reduction in current by 65% [55]. A carbon-liner at the interface of top electrode and GST for a confined cell reduced the current by 60% [56]. For perspective, a TBR of 50 $m^2K(GW)^{-1}$ reduces programming current by 20% and 30%, for 25nm and 75nm thickness, respectively Fig. 1.11 [57]. Fundamentally, these developments are based on acoustic mismatch and diffuse mismatch models which describe TBR as the partial transmission of phonons across interface. Materials with larger acoustic mismatch have larger TBR and provide better thermal insulation to the active region of PCM cell [58]. Different 2D materials can be introduced at the interfaces to improve the thermal insulation Fig. 1.12 [59].

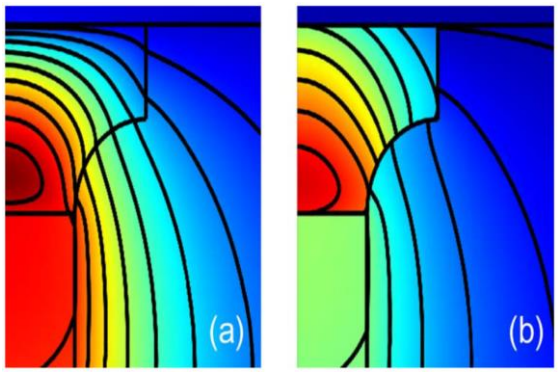

Fig. 1.11: Temperature profiles for reset simulations with GST thickness of 50 nm. (a) No TBR is applied between the GST interfaces. (b) Result of a TBR of 50 $m^2K(GW)^{-1}$. The temperature scale is the same in each figure. The peak temperature in (a) is 1092 K with a programming current of 1.6 mA, and the peak temperature in (b) is 1015 K with a programming current of 1.2 mA [57]

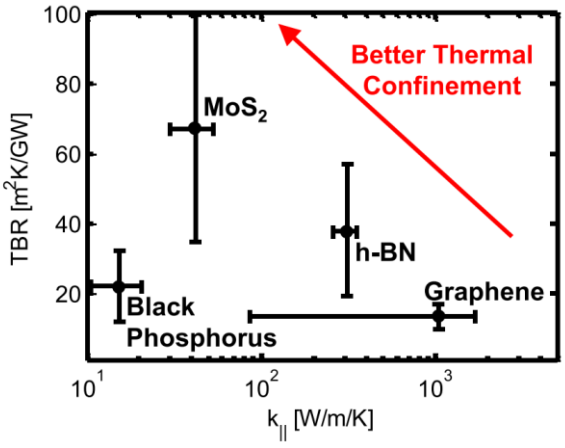

Fig. 1.12: Comparing thermal properties of some common 2D materials implemented at the interface of heater and GST, where experimental data is available: range of measured thermal boundary resistance (TBR) vs. in-plane thermal conductivity ($k_{||}$). Overall, better thermal confinement for PCM could be achieved using 2D material interfaces with lower $k_{||}$ and higher TBR [59]

Thermal boundary engineering at top and bottom electrodes showed a significant improvement in power consumption. Thermal resistance of heater/ GST/ TBR plays a crucial role in optimizing the performance of a PCM cell. For a confined cell the thermal boundary resistance of GST and thermal conductivity of heater dominate the temperature dependent thermal resistance. While for a planar cell configuration, GST thermal conductivity plays a greater role.

1.1.4 Current PCM standpoint

In the memory hierarchy, PCM has the potential to replace different components from hard drives, FLASH to DRAM. Depending on the application, be it stand-alone or embedded memory applications, the requirements vary. The operating temperature requirements for stand-alone is a moderate 85°C, but for embedded memory automotive applications the requirement stands at 150°C. These requirements along with the ability to retain data over 10 years can largely be correlated to the crystallization temperature, activation energy and thermal stability of the phases. The switching speed requirement ranges from µs to ns, which relies on the crystallization speed, and so on the material stoichiometry. In the case of endurance, 10^5 cycles are required to for FLASH applications, 10^8 for storage-class applications but a very high 10^{14} benchmark to replace DRAM.

PCMs have so far demonstrated cycles upwards of 10^8, depending on the architecture, material stoichiometry and application [60], [45], [61]. As PCM is a unipolar two-terminal device, reversing of polarity is not required to program opposite states. This enables the possibility to supply current by diode and BJT, instead of a MOSFET making its scalability better. Programming mechanism makes it immune to read disturbance along with a wide ON/OFF ratio compared to

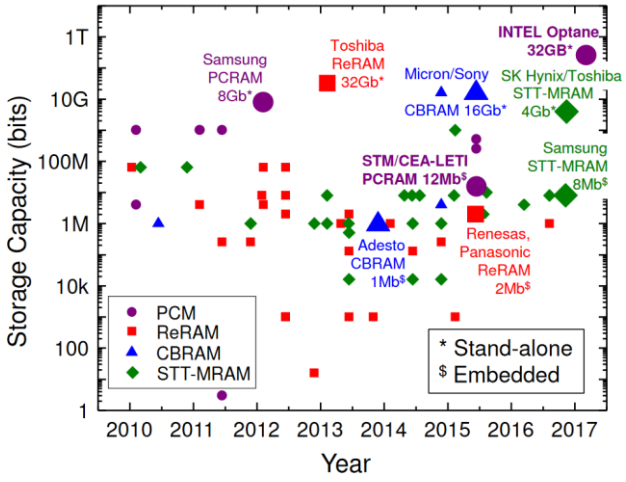

Fig.. 1.13: Storage capacity evolution along the years of different embedded and standalone non-volatile resistive memory technologies [33]

other NVMs [43]. In terms of storage density point of view, bits of 5nm are predicted to be thermodynamically stable which provides a feasibility of storage at Tb/in^2 and beyond [62].

State of art PCM devices demonstrated in the beginning of this century proved its potential as a most mature candidate amongst the non-volatile memory technologies. Compared to FLASH, its proved better read and write speed, lower power consumption, scalability and added advantage of bit-alterability led to its commercialization in 2010. The key characteristics required were fast SET and RESET speed (ns-µs), data retention, higher cycling endurance (1M cycles) and low programming energy (pJ) which enabled its introduction as a stand-alone memory product. Its CMOS and back end of line compatibility gives an added advantage of integration into any existing technology node. Intel presented this capability by introducing 128 Gb 3D XPoint™ chip which was reported to be 1000 times with respect to both, speed and endurance than NAND Flash along

with being 10 times denser than DRAM [14]. These devices are based on a novel cross-point structure (like dash-confined) with ovonic threshold switches (OTS) as the access device to the memory cell. The design of the cell provided excellent scalability with a $4F^2$ footprint and vertical stacking of cell making it possible to achieve effective area of $4F^2/L$.

Being a BEOL memory, its low temperature integration does not affect the FEOL transistors and its performance. For embedded automotive applications, the key requirement is high temperature data retention. The automotive compatibility standards set the criteria for 2 years at 150°C and sustain the soldering reflow thermal profile. This was achieved by materials engineering which will be seen in the next section. The reduction in power requirements by device and materials engineering, made its integration possible with the existing transistors in standard CMOS. For embedded class, STMicroelectronics has demonstrated its capability of a 16 MB PCM for a 28nm FD-SOI MCU application [63].

1.2 Phase Change Materials

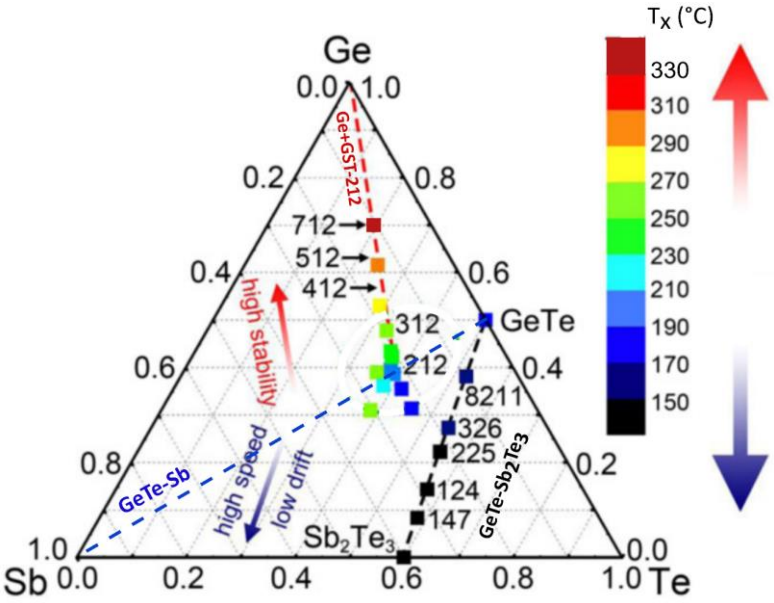

Fig. 1.14: Ge-Sb-Te ternary diagram presenting the crystallization temperature of different compositions ($Ge_xSb_yTe_z$ – GST-XYZ) as a function of crystallization temperature. The dashed lines present compositions investigated along different pseudo-binary lines [64]

Phase change materials primarily belong to the chalcogenide family of group VI-A elements. The first evidence of the reversible switching for potential memory storage was discovered with TeAsSiGe chalcogenide [17]. The first device for electronic storage of memory (Read Mostly Memory) using chalcogenide was fabricated as early as 1970's. The memory had high endurance cycles but the low switching speed (ms) and high power consumption (>10V) evidenced, inhibited its progress [19]. Over 2 decades later, the memory effect was implemented for optical storage of memory by the discovery of GST-225 [65] and AIST [66], triggered by nanosecond switching times. The alloys along the pseudo-binary line of GeTe-Sb_2Te_3, most notably GST-225 [23], showcased large optical and resistivity contrast between the amorphous and crystalline

phase. Further, materials exploration along the pseudo binary lines and device engineering led to realization of stand-alone memory devices by early 2000's. Materials have been engineered on basis of requirements with varying stoichiometries for high speed and high thermal stability devices as presented in Fig. 1.14.

The stoichiometry and the structural understanding of GST alloys has evolved over years and especially focused on the in-depth analysis of the flagship GST-225. Here, we try to give a brief overview of the structural details of amorphous and crystalline phase of the GST ternary system. We begin with an analysis of compounds along the pseudo-binary GeTe-Sb_2Te_3 tie-line, GeTe-Sb tie line and then move towards Ge-rich GST.

1.2.1 Meta-stable and stable crystalline phase

The pseudo binary system of GeTe-Sb_2Te_3, over its composition range shows two types of crystalline phase: a) A meta-stable phase NaCl type cubic phase and b) a stable hexagonal or rhombohedral phase depending on the stoichiometry. Beginning on the tie-line from GeTe, the structure is characterized by a high temperature cubic phase and a low temperature rhombohedral phase and at the end, Sb_2Te_3 has a rhombohedral structure [67]. As we move along the tie line, away from GeTe, the compounds up to GST-8211, compounds have structural characteristics similar to GeTe consisting of 2 phases. The general rule is that a crystallized amorphous thin film, crystallizes into NaCl type cubic phase from x= 0 to 2/3 in GeTe(1-x)-Sb_2Te_3(x) system [68]. Now, as Sb_2Te_3 content increases further, we move towards GST-225 and GST-124 which are favorable for the data storage application due to fast switching speeds.

GST-225 has 2 crystalline phases: a) A stable trigonal structure[7] and b) a metastable NaCl-type rock-salt cubic structure [69]. This was found for both laser irradiated or sputter annealed thin films [70]. In the cubic structure, Te atoms always fully occupy the Na octahedral lattice sites, whereas Ge and Sb atoms randomly occupy the Cl-octahedral lattice sites with 20% vacancies, leading to a distorted structure as illustrated in Fig. 1.16 [70]. The structure of GST-225 can be viewed as a cubic closed pack structure with 9 layered stacking of a particular Ge-Sb-Te sequence [71]. Along the tie-line, as Sb_2Te_3 ratio increases, vacancies are intrinsically generated and the % of vacancies increases starting from 8% for GST-629 to 25% for GST-124 as reported [72]. Presence of vacancies leads to a 20% presence of 6-membered rings with majority being 4-member rings. The stacking arrangement of the compounds also changes with change in stoichiometry, with 9-layered stacking of GST-225, 21 layered stacking of GST-124 to 12 layered stacking of GST-124 illustrated in Fig. 1.15 [71]. These metastable structures with ordered stacking sequence are preliminary for transition from distorted rock-salt like structure to a stable trigonal phase. Formation of trigonal phase requires a higher thermal budget to form long range order and a closed pack denser structure.

[7] GST-225 has a stable trigonal phase (or equivalently rhombohedral). In this manuscript, the phase of GST-225 and for Ge-rich GST (GST-225 based) compositions is stated as trigonal and not hexagonal (as indicated in several articles for GST-225).

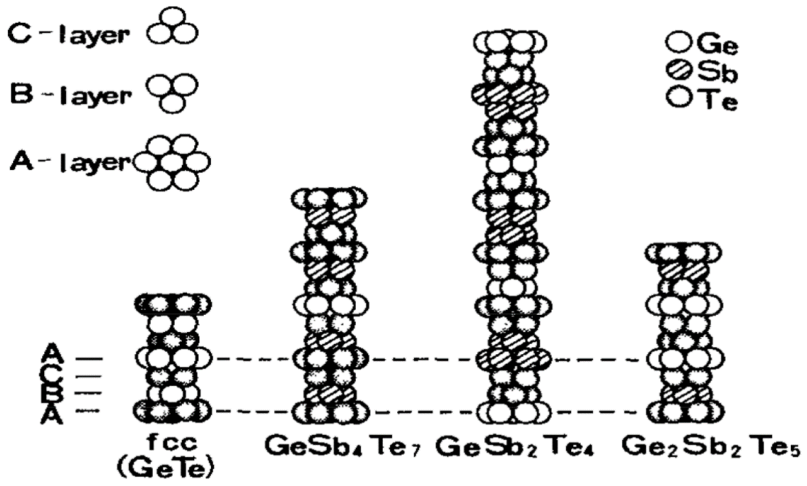

Fig. 1.15: Stacking models of three ternary compounds in GeTe-Sb2Te3 pseudo binary system and GeTe based on regular FCC stacking forming long periodical hexagonal lattices [23]

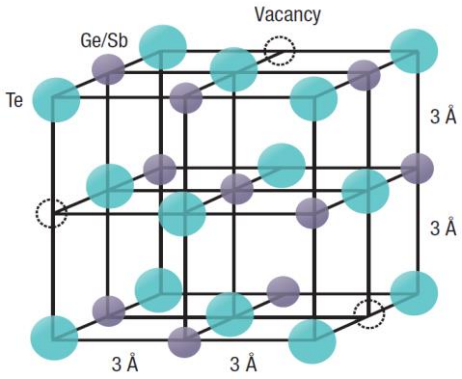

Fig. 1.16: Crystal structure of the rock-salt like phase of GST-225 [73]

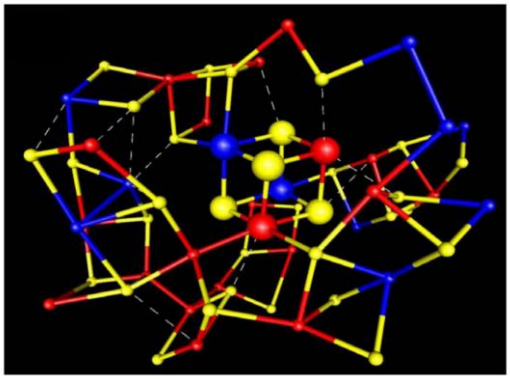

Fig. 1.17: Amorphous phase structure illustrated with local environment of ABAB cube. Red, Ge; blue, Sb; yellow, Te [74]

In this structure, crystalline phase does not follow the 8-N rule for covalent bonding, which defines the co-ordination number followed by each element. Here, this rule is stretched with an

octahedral setting. It is dominated by resonant bonding, where half-filled p-bonds form two bonds in both directions which leads to increase in electronic polarizability of the atoms. This provides the crystalline phase with long range order.

In summary, the alloys crucial for storage applications are characterized by a distorted metastable structure with Te occupying one octahedral site, and Ge/Sb occupying the other site with presence of vacancies and long-range order. This underlying structure, with presence of vacancies and p-bonding is crucial which defined the structure and aids fast phase transitions.

1.2.2 Amorphous phase

The structure of amorphous phase in this ternary system has been debated and its understanding has deeply evolved over years. Based on the random covalent network theory for amorphous solids [75], it is assumed that amorphous state lacks long range order but its atomic arrangement should resemble the crystalline state locally as presented in Fig. 1.17. So, the structure of amorphous was assumed to be a disordered version of the metastable cubic rock salt structure.

Extended X-ray absorption of fine structure (EXAFS) and X-ray absorption of near-edge structure (XANES) are the best tools to investigate bonding characteristics [76]. Preliminary studies suggested that, the best agreement with the experimental results was found when assumed that Ge is in a tetrahedral position bonded with Te in amorphous phase, switching from octahedral arrangement in the crystalline structure. This view does not align with the theory of atomic arrangement in glasses. Further EXAFS developments aided with bonding constraint theory concluded a different view, that Sb-Te bonds are in Sb_2Te_3 configuration, Ge-Ge homo polar bonds are present and as Te is over coordinated, Ge-Te bonds are present in a Te_3Ge-$GeTe_3$ configuration [77]. The key factors aiding this development is based on the 8-N rule, which suggests, the co-ordination number of Ge, Sb and Te are 4, 3 and 2 respectively. Finally, Angstrom beam electron diffraction (ABED) study confirmed the local structure of GST to be close to the crystal structure but could be heavily distorted due to difference in bonding nature between the phases [78].

Ab-initio studies for amorphous GST-225 strengthened its structural understanding. Note that, ab-initio studies are restricted to small unit cell sizes and material study is linked to the phase formed by melt-quenched. Here, we summarize the ab-initio developments: [74], [79]–[83]

1. Ge and Sb are fourfold coordinated, whereas Te is threefold coordinated which is larger than the previously stated rule. Coordination number larger than allowed by 8-N rule.
2. 73% Ge and all of Te, Sb are in a defective octahedral geometry and about 27% of Ge atoms display tetrahedral coordination.
3. Angular distributions confirm octahedral features with strong presence of 90° bonds and weak presence of tetrahedral bond angles, confirming similarity to octahedral cubic structure. The structure is dominated by right-angled motifs between Ge and Te caused by pure p-bonding.
4. The structure of amorphous phase can be characterized as even-numbered ring structure, with majority presence of four-fold and six-fold ABAB rings.

To summarize, in the amorphous phase, Sb-Te, Ge-Te and Ge-Ge are the most prominent bonds. Sb, Te and most of Ge are in a highly distorted defective octahedral configuration with higher coordination than allowed by covalent bond theory. Majority of the structure consists of 90° bonds with a slight presence tetrahedral configuration, confirming octahedral geometry. The structure is dominated by 4 and 6 even numbered ABAB rings.

1.2.3 Phase transition from amorphous to crystalline

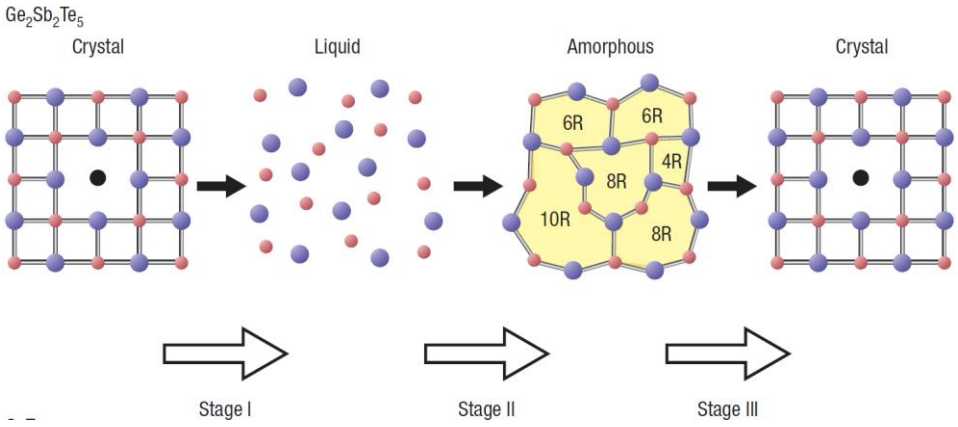

Fig. 1.18: Schematic representation of the possible ring structure transformation in the phase change from crystal to liquid to amorphous in GST-225 [73]

The phase change process for storage application is a continuous transition from amorphous to crystalline to re-amorphization and re-crystallization represented in Fig. (1.18). During this process, liquid phase also plays a prominent role as amorphization is fast quenching of the liquid phase. The liquid phase for most of the alloys with phase change capabilities was observed to be octahedral [84]. So, the structural basis of liquid, amorphous and crystalline phase is an octahedral structure which aids the nature of rapid phase change. Now, we dive into a more detailed structural analysis of phase transition which is responsible for the significant change in phase properties.

Initially, Kolobov et al proposed an umbrella flip mechanism where stronger covalent bonds remain intact whereas the weak bonds rupture, and leads to flipping of Ge in its preferred tetrahedral arrangement [76]. This mechanism, has been so partially refuted as strong octahedral evidence has been presented. The basis structure of both the phases is an octahedral arrangement which is one of the reasons for fast phase transition accompanied by the following:

Ring transition: Crystalline phase is defined by perfectly ordered ABAB squares, whereas in the amorphous phase too, distorted ABAB 4 and 6- membered rings are present. Easy reorientation of these rings, help form square rings and additional bonds for the cubic structure [79]. This partially explains the fast crystallization dynamics between the 2 phases.

Vacancies: Depending on the composition, the % of vacancies present changes, but these vacancies are crucial in ordering of the phases. “Vacancies with characteristically sharp edges, corners, and protrusions play a crucial role in providing the necessary space” [74]. % of vacancies present can influence the crystallization temperature and optical properties of the material, depending on the stoichiometry [85].

Bonding: Crystalline phase is characterized by resonance bonding with a long range order of aligned p-bonds. Resonant bonding requires long range order with second and the next neighbors aligned, losing the conventional 8-N rule and showing high coordination number. Whereas in amorphous phase, angular order is lost and so the long-range order is lost, as it loses second neighbor angular order. As high level ordering is not possible in amorphous phase, it

reverts to the conventional 8-N rule [86]. This medium range disorder, change in coordination number, loss of resonance bonding are the reasons for large contrast in optical and electrical properties of the phases.[86]–[88]

During transition the coordination number increases with angular rearrangement of atoms in a distorted octahedral or tetrahedral structure. These structural features like remarkable bonding mechanism in crystalline phase, the partial similarities between the amorphous and crystalline phase responsible for fast crystallization but the loss of long order reflecting in high contrast in resistivity/ reflectivity. Further, as we tune the stoichiometry - the crystallization temperature, crystallization kinetics, electrical resistivity contrast and thermal conductivity are affected.

1.2.4 Evolution of GST

The discovery of the alloys along the pseudo binary line with nanosecond switching speed, opened the avenue for extensive research and realization of PCM commercially. From the standpoint of application-based commercialization, to potentially replace FLASH for storage or memory-oriented applications, the requirements vary. Fundamental requirements like nanosecond switching speed, high endurance (10^8), operating temperature specifications based on application, thermal stability of amorphous phase, data retention triggered the exploration of different phase change materials in the chalcogenide family and other non-chalcogenides. The ternary alloys system has been explored most of the possible stoichiometries.

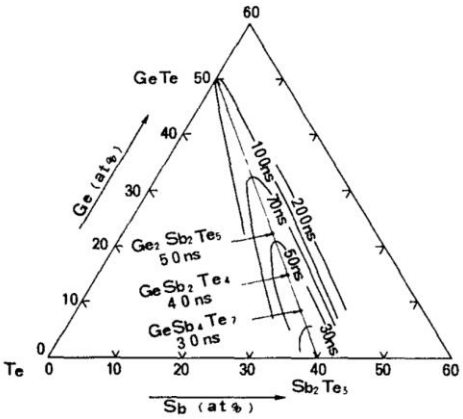

Fig. 1.19: Map of laser pulse duration required for crystallizing the alloys along pseudo-binary line of GeTe –Sb_2Te_3. The laser pulse amplitude was fixed at 8mW [23]

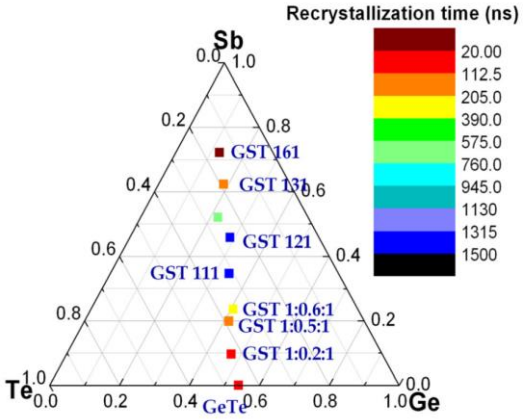

Fig. 1.20: Re-crystallization times of $Ge_1Sb_xTe_1$ materials along isoelectronic tie line in the Ge-Sb-Te ternary diagram [89]

The initial development began with the discovery of GST-225, showing crystallization temperature of 150°C and nanosecond switching times mainly for optical applications. Along the pseudo binary line, different stoichiometry's like GST-8211 to GST-124 showed similar crystallization temperature, with structural properties but with different stacking. Further, towards Sb_2Te_3 the switching speed improved considerably increased but with a downside of low crystallization temperature (85°C) [23]. The switching speeds are represented in Fig. 1.19. Alloys along Ge-Sb alloys were investigated which presented with a wide range of crystallization temperature from 130 to 350°C as Ge content increased with tunable crystallization speed with

control over Ge % [90]. These materials were showed the best performance for optical storage but were not suitable for IC applications due to slow SET speed, high power requirements compared to the existing technology standards and lack high temperature tolerance for automotive applications.

So further, materials along the pseudo-binary tie-line of GeTe-Sb were studied, where the crystallization temperature progressed from 170°C of GeTe to 250°C for GST-121 but it suffered from slow crystallization speed in the order of 100's of ns illustrated in Fig. 1.20 [89]. The key structural difference indicated that low Sb doped GST crystallized to cubic structure whereas highly Sb-doped crystallized to rhombohedral structure. Cheng et al identified GST-161 with 200°C and 20ns crystallization speed, with promising data retention but lower thermal stability. Sb content could be the reason for inverse correlation between speed and thermal stability. A solution to this, Ge-enriched GST-212, the "golden composition" was proposed by moving along the Ge-Sb_2Te_3 tie line [60]. This composition showed a high crystallization temperature of 300°C. The PCM test chip exhibited fast speed of 80 ns and 10^8 cycling endurance, withstanding 190°C testing. Ge-rich alloys showcased better thermal stability and higher crystallization temperature but with a downside of slower SET speed. Recently, Sb-rich GST alloys were realized in state of art devices with crystallization temperature above 200°C, along with high speed programming (30ns) and 10^7 endurance cycles [91].

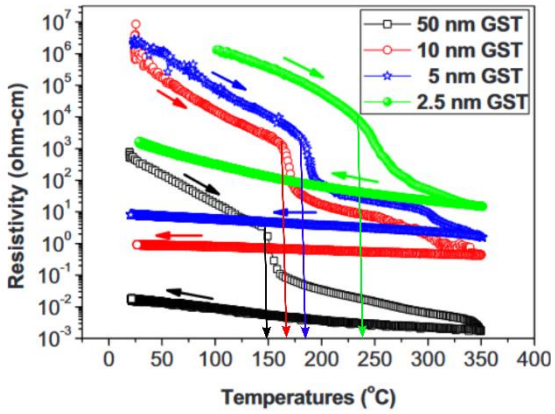

Fig. 1.21: Effect of scaling of GST thickness on resistivity and crystallization temperature [92]

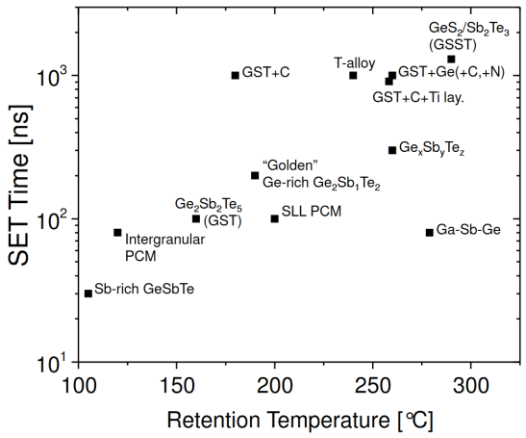

Fig. 1.22 SET time as a function of the retention temperature for 1 hour of data retention for different phase change materials engineered over years [33]

In other chalcogenide material system like $GeSe_{1-x}Te_x$, Se-rich GeSeTe exhibited exceptional thermal stability of 272°C for 10 years with crystallization temperature above 300°C [93]. For the non-chalcogenide Ga-Sb-Se system, with all materials studied in the system have crystallization temperature higher than 365°C. The reported device showed 80ns SET speed with excellent data retention of 220°C for 10 years [94]. With scaling of the devices, the thickness of GST would also decrease. The thickness scaling was also observed to have an effect on the ON/OFF ratio and crystallization temperature as presented in Fig. 1.21 [92].

Progressively, materials engineering over the years led to discovery of alloys based on specific requirements due to the versatile chalcogenide family. Fig.1.22 represents the various alloys

investigated with increasing retention temperature at a cost of slower SET speed. Different alloy combinations can be implemented based on the application. For standalone applications, faster switching speeds were crucial with the focus on higher density of PCM. So, the focus is on device engineering which led to cross-point architecture. Whereas, for embedded memories for automotive applications, the thermal stability of the material is crucial for compliance with soldering and automotive specifications. This led to extensive material engineering for improving the crystallization temperature and thermal stability of the material.

1.2.5 Doping of GST-225

Coming back to GST-225, it has been doped using C [95], N [96], O [97], Si [98] and simultaneous enrichment with Ge/Sb for improving the thermal stability and increasing crystallization temperature. Nitrogen doping showcased better control over resistivity ratio GST-225 tuned by control over N-doping and higher crystallization temperature. N-doping suppressed the grain growth of GST leading to higher resistivity and better thermal stability of the material [96], [99]. In case of doping with Carbon, the crystallization temperature showed a 100°C improvement over GST-225 [100]. This improved the thermal stability of the material with a significant reduction for I_{RESET}.

The structural origin of increased crystallization by doping is attributed to decrease in number of ABAB rings in doped GST-225, which slows down nucleation and growth of crystalline phase. The presence of tetrahedral Ge motifs significantly increases from 27% to 50% in C-doped structures, partially responsible for the thermal stability of the material. Microstructurally, these dopants restrict the grain growth. Comparing C and N-doping, stable Ge-N compounds are possible unlike Ge-C compounds. This results in C clustering along the grain boundaries affecting the resistivity. Ab-initio suggests these C-C bonds are formed during melt-quenching process and they do not break [100]. Similar for the other dopants too, these can act as micro heaters reducing the Reset current [100], [101].

To summarize, doping optimizes the Joule heating effect and improves the performance parameters in the following ways: a) It reduces the reset current which is correlated to an increase in the resistivity of crystalline phase. b) It reduces the thermal conductivity of the material and so improving the thermal confinement of the material. The disadvantage is increased resistivity of crystalline phase, which affects the SET performance. Give Preset formula!

1.2.6 Ge-rich doped GST

Embedded memories for high temperature data retention which are compliant with automotive applications require high crystallization temperature and thermal stability. During integration in the BEOL, the material should resist the thermal budget of 350-400°C. Also, it is crucial to guarantee data retention after solder reflow of 2 mins at 260°C to preserve the code. The crystallization temperature was increased by increasing the Germanium content in the GST alloys. This increased the crystallization temperature to above 300°C. This also resulted in increase in the activation energy of the material, improving the data retention from 120°C for GST-225 to 185°C for Ge-rich GST. Doping Ge-rich with Nitrogen or Carbon further improved the stability of the material by preserving the phase at higher temperatures as presented in Fig. 1.23 [102]. The combination of GST-Ge45% with N4% doping showed the best with crystallization temperature of above 300°C, and data retention increased to 210°C for 10 years.

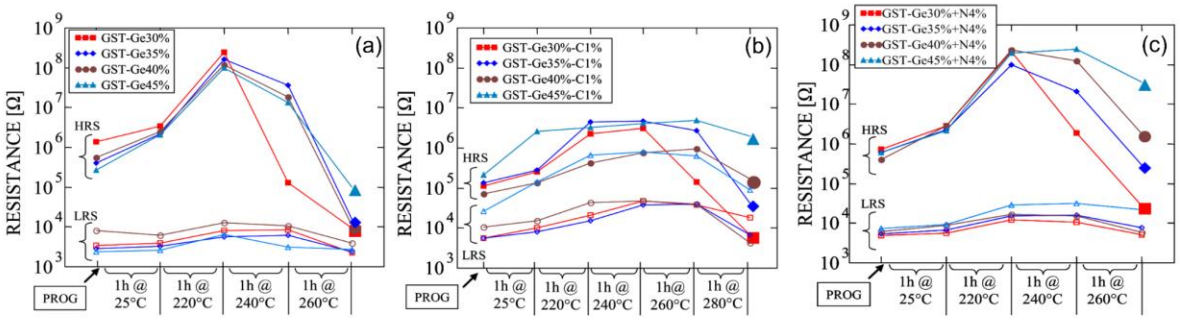

Fig. 1.23: Isochronal annealing steps procedure (IASP) at successively higher temperature. Ge enrichment increases the stability of the high resistance state (HRS), showing in all the samples a drift of the resistance till 220 ◦C and, then, a gradual recrystallization. Best stability is observed for high Ge content devices and 4% N-doped samples (b). C-doping (c) improves the stability of HRS up to 280 ◦C. Nevertheless, note that due to the programming window reduction N-doping offers a better trade-off. [102]

Materials aspect:

From a structural point of view, this increase in crystallization temperature is attributed to increase in tetrahedral Ge-Ge motifs and decrease in the number of ABAB rings as illustrated in Fig. 1.24 [64]. Increase in number of Ge-Ge bonds, formation of Ge-N bonds and its clustering into the voids retards the rearrangement and slows down the crystallization process. This results in reduced diffusivity of Ge responsible for the changes in crystallization kinetics. Increasing the N content from 2% to 10% can increase the crystallization temperature 300°C to 400°C. XRD results suggest that as N% increased and the propensity of Ge diffusion decreased, Ge segregation was affected and grain size decreased, as shown in Fig. 1.25 [103]. As the grains remained small, the thin film remained flat, which can be crucial during PCM device integration. The increase in N%, also affected the crystallization process, altering the usual transition from amorphous to FCC to trigonal. For N-doped Ge-rich GST, it was observed that as N% increases, the formation of trigonal phase is slowly suppressed.

The crystallization process of Ge-rich alloys is much more complex and not clearly understood. In-situ XRD for Ge-rich GST (Ge>45%) revealed that during crystallization process, first Ge crystallization takes place and once Ge is depleted from the matrix to GST-225 composition on pseudo binary line, cubic phase crystallizes [104]. TEM studies also concluded beginning of crystallization by segregation of Ge clusters and then of FCC-GST with composition close to GST-225 [105]. On the contrary, other studies suggest that Ge and GST crystallize simultaneously for the same composition. And, for Ge-rich GST (Ge<45%) crystallization begins with GST crystals and expulsion of Ge from the Ge-rich matrix, followed by crystallization of Ge. So, 3 different scenarios exist for the crystallization of Ge-rich GST. Further, annealing at temperatures higher than 450°C led to formation of trigonal grains and voids which could be detrimental for the PCM operation. So, in-depth understanding of Ge-rich GST alloys is crucial for its success in embedded memories.

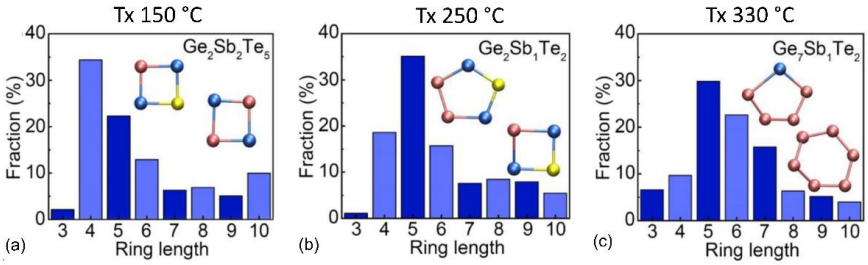

Fig. 1.24: The distribution of primitive rings for a) GST-225, b) GST-212 and c) GST-712 showing the trend of decrease in ABAB rings as Ge content increases. Inset shows a typical representation of ring fragments. Ge, Sb, Te are shown in red, yellow and blue, respectively. [64]

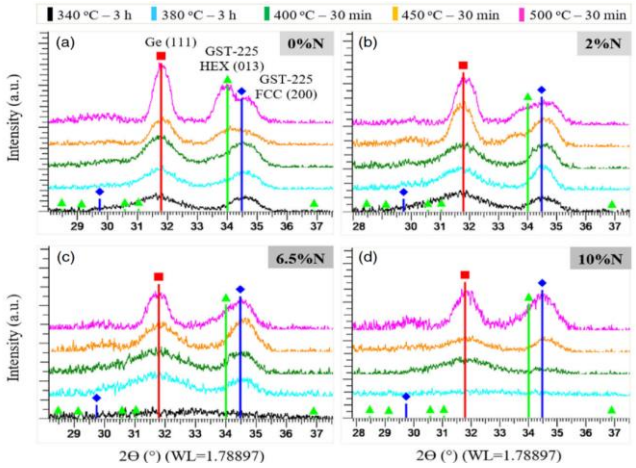

Fig. 1.25: XRD patterns of NGGST films containing different N concentrations. a) Un-doped system, and b–d) with 2 at% (b), 6.5 at% (c), and 10 at% (d) of N, respectively, annealed at different temperatures for different durations in the N2 ambient as mentioned. The vertical lines with filled red squares, green triangles, and blue diamond's show the expected 2θ positions of the diffraction peaks corresponding to the Ge 111, GST-225 trigonal 013, and cubic 200 indentation, respectively. [103]

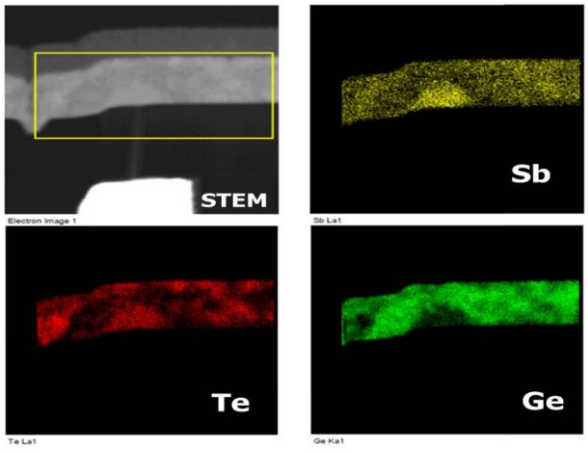

Fig. 1.26: TEM-EDX analysis of a T-alloy cell after programming: Ge, Sb, and Te maps [106].

Device aspect:

Increase in crystallization temperature by doping was accompanied by an increase in SET resistance. This led to a trade-off between improved I_{RESET}, thermal stability and slower programming speed as the crystallization mechanism is retarded [106]. But the speed of Ge-rich GST for embedded applications is still comparable with the floating gate memories currently used [43]. There are considerable differences between thin film samples and integrated devices for the behavior of the material. When integrated in a device, the phase change material is already in crystalline state. The first operation is called forming, where the amorphous dome in the cell is defined which will be formed during the consecutive operation of the PCM cell. During operation, similar to the thin film results, Ge segregation was observed around the dome with Sb enriched dome as shown in Fig. 1.26. These Ge clusters can be detrimental for operation as they provide a conductive path and so should be removed during the forming operation [107]. The forming pulses are crucial as it defines the working area composition and so defines the melting current and minimum resistance of the SET state [108]. The segregation issues could be improved by further understanding of the crystallization process of the Ge-rich GST alloys.

1.3 Chapter summary

Phase change materials have evolved from the novel concept of ovonic threshold switching and has progressed to be realized as non-volatile memory technology transitioning from optical storage systems. This progression was possible due to discovery of alloys with nanosecond switching times along the GeTe-Sb_2Te_3 pseudo binary line. Further, exploration of the alloys in the ternary system and device engineering improved the power consumption, programming speed and endurance, on-par and better than the existing technology led to its commercialization. PCMs were first developed for stand-alone applications and then for embedded applications.

From a device engineering aspect, the approach of wall architecture showed a good trade-off with reduced fabrication complexity and lower power consumption. For stand-alone applications, the goal for a denser memory was possible with the scaling advantages of PCM. The development of cross-point architecture and OTS selectors pushed the limits to fabrication of memory with the smallest footprint possible ($4F^2$). For embedded applications, the wall architecture was sufficient but required extensive materials engineering to be compliant with the automotive standards.

The understanding of phase change materials progressed with extensive efforts dedicated to explore every corner of the ternary alloy system, deposition techniques and novel 2D materials. The phase change materials can be tuned according to the requirements. The past years were focused on development of Ge-rich GST and its variants with respect to doping for its application for high temperature data retention embedded memory application. Ge-rich GST alloys were found to be stable up to 300°C for data retention with crystallization temperature over 400°C. This paved its way for commercialization in embedded memories for automotive applications. It certainly comes with some drawbacks like: Ge segregation affecting the retention of the memory, slower programming speed, drift of ON set resistance due to presence of amorphous phase.

The optimization of PCM grossly depends on optimization of its material properties, especially thermal resistances as they become very significant with scaling of the device. With this continuous evolution of materials and progressive scaling, it is very crucial to understand the thermal behavior of the cell. The knowledge of thermal properties of the PCM cell materials and

its interfaces play a key role in this development. Following are the thermal properties key to its development:

1. Thermal conductivity of dielectrics and amorphous, meta-stable cubic and trigonal/ hexagonal phase of phase change materials.
2. TBR at the following interface: amorphous-crystalline phase, dielectric-phase change material and heater-phase change material.

They are also important to understand the cross-talk between neighboring cells. Thermal characterization of materials is quite complex compared to electrical characterization. In the next chapters, we will discuss the thermal conductivity of phase change materials and its evolution with materials engineering. Then, thermal characterization techniques generally implemented for phase change materials with an in-depth focus on Raman thermometry for thermal characterization for phase change materials.

Chapter 2

Thermal characterization of Phase Change Materials

Temperature dependent material properties play a crucial role in understanding the cell's electro-thermal behavior. Extensive materials engineering aimed at improving the performance of PCMs led to dynamic evolution of different stoichiometries. Knowledge of the effect of change in stoichiometry of chalcogenides and doping on material transport properties is important to further optimize the cell behavior. The thermal resistances associated are key to reducing the power consumption of the cell and cross talk between the neighboring cells. Various well-established characterization methods have been implemented to extract the thermal properties of phase change materials. Detailed reports are present for the flagship 'GST-225'. These reports give an in-depth insight into the effect of structural transition on temperature dependent thermal conductivity of GST (mostly along the GeTe-Sb_2Te_3 pseudo binary line). But in recent years, there have not been many reports on the thermal properties of the newly evolved stoichiometries. Especially concerning the thermal properties of doped Ge-rich GST, which has been implemented for embedded memory automotive application due to its high thermal stability.

3ω method, thermoreflectance and photothermal radiometry are the well-established characterization techniques implemented for chalcogenides. They are quite reliable but could suffer from drawbacks. In this context, chapter 2 presents a review of thermal conductivity measurements of GeSbTe ternary alloy. The review accounts for the structural origin responsible for thermal conductivity, effect of thickness and doping. Then, a detailed comparison of different thermal characterization techniques is laid out to understand the available techniques.

2.1 Thermal conductivity of GeSbTe based Phase Change Materials

Materials engineering has led to realization of numerous stoichiometries implemented towards development of PCMs. The early material innovation was targeted specifically towards nanosecond switching times and lowering the power consumption to compete with the existing NAND and DRAM technology. Recent developments are aimed, more towards improving endurance, understanding the resistance drift and improving the thermal stability of the material. Alloys along the GeTe-Sb_2Te_3 pseudo-binary line are the most investigated alloys, continued with materials exploration along GeTe-Sb and Ge-Sb_2Te_3. Sb-rich compositions showed faster phase transition dynamics, and towards Ge-rich benefitted from increased crystallization temperature, crucial for high temperature data retention. Further, doping by C or N of Ge-rich alloys improved the amorphous phase thermal stability of the material. The commercial realization of PCM has evolved from such materials and device engineering.

The knowledge of thermal properties of these newly developed phase change materials (PMs) is important for simulating the electro thermal behavior of the cell. Hence, extensive thermal characterization of materials, plays a crucial role for their implementation in PCMs. The thermal resistances dictate the power consumption of the cell, so the knowledge of thermal properties as a function of temperature and phase is a necessity for its calculation. In a PCM cell array, as represented in Fig. 2.1, different thermal resistances are involved. During fabrication of the PCM cell, the deposited GST is crystallized following the thermal budget imposed by the BEOL upto a maximum of 400°C for varying time duration [109]. Depending on the stoichiometry and the corresponding thermal budget required, the as-deposited layer crystallizes in one of its crystalline phase – cubic or trigonal or hexagonal. Further, during forming operation of the virgin cell, the initial operating cycles define the dome – "memory storage area". This dome then transitions between amorphous and crystalline phase during the cell's lifetime operation. So, there might be a co-presence of 3 different phases in a PCM array during any given operation:

c-GST – the continuous bit line crystallized during fabrication of the cell, Rc – thermal resistance associated of the crystalline phase

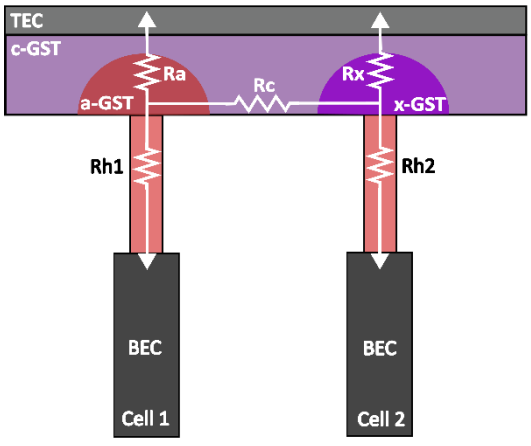

Fig 2.1 Schematic of phase-dependent thermal resistances involved in 2 neighboring PCM cells

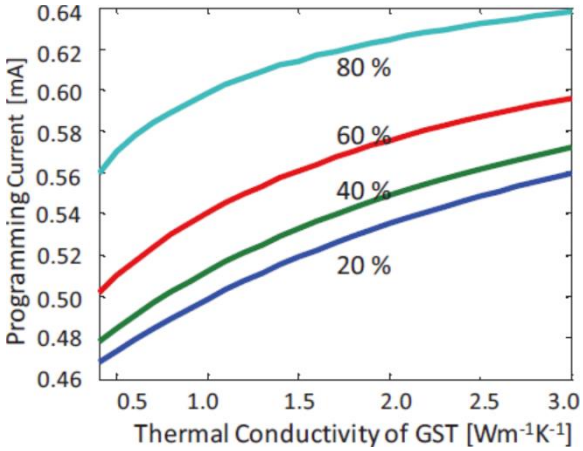

Fig 2.2 Effect of thermal conductivity of 100nm thick GST-225 on programming current evaluated for various amorphization rates [110]

a-GST, the amorphous plug created during the forming of the cell to define the dome and further cell operations – Ra – thermal resistance associated of the crystalline phase

x-GST – cubic or trigonal phase formed during memory operation depending on the temperature attained during the SET cycle, Rx – thermal resistance associated to the phase.

The programming current required for a cell is defined by these thermal resistances which are dependent and can be controlled by the thermal conductivity of the material, as discussed in the previous chapter. The sensitivity of programming current increases with increasing amorphization rate as depicted in Fig. 2.2 [110]. So, thermal properties are crucial for understanding and optimizing efficiency of the cell. Next, during the operation of a cell, the neighboring cell can be thermally disturbed. The temperature distribution of the neighboring cells can be correlated as [111],

$$\Delta T_2 = \frac{R_2}{R_2 + R_C} \Delta T_1 \qquad \textit{Eq 2- 1}$$

where R_2 represents the parallel resistance between R_X and R_{H2}, ΔT_1 is the temperature increase in cell 1 which is dependent on R_a and R_{H1} , and R_c is the thermal resistance between bits of both the cells. The thermal resistance increases with decreasing dimensions of the device and impacts the temperature distribution between cells. So, thermal properties are also key for understanding the cross-talk behavior of the cell which can aid progressive scaling and designing of the cell to avoid it.

The thermal transport properties of phase change materials rely on various factors like deposition techniques, annealing conditions, interfacing materials, thickness dependence and the temperature dependent phase employed in PCM. This section is dedicated to understanding the thermal conductivity of phase change materials and the physical significance of transport properties observed.

2.1.1 Transport properties and structural origin

The thermally induced phase transitions alter the transport properties of phase change materials. GST based phase change materials present tunable electrical conductivity spanning over four to five orders of magnitude at room temperature, Fig. 2.3. Amorphous phase has high structural disorder due to its distorted octahedral arrangement, resulting in low electrical conductivity. In context of GST- 225, annealing the as-deposited amorphous phase leads to crystallization of the material around 150°C. This leads to swift reordering of distorted structure leading to a metastable rock-salt, face-centered-cubic (FCC) phase. Here, the anionic sublattice is occupied by Te atoms, whereas the cationic sublattice is occupied by Ge, Sb atoms, with 25% vacancies in the cationic sublattice due to stoichiometric imbalance in the two sublattices. The conductivity transitions from low to moderate, increasing by a few orders of magnitude effected by improvement in structural order. Further annealing leads to vacancy ordering which successively reduces carrier localization and rearranges the cation sub lattice. In the resulting structure, Ge, Sb and Te atoms occupy separate closely packed layers and vacancies form Van der Waals gaps between two Te layers, forming a trigonal phase at 350°C. This improved structural ordering leads to an increased conductivity switching to metallic behavior (h-GST).

To generalize for other compounds along the GeTe-Sb_2Te_3 pseudo binary line, similar phase transitions were observed for GST-147, GST-124 and GST-326 [112]. For these compounds too, the crystallization behavior shows an irreversible change in resistivity of the material with annealing due to progressive structural ordering. Over the crystalline phase, from 150°C to 350°C the resistivity decreases by a factor of 500 changing the electronic transport mechanism from non-metallic (TCR<0)[8] to metallic (TCR>0) as the annealing temperature increases. Now, it would be interesting to observe these analogous effects on the thermal properties of these chalcogenides.

The thermal properties have been well documented for GST-225, with in-detail analysis into various factors affecting the thermal transport. Fig. 2.4 represents the thermal conductivity of GST-225 [113]. Lyeo et al present in-situ Time-Domain Thermoreflectance (TDTR) measurements plotted by blue hollow markers. The amorphous phase thermal conductivity lies around 0.2 $Wm^{-1}K^{-1}$. On ramping up the temperature, the thermal conductivity jumps from 2-3x on phase transition from amorphous to cubic phase at around 130°C. Further over, a wide range of temperature the thermal conductivity increases and becomes 7-8x that of the amorphous phase after transition from FCC to trigonal above 300°C. Thermal conductivity reports of thermal cycling of thin films for all the 3 phases, namely - amorphous phase, annealed at 180°C – cubic phase and at 400°C – trigonal phase, are presented by red markers [114]. 3ω measurements were performed on these annealed samples from 100K onwards. It is evident that phase transition causes irreversible shift in the thermal conductivity. XRD results for these annealed samples showed similar grain sizes for both c- and h-GST, whereas it displays a striking contrast between the thermal conductivities with c-GST showing glass-like trend similar to amorphous phase. Thermal conductivity of FCC phase behaves in a way that the thermal conductivity can be tuned with annealing temperature. This unique behavior of GST-225 results from an intermix of lattice contribution, increasing electronic contribution and role of vacancies upon phase transition.

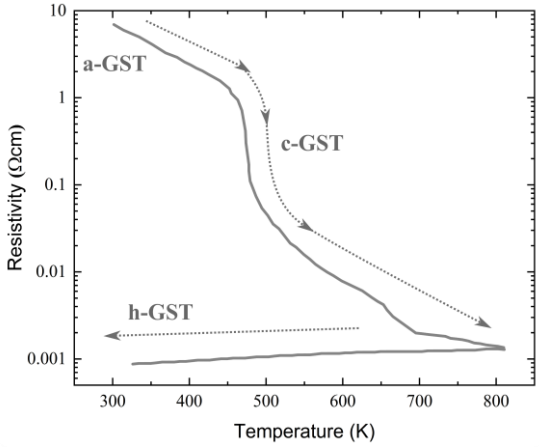

Fig 2.3 Electrical resistivity ρ of GST-225 as a function of temperature with phase transitions [107]

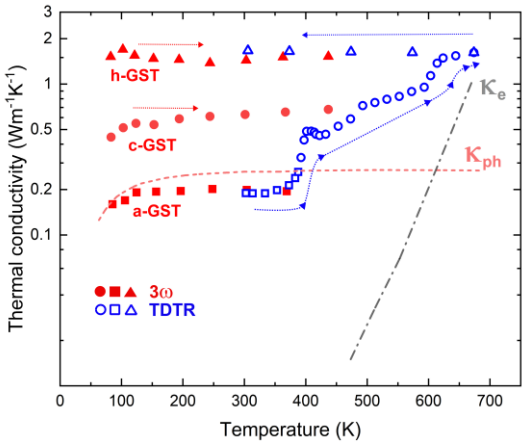

Fig 2.4 Evolution of thermal conductivity as a function of temperature. Data in blue represents transition of as-deposited material through phase transitions [113], and in red presents data of thermal cycling for pre-annealed samples.

[8] TCR – Temperature coefficient of resistance

Even though the electrical conductivity changes over orders of magnitude, GST alloys exhibit low thermal conductivity in its crystalline state, especially the cubic phase. This key characteristic indeed helps to reduce the power required to continuously cycle the memory between its crystalline and amorphous phase. If compared to ordinary covalent semiconductors like Ge, its thermal conductivity of sputtered Ge in amorphous is 1 $Wm^{-1}K^{-1}$, which rises to 45 $Wm^{-1}K^{-1}$ in its crystalline phase [115], [116]. Whereas, in case of GST, the cubic phase shows 2-fold increase in thermal conductivity to a modest 0.45 $Wm^{-1}K^{-1}$. This is attributed to the change in structural properties due to crystallization which is well documented. Heavy elements like Sb and Te in these ternary compounds decrease the phonon group velocity. The lattice distortions present in the structure reduce the mean free path down to lattice constant reducing the thermal conductivity [117].

To understand this further, we dwell into the factors that contribute to this special characteristic thermal conductivity of chalcogenides – the electronic, lattice contributions and mechanism that govern this behavior. This is followed by a detailed review of the studies for GST-225 available in literature and the experimental factors that contribute to some inconsistency in literature.

2.1.2 Electronic and lattice contribution to thermal conductivity – general theory

Structural and electronic properties both contribute to thermal conductivity and as the material transitions through phase changes, both of these contributions change. The measured total thermal conductivity can be considered an aggregate of phonon and electronic contributions:

$$k_{measured} = k_e + k_{ph} \qquad \textit{Eq 2- 2}$$

Fundamentally, thermal conductivity is the intrinsic measure of a material to conduct/ transfer heat. According to kinetic theory of thermal conduction for a gas of particles, the thermal conductivity, k is predicted as,

$$k = \frac{1}{3}\sum_{\alpha} C_\alpha v_\alpha l_\alpha \qquad \textit{Eq 2- 3}$$

where C is the total heat capacity, υ is the particle velocity and $l = \upsilon\tau$ is the particle mean free path, τ is the relaxation times, with summation over all excitations, denoted by α. In case of chalcogenides, the mean free path from experimental thermal conductivity values was found to be of the order of few nm's and frequency independent. So, the phonon contribution to thermal conductivity can be predicted by the using the model of lower limit of thermal conductivity by Pohl and Cahill [118]. It is based on the model for amorphous materials and disordered crystals which describes thermal transport as a random walk of thermal energy between localized harmonic oscillators encountering scattering events, is represented as,

$$k_{ph,min} = \frac{1}{2}\left(\frac{\pi}{6}\right)^{1/3} n^{2/3} K_b \sum_i \left(\frac{T}{\theta_i}\right)^2 \int_0^{\theta_i/T} \frac{x^3 e^x}{(e^x-1)^2} dx \qquad \textit{Eq 2- 4}$$

where K_b is the Boltzmann constant, n, the atomic number density as measured by Rutherford backscattering spectroscopy is 3.09 x 10^{28} m^{-3} in case of GST-225 [113] and T is the temperature. The summation is taken over the one longitudinal and two transverse phonon branches, each

with sound velocities υ_i and Debye temperature θ_i. For temperatures greater than the Debye temperature, it predicts no temperature dependence of the lattice component and the lower limit of phonon contribution can be simplified as,

$$k_{ph,min} = \frac{1}{2}\left(\frac{\pi}{6}\right)^{1/3} K_b n^{2/3}(v_l + 2v_t) \qquad \textit{Eq 2- 5}$$

where υ_l and υ_t are the longitudinal and transverse sound velocities. The physical quantities are tabulated in Table 2.1. As this, gives the lower limit of contribution of lattice component, the total lattice component can be evaluated by subtracting the electronic contribution from total experimentally calculated quantity.

Phase / Property	Amorphous	Cubic	Trigonal or Hexagonal
Mean free path (nm)		0.52 - 0.75 [119]	
Transverse velocity (ms^{-1})	1350*	1910*	1980*, 2240 [120]
Longitudinal velocity (ms^{-1})	2250 [113]	3190 [113]	3300[113],3120[120]
Heat capacity (10^6 J K^{-1} m^{-3})	1.28 [121] , 1.5 [114] (220 J kg^{-1} K^{-1} [122])		
Debye temperature T_D (K)	150 [123], 111 [124]	220 [123], 152[124],	230 [123], 310 [114]
Lorentz number (10^{-8}WΩK^{-2})	2.20 [119] , 2.45 (theoretical)		
k_{ph} (W $m^{-1}K^{-1}$)	0.27	0.4	0.45
k_e (W $m^{-1}K^{-1}$)	0.000024	0.015 - 0.07	1.1
$k_{measured}$ (W $m^{-1}K^{-1}$)	0.14 - 0.36	0.28 - 0.91	0.83 - 2.85

Table 2.1 : Thermal and material properties of the phase change material GST-225. The values shown here provide an idea for the expected values of these properties. * Represents transverse velocity calculated by assuming 60% of longitudinal velocity. The range of measured values for *k* represent those shown in Table 2.2

The electronic contribution can be calculated by using from the electrical conductivity measurements. The Wiedemann-Franz (WF) law is generally obeyed at high temperatures and allows us to relate the electronic contribution to thermal conductivity

$$\frac{k_e(T)}{\sigma(T)} = L_{WFL}T \qquad \textit{Eq 2- 6}$$

where L_{WFL} is the Lorentz number, T is the temperature and σ is the electrical conductivity. This rule is applicable when the material temperature is greater than half the Debye temperature, or

less than approximately 10K. The validity of Lorentz number (L_0) has been verified for different GST compounds and falls in good agreement with the theoretical L_0.

Further, a main contributor to lattice thermal conductivity in case of significant impurity level are phonon scattering processes. The possible scattering mechanisms are phonon-grain boundary, phonon-defect and phonon-phonon Umklapp scatterings. The resulting thermal conductivity after subtraction of electronic component can give an insight into these contributions.

2.1.3 Understanding the evolution of thermal conductivity on phase transition

Building on this context, the measured thermal conductivity of amorphous phase shows glass-like temperature dependence ($dk/dT > 0$). The experimental values fit well with the minimum thermal conductivity model estimated at 0.27 $Wm^{-1}K^{-1}$. As represented in Fig. 2.4, GST-225 deposited by various techniques and measured by thermoreflectance or 3ω method show no variation for the amorphous phase thermal conductivity. This occurs because, generally in amorphous materials the heat is conducted by a network of localized oscillators which are mostly not affected by structural defects. The only discrepancy could arise from partial crystallization of the amorphous phase during measurement or deposition techniques. The high resistivity of amorphous makes the electronic contribution to thermal conductivity negligible.

In FCC and trigonal phase, the predicted lower limits of thermal conductivity are estimated to be 0.40 $Wm^{-1}K^{-1}$ and 0.45 $Wm^{-1}K^{-1}$. The experimental thermal conductivity of FCC is about 2-3x that of amorphous phase with an abrupt change at crystallization temperature and then a temperature dependent increase until it transitions to trigonal phase. This increase is due to the rearrangement of the FCC lattice owing to the vacancies as the thermal budget increases. The close match of experimental results to the predicted thermal conductivity suggests that even though in its crystalline phase the thermal transport is still governed by atomic vibrations like in amorphous phase showing glass-like temperature dependence. The electronic contribution amounts to a mere 10% due to small carrier density. Due to the large increase in transverse velocity, Lyeo et al suggested that the increase can be accounted by increase in frequencies of vibrational modes [113]. The glass-like behavior could be normal as it is often observed in stabilized zirconia or feldspars containing large concentrations of interstitials and vacancies. Structural investigations have confirmed the presence of 25% vacancies in GST-225 which are agreeable with the observations.

This low thermal conductivity of FCC could be indicative of other phonon scattering processes, besides grain boundary scattering. The mean free path ranges in the order of few Angstroms, much less than the grain size and showed no temperature dependence. Siegert et al proposed an explanation for the thermal conductivity behavior of FCC phase upon annealing by including the effects of grain boundary, point defect, Umklapp and resonant phonon scattering through the phonon relaxation rate in the modified Debye model suggested by Cahill and Pohl [119]. They observed that as annealing temperature increased from 150°C to 225°C, the coefficient accounting for point defect scattering decreased by 70%, while contribution of other effects remained constant. So, the progressive increase in thermal conductivity as temperature increases is due to decrease in point scattering defects which arise from local fluctuations in mass density or bonding.

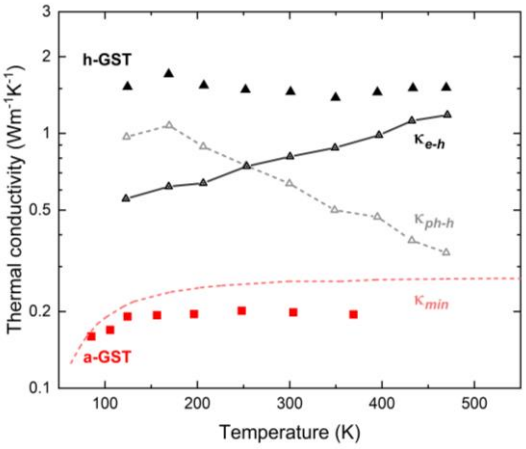

Fig 2.5 Thermal conductivity of amorphous and trigonal (h-GST) phase of GST-225 as a function of temperature. Black hollow triangles represent the electronic contribution to thermal conductivity, and the ones in grey present lattice contribution calculated by subtracting the electronic contribution. [114]

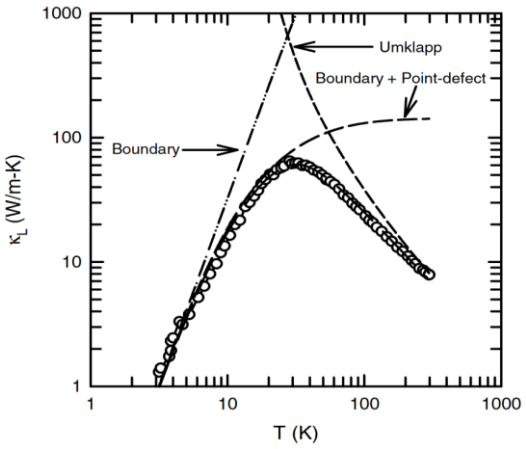

Fig 2.6 The lattice thermal conductivity versus temperature of a $CoSb_3$ sample. The dots and the solid line represent the experimental data and the theoretical, respectively. The dashed curves are the theoretical limits imposed on the phonon heat transport by boundary scatterings, a combination of boundary plus point-defect scatterings, and Umklapp scatterings [125]

Even though both FCC and trigonal phases show crystal-like behavior with similar heat capacities, density and phonon velocities there's a considerable difference in their thermal conductivities. The differences are reduced structural disorder and higher electrical conductivity for trigonal phase. This increase in carrier concentration is reflected in the thermal conductivity measurements as the electronic contribution to thermal conductivity increases as evaluated by WF law, Fig. 2.5. The electronic contribution increases and lattice contribution decreases as temperature increases reaching the lower limit. Different studies reported electronic contribution in the range of 65-70% to total thermal conductivity [58], [113], [114], [126]. The phonon contribution as presented in Fig. 2.5 was calculated after deducting the electronic contribution. The lower limit of 0.47 $Wm^{-1}K^{-1}$ as calculated by model indicates dominance of phonon-phonon scattering to the lattice contribution and not boundary or point defect scattering. This behavior is similar to that of a skutterudite $CoSb_3$ as presented in Fig. 2.6 with different phonon scattering contributions [125]. The decreasing phonon thermal conductivity is indicative of highly crystalline solids, as it occurs above Td/10 due to onset of three phonon process like Umklapp scattering. The transition from FCC to trigonal phase leads to reduction in vacancies and hence, a decrease in point defect scattering but highly crystalline behavior of trigonal phase leads to a dominant phonon scattering mechanism.

- Amorphous and cubic phase, the atomic vibrations are dominant heat carriers presenting glass like temperature dependence (dk/dT > 0). The increase in thermal conductivity from amorphous to FCC is due to ordered structure with decreasing point defect scattering with low contribution from charge carriers. Congruently, the velocity and density for cubic phase increases.
- Cubic to trigonal phase, the phonon contribution increases by 5% whereas 70% of total thermal conductivity is attributed to electronic contribution due to low resistivity. The

phonon contribution shows classic highly crystalline behavior (dk/dT < 0). Both being crystalline phases, the velocity and density are quite similar.

-

2.1.4 Thermal conductivity reports for GST-225

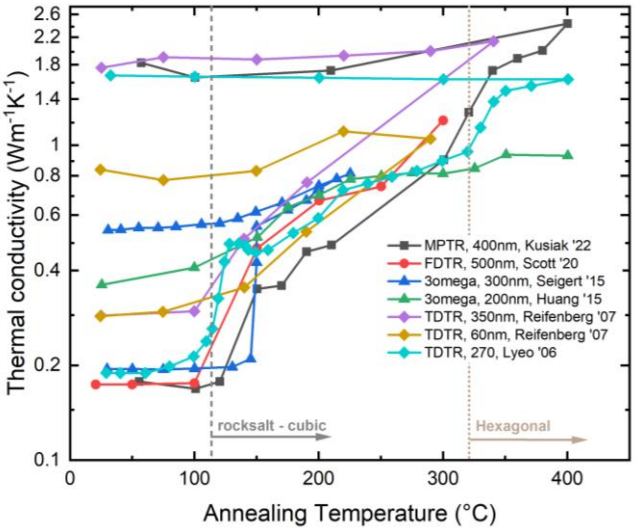

Fig 2.7 Temperature dependent thermal conductivity data collected from various articles to present a comparison of characterization techniques and thickness dependence, with details in the inset. Refs - Kusiak'22 [127], Scott '20 [128], Seigert '15 [119], Huang ' 15 [129], Reifenberg '07 [58], Lyeo '06 [113]

The thermal conductivity of GST-225 is well documented in the literature. Contact techniques like 3ω [119], [129]–[135], and thermoreflectance techniques like nanosecond transient thermoreflectance (n-TTR) [58], [122], [136], [137], Time-domain Thermoreflectance (TDTR) [113], [114], [123], Frequency-domain Thermoreflectance (FDTR) [128], [138], Modulated Photothermal Radiometry (MPTR) [126], [127] have been implemented. Different studies have characterized thin films of various thickness with, substrates and capping/ protection layer[9]. The preferred deposition technique in most of the studies is magnetron sputtering. Fig. 2.7 presents the temperature-dependent thermal conductivity studies for GST-225, separated according to the techniques used. For amorphous layers, process variation or thickness does not account for a lot of discrepancy in recorded values as discussed. Thermal conductivity of amorphous phase lies between 0.2-0.3 $Wm^{-1}K^{-1}$ for a wide range of thickness from 60-500nm.

Upon crystallization, most of the studies observed an abrupt change in the thermal conductivity with exception of studies for 60nm (yellow diamonds) and 200nm (green triangles) showing a gradual increase in thermal conductivity. Over the temperature range of cubic to trigonal phase transition, the thermal conductivity increases due to increasing electrical conductivity. For the cubic phase, annealing temperature plays a crucial role to understand the different values measured as illustrated in Table 2.2. Kim et al measured 0.536 $Wm^{-1}K^{-1}$ for thin annealed at

[9] To prevent oxidation of GST, it is capped with insulating layers or metals. These capping layers can affect the thermal conductivity characterization of GST.

Ref	Insulating layer	Technique	GST thickness	Thermal conductivity ($W\ m^{-1}K^{-1}$)			Annealing Conditions
				Amp	FCC	Trigonal or Hexagonal	
[130]	ZnS:SiO2 (100nm)	3ω	200nm	0.266	0.536		1 min @ 250°C
[131]	ZnS:SiO2 (100nm)	3ω	300nm	0.24	0.28		30 mins @ 207°C
[136]	Vanadium (70nm)	n-TTR	60nm		0.39-0.47		100 and 200°C
[113]	Al (80nm)	TDTR	270nm	0.19	0.57	1.58	20 mins @ 180°C and 360°C
[122]	TiN (100nm)	n-TTR	300nm			1.48	1h @ 300°C
[58]	Au (120nm)	n-TTR	350nm	0.29	0.42	1.76	150°C and 340°C
			120nm	0.17	0.28	1.1	
			60nm	0.17	0.28	0.83	
[133]	SiO2 (25nm)	3ω	180nm	0.14	0.39		200°C
[135]	SiO2 (80nm)	3ω	40-400nm	0.21	0.55	1.13	30 mins @ 350°C
[132]		3ω	50nm	0.22	0.6		RT and 180°C
[134]	70nm dielectric	3ω	600nm	0.17	0.55/1.01*	2.85/1.6*	15 mins @ 200 and 350°C
[126]	Pt (30nm)	PTR	100-840nm	0.19	0.42-0.91	1.6-2	in-situ (20°C/min) annealed for 5 mins
[137]	Ti/ TiN/ C (5nm)	n-TTR	50-150nm	0.2-0.33	0.69		
[110]	25nm dielectric	3ω TDTR	230nm	0.26	0.57		15 mins @ 160°C
[138]	Au (100nm)	FDTR	50nm	0.15	0.35		2 mins @ 300°C
[123]	TiN (80nm)	PTDR	50,150nm	0.25	0.45	1.32	10 mins @130°C and250°C
[129]	ZnS:SiO2 (80nm)	3ω		0.36		0.94	in-situ
[119]	ZnS:SiO2 (100nm)	3ω	300nm	0.2	0.5		in-situ (thermal cycling RT - 200°C)
[139]	TiN (23.5nm)	3ω		0.16	0.45	1.2	in-situ
[127]	Au (120nm)	FDTR	500nm	0.17	0.45	1.19	60 mins @ 150°C and 300°C
[114]	Al	TDTR	200nm	0.5	0.68	1.45	20 mins @ 180°C and 400°C

Table 2.2 A compilation of thermal characterization performed for GST-225 with different characterization techniques. Key aspects to consider are the annealing conditions implemented and the insulating layers deposited. Key differences in the thermal conductivity values can be observed depending of the annealing conditions.

250°C for 1 min, for Giraud et al were 0.26 $Wm^{-1}K^{-1}$ at 210°C, Lyeo et al 0.57 $Wm^{-1}K^{-1}$ at 180°C for 20mins, Kuhwara et al 0.39 $Wm^{-1}K^{-1}$ at 200°C for 30 min. The dispersion in the values is due to the annealing parameters, which has played a key role ordering the cubic structure. Similar contrast of measured thermal conductivity can be found for trigonal phase, where Battaglia et al reported 1.65 $Wm^{-1}K^{-1}$, whereas Huang et al reported 0.9 $Wm^{-1}K^{-1}$ at 400°C for GST-225 capped with SiO_2 and TiN respectively.

Wealth of is data available for GST-225 but still poses some uncertainty about the thermal conductivity of phases. Evaluation of thermal conductivity can be affected by the capping materials used and the annealing conditions implemented. Table 2.2 gives an insight into this discrepancy over a large set of data available in literature.

2.1.5 Pseudo-binary alloys and effect of doping

Along the pseudo-binary line, GeTe crystallizes into a stable trigonal phase and Sb_2Te_3 into a rhombohedral phase. For, GST-225 it crystallizes first in a cubic phase and then a trigonal/ hexagonal phase with 9 layers stacked according to Kooi structure [140], Petrov structure [141] or randomly occupied by Ge and Sb in the same layers as confirmed recently [69]. First principle calculations showed the effect of vacancies on the thermal conductivity of these alloys where introduction of disorder to the Sb/Ge sublattices was required to bring the thermal conductivity close to the experimentally measured values. Scattering due to disorder affected the lattice thermal conductivity and can be controlled by vacancy concentration [120]. The % of vacancy concentration varies along this pseudo-binary line impacting the thermal conductivity

Moving along the pseudo-binary line from GeTe to Sb_2Te_3, starting at, GeTe shows a high crystalline thermal conductivity of 1.98 $Wm^{-1}K^{-1}$ and amorphous phase of 0.19 $Wm^{-1}K^{-1}$. The amorphous phase thermal conductivity is low, of the order of 0.2 $Wm^{-1}K^{-1}$ for most of the alloys along this pseudo binary line, shown in Fig. 2.8. From a structural aspect, GeTe and GST-8211 crystallize in a stable structure without the need of ordering of empty lattice sites into different layers. Progressing along the pseudo-binary line, for stoichiometry's GST-326, GST-225 and GST-124, the phases transition from a rock-salt cubic phase to trigonal phase with increasing vacancy sites. These pseudo-binary alloys have sub lattice configuration with chemically ordered layers of Ge, Sb and Te atoms which does not exist in GST-8211 or GeTe. Annealing these alloys, leads to cation sub lattice ordering, and the structure transitions from cubic to trigonal/ hexagonal phase. The thermal conductivity for these alloys shows temperature dependence due to pronounced effect of vacancy ordering with annealing of the cubic phase, as illustrated in Fig. 2.8. These unique structural properties can be implemented in tailoring the transport properties.

Stoichiometry's have been doped with C [128] or N[138], to improve the crystallization temperature and hence improved the thermal stability of the material. As presented in Fig. 2.9, it led to a decrease in the thermal conductivity. Scott et al suggested that doping does not primarily impact the thermal (electrical) conductivity of the material through alloy scattering [128]. In turn, doping impacts the phase stability of the material which dictates the structural order achieved for a given annealing temperature. This means that the formation of FCC or trigonal phases are delayed and would need higher thermal budget compared to their undoped versions. Increasing the doping content would increase the disorder in the material and decrease the thermal conductivity. If sufficient order is achieved by inducing higher thermal budget, the thermal conductivity can reach comparable values. XRD results show that intensity of doped alloys is lower comparatively,

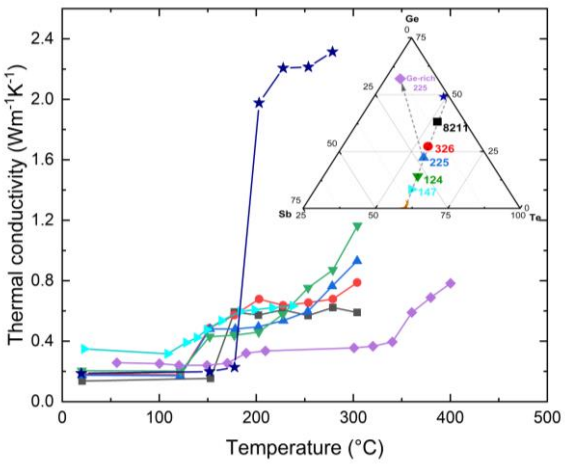

Fig 2.8 Temperature dependent evolution of thermal conductivity for stoichiometries along GeTe-Sb2Te3 pseudo binary line [119] with an additional compound - Ge-rich GST [127]

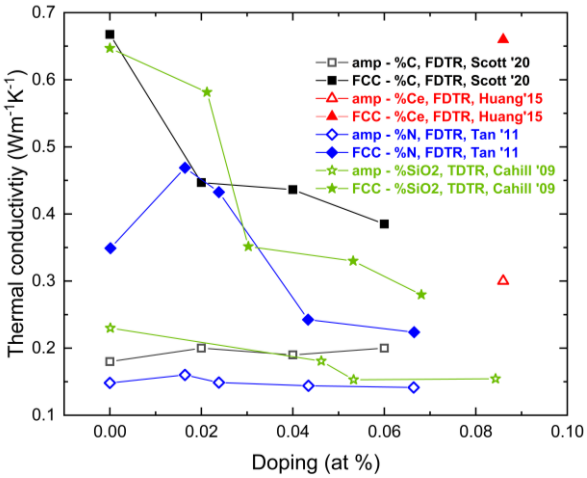

Fig 2.9 Effect of different dopants and their concentration on thermal conductivity. C% - Scott '20 [128], Ce% Huang '15 [129], N% - Tan '11 [138], SiO2% -Lee' 09 [132]

with wider FWHM of diffraction peaks. This signifies a reduction in crystallite size. Dopants like N, forms nitride bonds with Ge in GST and segregate at grain boundaries which restricts the grain size [142]. As the % of dopant increases, the defect density increases which is likely to affect the phonon mean free path, reflecting in the decreasing trend of thermal conductivity. Increasing the Ge content in GST-225 also leads to a decrease in the thermal conductivity.

Evaluation of precise temperature dependence of thermal conductivity is necessary to simulate the PCM cell and understand the heat dissipation pathways. Depending on the phase employed in a PCM cell, the thermal conductivity can vary which affects the evaluation of performance parameters and thermal cross-talk phenomena. PCM cells undergo a maximum thermal budget of 400°C for a varying period when embedded in the BEOL which defined the crystalline phase along the bit line. GST-225 crystallized to a trigonal phase at this temperature which affected the material reliability as large voids were formed. Other alloys like Ge-rich, Sb-rich and doped GeSbTe helped solve this issue.

Ge-rich doped alloys are extensively studied due to its superior material properties for its realization towards embedded memories application in automotive MCUs. Its structural evolution[104], phase separation [143], [144], reliability [145], effect of N-doping [103], [146], [147], modelling [148] have been probed to understand the physical properties as it is different from the pseudo-binary alloys behavior. For the flagship alloy – GST-225, extensive thermal investigation is available but it lacks for the newly engineered Ge-rich stoichiometries. Analysis of Ge-rich GST is focus of the thesis.

The thermal characterization techniques available have their respective advantages and disadvantages concerning high temperatures characterization. For alloys of the GST ternary family, it is important to extract the phase and temperature dependence of thermal conductivity. I will now discuss the thermal characterization techniques in brief from the chalcogenide point of view.

2.2 Thermal characterization techniques

Investigation of thermal properties of materials used in microelectronic devices is of paramount interest. It helps to address the crucial issue of Joule heating which limits the device performance due to insufficient heat dissipation. In PCM, it is aimed at understanding the intrinsic and interface thermal properties to curb the heat dissipation and optimize efficiency. As the characteristic dimension of material shrinks, the measurement techniques have grown sophisticated over years to precisely characterize micro/ nano heat scale heat dissipation. At micro/ nano scale depending on the material the apparent thermal conductivity is lower than bulk, as the characteristic dimension becomes comparable to the mean free path of the heat carriers in the material. As observed in PM, thermal properties are affected by increased scattering of heat carriers due to lattice defects, grain boundaries and partial transmission of heat carriers at interfaces which gives rise to thermal boundary resistance [149]. Continuous evolution of material stoichiometries and dopants, changes the structural properties, and hence impacts the thermal conductivity as discussed.

Thermal characterization techniques have relevantly evolved over the past three decades and can be classified as; contact or non-contact methods and transient or steady state measurements. Accurate measurement of thermal conductivity is a challenging task and usually involves measurement of temperature gradient across a sample in response to the introduction of thermal flux into the system. Table 2.3 provides brief description and classification of the techniques discussed in this section. For steady state techniques, the applied heat flux is constant with time and temperature gradient is calculated using temperature sensors. Whereas in transient method, a time-dependent heat source is used with a localized temperature probe laser.

1. Contact and transient – 3omega
2. Contact and steady – SThM
3. Non-contact and transient – Optical - Thermoreflectance and Photothermal radiometry
4. Non-contact and steady – Optical - Raman thermometry

The characteristic time pulse or the applied frequency of the heat source determines the type of thermal properties accessible via the technique. The minimum investigated depth within material is classified on basis of frequency or time domain heat source for transient measurements. The thermal diffusion length when a heat flux heats the sample surface periodically at frequency f is $\sqrt{a/\pi f}$, and when the heat flux is pulsed duration τ is $\sqrt{a\tau}$, where a is the thermal diffusivity of the materials. ($a = k/\rho C_p$). The heat penetration depth as a function of frequency and time is illustrated in Fig. 2.10.

Thermal properties of chalcogenides have been measured using 3ω technique and optical techniques like nanosecond transient thermoreflectance (n-TTR), time domain thermoreflectance (TDTR), frequency domain thermoreflectance (FDTR), modulated photothermal radiometry (MPTR) and pulsed photothermal radiometry (PPTR). This section reviews these techniques with a brief introduction of their principle, requirements, their application to phase change materials and drawbacks.

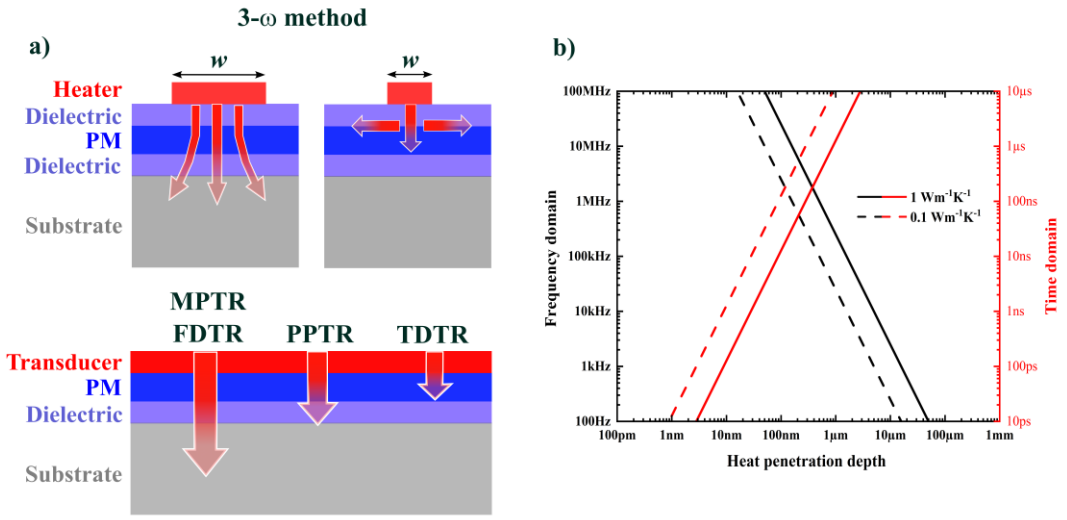

Fig 2.10 a) A schemtic representation of different characterization techniques with red arrows indicating the investigated heat penetration depth. b) A map detailing the heat penetration depth of laser for characterization of 1 and 0.1 $Wm^{-1}K^{-1}$ material depending on frequency domain or time domain technique

2.2.1 3-omega Technique

The 3ω-method is a well-established and sensitive electrical-contact technique used to measure the thermal properties of thin films, widely used for chalcogenides [119], [123], [129], [131], [133]–[135], [139], [150]–[152]. This electro thermal technique uses heater to induce Joule heating and using the temperature dependent electrical resistance of the heater, probes the temperature changes in the materials. A metal strip of precise dimensions is micro fabricated on top of the substrate which acts as both an electrical heater and a thermometer. A known amount of current I_ω, oscillating at frequency ω passes through the heater, which induces Joule heating of the resistive heater at 2ω frequency because of its electrical resistance. This leads to a temperature rise in the heater at frequency 2ω, which results in perturbation of the electrical resistance of the heater $R_{2\omega}$. The resulting temperature rise is determined by measuring the oscillating voltage at 3ω, by a lock-in amplifier. For the 1D approximation of heater as a line source, the heater half width (b) should be lower than the thermal depth of penetration $L_p = \sqrt{\alpha_s/\omega}$, where α_s is the substrate thermal diffusivity. Then, the thermal conductivity of the substrate is determined by the slope of the real part of the temperature rise as a linear function of logarithm frequency.

$$\Delta T_s = \frac{Q}{\pi L k_s} f_{linear}(ln\omega) \qquad Eq\ 2\text{-}7$$

Where k_s is substrate thermal conductivity, Q is total heating power, L is the heater length and ΔT_s is the temperature rise across the substrate. The primary advantage of this technique is the measurement of absolute temperature rise and heat flux dissipated in the material. In case of thin films on a substrate, this technique evaluates the frequency dependent thermal response of the thin films plus the substrate. So, the calibration of substrate and heater material is critical. The temperature difference across thin film is calculated by taking a difference between the thermal

Technique	**3-omega**	**Thermoreflectance**	**Raman thermometry**	**SThM**
Principle	***Contact, transient***	***Non-contact, transient***	***Non-contact, steady***	***Contact, steady***
Measured properties	κ - cross and in-plane, heat capacity	κ, cross and in-plane, TBR, acoustic properties	κ, TBR, vibrational and structural properties	κ, TBR
Geometry	Bulk, thin films in a stack	Bulk, thin films in a stack, suspended structures	Bulk, thin films in a stack, suspended, 2D materials, nanowires	Bulk, thin films in a stack, suspended structures
Sample requirements	Metal strip fabrication, thermal insulation, smooth surfaces	Metal transducer deposition, smooth surfaces	No	No
Material requirements	TCR	ρ, C	Raman active modes Optical properties	
Advantages	- Highest accuracy for bulk materials and low thermal conductivity dielectric films	- Time resolution of ps - Micrometer to nanometer scale thermal depth resolution - Submicron resolution - High sensitivity	- No prefabrication and smooth surfaces required - Submicron resolution - Simultaneous knowledge of structural properties and temperature profile of device	- No prefabrication and smooth surfaces required - Submicron resolution - Absolute temperature measurement
Disadvantages	- Accuracy reduced for semiconducting thin films and high k_{th} materials - Pre-fabrication, electrical insulation of material of interest and smooth surface - Calibration of heater - Complex post processing	- Complex and expensive experimental setup, - Pre-fabrication and smooth surface, Samples with multiple thickness might be required - Temperature limitations due to transducer -Complex post processing	- Not suitable for materials without active Raman modes - Low temperature sensitivity - Raman peak features sensitive to strain and impurities	- Contact resistance - Low thermal conductivity sensitivity -Extensive modeling of tip-surface interaction
Uncertainty	~10%	10%	10-20%	

Table 2.3 Comparison of characterization techniques (Inspired from [153])

response of film-on-substrate and only substrate. Following many assumptions as described in [154], the relation between temperature rise across thin film (ΔT_{film}) and effective thermal conductivity (k_{eff}) is reported as

$$\Delta T_{film} = \Delta T_{s+film} - \Delta T_s = \frac{Q d_{film}}{2wLk_{eff}} \qquad \textit{Eq 2- 8}$$

where d_{film} is the thin film thickness and L is the heater length. This technique has proven to of very high accuracy for bulk materials and low thermal conductivity thin films. In case of electrically conductive thin films, the metallic heater must be well isolated from the film by depositing a thin dielectric layer for isolation. This leads to an interface resistance contribution from dielectric, in addition to the one present from the metallic heaters.

As PMs are electrically conductive, it is important to completely isolate the heater to prevent measurement errors due to leakage current. So, the material has been sandwiched between passivating thin films like SiO_2 [135], [151], [152], Si_3N_4 and ZnS:SiO_2 [119], [129]–[131]. The extraction of ΔT_{film} is performed by measuring samples with and without the PM. So, the effective thermal conductivity measured comprises of contribution from both – the thermal conductivity of the PM and thermal boundary resistance between PM and the passivating layers. Further by fabricating various samples of different PM thickness, the TBR can be separated from the intrinsic thermal conductivity. The thermal penetration depth is dictated by the width of the heater and frequency. By fabricating samples with narrower heaters it is possible to extract in-plane thermal conductivity as presented in Fig. 2.10 a [155].

The primary limitation is that the intrinsic thermal properties are not directly accessible. In order to extract the thermal properties, samples of various thickness and heater sizes are required. This involves fabrication of multiple samples with deposition of passivating layer, lithography, metal strip deposition and then bonding of electrical contacts. The fabrication process can be challenging to ensure high sample quality. Possible pinholes in the passivating layer or damage due to probes and wire bonds can cause current leakage reducing the sensitivity of the technique [149]. It should be ensured that unintended crystallization of PM samples do not occur. Requirement of electrical contacts complicates the high temperature measurements for PM.

Number of studies implemented 3ω to extract the effective thermal conductivity of the thin film stack as presented in Table 2.2. Kim et al used multilayer samples to extract the intrinsic thermal conductivity of GST-225 in amorphous and crystalline phase and the TBR of ZnS/SiO2 interface [130]. They report an error of 5% for intrinsic thermal conductivity and 10-15% for TBR measurements. Giraud et al fabricated samples with varying sizes of heater but reported similar values of amorphous and FCC phase of 0.24 and 0.28 respectively [131]. Thermal conductivity values by Risk et al do not account for the effect of interface and report the effective thermal conductivity, and only a lower bound for the intrinsic thermal conductivity [133]. Seigert et al suggested on basis of previous experiments that for sample geometries of 300nm of GST-225 the interface effect could be neglected [119]. Most of the studies cited in Table 2.2 have limited the characterization to thicker samples (~200nm) and intermediate temperature (~200 – 250°C).

2.2.2 Thermoreflectance

Thermoreflectance (TR) measurements provide a wealth of information about the thermal and acoustic properties of materials, and have been extensively implemented for PM. Depending on

the system used it can measure thermal decays in the range of nanoseconds and electron-phonon interactions at time scales less than 10 picoseconds [149]. In contrast to 3ω measurements, TR requires deposition of a blanket metal optical-to-thermal transducer instead of heaters and passivation layers, simplifying the fabrication requirements. It measures the transient change in the reflectance of the transducer to probe the thermal response of the thin film stack. A high intensity pulsed or frequency modulated laser (the pump beam) causes the change in the local temperature of sample due to optical absorption. A second laser (probe beam) measures this temperature change by monitoring the relative reflectance change. This temperature perturbation alters the optical constants of the transducer and leads to change in reflectivity. In the transducer, the reflectivity (R) and temperature (T) change is linear over a temperature of few degrees,

$$\frac{\Delta R}{R} = \left(\frac{1}{R}\frac{\partial R}{\partial T}\right)\Delta T = C_{TR}\Delta T \qquad \textit{Eq 2- 9}$$

C_{TR} is the material dependent thermoreflectance coefficient, it is usually known or measured. This linearity eliminates the need for knowledge of absolute temperature rise. The size of the pump beam is generally much larger than the film thickness to consider one dimensional solution for heat diffusion equation to model the data and obtain the quantities of interest. The transient TR technique can be implemented as either time-domain thermoreflectance (TDTR) or frequency-domain thermoreflectance (FDTR). Detailed description and reviews of these techniques are precisely explained in [153], [156].

TDTR measures the thermoreflectance response as a function of time delay between the arrival or the probe and the pump pulses at the sample surface. Whereas, FDTR measures the thermoreflectance response as a function of the modulation frequency of the pump beam. FDTR is comparatively easier to implement and cheaper than TDTR. First, the ratio of in-phase and out-of-phase responses of the thermoreflectance at the modulation frequency of the pump beam is measured. This measured response is fitted against the predicted thermal response data using the unknown parameter as the fitting parameter, to obtain the best fit in the thermal model.

- Requirements for TR methods:

Based on the review, following are some key considerations [153].The thermal model requires precise knowledge of thickness of the films in the stack which are usually determined by AFM or ellipsometry or SEM. The thermal properties of the transducer should be determined by depositing the transducer on a known substrate under the same deposition conditions, as properties are sensitive to deposition conditions. The surface smoothness of the transducer should be enough to not cause any modulation of laser due to scattering. As a rule of thumb, roughness should be less than 15nm. Generally, a material who has a large reflectivity variation as a function of temperature is preferred. The laser spot radii have to be precisely calculated as it can be a main source of error, usually 5-8%. The input power should be precisely known to avoid temperature changes of more than a few Ks, or the linear thermoreflectance relation can no longer be assumed. Knowledge of these parameters leads to extraction of thermal effusivity, the product of thermal conductivity and heat capacity. Following these requirements, TR measurements help discover wealth of information of like thermal and acoustic properties of the materials [113].

Initial reports measured the thermal conductivity of GST-225 by nanosecond thermoreflectance [58], [122], [136], [137] and TDTR methods using different electrodes is elaborated in Table 2.2. It can be observed that different electrodes and annealing conditions lead to range of values as discussed before. Depending on the depth of penetration of the technique, for example nanosecond gives a spatial average of the thermal properties whereas pico-second-TDTR enables precise evaluation of intrinsic thermal conductivity and thermal boundary resistance. In case of electrodes, Vanadium inter-diffuses into GST over 200°C as reported by Kuwhara using n-TTR and reported an error of 30% [122]. Comprehensive temperature and thickness dependent studies presented by Reifenberg et al used an Au electrode, reporting a relative error between 5-15% [58]. The thermal conductivity variation with thickness was attributed to the boundary resistances and variations in microstructural quality. Later it was reported that Au diffuses quickly in PM as soon as the temperature rises. Typical error due to thickness measurement amounts to 5-10%.

Scott et al reported the thermal conductivity values from room temperature to 350°C using an Au electrode [128]. The thermal model was insensitive to Au/GST interface and FDTR was insufficiently sensitive to volumetric heat capacity when the thermal conductivity was in excess of $1 Wm^{-1}K^{-1}$. For TR techniques, Pt and TiN are not suitable which would be ideal [156]. So, Al is generally preferred, and as reported by Lyeo et al the temperature dependent thermal conductivity upto 400°C [113]. But ToF-SIMS[10] analysis showed diffusion of Ge, Sb and Te species into the Al layer for a sample annealed at 400°C [157]. Irrespective of the choice of transducer deposited, the maximum operating temperature would be 300°C above which interdiffusion of species or cracking was observed. Beyond that temperature TDTR would be less suitable.

2.2.2 Photo thermal radiometry

The PTR technique is based on measurement of emitted infrared radiation from surface of sample induced by excitation from a photo thermal laser source. As PM are generally transparent to the wavelength of the laser, an optical-to-thermal transducer is required to produce a heat flux, similar to TR methods. The absorbed radiation from the laser leads to a surface heat flux, resulting in an increase of temperature at the aimed area. The resulting temperature rise leads to an infrared radiation emitted as a function of surface temperature as explained by Stephan-Boltzman law. Assuming a small temperature increase due to a weak thermal disturbance, the transient part of emitted radiation is linked to temperature variation as,

$$\Delta M = 4\varepsilon\sigma_s T_0^{\,3}\Delta T \qquad \textit{Eq 2- 10}$$

where ε is the surface emissivity, σ_s is the Stephan-Boltzmann constant. The variation in temperature should be small enough to assume linear relationship between measured radiative emission (ΔM) and temperature change (ΔT). In PTR, the emitted infrared radiation from heated surface is measured by an IR detector. The input photo-thermal laser is measured by a photodiode to provide a reference for the measurement of amplitude and phase. A lock-in amplifier is used to measure the amplitude and phase lag between the reference and excited radiation from the IR detector. Both quantities are sensitive to the thermal resistance of the layers, and required for its measurement.

[10] Time-of-Flight Secondary Ion Mass Spectrometry

PTR can be implemented in different variations: Modulated Photothermal Radiometry (MPTR) where a continuous wave laser source is modulated to provide a periodically varying radiation and Pulsed Photothermal Radiometry (PPTR) where the photothermal source is continuously emitting nanosecond heat pulses. The requirements for PTR technique is similar to TR; measurements of laser beam waist, ensuring smoothness and precise transducer calibration, knowledge of layer thickness, and extensive mathematical modelling. Similar to 3ω, MPTR allows measurement of the global thermal resistance of the thin film stack, whereas for the pulsed variant it is possible to probe just the thin film of interest with precision like in TDTR.

MPTR implemented for GST-225, and other doped chalcogenides provided accurate thermal conductivity and boundary resistance estimates [156]. As it provides the global thermal resistance, Battaglia et al implemented the technique on samples with various thicknesses [158]. This enabled the measurement of intrinsic resistance and thermal resistance at interfaces by implementing linear regression to the resistance measurements as function of thickness and temperature. In case, of GST-225, sputtering is limited to a certain thickness, thus the use of multiple deposition cycles for thicker samples can impact heat transfer during characterization. The newly developed PPTR technique shows certain advantages over its counterpart [159]. It has higher sensitivity of two orders of magnitude better than the thermoreflectance methods. It is possible to characterize layers upto 500°C by implementing transducers like Pt which has low chemical affinity towards PMs [156].

2.2.3 Current perspective of thermal characterization for chalcogenides:

During the operation of PCM, the material is cycled through a thermal budget using electric pulses. During phase transitions the temperature reaches above the melting point at the hotspot and further temperature gradient along the bit line affecting neighboring cells. So, the thermal conductivity measurement must be performed over the entire working temperature range as a function of the amorphous or crystalline state. Most of the studies listed in Table 2.2, restrict the working temperature upto 200-250°C with a few exceptions of Kusiak et al [127] Scott et al [128]. It is critical to note that the thermal budget imposed during programming of a PCM cell and one applied to the sample during characterization is significantly different. This affects the way the material and interfaces are modified. Also, the studies do not provide sufficient information regarding the details and conditions of the thermal annealing conditions during sample preparation. So, the reported values might not be reliable and it leads to inconsistency in between the reported values as presented in Table 2.2. An additional step would be to continuously monitor the sample with structural characterization to ensure and confirm the phase present (no evolution of unwanted phases).

The evolution of characterization techniques has helped in realization of thermal properties of nanoscale thin films and interfaces. 3ω method is the most versatile with the lowest uncertainty with measurements, followed by the later developed - optical thermoreflectance and radiometry techniques. The techniques of 3ω, MPTR and FDTR, measure the global resistance of the thin film stack, whereas PPTR and TDTR can measure the intrinsic thermal conductivity of the material. In a sense these methods can act complementary to each other and can provide comprehensive information about the thermal properties when coupled with physiochemical and structural analysis. As summarized in this section, the methods face a few drawbacks.

For 3ω method, presents the lowest uncertainty in measured data. But ample requirements need microfabrication of heaters and multiple samples access the spatial distribution of thermal

properties. The sample design comprises of a series of trade-offs between signal maximization, analysis complexity and the possibility of leakage current which hampers the reliability of the technique [149]. Precise calibration of heater and substrate material is required to guarantee its precision. Frequency limitations results in effective thermal properties and high temperature measurements are complex due to the requirement of electrical contacts. For chalcogenides, it has been implemented for a variety of stoichiometry's along the pseudo-binary line but the studies are limited to 200-300°C in the literature.

Optical methods, have been popular in the recent years as the local thermal properties can be accessed. These methods too have fabrication requirements pertaining to the transducer, its quality and reliability. There have not been any high temperature (>300°C) for FDTR or TDTR reports as the sensitivity of the measurement technique is harmed by the choice of transducer or insensitivity to the thermal model. Aluminum was an appropriate choice but faces inter-diffusion with PM at high temperature. These methods help extract the thermal effusivity of the sample from the ratio of in-phase and out of phase responses. Precise knowledge of material properties and geometries is required as the fit is sensitive to these parameters. Incase of MPTR, effective thermal properties are extracted and intrinsic values can be measured with help of combination of samples. It has been implemented for materials like GST-225 [157], [158], GeTe [160], InSbTe [161] and to investigate the interfacing TBR. For PPTR, due to its better spatial resolution helps extract the intrinsic thermal conductivity. The choice of Platinum as the transducer, measurements are valid up to 500°C as it shows limited diffusion in PMs [156]. The transducer material consideration indicates to limit the use of these optical techniques whose thickness is more than 100nm to not be significantly affected by material diffusion. TDTR has the highest spatial resolution but high temperature measurements are not feasible. PPTR operates at higher temperature but with higher heat penetration depth. Lower depth can be achieved by technological progresses with higher acquisition frequencies.

In overview, each characterization technique is limited to a specific range, depending on a). the investigation depth possible, b) requirements for fabrication for fabrication of transducers, electrical contacts and multiple samples with thickness variation, c) experimental conditions - possible temperature or frequency range or vacuum measurements. The applicability of measurement techniques is quite material specific and as discussed for chalcogenides, faces some problems but complementarity of the techniques can provide a complete thermal investigation of chalcogenides.

2.3 Conclusion

Extensive studies investigating the thermal conductivity of GST-225 have been reported. Inconsistency in the reported values rose from either varying annealing conditions or capping dielectrics/ electrodes or measurement approach. One key aspect would be the phase of the material during characterization as thermal budget undergone by the sample has a significant role on structure of the material. This could impact the evaluated thermal conductivity, as from FCC to trigonal phase it increases, in case of GST-225. For the newly developed stoichiometry's, only a few reports exist. Doping of the stoichiometry's has led to a delay in crystallization temperature and the evolution of the crystallized structure which can impact the thermal conductivity.

The techniques summarized in this chapter provide an outlook of their essential requirements, advantages and disadvantages. These techniques are quite complementary to provide a complete

analysis of the intrinsic and interfacial thermal properties. Certain drawbacks regarding microfabrication of multiple samples, choice of optical to thermal transducer leading to the inter diffusion of elements or experimental errors in case of contact measurements affect the results. Thermal characterization accompanied with physiochemical characterization is crucial to validate the results as the thermal budget imposed during various studies can affect the material differently.

Chapter 3

Raman thermometry for GeSbTe alloys

A relatively unconventional technique for thermal characterization, Raman thermometry can provide an insight into the structural evolution of the material and measure the thermal properties of the material, simultaneously. It has been implemented for different materials over the years to extract the thermal conductivity, thermal boundary resistance or even yield a temperature map of an active device. So far, it has not been implemented for thermal conductivity extraction of phase change materials. Analysis of ternary materials like chalcogenides with Raman thermometry is not straightforward as the Raman spectra is a combination of multiple peaks in close wavenumber proximity.

In this chapter, a we present the technique of Raman thermometry and its successful application for different materials. Then, we dwell deep into its experimental details and simulation aspect crucial for extracting the thermal conductivity.

3.1 From Raman spectroscopy to thermometry

Raman thermometry is a powerful thermal characterization technique based on Raman spectroscopy. It is a noncontact (optical) and steady state technique employed to extract the thermal properties and thermography of microelectronic devices. The key advantages stem from the fact that it enables direct probing of the material of interest without any need of microfabrication of heater electrodes, metallic transducer layers or samples with varying thicknesses. Being a spectroscopy-based technique, it provides the structural signature of material compositions based on the vibrational modes of molecules. The technique allows measurement of local temperature and thermal conductivity. Implementation of the technique was first demonstrated for Silicon based on the temperature dependence of Raman scattering phenomena in Silicon [162]. The key materials implemented in the microelectronic and nano-electronic industry can be characterized by this technique. It has been extensively implemented for devices fabricated from poly-Si MEMS [163], GaN/AlGaN, [164], [165] , GaAs/SiC [166] for extracting the thermal properties of material and interfaces, in addition to thermography of the devices. Further, the technique became popular for investigation of 2D materials after the work of Balandin et al for suspended graphene [167]. Post this, the method gained popularity for investigation of thermal properties of 2D materials [168]–[171]. This was possible due its material specificity and ability to characterize suspended materials, as any contact with substrate drastically influences properties of 2D materials.

This section is dedicated to understanding the translation of Raman spectroscopy to thermometry – staring from principle of Raman spectroscopy, Raman selection rules, the experimental setup, requirements aligned with chalcogenides characterization, data analysis and simulation support. The applicability of the method is portrayed by an example of Ge-rich GST. Further chapter 3 is dedicated to Raman spectroscopy results and chapter 4 to thermal conductivity extraction by Raman thermometry of all the GeSbTe based chalcogenides characterized in this thesis.

3.1.1 Raman spectroscopy

Raman spectroscopy is an analytical technique well-established for characterizing chemical bonding and solid-state structure of material by studying the vibrational properties of materials based on light-matter interaction. Photons (light - monochromatic laser) are used to measure the energy (E) of vibrations in a lattice or molecules in a material [172],

$$E = h\omega = \frac{hc}{\lambda} = hc\tilde{\omega} \qquad \textit{Eq 3- 1}$$

where ω is the frequency of the incident light, λ is the wavelength and $\tilde{\omega}$ is the wavenumber. When this light of a certain frequency is incident on a material, scattering occurs. Most of the scattered light will be of the same energy as the incident light, however a small fraction of light will be energetically shifted. The elastically scattered light emitted at the same frequency is due to Rayleigh scattering, and the inelastically scattered light to shorter or longer frequencies is due to Raman scattering. Here, the photons absorbed by the molecules in a material, jump to higher virtual states, transmit to different energy states and release the rest energy to surroundings. This phenomenon is illustrated in Fig. 3.1. If the energy of the emitted light is higher, then it's called anti-Stokes Raman scattering. And if the energy of the emitted light is lower it's called

Stokes Raman scattering. This change in energy is due to interaction of photons with the lattice, stokes scattering creates an excited vibrational state and anti-stokes scattering annihilates an excited vibrational state. As the density of ground state is higher than the excited states, the strength of Stokes scattering is stronger than the strength of anti-Stokes scattering as depicted in the schematic. However, this intensity ratio can change with temperature as photons jump to an excited vibrational state, strengthening the anti-Stokes scattering. From a momentum point of view, photons have very small momentum. Considering a typical dispersion relation of change in phonon energy with momentum, acoustic phonons have low energy at small momentums, whereas optical phonons have higher energy. Due to this, optical phonon modes are the ones observed in Raman spectra. A typical Raman spectra consists of a set of peaks located at specific frequencies that depend on the vibrational energy of the material. As these scatterings are a signature of the collision between incident photons from a laser and phonons in a material, the change of energy, termed as Raman shift/ frequency is unique and gives characteristic information of the material [173].

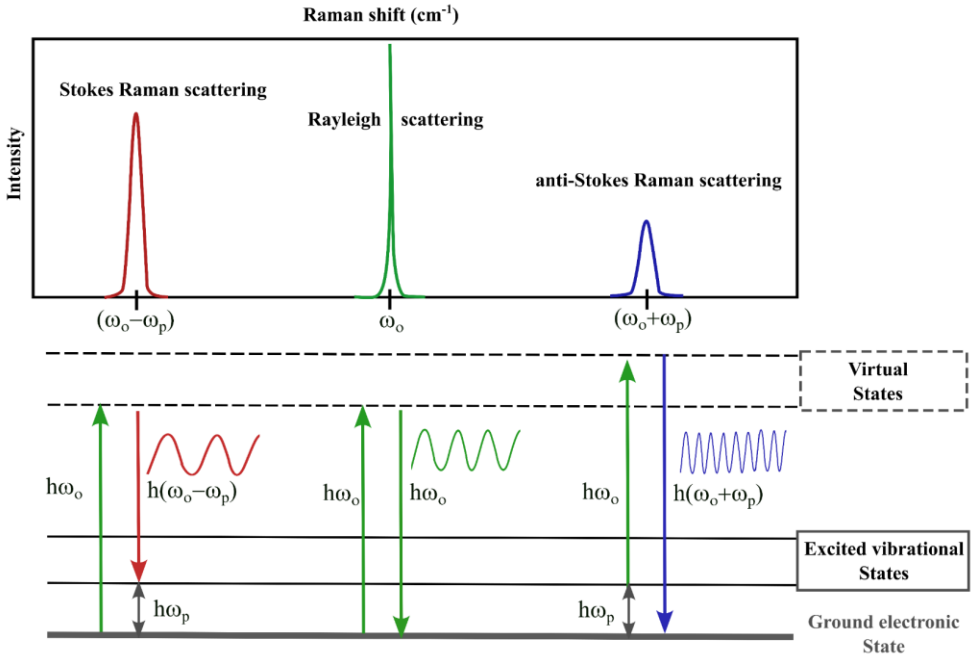

Fig 3.1 The mechanism of Raman – Stokes and anti-Stokes scattering presented with respective peaks

For a specific atomic group, this vibration is unique and is a fingerprint of the material. The acquired spectrum consisting of Lorentzian peaks can characterize a number of features of the material. The Raman shift is indicative of the composition of the materials based on identifying the vibrational frequencies of various molecular bonds. The linewidth of a Raman peak depends on the population of phonons in the material and broadens as the lifetime shortens. The intensity of the Raman peaks indicates the population of phonons [174].

3.1.2 Raman selection rules

This phenomenon is not valid for every phonon mode present in a material, but only for the most sensitive. When the laser is incident on the material, the electric field (E) of the laser excites the molecule to higher energy state,

$$E = E_0 \cos(2\pi\omega_0 t) \qquad \textit{Eq 3-2}$$

where ω_0 is the frequency of the incident light. This causes vibrations in the molecule and displaces (q) the atoms,

$$q = q_0 \cos(2\pi\omega_p t) \qquad \textit{Eq 3-3}$$

where ω_p is the frequency of the phonon (vibrational displacement). The displacement of atoms due to vibration causes the electron cloud of the atoms to deform by inducing a dipole moment (P) in the molecule,

$$P = \alpha E \qquad \textit{Eq 3-4}$$

The resistance of the electron cloud to deformation by an electric field is called polarizability (α), defined as,

$$\alpha = \alpha_0 + \left(\frac{\partial\alpha}{\partial q}\right)_0 q \qquad \textit{Eq 3- 5}$$

So, the detailed expression of polarizability by combining equation (3-2) to (3-5) becomes,

$$P = \underbrace{\alpha_0 E_0 \cos(2\pi\boldsymbol{\omega_0} t)}_{\text{Rayleigh}} + \underbrace{\frac{1}{2}\left(\frac{\partial\alpha}{\partial q}\right)_0 q_0 E_0 \cos\left(2\pi(\boldsymbol{\omega_0} + \boldsymbol{\omega_p})t\right)}_{\text{Anti-Stokes}} + \underbrace{\frac{1}{2}\left(\frac{\partial\alpha}{\partial q}\right)_0 q_0 E_0 \cos\left(2\pi(\boldsymbol{\omega_0} - \boldsymbol{\omega_p})t\right)}_{\text{Stokes}} \qquad \textit{Eq 3-6}$$

which consist of Rayleigh scattering, anti-Stokes scattering and Stokes scattering components based on polarizability of the atom as highlighted. So, if there is no change in polarizability of the atom ($d\alpha$) due to change in vibrational displacement (dq) (indicated in blue), then Raman scattering does not occur. A particular vibrational mode is "Raman active" if there is a difference in the size, shape or orientation of the polarizability at its extreme displacements. This characteristic is unique for every molecule and the Raman active materials produce a Lorentzian peak like signature in Raman spectra due to these vibrational displacements. The peaks in the Raman spectra have characteristic spectral features: frequency peak position (Raman-shift), linewidth and anti-Stokes to Stokes peak intensity ratio.

These active optical phonons in the material are also sensitive to temperature, which can be monitored by studying the listed spectral features. As the temperature of the material increases, there are more phonons with higher energies causing vibrations with greater amplitudes. Due to the anharmonicity of the lattice potential curve, the repulsive force between atoms become greater than the attractive force. This results in a shift in the equilibrium interatomic distance

leading to thermal expansion and change in interatomic force constant (K) which affects the frequency of vibrations indicated by change in peak position,

$$\omega = \frac{1}{2\pi}\sqrt{\frac{K}{\mu}} \qquad \textit{Eq 3- 11}$$

So, as the temperature increases, the bond length will increase ad result in a decrease in the energy of a vibrational mode [175]. A signature of increase in temperature is imprinted on the Raman spectra as the Raman shift (peak position) moves to lower wave numbers due to increasing temperature. As the vibrational amplitude of phonons increases; the phonons scatter more frequently. This increases the probability of phonon scattering, hence the average time before a phonon scatters decreases, and so does the lifetimes of phonons. This results in a larger spread in energies of phonons, indicated in the Raman spectrum by the increase of linewidth of the peak. The final effect is on the anti-Stokes/ Stokes intensity ratio in the Raman spectra. Again as the temperature increases, the phonon population also increases and more phonons occupy excited vibrational states. The probability of a photon interacting with a phonon in the higher energy vibrational states increases. So, the emitted photon would have greater energy than the incident one and would progressively increase with increasing in temperature. This increases the intensity of anti-Stokes scattering peak, impacting the anti-Stokes/Stokes ratio.

The temperature responses of these Raman spectral features is analyzed by fitting the spectral position and linewidth of the Raman peak or taking ratio of the Stokes to anti-Stoke peak intensity. The temperature variation of these Raman properties can be expressed using the following equation [162], [176]:

Raman shift based:

$$\omega(T) = \omega_0 + A\left(1 + \frac{2}{e^{\frac{h\omega_0}{4\pi kT}} - 1}\right) + B\left(1 + \frac{3}{e^{\frac{h\omega_0}{4\pi kT}} - 1} + \frac{3}{\left(e^{\frac{h\omega_0}{4\pi kT}} - 1\right)^2}\right) \qquad \textit{Eq 3- 12}$$

where ω is the shift/frequency of a specific Raman peak, ω_0 is the Raman shift/frequency at 0K, A and B are constants specific to the material, h is the Planck constant, k is the Boltzmann constant, and T is the absolute temperature. For most materials, the Raman peak shift position moves to lower values as the temperature increases. The shift can also be sensitive to temperature induced stress in materials and can affect the accuracy of the results, but for low temperature rise the stress effect could be neglected.

Raman line-width based:

$$\Gamma(T) = C\left(1 + \frac{2}{e^{\frac{h\omega_0}{4\pi kT}} - 1}\right) + D\left(1 + \frac{3}{e^{\frac{h\omega_0}{4\pi kT}} - 1} + \frac{3}{\left(e^{\frac{h\omega_0}{4\pi kT}} - 1\right)^2}\right) \qquad \textit{Eq 3- 13}$$

Where Γ is the peak linewidth, C and D constants specific to the material. Generally, linewidth is less sensitive to temperature and is not regarded practical for temperature determination. Moreover, a sound Raman signal is required for obtaining a good linewidth otherwise a large error is induced in the measurement.

Raman intensity based:

$$\frac{I_S}{I_{AS}} = Eexp\left(\frac{h\omega}{2\pi kT}\right) \qquad \textit{Eq 3-10}$$

where I_S/I_{AS} is the stokes to anti-Stokes intensity ratio, ω is the shift/frequency of the Raman peak and E is the calibration constant determined experimentally. The main advantage of the method is simplicity as it does not require any precise peak fitting and is not affected by strain in the material. However, both the peak intensities cannot be measured simultaneously for most of the commercially available Raman setups, except for materials having Raman active modes with low vibrational energies. In most cases, the grating of the spectrometer must move to cover the entire range and can cause amount of light reaching the detector to vary due to its mechanical movement. Also, the intensity of anti-Stokes scattering is much weaker due to lower population of excited state, which reduces the accuracy of this method. In general, the absolute intensity method is a difficult parameter to measure accurately and consistently. Out of these 3 methods, the Raman-shift based method is the most preferred one for temperature measurement.

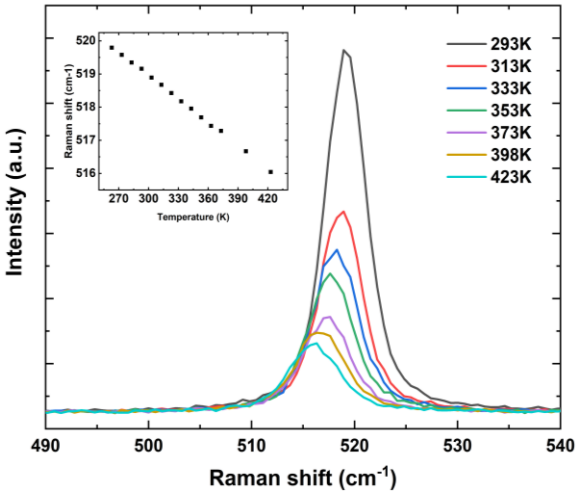

Fig 3.2 Temperature dependent evolution of Si Raman scattering peak, Inset – Linear shift in Raman shift peak position with increasing temperature

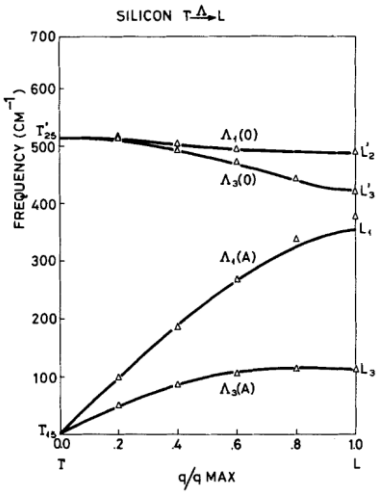

Fig 3.3 Dispersion curve for Si calculated along the symmetry line Γ-L [177]

In the case of Silicon, the Raman scattering phenomena is observed by a strong narrow peak at 519 cm^{-1} Fig. 3.2. As the temperature increases, the peak position moves to smaller wavenumber and fitting these peaks can yield a linear relationship between Raman shift and temperature Fig. 3.2 (inset). This is a characteristic of a transverse optical phonon mode at the centre Brillouin zone as presented in Fig. 3.3 [177]. The phenomenon occurs because of the translational symmetry of a perfect lattice where the momentum conservation law states that when a photon is absorbed by the lattice, only the phonons with $q \cong 0$ are transmitted, giving rise to the optical

Raman spectra. This peak is associated with the crystalline phase of Silicon. In amorphous Silicon, the selection rules do not apply as there is loss of long-range order and breakdown of translational symmetry. So, all the phonons are optically allowed and are represented by a broadband (and not a narrow peak) in the 460 to 490 cm^{-1} range, resembling the phonon density of states for amorphous phase [178]. Similarly, for defect-containing lattices, as is the case for chalcogenides, the momentum conservation laws do not hold and most of the lattice modes gain some dipole moment change. This results in an increased interaction with the electromagnetic radiation and more information gathered from the optical spectra.

Next, it was experimentally found that for diamond-like covalent crystals, namely Si, Ge show a temperature dependent absorption at frequencies higher than those which the lattice can transmit [177]. The light scattering process can be viewed as absorption of the incident photon, emission of a photon (recorded experimentally), and creation of an optical phonon which then decays via anharmonicity into two or more phonons. The equations (3-8), (3-9) and (3-10) represent these anharmonic effects of light scattering due to optical phonons on characteristics of the Raman peak. This temperature dependent behavior of crystals is the basis of using Raman spectroscopy as a thermometry technique. In case of GeSbTe based chalcogenides, the Raman spectra has been extensively studied but temperature dependence has not been evidenced with an exception of one report [179]

3.1.3 Raman thermometry

This steady state thermal characterization technique utilizes the temperature sensitivity of Raman scattering peak as local thermometers, as discussed. It is a non-destructive optical technique providing sub-micrometer spatial resolution, with no requirement of microfabrication and high material selectivity as its key advantages [180]. The technique is based on the initial reports for a single substrate of Silicon, where it provides the temperature dependent signature of the optical phonon related Raman peak at 521 cm^{-1} [162]. In case of a multi thin film stack, it can provide information of the layers in a stack demonstrating material selectivity.

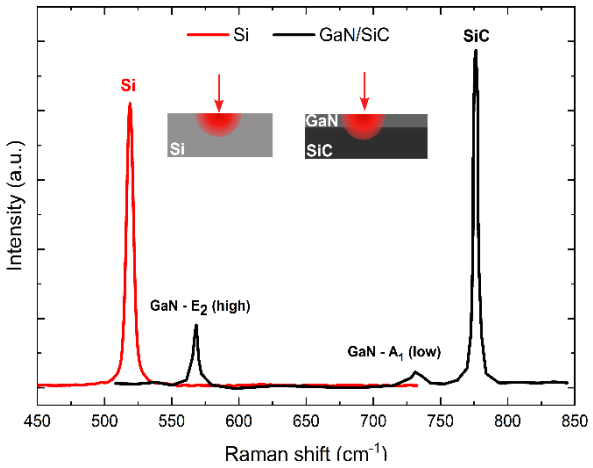

Fig 3.4 A typical Raman signal for a single substrate Si in red, and for GaN on SiC in black consisting of apparent Raman scattering peaks from phonon mods of both GaN and SiC [166]

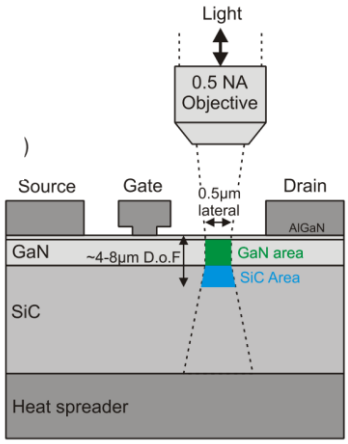

Fig 3.5 Raman thermography setup where both the device structure and substrate are transparent to laser light, giving a Raman signal for both materials in the spectrograph [166]

For example, GaN on SiC based devices used for high electron mobility transistors [166], Raman peaks from both GaN and SiC optical modes can be obtained Fig. 3.4. Hence, it enables characterization of both the materials temperature characteristics and the interface. This ability depends on the depth of penetration of the incident laser related to the material absorption coefficients as shown in Fig. 3.5. This depth, also known as the skin depth is defined as the point where the power of the laser decreases by $1/e^2$ (about 13%) of its surface value. It can be determined by the extinction coefficient of the materials (k) and laser wavelength (λ), given by,

$$\delta_e = \frac{\lambda}{2\pi k} \qquad \textit{Eq 3- 11}$$

For a multi-layer thin film stack, the absorbance of the laser of a particular wavelength into a multilayer stack of material can be evaluated by performing optical calculation based on Fresnel equations [181].

So, the basic material requirements for the possibility of probing a material using Raman thermometry are:

1. The material should be Raman active – should produce a non-negligible vibrational signature in the Raman spectra from one of its optical modes.
2. The vibrational modes should be sensitive to temperature, affecting the peak position/ the line width of the peak/ Stokes to anti-Stokes intensity ratio. Any of these characteristics can be used as they demonstrate various advantages depending on the material under study.

In theory, for a steady-state technique, the heat flux input in the system is known and the spatial temperature gradient is measured using temperature sensors. The extraction of thermal conductivity is based on the Fourier law of heat conduction,

$$q = -k\nabla T \qquad \textit{Eq 3- 12}$$

where q is heat flux density, k is the thermal conductivity and ∇T is the temperature gradient. By knowing the heat flux injected in the system and sensing the local temperature change, the thermal conductivity can be extracted.

Analogously in Raman thermometry, a focused Gaussian laser beam provides the input power to locally heat the material connected to a heat sink. The laser increases the temperature of the material locally to T_H. This local increase in temperature is probed by recording the spectral features of material with a spectrometer. Sensitivity of spectral features of Raman peaks act as local thermometers providing the local temperature (T_H) based on the Raman peak shift observed. Firstly, a calibration of the material is performed to extract the sensitivity of the spectral features Fig. 3.6 (bottom inset). This calibration is performed by changing the sample temperature while using very low laser power to avoid local heating and local structural changes. The spectral position (Raman shift) of the Raman active peak is recorded as a function of temperature and is called as the calibration curve (ω_T (calibration coefficient) $= d\omega/dT$). This coefficient is used as an optical thermometer.

Next, the change in spectral peak position as a function of increasing laser power is recorded ($\omega_P = d\omega/dP_{abs}$) Fig. 3.6 (top inset). The local temperature rise (ΔT_i) in the system due to the

power input (P_i), is extracted by correlating the change in peak position due to input power to the calibration curve by,

$$\Delta T_i = \frac{\omega_i - \omega_0}{\omega_T} \quad [K] \qquad \textit{Eq 3-13}$$

where ω_i is the spectral position of a peak for a given input power P_i, ω_0 is the spectral position of a peak recorded at 0°C and ω_T is the calibration coefficient. Further the thermal conductance (G) of the material can be extracted correlating the temperature and power related coefficients as follows,

$$G = \frac{\frac{d\omega}{dT}}{\frac{d\omega}{dP_{abs}}} = \frac{\Delta P_\omega}{\Delta T_\omega} \quad \left[\frac{W}{K}\right] \qquad \textit{Eq 3- 14}$$

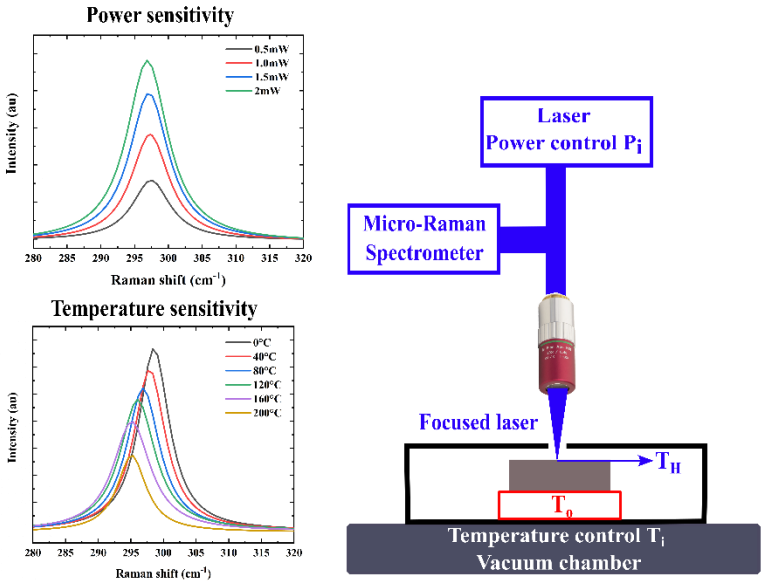

Fig 3.6 Schematic of Raman thermometry with insets showing temperature sensitivity and power sensitivity of Raman peaks

This correlation between temperature rise and power absorbed in the system coupled with solution of the steady-state heat diffusion for a particular system, yields the thermal conductivity. In case of a Gaussian laser beam incident on a surface of homogenous and semi-infinite bulk material, the induced temperature rise was calculated by solving the steady state equation [180], [182], [183]:

$$k\nabla^2 T = \frac{2P_{abs}}{\pi w^2} exp\left[-2\frac{x^2}{w^2}\right] \qquad \textit{Eq 3-15}$$

where k is the thermal conductivity, P_{abs} is the power absorbed defined as $P_{abs} = P_{input} * A$, and w is the beam waist of the laser. This follows the assumption that the laser power is strongly

absorbed at the surface, the penetration depth of laser in the material approaches zero within the semi-infinite sample. An analytical linear solution derived for equation is [184]:

$$k = \frac{P_{abs}}{4\sqrt{\pi}\,\Delta T\,w} = \frac{P_{abs}}{4\sqrt{\pi}\,(T_{Raman} - T_{stage})\,w} \qquad \textit{Eq 3-15}$$

To enhance accuracy of the measurement, we performed measurement for a series of power values and not only for one excitation. the solution can be represented as a ratio of the two sensitivity coefficients as suggested by Stoib et al [180]:

$$k = \frac{\frac{d\omega}{dT}}{4\sqrt{\pi}\,w\,\frac{d\omega}{dP_{abs}}} = \frac{G}{4\sqrt{\pi}\,w} \qquad \textit{Eq 3-16}$$

This solution is for an isotropic semi-infinite material. In complex cases for suspended membranes or thin films in a stack various analytical [163], [167], [185] and modelling solutions were developed. In context of this thesis, we elaborate the procedure in the next section by presenting an example.

Pre-requisites for Raman thermometry:

1. Map out vibrational modes possible in chalcogenide stoichiometry's – to create knowledge base of the chemical structure and identify vibrational modes with temperature sensitivity
2. Evaluate the laser beam profile
3. Evaluate the absorbance of the material
4. Develop a finite element model to mimic the heat transfer in Raman thermometry and build an abacus of thermal conductance as a function of thermal conductivity.

Methodology for Raman thermometry:

1. Acquire Raman spectra for the material at low input power (avoid local structural changes)
2. Identify the vibrational modes present for the material and its position by performing Lorentizan fitting for the Raman spectra
3. Perform temperature dependent Raman acquisition at very low power
    a. To select the most sensitivity mode to temperature
    b. Extract the temperature dependence of the particular vibrational mode to temperature – Calibration coefficient
4. Perform power dependent Raman acquisition at constant temperature
    a. Extract the power dependence of the selected mode
    b. Repeat this as a function of temperature
5. Co-relate the calibration coefficient to the power dependence of vibrational modes to extract the thermal conductance of the material.

3.2 Experimental development of Raman thermometry for chalcogenides

3.2.1 Experimental setup

The Raman thermometry measurements were performed using a LabRAM HR confocal system from Horiba Jobin-Yvon. The detailed description of the setup discussed henceforth is provided in the schematic Fig. 3.8. The system is equipped with a continuous wave diode pumped laser (λ = 473.11nm). The laser from the source passes via density filters which are used to control the input power. The laser is focused on the sample using long distance microscope objectives. The sample is installed in a chamber with temperature and vacuum control. The backscattered light travels via the optics and is focused in the spectrometer yielding a Raman spectrum. The Raman setup was previously installed with a translation stage offering automatic control over the stage. The key aspects for optical Raman thermometry measurement are divided in the following 3 sections: 1. Optics and spectrometer, 2. Laser and 3. Temperature control.

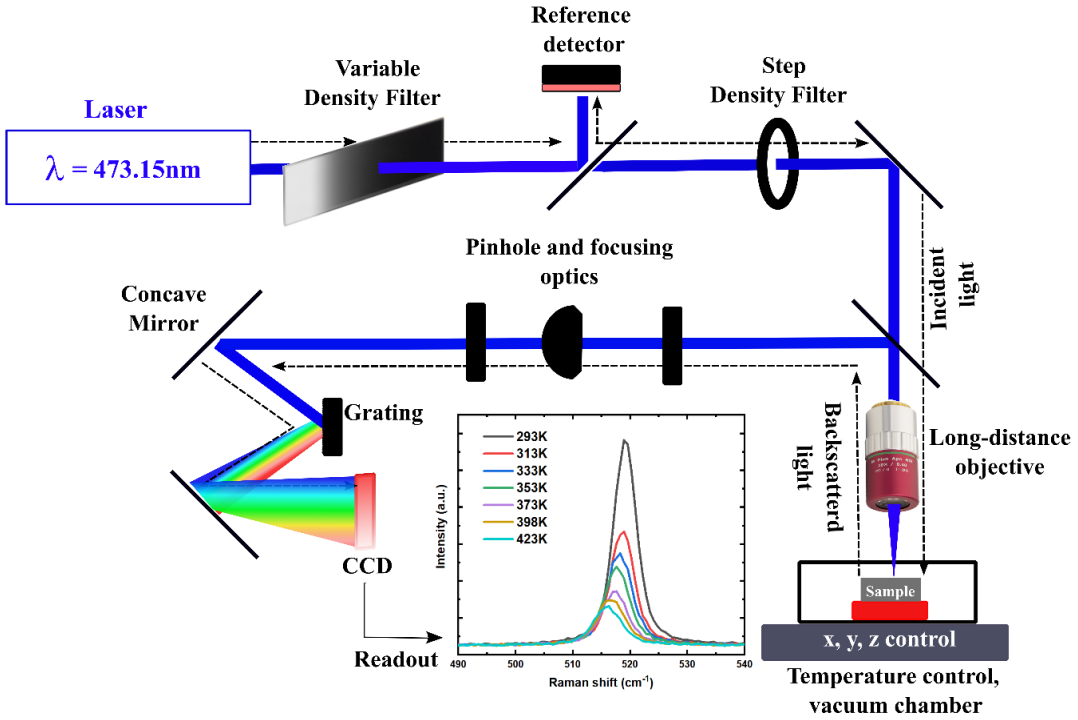

Fig 3.8 Schematic of Raman setup from Horiba Jobin-Yvon with the dotted light presenting the path of laser.

Optics and spectrometer

Spectrometer characteristics are associated to high spectral resolution of the Raman spectra in order to extract precise peak position. The focal length of the spectrometer and the groove density of the grating are key to ensure high spectral resolution of the recorded Raman spectra. The features of the confocal system to ensure this high spectral resolution to resolve peaks are:

a. Spectrometer with a focal length of 800mm
b. Diffraction grating with 1800 grooves/ mm
c. Spectral resolution @ 473.11nm < 0.7 cm^{-1}

The equipped confocal pinhole and focusing optics allows for control over depth of field to achieve highest axial and spectral resolution. The control over confocal hole size (0 to 300 μm) blocks the "out of focus" light into the spectrometer if required when probing the sample in depth. It helps reduce or eliminate background noise and unwanted information apart from the sample focal plane.

Temperature control chamber

Calibration curve is a primary requirement for thermal characterization of material by Raman thermometry. So, for the purpose of temperature control, during the course of this work a new heating stage was installed with the existing Raman setup as shown in Fig. 3.9. The heating stage from LINKAM was equipped with 2 different kinds of heater configurations:

a. THMS350 EV: Temperature range: -195°C to 350°C (Heating rate - 0.01 to 30°C/min), Vacuum compatible 0.001 mbar, liquid nitrogen cooling.
b. THMS600 E: Temperature range: -195°C to 600°C (Heating rate - 0.01 to 150°C/min), not vacuum compatible, water cooling.

Both the heater variations have a temperature stability of <0.01°C. The heater stages are made of silver. The stage is connected to a liquid nitrogen dewar and a cooling system controller for having precise control over liquid nitrogen flow. The unique design of the system reduces noise and vibrations. The universal controller monitors all the functions - cooling system, heating system and vacuum gauge sensor to ensure precise temperature control and vacuum measurements Fig. 3.10. The objective working distance required was 5.8mm which was sufficed by the use of long-distance objectives. The chamber is equipped with 4 probes for the possibility of performing *in-situ* electrical characterization along with Raman measurements for an operational device, if required. A vacuum compatible paste is used when performing experiments to ensure that the sample does not drift and a good thermal contact is established between the stage and the sample. An additional mounting stage was fabricated to mount to the heating stage at precise working distance from the microscope objective.

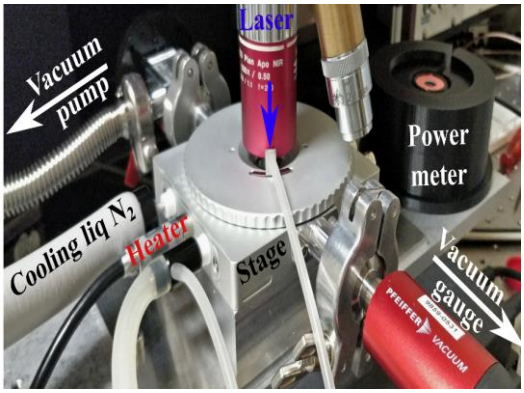

Fig 3.9 Heating/ cooling stage from Linkam – connections showing vacuum gauge, liquid N2 cooling and heater attachment. A Si-photo diode power meter from Thorlabs

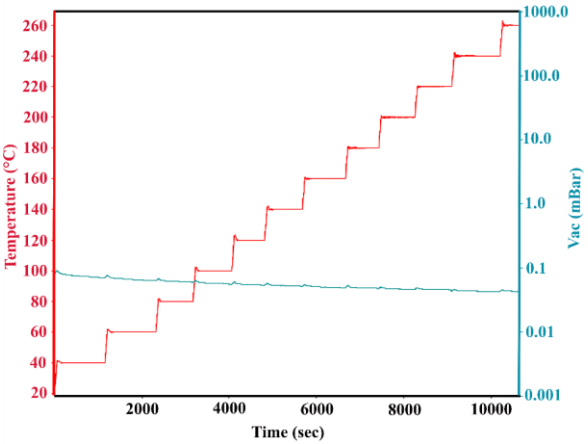

Fig 3.10 Graph from universal controller of Linkam stage showing precise temperature and pressure control. This schematic presents a cycle of experiments to extract the temperature sensitivity of material

Characteristics of the laser:

Another primary requirement for a Raman thermometry study is control over the power of the laser. As stated, this is crucial to extract the power dependence of the vibrational modes at a given temperature. The laser implemented for this study is a 473nm continuous wave diode pumped blue laser. The maximum input power of the laser is 25mW, and when focused with a 100x objective drops down to 13mW. The Raman setup was pre-equipped with **a *step density filter*** which provided with limited input power options over a wide range of intensity. Each filter is characterized by the optical density (OD)number defined as,

$$OD = log\left(\frac{P_{input}}{P_{output}}\right), \qquad Eq\ 3\text{-}17$$

with the OD values = [2, 1, 0.6, 0.3, 0] as presented in Fig. 3.11. Such few options of input power over a wide range from 0.013mW to 13mW are not optimal for Raman thermometry measurements. Firstly, high powers could lead to local structural changes in the material or damage the material. Next, it can cause high local temperature rise in the material, not suitable for Raman thermometry experiments and linear regression. And at last, 3 possible suitable options with respect to intensity are sufficient to statistically estimate the desired sensitivity coefficients. So, in this regard, a rectangular continuously variable neutral density filter was installed and calibrated during the course of this work. The OD of the filter continuously ranged from 0.04 to 4 and was mounted at the source of the laser. The filter is composed of a UV fused Silica substrate, which exhibits high transmission from ultraviolet to near-infrared range. The filter was fitted on a one axis translation mount to move the density filter and attenuate the laser. The mount is marked with a Vernier scale which provides a resolution of 100μm along the x-axis and can be precisely moved by hand or with a hex key. Fig. 3.12 presents the attenuation curve of the laser as the filter is moved along the x-axis.

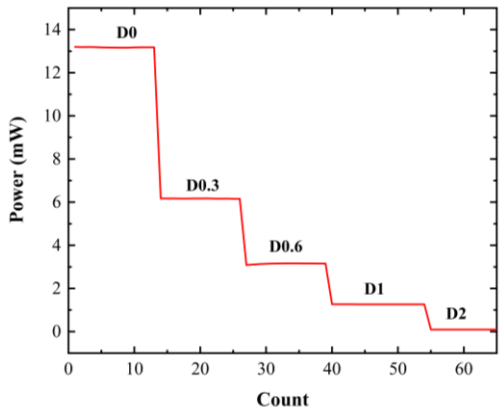

Fig 3.11 Measure power of laser varying with the change of step density filters denoted in the graph.

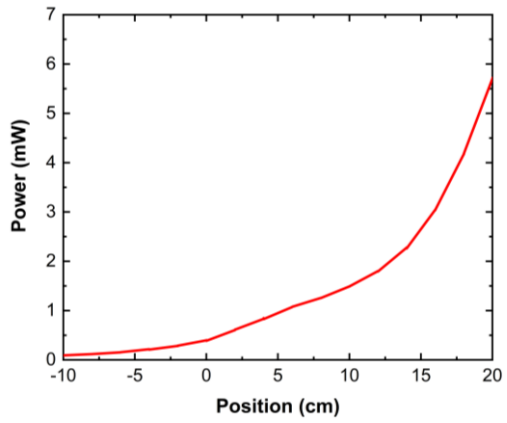

Fig 3.12 Measure power of laser varying with the translation of continuous density providing a wider control on input power

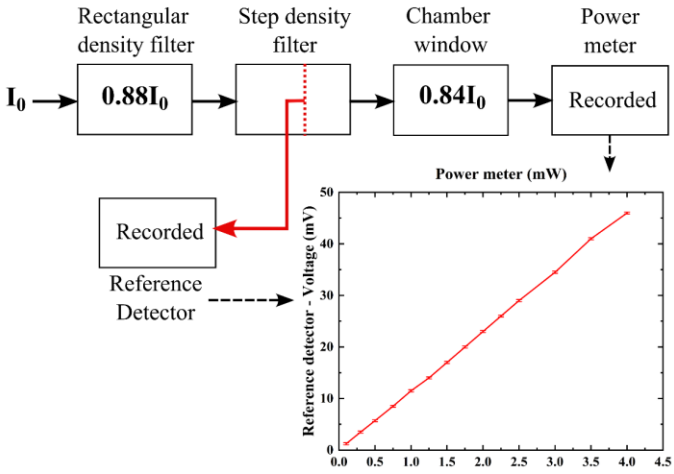

Fig. 3.13 The input laser power (I_0) is measured at the source after it passes via the rectangular density filter by a photo-diode in mVs. After it passes via the log-distance objective it is measured by a power meter in mWs. Reference detector measured voltage vs Power meter presents a calibration curve between both the measurements. This is performed for ease of measurements.

Next, key aspect is measurement of input power which is crucial for the thermal measurements. For this purpose, the power was measured at the source of the laser and the exit of the objective after it has passed *via* the Raman optics to account for any attenuation. At the exit, a standard photodiode power sensor from ThorLabs was installed which is compatible with the required laser wavelength and provides a resolution of 1nW. This sensor was mounted on a small holder having the same height as that of the heating stage. At the source after the continuous density filter, a silicon photo diode was installed into the optical path of the laser. This diode measured the reflected laser intensity when the optical path was blocked. This work was carried out during a previous PhD [186]. Photo voltaic mode at zero voltage bias was chosen as it is appropriate for low light level detection. The reflected power of the laser was measured and converted to voltage signal by the Silicon photodiode. This measured output voltage was correlated with the power measurements at the exit and calibration curve is presented in Fig. 3.13. So, installation of a rectangular density filter, with 2 reference power measurements and their correlation provided with the functionality of performing multiple power measurements with low error and precise power measurement.[11]

To focus the laser on the material of study, long distance objectives were adopted as the laser was focused via a transparent heating stage window. Standard microscope objectives do not allow for measurements when the setup is equipped with a temperature control chamber due to their small working distance. 50x and 100x Mitutoyo Apochromatic NIR objective were used for Raman thermometry measurements.

a. 50x, NA = 0.42, working distance = 17mm and theoretical beam radius = 0.68µm
b. 100x, NA = 0.50, working distance = 10mm and theoretical beam radius = 0.57µm

[11] Note – To measure the exit power after every measurement would require movement of the objective from the heating stage to the power meter, this could disturb the focus of the laser and involve manual errors

Where NA is the numerical aperture and the theoretical beam radius is calculated by using the formulism 0.61λ/NA for theoretical Rayleigh resolution.

Laser beam spatial profile:

The spatial mode for emission of this laser is lowest-order transverse mode (TEM_{00}) which has an irradiance distribution of a Gaussian function. So, the intensity profile of the laser can be defined as,

$$I(r) = I_0 \exp\left(\frac{-2r^2}{w^2}\right) \qquad \textit{Eq 3-18}$$

here I_0 denotes the peak intensity at the center of the beam, r is the radial distance from the axis and w is defined as the beam waist where the intensity is $1/e^2$ (13.5%) of the peak intensity. We assume that the beam is near-Gaussian and circularly symmetric as $M^2 < 1.1$ and high beam symmetry from the manufacturers. Integration of the intensity profile over the radial plane gives the total optical power (P),

$$P = \int I(r)dr \qquad \textit{Eq 3-19}$$

from a practical standpoint of power measurement by a sensor, 99% of the total power is concentrated in a radial distance of $1.5w$. To characterize the laser beam waist, the knife edge method was used. The laser beam waist is key to evaluate the thermal conductivity by Raman thermometry as stated in equation.

In knife edge method, the laser beam is attenuated by placing a knife edge blade in its optical path changing the attenuation level of the laser from 0 to 1 of the measured normalized power. A sharp Si wafer was used as a knife edge and the power was measured simultaneously by the Si photodiode power sensor placed on a motorized platform. The laser was focused on the power sensor and the Si wafer was placed above the sensor. When the knife edge object does not block the path of the laser, full power received by the sensor as represented in Fig. 3.14. Now the knife edge was gradually scanned across the laser beam by micrometer motorized steps. The

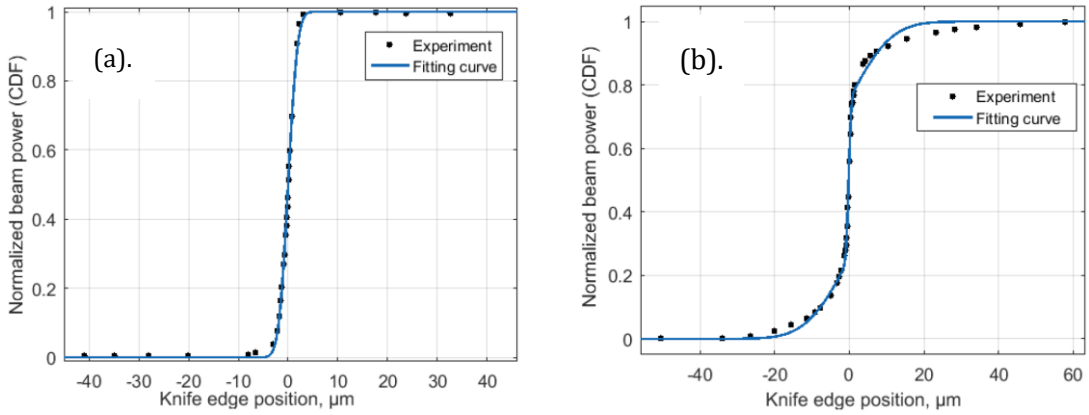

Fig. 3.14 Analysis of the knife-edge experiment done for two lenses: (a) 50x (NA=0.42) and (b) 100x (NA=0.5) for normalized beam power and a fitting curve (CDF) to extract the laser beam waist. The extracted beam waists are: 50x, w = 1.48μm and 100x, w_1 = 0.56μm, w_2 = 8.96μm [186]

knife edge moves in perpendicular direction to the propagation of laser and blocks its path gradually decreasing the power. The behavior of this measured power on integrating the intensity function, is a complementary error function defined as,

$$P(D) = \frac{P_0}{2}\left[erfc\left(\frac{(D - D_0)}{w/\sqrt{2}}\right)\right] \qquad \textit{Eq 3-20}$$

where, $P(D)$ is the power measured as a function of the knife P_0 is the maximum laser power measured and D_0 is the position when the knife edge is at the middle of the beam transmitting 50% of the power to the power sensor. Following the experimental process, the measured intensity was fitted using the error function to extract the beam waist as shown in Fig. 3.14. For 100x lens, two weighted erf functions were required to fit the measured data. The cause was due to presence of a second Gaussian beam artefact rising from the complex optics of the objective. According to results, they were weighted as μ=55% for the narrow beam and 45% for the broader beam,

$$\frac{P(D)}{P_0} = \frac{\mu}{2}\left[erfc\left(\frac{(D - D_0)}{w_1/\sqrt{2}}\right)\right] + \frac{1-\mu}{2}\left[erfc\left(\frac{(D - D_0)}{w_2/\sqrt{2}}\right)\right] \qquad \textit{Eq 3-21}$$

This led to the Gaussian laser beam profile from the 100x lens defined by 2 Gaussian functions and hence, 2 beam waists.

3.2.2 Material and thickness considerations

The experiments were performed on different phase change materials listed as follows:

1. $Ge_4Sb_4Te_7$ (GST-447)
2. Ge-rich GeSbTe (GGST)
3. Ge-rich GeSbTe N-doped (GGSTN)
4. GeTe

The final important pre-requisite parameter before getting into the Raman thermometry experimental procedure is the absorbance of the material. The absorbance of the material can be evaluated experimentally and theoretically. Initially, it was evaluated theoretically for design of the stacks. The goal was to design the thin film stack thickness to optimize the absorbance of the laser in the phase change material. Absorption of light into a material is determined by the extinction coefficient (k), which indicates the amount of attenuation of an electromagnetic wave when it propagates through a material. A set of refractive index values of phase change materials from literature were mapped out as shown in Fig. 3.15. Phase change materials are very absorptive in both, amorphous and crystalline phases. Depending on the stoichiometry, ranging from GeTe to GST-225 to Ge-rich GST, it can be seen that the values span in a range as denoted by the vertical line in Fig. 3.15.

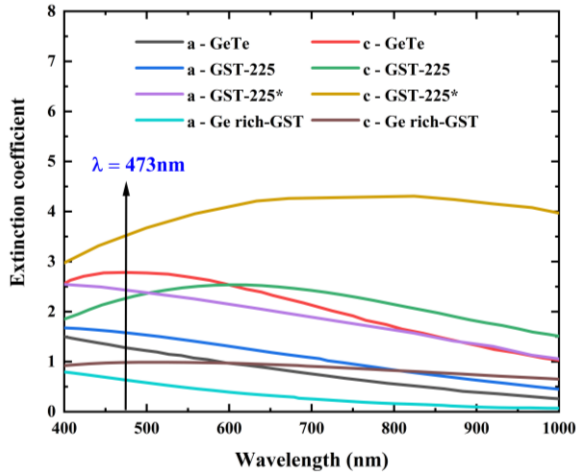

Fig 3.15 Extinction coefficient (k) for various phase change materials as listed

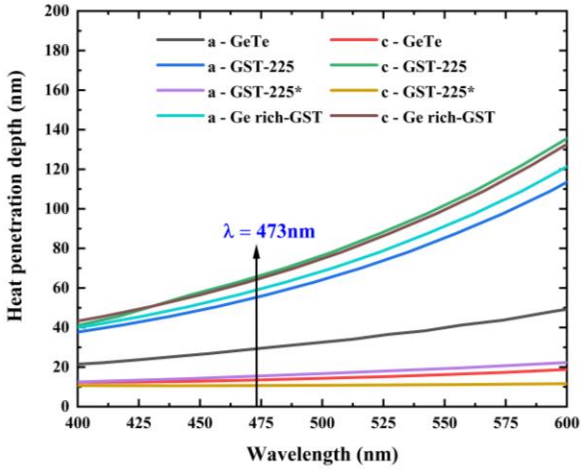

Fig 3.16 Heat penetration depth (skin depth) of laser into the materials listed

Fig. 3.15 comprises of the maximum and minimum extent of values reported in literature [144], [187], [188]. Note – this was done to ensure appropriate selection of thickness for a range of phase change materials which were characterized. Also, the values reported in literature can vary quite significantly for similar compositions and deposition techniques [189]. Correspondingly, the heat penetration depth, also known as the skin depth was evaluated for the range of materials shown in Fig. 3.16. This depth is the point in the material at which the power of incident light decreases to $1/e^2$ (13%) to its surface magnitude. The penetration depth ranges from 10 to 60nm for the laser (473nm) used in this study. This indicate that a thickness of more than 60nm could be used to avoid any Raman signal from the substrate, interface contributions and extract the intrinsic thermal conductivity of the material of concern. Also, as discussed, electrical resistivity of GST does not show much dependence upon thickness up to 50nm. So, 100 and 200nm thick films were an appropriate choice for thermal characterization.

Next step is to protect chalcogenides with an additional protective thin film as oxidize in air. The material of choice for protection was silicon nitride (SiNx) due to its extinction coefficient (k~0), so that laser travels through the thin film without loss of intensity. One can calculate the coefficients of reflection and absorption of light by using the transfer matrix formulism [181]. The calculation was performed iteratively from 0 to 150nm of SiNx thickness. Due to the refractive index of SiNx [190], the absorbance of the laser in GST oscillates with the thickness of SiN as depicted in Fig. 3.17. Maximum laser power is absorbed in GST for thickness of SiN ranging between 40-50nm. The same procedure was followed for other chalcogenide stoichiometries and phases, Fig. 3.18. SiN thickness of 45nm was chosen as, maximum laser absorption in the range of 90-100% was observed. So the stack was defined as follows: SiN/ PM/ Native oxide/ Si : 45nm/ 200nm/ substrate. This is a crucial step to optimize the signal to noise ratio as the temperature measurements depend on the choice of vibrational mode implemented as the thermometer. This way the signal of the Raman spectra is improved as the without any interference from the substrate to the Raman signal.

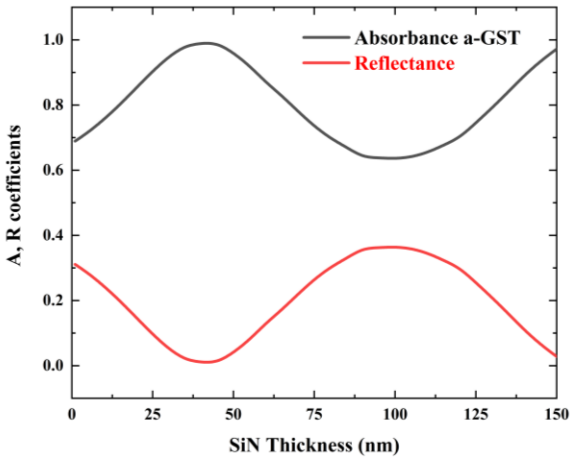

Fig 3.17 Absorption and reflection coefficients of 473.15 nm laser in a stack with varying SiN_x thickness and GST thickness fixed at 200nm

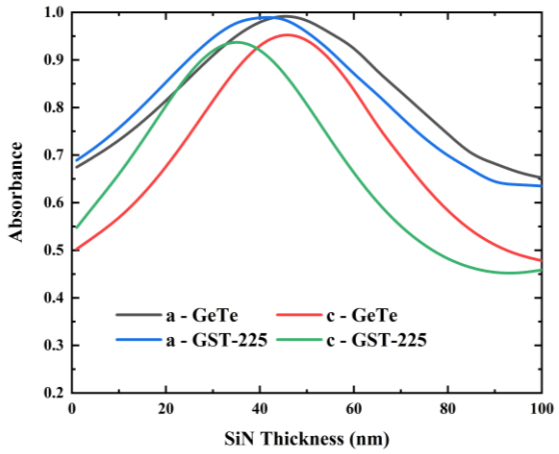

Fig 3.18 Absorption coefficient of 473.15nm laser in amorphous and crystalline phases of GeTe and GST-225 with varying SiN thickness (protective layer)

3.2.3 Example of Raman thermometry

The procedure illustrated is treated with an example of crystalline Ge-rich GST in the following section to understand the characterization process.

a. Raman setup

Raman setup calibration procedure was followed to ensure the consistency of the measurement setup output. The instrument was repetitively calibrated to ensure the zero position of the spectrometer as shown in Fig. 3.19. If the spectrometer is not centered, it can result in an error for the wavelength of the laser (Fig. 3.20) and consequently produce an uncertainty in the position of Raman peaks acquired as shown in Fig. 3.21. Then the spectrometer was moved in the range of wavenumbers (Raman shift) expected for the material under study, in this case 100 to 700 cm^{-1}. A measurement of background noise was performed and the focus was adjusted to ensure low background noise. All the experiments were performed in dark. Next, the sample was placed in the newly adapted heating stage under vacuum (10^{-2} mbar). Each acquisition was performed after ensuring stable temperature and pressure after any heating cycle. The material was observed *via* the microscope to ensure no possible drift of the sample. Raman spectra was acquired at very low power 0.5mW to avoid any local structural changes. Different combinations of acquisition times and averaging via trial and error to choose an appropriate combination for measurements. Before every measurement, fluctuation of power was observed if any, and constant input power was ensured by combination of continuous and step density filters. Before and after every measurement, power amplitude was recorded to ensure consistency. Prior to every acquisition, the focus of the laser spot on the sample was optimized for highest intensity (focus of camera and laser are different) as shown in Fig. 3.22. It is crucial to acquire a Raman spectrum without any noise/ error data points as it can influence the peak fitting procedure and hence the position of the peaks.

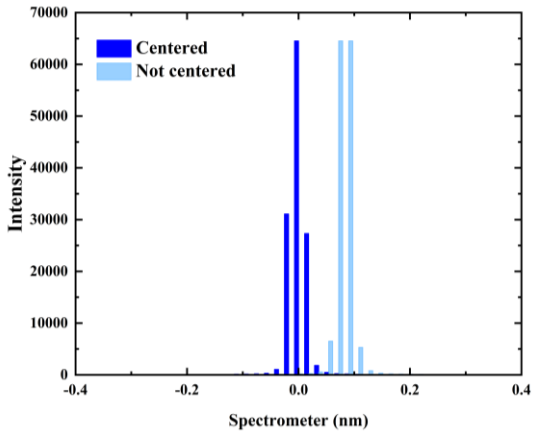

Fig 3.19 Schematic of shift in the position of spectrometer. Repetitive use of setup can lead to a shift in the zero position of spectrometer

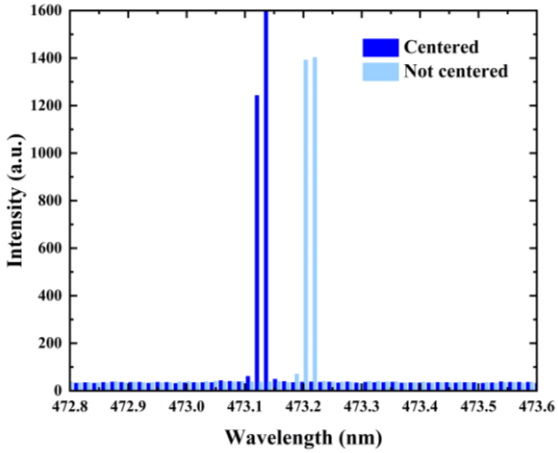

Fig 3.20 Schematic comparing the position of 473.12 nm laser for centered and not centered spectrometer.

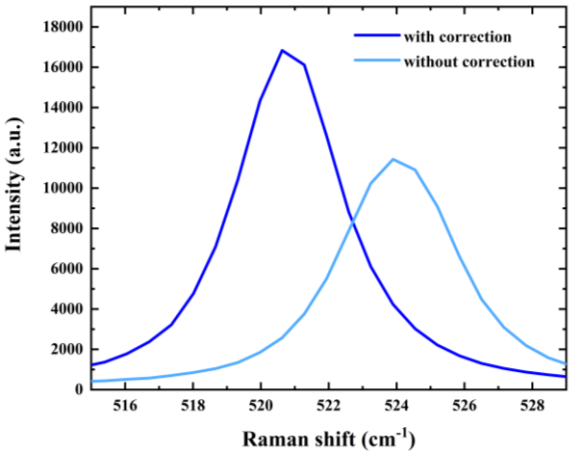

Fig 3.21 Si Raman peak position at 521 cm^{-1} impacted by uncentered spectrometer leading to a shift of 3 cm^{-1} to 524 cm^{-1}

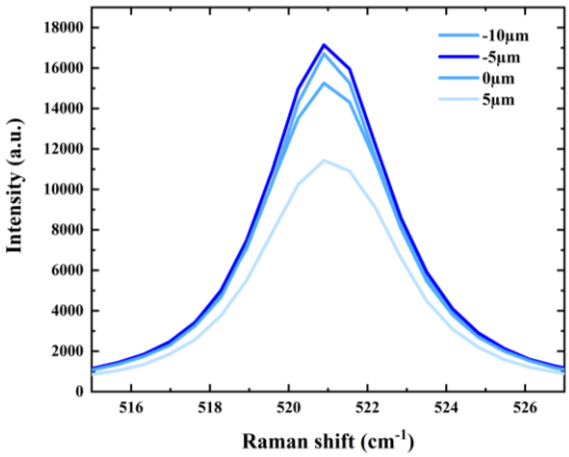

Fig 3.22 Change in intensity of acquired signal due to change of focus in z – direction. 0µm focus is for the microscopic image whereas the laser focuses to maximum intensity at -5µm

b. Raman acquisition

Fig. 3.23 presents the Raman acquisition performed for crystalline Ge-rich GST material. The Raman spectrum provides useful information regarding the vibrations present in the material. These vibrations give an insight into the structural arrangement of the material, their temperature dependence provides with information about the stability of the material. To understand the structure. First the vibrational modes present in the spectrum were identified. A detailed explanation regarding the identification of the vibrational modes and its correlation with the structure of the materials is presented in Chapter 4. From the spectrum, the structure of the material could simultaneously be identified. For the purpose of this section the identified modes are listed alongside the Fig. 3.23. Here, the presence of Sb-Te vibrations belonging to Sb_2Te_3 pyramidal structure suggests the possibility of a trigonal or hexagonal GST phase. Next, the

Raman spectra was treated, first to subtract baseline and then Lorentzian peak fitting. Thanks to the choice of laser and quality of sample, a clean Raman spectrum was acquired. So, a straight line (end to end points) baseline subtraction was followed. Next, the Lorentzian peak fitting was performed for various choice of peaks to identify the best fit with the highest R^2 value. The peaks listed and the number of peaks accounted during fitting can differ to get the best fit.

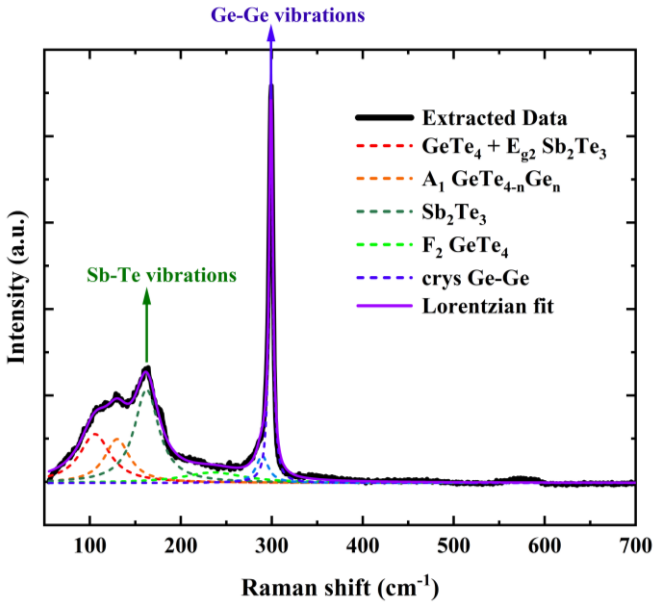

Vibrational modes	Raman shift (cm^{-1})
$GeTe_4$ + E_{g2} Sb_2Te_3	105.51 ± 1.12
A_1 $GeTe_{4-n}Ge_n$	129.97 ± 0.80
Pyramidal Sb_2Te_3	162.28 ± 0.25
F2 $GeTe_4$	235.93 ± 2.72
c – Ge-Ge	299.04 ± 0.012
R-Square = 0.99407	

Fig 3.23 Raman spectrum of crystalline Ge-rich GST with Lorentzian fit for the spectra with peaks assignment in the table

c. Temperature dependent Raman acquisition

After acquiring a Raman spectrum at room temperature and identifying the peak position and best fit, temperature dependent measurements were performed. The temperature was ramped up at 20°C/min and at every step a 5 mins of thermalization period was maintained to ensure stable temperature and vacuum conditions, Fig. 3.10. The Raman spectrum was acquired at each step and followed by Lorentzian fitting procedure. The sensitivity of all the vibrational modes was analyzed by peak fitting and identifying the peak position. The most sensitive peaks were chosen as local thermometers – Sb-Te and c-Ge-Ge as they have the highest intensity and lowest uncertainty in the peak position. This choice of a phonon mode to be a non-contact local thermometer largely depends on the optimum signal to noise ratio. This ratio plays a crucial part at high temperature measurements as noise from the system increases. Fig. 3.24 shows the effect of temperature on the position of Raman peak of crystalline Germanium. By linear fitting the change in position of Raman shift with temperature, calibration coefficient was extracted – the first required quantity listed in Table 3.1. Further, the spectra were fitted with different number of peaks as a parameter to observe its influence on the calibration coefficient.

d. Power dependent Raman acquisition

Now, the input power was varied and the material was held at constant temperature. The input power values were finalized by trial and error to ensure no structural changes and burning of the sample. The continuous density filter was used to vary the input power and was regulated by power measurements. This process was followed at different temperatures to extract the temperature dependent behavior. Fig. 3.25 shows the sensitivity of peak position to input power at room temperature and fit gives the sensitivity coefficient listed in Table 3.1.

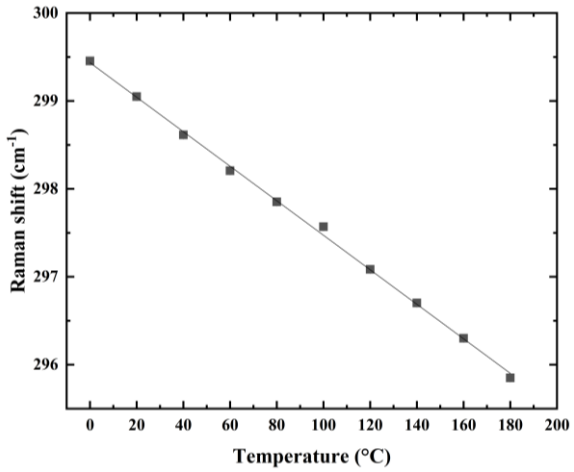

Fig 3.24 Temperature calibration curve of c-Ge phonon mode at 299 cm-1 for GGST

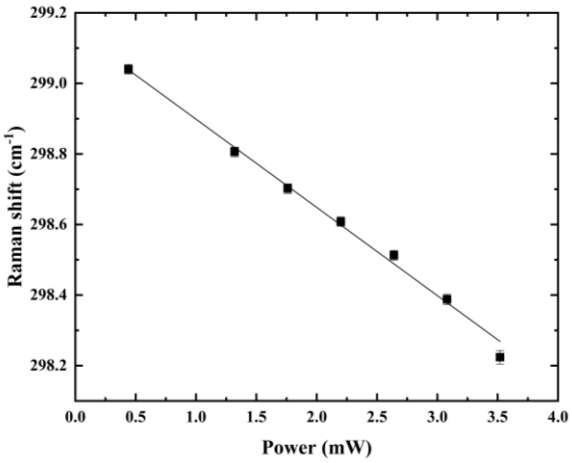

Fig 3.25 Power calibration curve of c-Ge phonon mode at 299 cm-1 for GGST

Calibration coefficient (Temperature) ω_{dT}	Calibration coefficient (Power) ω_{dPabs}	Thermal conductance G
-0.01963 ± 0.00058 [$cm^{-1}K^{-1}$]	-0.25001 ± 0.00832 [$cm^{-1}mW^{-1}$]	76.8 ± 4.74 [$\mu W.K^{-1}$]

Table 3.1. Listed are the temperature and power calibration coefficients of the c-Ge-Ge mode of Ge-rich GST material and their ratio yielding the experimental global thermal conductance

Power measurements at multiple excitation values were performed to enhance the accuracy of the measurement. The experimental thermal conductance was then calculated from the ratio of temperature and power calibration coefficients. This thermal conductance is the global thermal conductance of the system.

e. Measurement approach – errors

A crucial consideration for calculating the thermal conductance precisely is to account for all the errors. The errors as shown in Table 3.1 can arise from both experimental and data analysis uncertainties from the following equation:

$$G = \frac{\omega_{dT}}{\omega_{dPabs}} \qquad \textit{Eq 3-22}$$

$$where\ \omega_{dT} = \frac{d\omega}{dT}, \omega_{dPabs} = \frac{d\omega}{dP_{abs}} \text{ and } P_{abs} = (P_{in} + \Delta P_{in}).Absorbance$$

$$\Delta G = G\left(\sqrt[2]{\left(\frac{\Delta\omega_{dT}}{\omega_{dT}}\right)^2 + \left(\frac{\Delta\omega_{dPabs}}{\omega_{dPabs}}\right)^2}\right) \quad \textit{Eq 3-23}$$

The uncertainty in power accounts for a 2% systematic error in the measurement of power, observed from the fluctuations of the power as recorded during every measurement. The peak fitting errors arise from the uncertainty in the peak position when fitting the Raman spectrum and further linear regression of the fitted points for extracting the calibration coefficient as shown in Fig. 3.24. It is important to note that the error in peak position for different vibrational modes can vary as per the characteristics of the peak. As listed in Table of Fig. 3.23, the crystalline Ge peak is an intense narrow peak resulting in very low uncertainty in peak position which reflects in the calibration curve of Fig. 3.24. Whereas the uncertainty in peak position of the next most intense and observable peak i.e., $SbTe_3$ peak, is higher which would lead to a higher error in the thermal conductance value. In case of amorphous material, the crystalline Ge peak does not appear, so the $SbTe_3$ peak is selected as a local thermometer (discussed in depth in Chapter 5).

Regarding the fitting of a Raman spectrum, different number of peaks are fitted to yield the fitting with least uncertainty on the peak position and the highest R^2 value. When the spectrum shown in Fig. 3.23 was fitted with 4 peaks which are clearly noticeable, yielded a R^2 value of 0.986. Selecting 2 extra peaks to better the fit improved the R^2 to 0.994, minimizing the mean square weighted deviation.

f. Simulation model

The solution for heat conduction into a semi-infinite half space is readily available, as presented in the previous section. In the case of heat conduction in multilayer thin films, an analytical solution is not possible. So, a Finite Element Model (FEM) was developed in COMSOL to understand the heat transfer in the system induced by the Raman laser beam. The heat transfer model was built in a 2D axisymmetric space dimension with material dependent properties, A Gaussian laser beam from a 100x long distance objective was defined as:

$$P_{abs}(r) = P_{in}\, A\left(\mu\, exp\left(-\frac{r^2}{R_{w1}^2}\right) + (1-\mu) exp\left(-\frac{r^2}{R_{w2}^2}\right)\right), \quad \textit{Eq 3-24}$$

Where P_{in} is the incident power as measured on the power meter, A is the absorbance of the material, R_{w1} is the narrow beam waist and R_{w2} is the broader beam waist, μ is the contribution of the narrower beam waist. The laser beam was defined in the model as incident on the SiN/PM interface. The area selected to define the laser was considered large enough to account for the complete spatial distribution of the laser. Multilayer optical estimations were independently performed, where SiN is non-absorbent and the absorbance of the laser in PM was calculated. The absorbance of the 473.12nm laser in the stack was 0.88 as calculated by reflectometry.

Material dependent properties for the substrate Si and the capping layer SiN_x were defined as follows:

$$k_{Si} = 149 * \left(\frac{300}{T}\right)^{1.65}, \qquad k_{SIN} = 0.1 + 0.00401 * T \qquad \textit{Eq 3-25}$$

The thermal conductivity of PM was parametrized as $k_{GST}(T)$. The boundaries of the system (except the top surface) were defined as the temperature of the heating stage. The size of the system was defined by performing iterations in order to eliminate effects of the boundary conditions at the local heat transfer area. Next, the most important objective is to extract the local hotspot temperature in Raman to evaluate the thermal conductance from simulations.

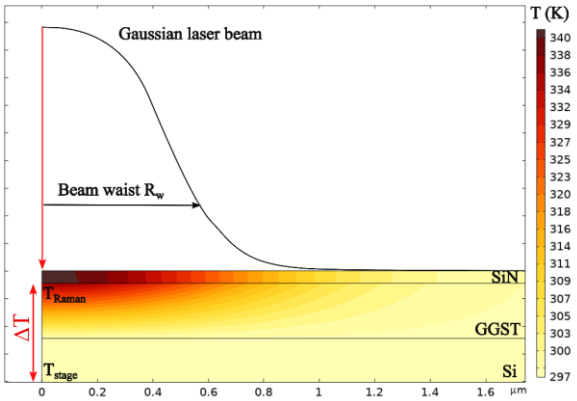

Fig 3.26 Schematic of FEM in COMSOL. Thin film stack with an incident Gaussian laser, ΔT presents the local temperature difference between hotspot (T_{Raman}) and stage temperature (T_{stage}) due to incident laser

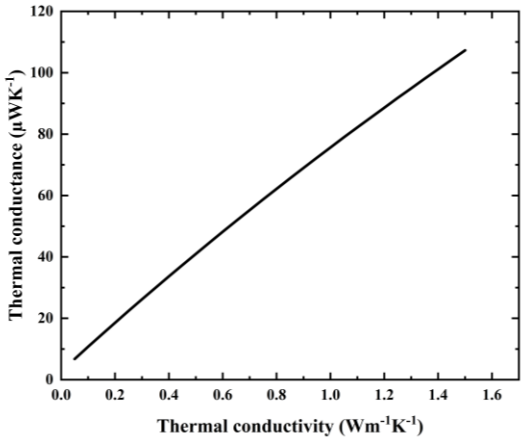

Fig 3.27 Thermal conductance extracted as a function of thermal conductivity of GGST extracted from FEM.

The temperature induced by the incident laser in the sample region where it is Raman scattered is not homogeneous. As the laser beam is defined as a Gaussian distribution, it is crucial to define the temperature distribution along the incident plane, accordingly. This is because, temperature sensed by the local thermometers experimentally would be a distribution of hot and cold regions aligning with the varying spatial heating depending on the Gaussian intensity distribution of the laser. Just extracting the hotspot temperature as a local average or maximum temperature of the sample would differ from the effective Raman temperature. It was suggested to assume the local temperature $T(\vec{r})$ at that every location $\vec{r}$ on the sample would contribute to the effective Raman temperature when weighted by the local laser power density $P(\vec{r})$ [180]. So, the effective Raman temperature can be addressed as

$$T_{Raman} = \frac{1}{P_{abs}} \int P(\vec{r})\, T(\vec{r}) dS \qquad \textit{Eq 3-26}$$

where dS is the surface element of the sample. This provides with a more accurate approximation of the temperature induced by the Gaussian laser beam and the one distributed by its Raman scattering.

The quantity extracted experimentally is the thermal conductance (G) of the stack. From the FEM calculations, the thermal conductance (G) of the stack is extracted as a function of the PM thermal conductivity (k). Here the local temperature i.e. the effective Raman temperature is a function of the thermal conductivity, and the thermal conductance is defined as

$$G(k) = \frac{P_{abs}}{T_{Raman}(k) - T_{stage}} \qquad \textit{Eq 3-27}$$

This provides a correlation between thermal conductance as a function of the thermal conductivity of PM as shown in Fig. 3.27. Room temperature thermal conductance of 76.68 ± 4.74 μWK^{-1} for Ge-rich GST as evaluated experimentally, matches with the thermal conductivity of 1.02 ± 0.03 $Wm^{-1}K^{-1}$. This way the thermal conductivity of Ge-rich GST can be extracted successfully by implementing Raman thermometry. For temperature dependent thermal conductivity, the modelling done is at every temperature.

3.3 Conclusion

Thermal characterization accompanied with physiochemical characterization is crucial to validate the results as the thermal budget imposed during various studies can affect the material differently. For these efforts, we introduce the possibility of thermal characterization of GST based compounds by Raman thermometry. In Raman thermometry, thermal characterization is aided with simultaneous monitoring of the vibrational properties which give an insight into the phase of the material. By protecting the layer of interest with a transparent thin film like SiN, we showed the possibility of extracting the thermal conductivity of Ge-rich GST. In the next chapters, we show comprehensive temperature dependent structural and thermal characterization of different GeSbTe based materials.

Chapter 4

Structural investigation of Ge-rich GST and GeTe

The structural evolution of GeSbTe based phase change materials with temperature differ depending on the stoichiometry of the chalcogenide. GST-225 transitions from amorphous to FCC to trigonal, GeTe transitions from amorphous to a trigonal phase, whereas the phase transition in Ge-rich GST alloys begins with Ge crystallization and then a formation of a stable FCC phase. As discussed in Chapter 2, for chalcogenides, it would be crucial to monitor the structure of the material during its thermal characterization.

In this chapter, we investigate the structural evolution of the following alloys: Ge-rich GST, Ge-rich GST N-doped and GeTe. Temperature dependent ex-situ and in-situ investigations are by Raman spectroscopy are presented, with XRD and TEM support. The recently understood novel crystallization story of Ge-rich GST alloys is discussed, along with understanding the effect of N-doping. These structural investigations were crucial to know and monitor the phase of the material for thermal characterization.

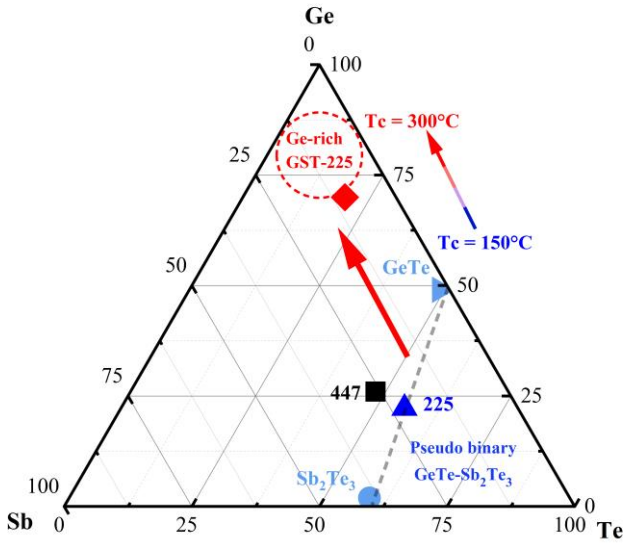

Illustration of the materials under study in the ternary plot

4.1 Vibrational modes of GeSbTe based alloys: context

This section presents a brief explanation of the vibrational modes present in the Ge-Sb-Te ternary system. The primary goal is to understand the vibrational properties and the responsible bonding arrangements in the Ge, Sb, Te elemental and ternary systems examined in literature. This information would help analyze the Raman spectra of the alloys investigated in this thesis.

4.1.1 Elemental Ge, Sb and Te:

Information about the elemental characteristics is beneficial as Ge-rich or Sb-rich GST alloys were targeted recently to improve the performance of PCMs. Ge-rich alloys benefitted from improved thermal stability of the PCM cell [191]. Sb-rich alloys improved the programing speed with swift single phase transition without elemental segregation [91]. GeSbTe alloys can comprise of vibrations arising from Ge-Ge, Sb-Sb, Te-Te, Ge-Te, Sb-Te and Ge-Sb bonds. The observed vibrational modes from the elemental studies would simplify the complex chalcogenides understanding.

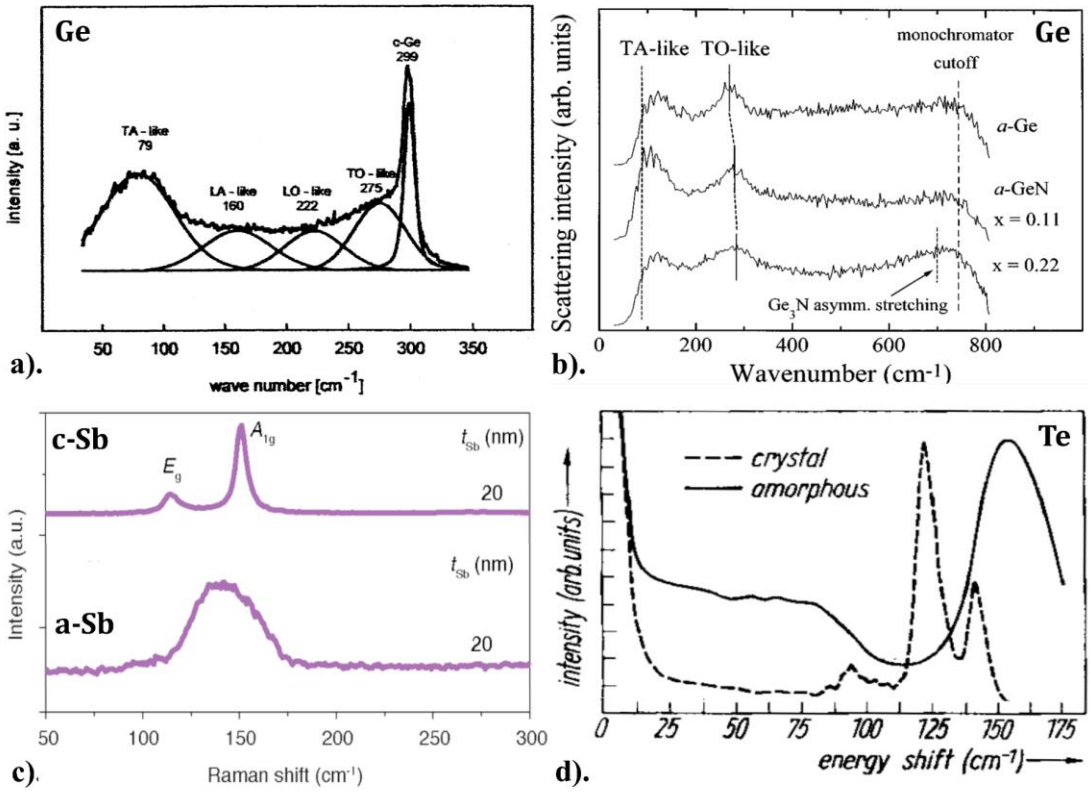

Fig. 4.1. a) Raman spectrum of Germanium thin film showing amorphous Ge (a-Ge) modes and crystalline Ge (c-Ge) peak at 300 cm^{-1} with the fit and respective modes labelled [192]; b) Reduced Raman spectra of a-Ge samples with increasing N concentration presenting the presence of asymmetric stretching vibrations of GeN [193]; c) Raman spectrum of amorphous Sb (a-Sb) and crystalline Sb (c-Sb) indicated with the respective vibrational modes [194]; d) Raman spectra of amorphous Te consists of a broad band at 150 cm^{-1} and crystalline Te has 2 sharp peaks at 120 and 140 cm^{-1}

1. Ge

The Raman spectrum of elemental Ge in amorphous phase presents four main peaks as shown in Fig. 4.1 (a). These scattering peaks correspond with: TA-like (transverse acoustic) at 79 cm^{-1}, LA-like (quasi-longitudinal acoustic) at 160 cm^{-1}, LO-like (quasi-longitudinal optic) at 222 cm^{-1} and TO-like (quasi-transverse optic) at 275 cm^{-1} modes [192]. The full width half maximum (FWHM) ratio of TA and TO scattering peaks for the non-crystalline tetrahedral solids provide information regarding the degree of disorder in the structure [195]. The feature of TO band are affected by thickness, associated with the variations in the distribution of bond angels and dangling bonds in amorphous structure [196]. For crystalline Germanium (c-Ge), the Raman scattering peak appears at 299 cm^{-1}. The difference in amorphous and crystalline peak features highlights the difference in nature of bonding order in amorphous and crystalline materials. Choi et al correlated the FWHM of the c-Ge peaks with the nanocrystal size for different annealing conditions by TEM and spectroscopy, as an example a 10 cm^{-1} FWHM corresponds to a 5nm size [197]. This study was carried out for Ge nanocrystals embedded in an amorphous silicon dioxide matrix. In case of N doping as it is of interest for PCM, N bonds to Ge giving rise to an asymmetric stretching vibration group at 700cm^{-1}. For lower Nitrogen content (<10^{22} atoms cm^{-3}), the sp^3 like character of Ge-Ge bond is not affected. Increasing N content leads to Ge_3N environment causing bond angle distortions, affecting the TO band and giving rise to the asymmetric stretching band at 700cm^{-1} as shown in Fig. 4.1 (b) [193]. Information of the Raman modes related to Ge give an idea of the structural features of the Ge-rich alloys and observe the influence of N-doping.

2. Sb and Te

The spectrum of amorphous Sb shows a broad peak at 150 cm^{-1}, without any distinct features showing no specific structure with a wide-frequency band as shown in Fig. 4.1 (c) [195]. The crystalline spectrum shows 2 narrow peaks at 110 cm^{-1} and 150 cm^{-1}, consistent with bulk Sb [194]. These peaks correlate to two Raman active optical phonons of E_g and A_{1g} symmetries. In case of Te thin films, amorphous spectrum consists of broad maxima at 90 cm^{-1} and 157 cm^{-1}. These vibrations are interpretable in terms of Te-Te disordered chains. For crystalline Te the ordered chains have lower energies than the disordered chains with a peaks at 120 cm^{-1} and 140 cm^{-1}, Fig. 4.1 (d). The stable form of crystalline Te is trigonal and chain-like along the c-axis [198].

4.1.2 GeTe- Sb_2Te_3 pseudo binary line

The widely studied vibrational properties of Sb_2Te_3, GeTe and GST-225 are presented with goal of understanding different GeSbTe based alloys.

- **Sb_2Te_3**

In case of amorphous Sb_2Te_3, the origin of the broad Raman bands can be correlated to 2 structural units: $(Te_2)Sb$-$Sb(Te_2)$ and $SbTe_3$ units. In Fig. 4.2 (a), the band at 150 cm^{-1} corresponds to the Sb-Te vibration of $SbTe_3$ pyramidal units. This was derived from scaling of the Raman spectra of Sb_2S_3, where SbS_3 pyramidal units dominated the spectrum at 300cm^{-1} [199]. For SbS, $(S_2)Sb$-$Sb(S_2)$ were observed at lower wavenumbers when the Sb content increased away from the stoichiometric value [200]. Preferentially, Sb bonds with Te along with a considerable fraction of Sb-Sb (35%) and Te-Te bonds (28.5%) [201]. These vibrations are not visible in the Raman spectrum. Due to absence of Ge, Sb_2Te_3 has no tetrahedral sites but the structure is similar to GST-225 where Sb and Te occupy the defective octahedral sites with 28% nanocavities.

Crystalline Sb_2Te_3 has a rhombohedral geometry. It can be viewed as a slab of five hexagonal layers stacked along c in the sequence of Te-Sb-Te-Sb-Te, with weak Te bonds connecting adjacent slabs [202]. The Raman spectrum presented in Fig. 4.2 (b), the modes at 110 cm^{-1} and 165 cm^{-1} are assigned to the Raman active E_g (2) and A_{1g} (2) Sb-Te vibrations. These modes are in accordance with the bulk [203] and theoretical studies [202]. The Sb-Te vibrations dominates the spectrum with no clear signature of weak Te-Te chains/ bonds. The binary compound of Sb_2Te_3 show very high crystallization speed and low reset power, but its application is limited due to low crystallization temperature.

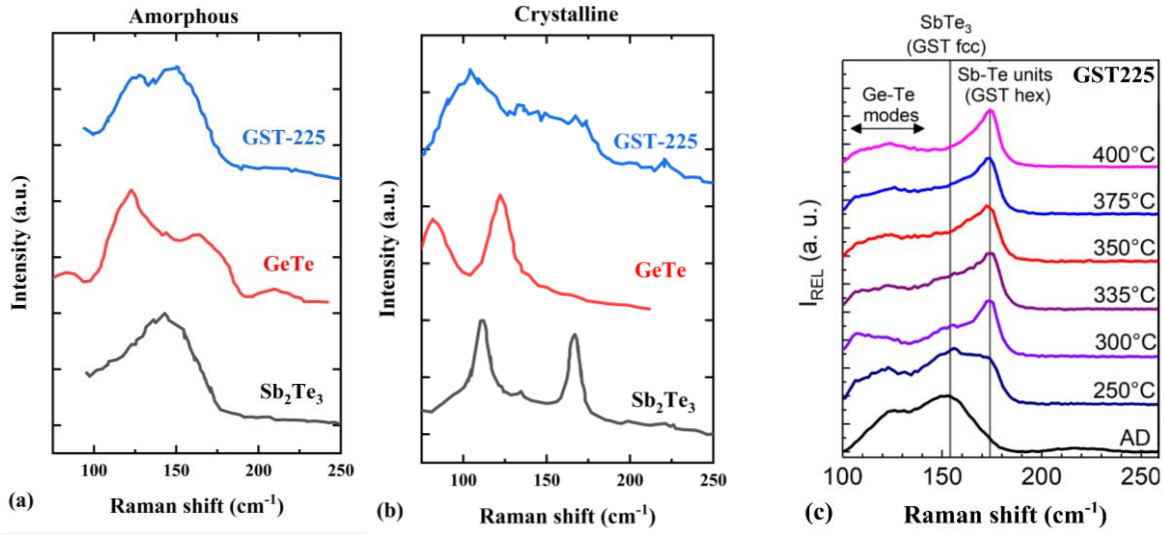

Fig 4.2. Raman spectra of GeTe, Sb2Te3 and GST-225 : a) amorphous phase, b) annealing crystallized [203] and c) Temperature dependent evolution of GST-225 [204]

- **GeTe**

The structure and vibrational properties of GeTe has been studied extensively as it is a well-known ferroelectric material, in addition to its PCM interest [205]–[211]. The GeTe amorphous network consists of 4 primary peaks at 88 cm^{-1}, 127 cm^{-1}, 162 cm^{-1} and 217 cm^{-1}. These peaks are a combination of multiple peaks as presented in Fig. 4.2 (a). In the amorphous GeTe network, Ge atoms are mostly fourfold coordinated in tetrahedral coordination and Te are threefold coordinated [209]. So, the vibrational modes were assigned as edge and corner sharing $GeTe_{4-n}Ge_n$ tetrahedral, respectively [210]. Studies revealed that Ge are mostly fourfold coordinated, but only 23% of the of the Ge atoms are in tetrahedral co-ordination. Whereas, rest of Ge and all of Te exist in a defective octahedral geometry, which is similar to structure of GST-225 [211]. According to preference, the vibrational modes between 110 to 175 cm^{-1} can be assigned to defective octahedral structure, rather than specific edge and corner sharing tetrahedral. Defining it as a defective octahedral structure would prevent from assignment of normal stretching and bending modes. The bands above 200cm^{-1}, like the Ge-Te vibration at 217 cm^{-1} is assigned to tetrahedral environment. The Raman bands related to Te-Te bonds are not expected to be seen as Te is over co-ordinated with Ge. The structure of crystalline GeTe possesses a rhombohedral (distorted rocksalt) structure. Ge and Te are six-fold coordinated and structure consists of 20% vacancies at Ge site. The Raman spectrum has one sharp peak attributed to the Γ_1A_1 mode at 120

cm^{-1} and at 90 cm^{-1} as in bulk crystal as represented Fig. 4.2 (b) [207]. Vacancies lead to a broad peak instead of a well-defined sharp peak.

- **GST-225**

The amorphous GST-225 Raman spectrum can be understood from the discussed contribution of Sb_2Te_3 and GeTe between 100 to 200 cm^{-1}. The main feature is a broad band at 150cm^{-1} associated to the Sb-Te stretching mode of $SbTe_3$ pyramidal unit similar to Sb_2Te_3 amorphous band as shown in Fig. 4.1 (a). Te-Te vibrations at 150cm^{-1} can be ruled out, as structural studies show that Te is over coordinated with no possibility of Te-Te bonds in GST-225 [77]. The contribution at 120cm^{-1} arises from $GeTe_{4-n}Ge_n$ vibrations. Similar to the findings of GeTe, all Te and Sb and 73% of Ge in GST-225 are in a defective octahedral-like geometry with octahedral bonding angles [81]. So, most of the contributions in the lower range (100 – 200 cm^{-1}) arise from Sb-Te and Ge-Te vibrations from the defective octahedral-like sites. Generally, the Raman spectra of amorphous GST is dominated by vibrations of the Sb-Te bonds, as they are more polarizable than Ge-Te bonds [81]. The wide band at 120 cm^{-1} could be attributed to the Ge-Te vibrations in defective octahedral-like sites. Other Ge-Te tetrahedral or defective octahedral vibrational modes at 160 cm^{-1} are not observable in GST spectrum due to the dominance of this Sb-Te vibration. Bouska et al witnessed this dominance by studying 6 different alloys along GeTe-Sb_2Te_3 pseudo binary line, moving from GeTe towards Sb_2Te_3 richer, GST-225 [212].

In case of crystalline GST-225, the Raman spectrum is as broad as the amorphous spectrum. This is due to the presence of 20% vacancy sites in one sublattice of crystalline GST-225. The spectrum presented in Fig. 4.2 (b), is a contribution of the hexagonal Sb_2Te_3 at 110 cm^{-1} and 165 cm^{-1},and Ge-Te vibrations, defective-octahedral arrangement at 120 cm^{-1} and tetrahedral at 220 cm^{-1}. These modes are assigned to the cubic crystalline phase. Various studies witnessed different Raman spectrum for GST-225 depending on the deposition and annealing temperatures [199], [203], [204], [213]–[216]. Recently, Prazakova et al witnessed a change in the Raman spectra when GST-225 transitioned from cubic phase (at 250°C) to trigonal phase (at 300°C), as presented in Fig. 4.3. Here, the Sb-Te vibrations of $SbTe_3$ pyramidal units at 150 cm^{-1} transitioned to Sb-Sb vibrations of (Te_2)Sb-Sb(Te_2) at 174 cm^{-1}. This gives an insight into the effect of structural transition upon Raman vibrations.

The wealth of information from elemental: Ge, Sb and Te and alloys along the pseudo binary line: GeTe, Sb_2Te_3 and GST-225 broadens the understanding of Ge-Sb-Te ternary family. So, depending on the phase: amorphous or different crystalline phases, information from different stoichiometric alloys can improve understanding of more complex alloys.

4.2 Structural investigation of Ge-rich GeSbTe alloys

The Ge-rich GST (GGST) and Ge-rich GST N-doped 200 nm thick films were deposited by physical vapor deposition on 300 mm silicon (100) wafers using an industrial tool. The GGSTN thin films were capped by a 45 nm Silicon Nitride thin film to avoid oxidation. The Ge content of both these materials is greater than 45%. The samples were obtained from STMicroelectronics. Fig. 4.3 shows a TEM cut of the GGST sample with SiN coating. This thickness of SiN was selected to enhance the absorbance of laser in GGSTN thin film to maximize the Raman scattering signal. The alloys are studied by in-situ and ex-situ Raman, in-situ XRD and TEM characterization techniques. First, the results of Raman and XRD studies are independently presented. Then an interpretation

of the results in terms of crystallization steps is proposed which agrees well with recent literature.

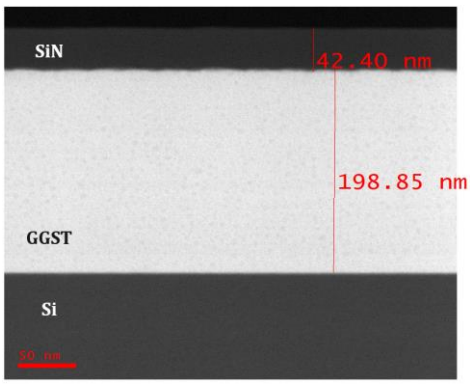

Fig. 4.3. TEM cut of the GGST deposited on a Si substrate and capped with a SiN layer

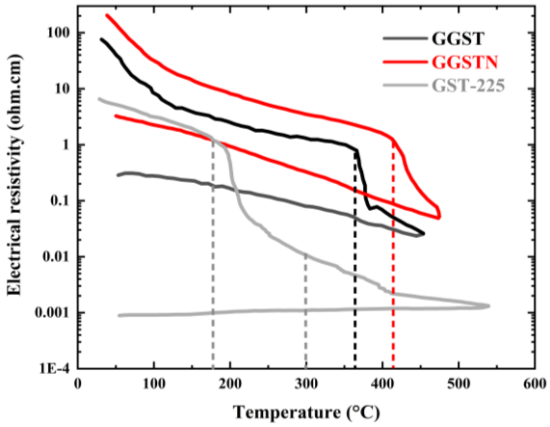

Fig. 4.4. Electrical resistivity vs temperature measurements GST-225, GGST and GGSTN with phase transitions indicated by dashed lines.

Fig. 4.4 presents the evolution of resistivity as a function of annealing temperature. The data for GGST and GGSTN is compared with GST-225 [107] to provide a reference for crystallization temperature, ON/OFF resistivity ratio and nature of crystallization caused due to enrichment of Ge and addition of N. GST-225 shows a two-step transition, crystallization at 170°C from amorphous to cubic (FCC) and then at 300°C from transition FCC to trigonal phase. Increasing the Ge content has increased the crystallization temperature from 170°C to 350°C. Further, addition of N in GGST led to a further increase of Tc. Enrichment of Ge leads to a drop in the ON/OFF resistivity window 5 down to 2/3. The slope of the resistivity curves gives a fair idea about the nature of crystallization process. For GST-225, the first transition from amorphous to FCC for GST-225 showing a sharp drop. This correlates to rapid growth dominated crystallization process. Whereas the transition from FCC to trigonal is a slower transition. Whereas, the amorphous phase of GGST and GGSTN are stable up to higher temperature and followed by crystallization process. These structural characteristics of GGST and GGSTN are elaborated in this section.

4.2.1 Raman spectrum of amorphous GGST and GGSTN

Fig. 4.5 illustrates the Raman spectrum of as-deposited GGST and GGSTN with a Lorentzian fit to extract the precise peak position. Note that the peak positions might be shifted to extract an optimized R^2 fit. The spectra can be divided into Sb-Te, Ge-Te and Ge-Ge vibrations. All the spectra were acquired at very low power (0.5mW) to avoid any structural modifications. The acquisition time and averaging of a spectrum were optimized for an optimum signal to noise ratio by trial and error.

- The most intense peak (B1) in GGST and GGSTN at ~155 cm^{-1} can be attributed to the stretching mode of Sb-Te vibrations in $SbTe_3$ pyramidal units. This is similar to the case of Sb_2Te_3 and GST-225, where presence of Sb-Te vibrations were evident due to its high polarizability.

- In the low frequency range, a significant peak A1 and a minor peak A2 are evident, one around 100 cm^{-1} and a second minor peak at 130 cm^{-1}. The first can be assigned to a contribution arising from both, Te-Te stretching mode or Ge-Te stretching mode at 90 and 110 cm^{-1}, respectively. The band at 100 cm^{-1} associates with symmetric stretching of Ge-Te vibrations in $GeTe_{4-n}Ge_n$ (n=0), corner-sharing units. The vibrations observed in GGST and GGSTN arise from the bonds in a distorted octahedral arrangement, like in GST-225. But, for convenience are named with the stretching modes based on their parent alloys. In case of GST-225, EXAFS analysis shows absence of homopolar Te-Te bonds. So, the possibility of Te-Te chains like structure existing is low but cannot be ignored.
- In the high frequency range, peaks related to Ge in tetrahedral units are present. The peak A3 is assigned to Ge-Te vibrations in $GeTe_4$ tetrahedral units at 217 cm^{-1}. This peak can be considered as a convolution arising from a LO-like (longitudinal optic) at 222 cm^{-1}. The peak A4 at 272 cm^{-1} is assigned to TO-like (transverse optic) mode of amorphous Ge. Presence of this peak confirms presence of excess Ge and assures the amorphous nature of material.

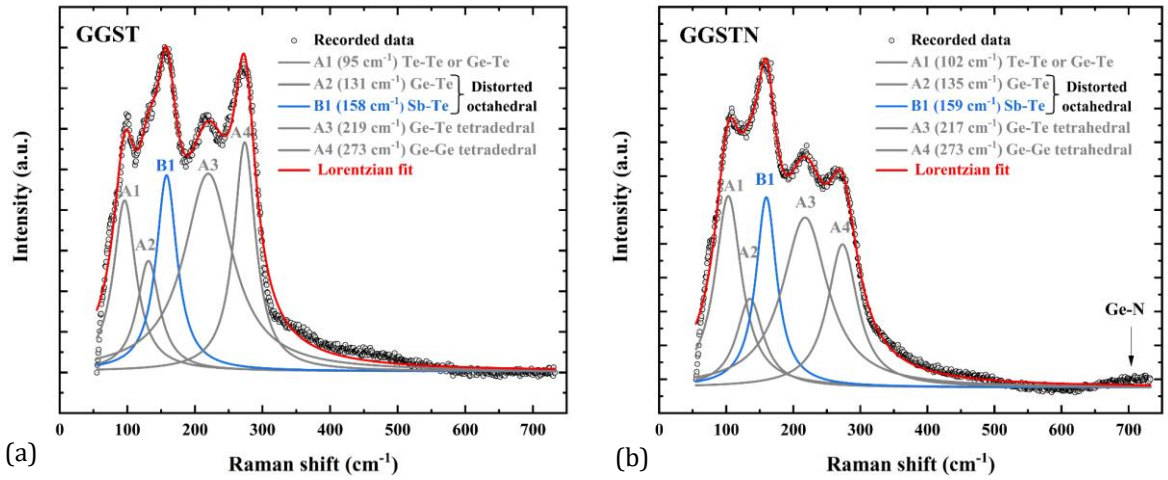

Fig. 4.5 Fitted Raman spectrum of amorphous a). GGST and b). GGSTN presented in a range of 50 to 750 cm^{-1}, the inset of the graphs denotes the vibrations responsible for the peaks.

An evident difference of doping with Nitrogen on the as-deposited (amorphous) phase is observed by its effect on the a-Ge TO-like vibrational mode at 272 cm^{-1}. A noticeable signature of asymmetric stretching caused by Ge-N vibrations is observed at 700cm^{-1}. This due to bonding propensity of N to Ge, which affects the intensity of Ge-Ge tetrahedral vibrations. Depending on the % of N doping, the stretching behavior is shifted as inductive effect of N creates different chemical environments around Ge [204].On the contrary, the intensity of the A3 peak was not affected due to N-doping. This helps confirm the origin of peak A3 is due to Ge-Te vibrations. Next, the Sb-Te vibration are not affected by N- doping. In the low frequency region (< 150 cm^{-1}) some rearrangement takes place with a shift of peak A1 with increase in intensity. The nature of this change in unclear.

4.2.2 Transition from amorphous to crystalline: Ex-situ Raman analysis

The samples were annealed *ex-situ* at the respective temperatures as presented in Fig. 4.6, for 10 mins at a heating rate of 0.5°C/sec under N_2 atmosphere. Raman spectra was acquired at ambient temperature with the setup illustrated in Chapter 3 (3.2.1). The material was annealed at a step of 10°C to precisely identify the crystallization temperature.

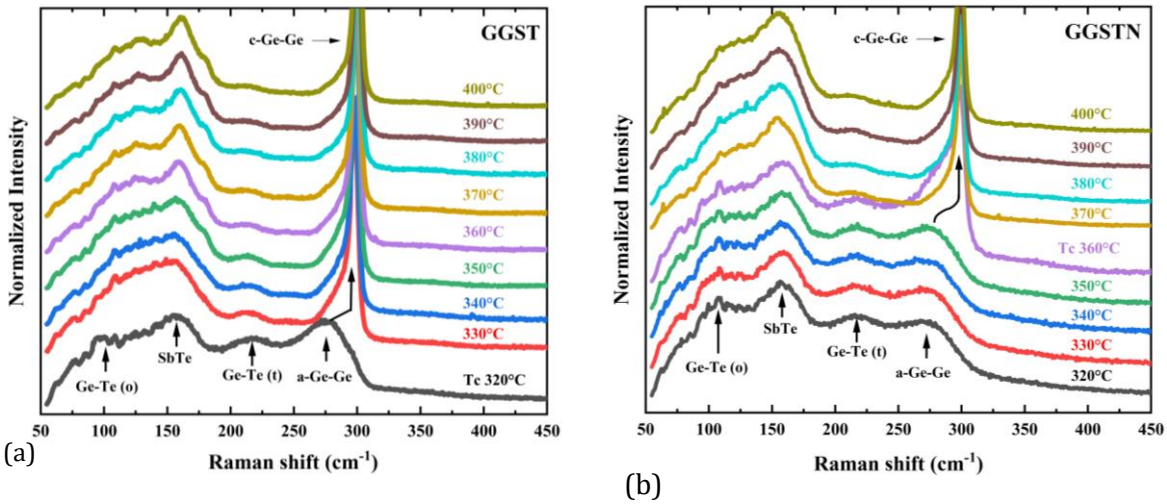

Fig. 4.6 Raman spectrum of a). GGST and b). GGSTN annealed at different temperatures presented in a range of 50 to 450 cm^{-1}. The respective peaks are denoted in the spectra.

For GGST, crystallization process begins between 320°C and 330°C as observed in the spectrum. This is evident due to transition of TO-like (transverse optic) mode of amorphous Ge to a crystalline Ge tetrahedral peak at 299 cm^{-1}. In, GGSTN, this crystallization process is delayed and occurs gradually between 350°C and 370°C. At 360°C, the presence of c-Ge mode at 299 cm^{-1} along with a shoulder of TO-like (quasi-transverse optic) mode of amorphous Ge at 272 cm^{-1} is observed, Fig. 4.6 (a). This affirms the nature of N-doping, as it slows down the crystallization kinetics and increases the crystallization temperature. Now as the annealing temperature increases, the c-Ge mode at 299cm^{-1} grows narrower in intensity and shoulder from amorphous TO-like mode disappears, indicating an on-going crystallization process. The fast and completer nature of crystallization in GGST is presented by shift of c-Ge peak position to higher wavenumbers than GGSTN. In GGST, the FWHM of the peak is lower compared to GGSTN indicating larger Ge grains, Fig. 4.7. This is supported by the in-situ X-ray diffraction studies for a similar composition where Ge underwent abrupt crystallization followed by grain growth via Ostwald ripening phenomena [147].

In GGST, the characteristic peak of Sb-Te vibrations immediately after crystallization appears to be of the same nature as in amorphous phase, denoting the structural environment in both phases. From 350°C onwards, the peak grows narrower in intensity and a shoulder at 180cm^{-1} appears. In addition, the peak related to $SbTe_3$ vibrations moves towards 162cm^{-1} as the annealing temperature further increases, Fig. 4.8. There's a possibility of a fraction of bonds existing in a trigonal configuration as the A_{1g} mode of Sb_2Te_3 hexagonal symmetry is positioned at 164 cm^{-1}. This speculation aligns with a second phase transition observed in the ρ vs T measurements. The shoulder arising at 180cm^{-1} could be because of 2 reasons, i) vibrations from Sb-Sb bonds arising from (Te_2)Sb-Sb(Te_2) units present at 174cm^{-1} or ii) vibrations arising from

symmetric stretching of Ge-Te bonds in edge-sharing $GeTe_{4-n}Ge_n$ units at 180 cm^{-1}. This also indicates a transition from cubic to trigonal like structure for GGST. On the contrary for GGSTN, the Sb-Te vibrations move towards the 153 cm^{-1} of $SbTe_3$. The Sb-Te vibrations arising from $SbTe_3$ in GGST or GGSTN are correlated to the cubic structure of GST. It is understood from this behavior that GGST transition from amorphous to cubic and then to trigonal phase, whereas the thermal budget implemented for GGSTN were not sufficient to foresee the transition to trigonal phase.

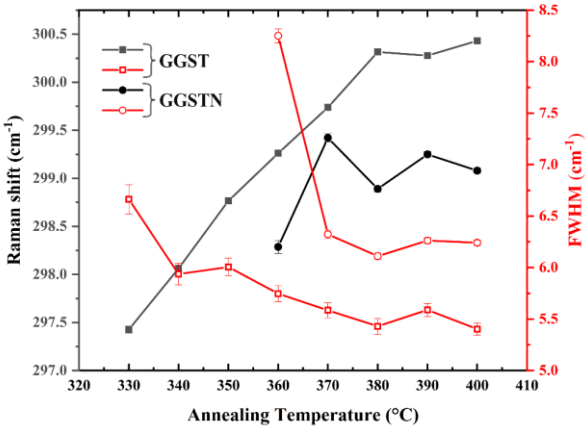

Fig. 4.7. Raman shift and FWHM behavior of the c-Ge peak for GGST and GGSTN examined with increasing annealing temperature

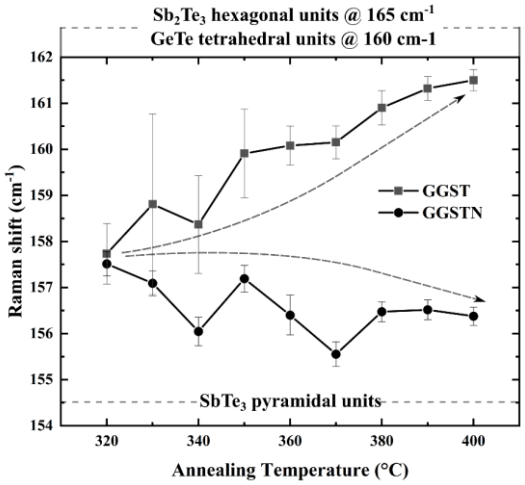

Fig. 4.8. Influence of temperature on the SbTe vibrations in GGST and GGSTN. The dashed arrows present the difference in influence of temperature on these vibrations towards different structural motifs as indicated.

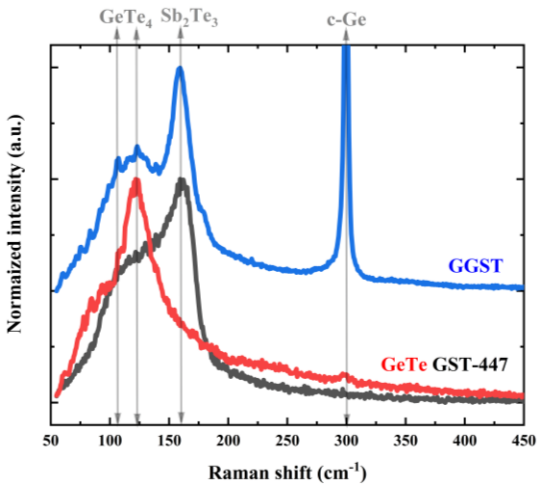

Fig. 4.9. Raman spectra of annealed – crystallized GGST, GST-447 and GeTe. The combined characteristics of GeTe and GST-447 contribute to understanding the GGST spectrum

In the low frequency region (100 to 150 cm^{-1}), the more dominant mode at 100 cm^{-1} associated with symmetric stretching of Ge-Te vibrations in $GeTe_{4-n}Ge_n$ (n=0), corner-sharing units decreases in intensity. The vibrations at 128 cm^{-1} associated with bending modes in $GeTe_4$, grow

relatively stronger in intensity. Presence of this mode is associated with presence of octahedral species [210]. On the contrary, for GGSTN this effect is not profoundly observed. The localized $GeTe_4$ F4 stretching mode at 220cm^{-1}, is observed in both the materials even after crystallization. To summarize observations from ex-situ Raman spectroscopy analysis:

- Ge crystallization is evident by transition of amorphous Ge signature at 272 cm^{-1} to crystalline Ge at 299 cm^{-1}. N-doping delays crystallization from 320°C in GGST to 350°C in GGSTN, as observed by delayed appearance of the c-Ge mode. Ge crystallizes abruptly followed by grain growth indicated by decrease in FWHM. Some rearrangement in observed for Ge-Te related vibrations but is not conclusive.
- On the onset of crystallization, Sb-Te motif appears to be at the same position in both amorphous and crystalline phase. It proves presence of $SbTe_3$ units in defective octahedral like amorphous structure and cubic crystalline structure. This Sb-Te peak indicates a trigonal structure of GST matrix. For GGST, this mode moves closer to the vibrations of Sb_2Te_3 structural units which is not observed for GGSTN. This was further concluded by comparing the Raman spectra of crystallized GST447 and GeTe to GGST, Fig. 4.9. Crystallized GST-447 is composed of vibrations related to hexagonal Sb_2Te_3 motif dominating the spectra. The Raman peaks of crystallized GeTe align with the Ge-Te vibrations observed in GGST. This highlights the composition of GGST composing of Ge-Te and Sb-Te vibrational units arising from the simpler stoichiometric alloys.

4.2.3 In-situ XRD characterization of GGST and GGSTN

X-ray powder diffraction (XRD) was performed on a 9kW rotated anode Rigaku Smartlab diffractometer working in Bragg-Brentano geometry using Cu Kα radiation (λ = 1.5418 Å), equipped with a 2D Hypix Detector detector. To avoid saturation of the detector by the 004 peak of the single-crystal Silicon substrate, after having verified that possible texture effects were negligible, a 2° mis-orientation was applied to the sample. Patterns were collected both at room temperature, on ex-situ pristine and annealed samples, and in-situ during heating. Taking advantage of the high flux of the X-ray beam delivered by the rotated anode and of the high sensitivity, of the 2D detector, patterns were acquired on the fly every 5°C (heating from RT to 600°C at 2°C/min). The EVA 6.1, 2023, Bruker AXS GmbH, Karlsruhe, Germany software was used for phase identification. This was performed at Institute Chevreul in collaboration with Prof Pascal Roussel.

Note: the crystallization temperatures recorded in in-situ XRD analysis are higher than ones observed during Raman analysis. An offset of 30°C is considered to align the XRD results with Raman analysis. The spectra are presented as received after recording.

- **GGST**

Fig. 4.10 presents the in-situ XRD map and patterns of GGST. The as-deposited thin film does not show any diffraction peaks up to 350°C. This confirms the amorphous nature of material and its high thermal stability. Upon crystallization, the XRD pattern shows presence of 2 primary peaks: Ge 111 and FCC-GST 200. The transition from amorphous to crystalline was abrupt with both peaks appearing together. The line-cut at 400°C in the diffractogram aligns well with the coexistence of peaks of the Ge cubic phase and GST cubic phase (GST^c) belonging to the Fd-3m space group. This indicated presence of Ge grains and GST grains. As the temperature increases, the intensity of the Ge peaks increases with narrowing of FWHM. For the GST phase, from 420°C

Heating - GGST

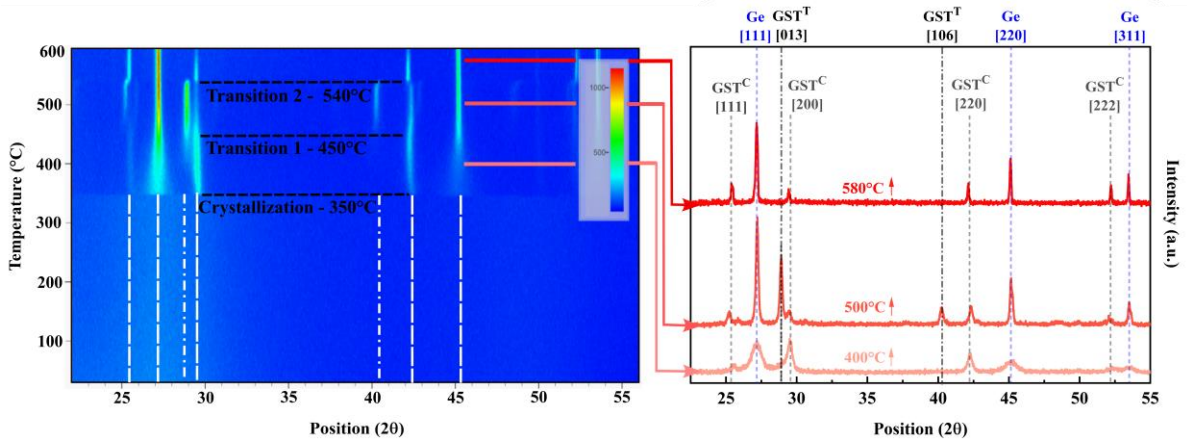

Fig. 4.10. Left: XRD map for in-situ annealing of GGST during the heating ramp, Right: XRD patterns at 400, 500 and 580°C annealing temperature extracted from the XRD map. PDF card information: c-Ge (00-004-0545), cubic GST - GST^C (00-054-0484), trigonal GST – GST^T (89-2233)

Cooling – GGST

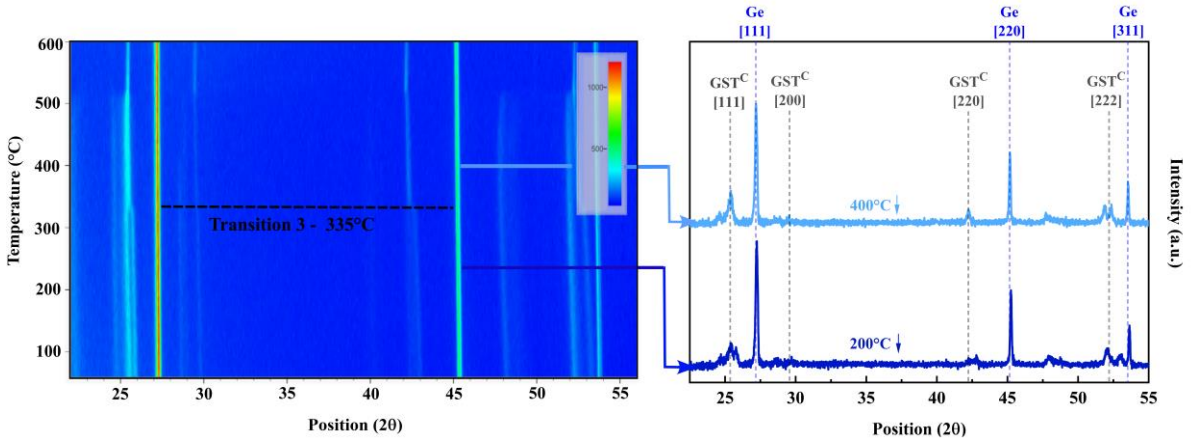

Fig. 4.11. Left: XRD map for in-situ annealing of GGST during the cooling ramp, Right: XRD patterns at 400 and 510°C annealing temperature extracted from the XRD map. PDF card information: c-Ge (00-004-0545), cubic GST - GST^C (00-054-0484)

a signature of trigonal-GST phase belonging to the P-3m1 space group appears. This transition occurs gradually over a range of 50°C with the [013] peak increasing in intensity. The line-cut at 500°C shows presence of two trigonal GST (GST^T) features of 013 and 106 hexagonal indexation. This occurs at the expense of cubic phase of GST, as its intensity fades. Then a second phase transition is initiated at 530°C, where the trigonal phase gradually disappears and the cubic phase reappears. The peaks related to Ge: 111, 220 , 311 peaks do not change in position and get narrower indicating an increase in the Ge crystallite size, in agreement with the Raman investigation and other reports [147], [204], [217]. The crystalline GGST show stability up to 600°C showing no signs of melting. During the cooling ramp as presented in Fig. 4.11, the crystallinity of Ge cubic peaks is preserved with minor changes in the FWHM. For GST cubic peaks, a transition is observed at 335°C where a clear split of GST peak at ~ 29.5° is observed. On

comparing the shoulder peaks could belong to GeTe rhombohedral R3m space group. As the peaks are very close, this transition is not conclusive. The transition from amorphous to cubic to trigonal aligns well with the observations from Raman vibrational properties analysis.

- **GGSTN**

Fig. 4.12 presents the in-situ XRD map and patterns of GGST. The as-deposited thin film remains stable up to 400°C indicating better thermal stability and retarded crystallization due to N-doping. On the on-set of crystallization, the primary peaks Ge 111 and GST 200 of cubic indexation appear along with other secondary peaks. On comparison with GGST, these Bragg peaks belonging to Fd-3m space group appear wider indicating finer grains. This is due to N-doping as it slows down the crystallization process and segregates around grain boundaries restricting grain growth [142], [218]. On crystallization, GGSTN is in its FCC phase and a second transition similar to GGST is not observed for GGSTN. These features agree well with the spectral features of Raman analysis where the Ge peaks were broader for GGSTN indicating smaller grains and no change in the position of Sb-Te vibrations indicating stable cubic phase. On further heating the material, a second transition is observed where the Ge Bragg peaks become narrower and dominate the spectrum. The GST motifs show decreases significantly in intensity or completely disappears. This transition is unusual and has not been observed in other studies. Then at around 570°C - 580°C the material completely melts. The melting point of GST alloys studied along the pseudo-binary line ranges around 600-630°C. GGST did not show any sign of melting up to 600°C. In case of pure Ge thin films, the melting temperature is ~ 900°C. So, two things could be concluded from this observation: 1) N-doping causes a reduction in the melting temperature of the material. 2) The disappearance of GST related peaks could indicate initiation of melting of GST matrix or loss in crystallinity. As Ge segregates and has comparatively higher melting point it melts at later.

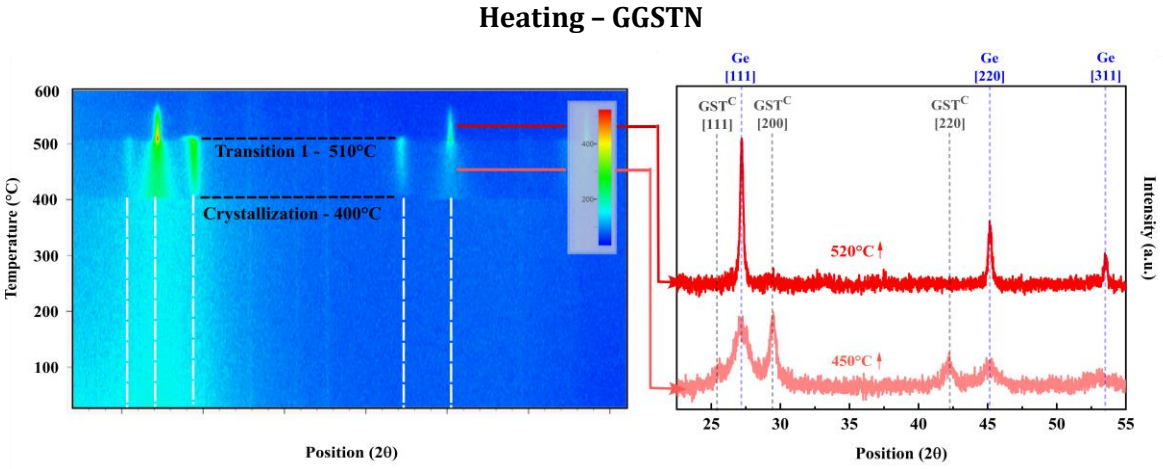

Fig. 4.12. Left: XRD map for in-situ annealing of GGSTN during the heating ramp, Right: XRD patterns at 450 and 520°C annealing temperature extracted from the XRD map. PDF card information: c-Ge (00-004-0545), cubic GST - GST^{C} (00-054-0484)

The complete analysis from Raman and XRD provides a clearer picture of the crystallization and other transitions occurring in GGST and GGSTN with considerable effect of N-doping. In the next

section, we try to make sense of this analysis and portray a crystallization story and in comparison, with some similar studies.

4.3 Crystallization story: Ge-rich GST

Raman spectroscopy and in-situ XRD provided substantial insight into the crystallization and structural evolution of GGST and GGSTN. In-depth studies for similar alloys like GGST and GGSTN have been performed using techniques like in-situ synchrotron XRD [104], [147], [217], in-situ TEM [219], ex-situ TEM [105], [204], [218], [220]–[222] and Raman [204], [223]. These studies performed in the past 3-4 years progressed the understanding of impact of N-doping and Ge enrichment on crystallization kinetics and temperature, resulting phase segregation and multi-step crystallization transitions. In this section, the results presented in the recent past are correlated with the crystallization theories established to further its understanding. Along with this, an additional goal is to correlate the Raman analysis with XRD results in detail. This would help in realizing the viability of Raman thermometry to function as a simultaneous structural and thermal characterization technique.

The crystallization process for alloys like Ge-rich GST has been a mystery and is debated compared to the straightforward and broadly accepted crystallization of GST-225.

GST evolution recap:

GST-225 transitioned from amorphous to FCC to trigonal phase at 150°C and 300-350°C, respectively. In context of a PCM cell, during fabrication of the memory the BEOL endures a thermal budget of around 400°C for a certain duration. In case of GST-225, due to its transition to trigonal phase from metastable cubic phase caused formation of big column structure of the trigonal grains that caused grain size variation and void formation [60]. This impacted the yield and endurance of PCMs. The enrichment and doping efforts were performed to improve the thermal stability of the material and decrease the programming current requirements. The usual trend yielding improved results has been Ge enrichment and doping with Nitrogen. The first efforts involving Ge-rich alloys comprised of Ge enriched GST-212 stoichiometry, known as the "golden composition" [60] and then Ge enrichment of GST-225 [224], [225]. For the enriched golden composition the crystallization improved to 295°C and further to 400°C with N incorporation [109] with trigonal transition witnessed at 500°C. The Ge-rich GST 225 alloys showed similar improvements with crystallization temperature to FCC phase ranging from 250°C to 400°C depending on % Ge [102], [225]. These newly developed alloys were resistant to this issue as the grain size remained considerably smaller and uniform for the FCC phase with no apparent voids. But the developments introduced new issues like elemental segregation of Ge, phase separation and presence of amorphous residuals during PCM cell operation. To clarify, the dynamics observed during studies of blanket thin films and the ones undergone during PCM cell programming might differ. But the study of thin films gives an insight into the details of the crystallization process, possibility of formation of different phases influenced by heating conditions and the impact of thermal budget on them during the BEOL process. To add, the issues of phase separation have been observed during the initialization operation (electrical activation) of PCM cell which is carried after the BEOL [108].

Ge-rich GST, so far:

The novel crystallization process of GGST alloys has been of interest to understand the onset of crystallization, phase transitions and resulting elemental segregation. Different views have been proposed to understand the crystallization process of GGST.

- A study of 45% Ge + 55% GST-225 suggested that the onset of crystallization begins with formation of cubic GST phase. Prazakova et al postulated that once a stable GST phase is reached with simultaneous expulsion of Ge atoms, the GST grains serve as a site for nucleation and crystallization of Ge [204].
- On the contrary, other studies suggest segregation of Ge crystallites before onset of crystallization of GST phase [104], [105], [222]. An isothermal annealing study at 310°C for 16h revealed that phase segregation begins in the amorphous phase leading to formation of Ge-rich amorphous clusters. After 7h, small nanocrystals identified at GeTe are formed which trigger the heterogeneous nucleation of Ge nanocrystals which are 5nm in diameter with Sb distributed uniformly. When 80% of Ge is crystallized, GST grains start nucleating which are bigger in size > 20nm. In agreement with this, in-situ synchrotron study carried out for a Ge-rich GST alloy by annealing up to 500°C at a heating rate of 2°C/min revealed the Ge crystallizes 15°C before GST crystallization. Ge crystallization is followed by grain growth of Ge during GST crystallization [147].
- A final view, studying Ge (15 to 55 at%) + GST225 suggested that for alloys with Ge content > 45%, Ge and GST crystalline phases appear at the same annealing temperature. These are different contrasting views presented so far. Critically, it does depend on the composition of the alloy, preparation conditions of amorphous phase and factors like heating rate and duration of annealing leading to evolution of different phases [220]–[222].

The homogeneous composition of as-deposited Ge-rich GST in its amorphous phase changes substantially upon onset of crystallization. The common suggestion is that phase separation of Ge and GST begins in the amorphous phase before approaching crystallization temperature, irrespective of preference for crystallization. This occurs as there is no crystalline phase which exists for Ge rich alloys like GST-523 [226], GST-212[60], 45% Ge + 55% GST-225 and so on. Thermodynamics dictates that the alloy will separate into different distinct stable phases upon receiving sufficient thermal energy. The mass transport process of pumping the Ge out of the GST matrix delays the crystallization process. This is what has been experienced for Ge-rich alloys. The decomposition pathways suggested for a Ge (lesser) rich alloy like GST-523 can be differentiated on the basis of thermodynamically or kinetically favored. The trigonal phases with Ge clusters a thermodynamically favored, whereas metastable cubic GST or GeTe phases are kinetically favored. Considering the rapid operations of PCM cell, the metastable structures and composition are favored [227]. From STEM and EDX mappings for Ge-rich GST annealed at 450°C for 30 mins, the decomposition pathways led to formation of Ge clusters and metastable cubic, Ge poor phases lying between GeTe- Sb_2Te_3 and Ge-Sb_2Te_3 tie line and not trigonal ones.

It is observed that annealing at 400°C for 30 mins is sufficient to completely crystallize the material [105], [217], [221], [222]. TEM characterization has showed presence of large GST grains in a uniform matrix of Ge grains. The general consensus is that as temperature increases, the grain size increases due to Ostwald ripening. And, that the Ge grains are always smaller than the GST grains. Further annealing at higher temperatures > 450°C, showed the formation of trigonal phase along with voids [222]. As the temperature increased the trigonal grains and voids increased in size causing a wavy surface with the capped layer. This is similar to the phenomena

observed for GST-225 but occurs at a temperature which is higher than the BEOL processing temperature which is beneficial. N-doping further retards the crystallization kinetics by slowing down the mass diffusion of Ge. This leads to more delayed or avoiding formation of the trigonal GST phase. It also renders the crystallization to be nucleation dominated rather than growth dominated controlling the size of grains [146]. N segregates and forms nitrides (GeNx) at the grain boundaries, controlling the grain size [142]. These smaller grains would ensure homogeneity of the thin film and hence the transport properties. Another added benefit is that N-doping helps to keep the thin films flat instead of the waviness observed on the contrary.

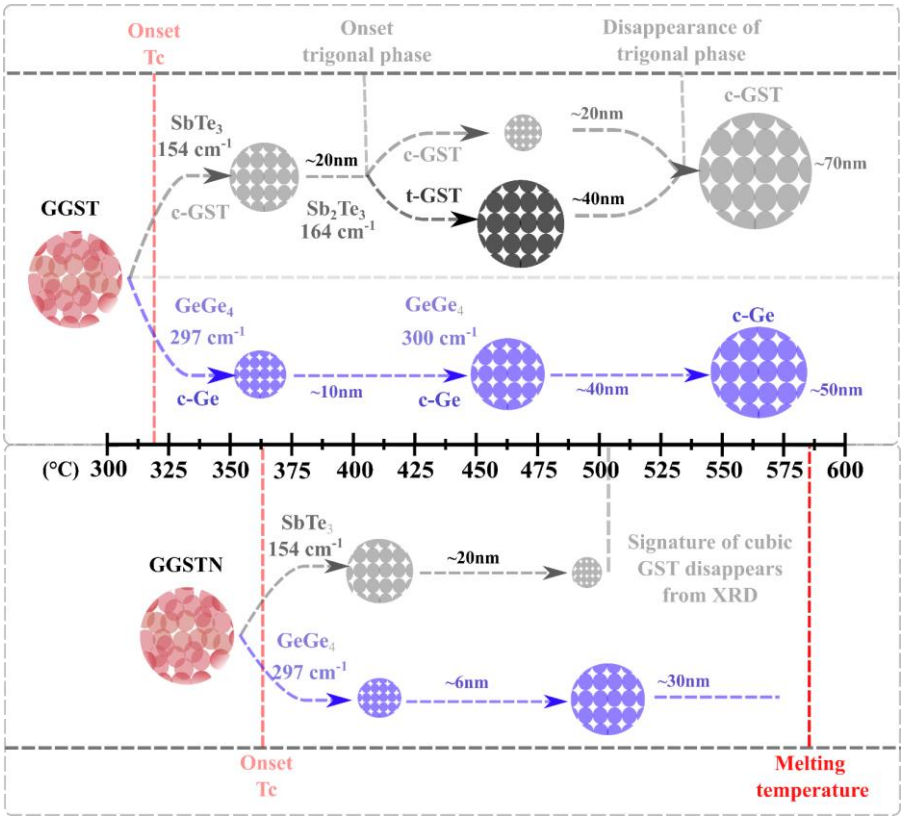

Fig. 4.13. The schematic presents the crystallization paths of GGST and GGSTN divided in two routes of Ge (blue) and GST (grey). The Ge crystallization is tracked by Ge peaks in both XRD and Raman, for GST crystallization the GST peaks in XRD and SbTe peaks in Raman are analyzed.

Our interpretation:

Building up on these aspects, we present the observations in our work. A schematic of this presented story is illustrated in Fig. 4.13. The onset of crystallization of GGSTN is delayed by 30°C compared to GGST due to N-doping. The crystallization process for both alloys begins with phase separation of Ge and GST simultaneously at respective temperatures with no delay.

For Ge crystallites, the size increases as the annealing temperature increases to a maximum of 50 nm in GGST. This reflected in the Raman spectra by a shift of Ge-Ge peak to higher wavenumbers and narrowing of the peak width, Fig. 4.7. N-doping substantially controls the size of the grains by bonding to Ge and slowing down the migration of atoms, restricting the size of grains to 30 nm in GGSTN. In case of GST phase, the grains formed upon crystallization are larger than Ge grains

in both alloys. For GGST, a transition is observed at 420°C from metastable cubic to a "stable" trigonal phase. So, upon provision of sufficient thermal budget, transition to a trigonal phase is possible in Ge-rich alloys. In Raman spectra, this is evidenced by shift of the $SbTe_3$ cubic related peak towards Sb-Te vibrations in Sb_2Te_3. This trigonal phase grows at the expense of cubic phase as its intensity diminishes and the trigonal crystallite size increases to 50nm. At 540°C, this "stable" trigonal phase abruptly disappears with the resurgence of cubic GST phase. The cause of this is unclear. Further as temperature increases, the cubic GST grains grow to a size of 70 nm.

As previous studies suggest, N-doping avoided the transition in GGSTN to the less resistive trigonal phase which comes along with void formation. N-doping kept the size of the Ge grains in GGSTN smaller by 20nm. At 500°C an abrupt disappearance of GST signature in the XRD spectra is observed. The reason behind this behavior of GGSTN is unclear. Raman results up to 450°C indicate presence of $SbTe_3$ peaks which indicate the presence of GST phase. Unfortunately, acquisition at and annealing at higher temperature was not possible due to delamination of SiN capping layer. At last, the material melts at 580°C, again due to the influence of nitrogen. The study was performed twice to check the consistency of this behavior. So, a greater part the of results for GGST and GGSTN alloys under study agree with the general established reasoning of crystallization with minor modifications. Raman spectra gives comprehensive understanding which is in agreement with XRD results. The two abrupt phenomenon observed in GGSTN cannot be explained at the moment.

4.4 Structural investigation of GeTe

The material-GeTe was studied to contribute towards the on-going development of a GeTe based phase change RF-switch at CEA-Leti and STMicroelectronics. The thin films were deposited by physical vapor deposition on 200 mm silicon (100) wafers using an industrial tool. They were capped by a 13 nm Silicon Nitride thin film to avoid oxidation. Fig. 4.14 shows a TEM cut of the GeTe sample with SiN coating. The alloy is studied by in-situ and ex-situ Raman, in-situ XRD and TEM characterization techniques. The results of Raman and XRD are presented to understand the temperature dependent phase transitions.

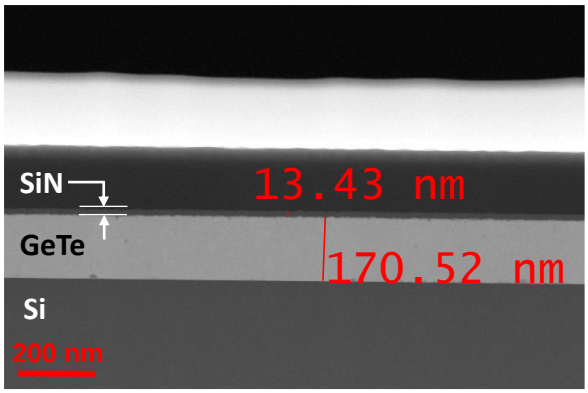

Fig. 4.14 TEM cut of the GeTe deposited on a Si substrate and capped with a SiN layer

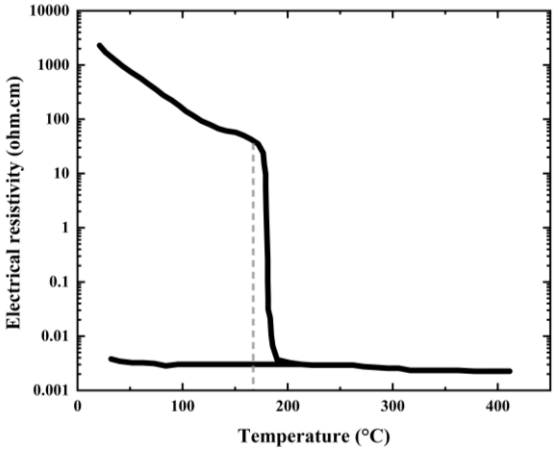

Fig. 4.15 Electrical resistivity vs temperature measurements GeTe with phase transition indicated by dashed lines.

GeTe is a well-known ferroelectric and phase change material implemented for non-volatile memory storage and RF switches application. Resistivity – temperature shows an ON/OFF ratio of 105 with swift transition over after crystallization as presented in Fig. 4.15. The material transitions from amorphous to crystalline phase between 150 to 200°C depending on the thickness of the thin film. It crystallizes into a rhombohedral (R3m) phase with α = 88.35° denoted as α-GeTe. This structure is visualized as a distortion of the cubic rock-salt structure with a small sheer relaxation along the pseudo-cubic 111 direction. Around 350°C a transition from ferroelectric (α-GeTe) to paraelectric phase (β-GeTe) occurs. This accompanied by a relative shift of the cation and anion sublattice and change of to α = 90° transitioning into a rock-salt cubic structure [228]. The local environments in both amorphous and crystalline phase were suggested be similar with EXAFS measurements [208].

4.4.1 Raman spectrum of amorphous phase

Fig. 4.16 presents Raman spectrum of amorphous GeTe. The vibrational modes presented in the inset are recognized on the basis of the seminal study of a-GeTe published by Andrikpolous et al [210]. These are assigned based on the GeTe vibrations in tetrahedral symmetry of $GeTe_{4-n}Ge_n$ believed to be the

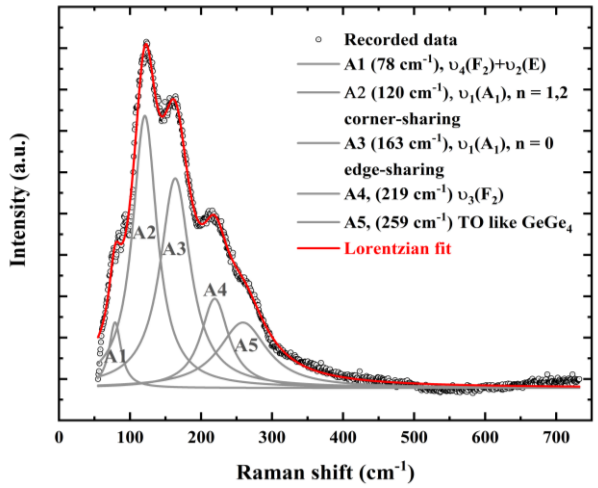

Fig. 4.16 Raman spectrum of amorphous as-deposited GeTe with Lorentzian fit. The inset indicated the fitted peak and its vibrations assignment

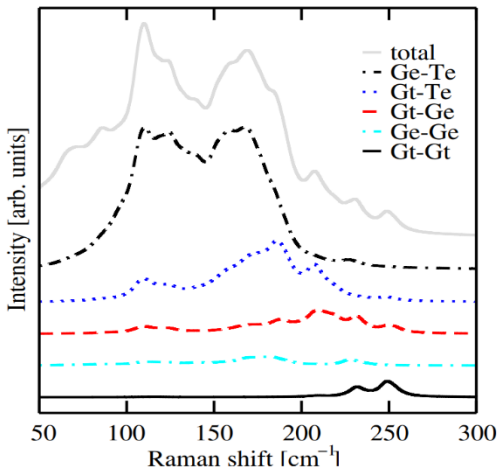

Fig. 4.17. Projection of contribution from different bond and structural configurations on the reduced Raman spectrum of GeTe. [211]

building blocks of GeTe structure. Comprehensive analysis based on EXAFS [208] suggested that Ge is indeed four-fold coordinated, but only 23% of Ge exist in tetrahedral configuration. Whereas, rest of Ge and all of Te atoms are present in a defective octahedral geometry with octahedral bonding angles and not edge or corner sharing tetrahedral [211]. This defective octahedral classification leads to 1-2 longer bonds and misalignment of 4 membered rings in a-GeTe which prevents the categorization of normal modes as stretching and bending like displacements. So, the modes presented in the range of 100 cm^{-1} to 190 cm^{-1} denoted A2 and A3, Fig. 4.16 can be argued to be Ge-Te vibrations of defective octahedral symmetry. A2 band corresponds to tetrahedral structures $GeTe_{4-n}Ge_n$ (n = 1,2) of corner-sharing nature and A3 $GeTe_{4-}$

$_nGe_n$ (n = 0) of edge-sharing nature. The higher intensity of A2 band over A3 band indicates the higher distributions of $GeTeGe_3$, $GeTe_2Ge_2$, $GeTe_3Ge$ tetrahedra types over $GeTe_4$. This distribution for $Ge_{50}Te_{50}$ aligns with the relative distribution of various $GeTe_{4-n}Ge_n$ tetrahedra types as a function of chalcogen atomic fraction according to Phillips model [210]. Fig. 4.17 presents the distribution of vibrations arising from different symmetries calculated by ab-initio simulations [211]. The tetrahedral vibrations arising from Ge-Te (denoted as Gt-Te) and Ge-Ge (denoted as Gt-Gt) dominate the spectra after 190 cm^{-1}. First principle evaluations coincide well with the experimentally recorded Raman spectrum. The Raman spectrum in literature present changing distributions of Ge-Te bonds depending on the method of deposition and being melt-quenched or as-deposited [229]. The modes below 100 cm^{-1} (A1) primarily arise from the three-fold coordinated Te-Te vibrations of disordered Te chains [198]. The amorphous GeTe structure consists of majority contribution from various GeTe tetrahedral arrangements along with minor Ge-Ge and Te-Te contribution. These observations are to conclude that Raman characterization gives a comprehensive picture of the arrangement of GeTe symmetry, based on the history of structural analysis.

4.4.2 Transition from amorphous to crystalline: Raman analysis

- Ex-situ and in-situ

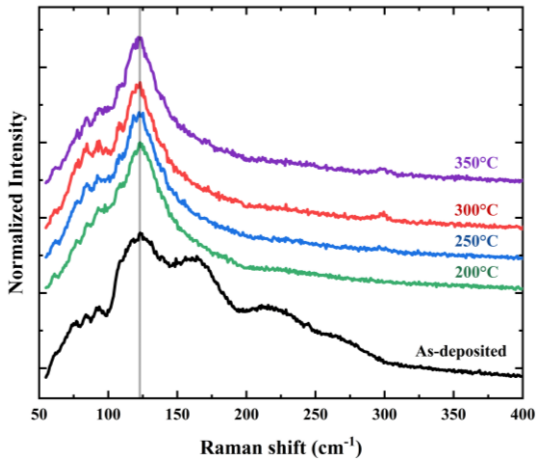

Fig. 4.18 Raman spectrum of GeTe annealed at different temperatures in comparison with as-deposited amorphous spectra presented in a range of 50 to 400 cm^{-1}. The spectra are acquired at room temperature respective peaks are denoted in the spectra.

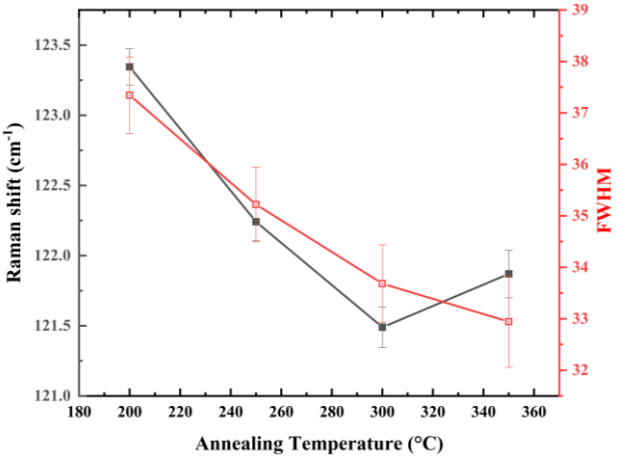

Fig. 4.19. Influence of annealing temperature on Raman shift and FWHM of the Raman peaks. Annealing temperature influences the grain size as the FWHM becomes narrower.

The samples were annealed ex-situ at the respective temperatures as presented in Fig. 4.18 for 10 mins in at a heating rate of 0.5°C/sec under N_2 atmosphere. Amorphous GeTe has a defective octahedral geometry with Ge present in a local environment of six Te atoms, where three Te atoms in close proximity and rest at a larger distance [209]. Ge is indeed four-fold coordinated but exists in an environment offering octahedral coordination. The crystallization temperature of GeTe is between 150-200°C depending on the thickness of the thin film [205]. For a 200nm thin film, it transitions to crystalline phase at 160°C. Fig. 4.18 presents the spectra of GeTe annealed at different temperatures and compared to as-deposited spectra. Upon crystallization

the as-deposited amorphous phase transitions to rhombohedral (distorted-rocksalt) structure. The pre-existing octahedral environment aids the fast transition to this crystalline phase. The annealed samples show a strong peak at 120 cm^{-1} assigned to the $\Gamma_1(A_1)$ optical mode of longitudinal symmetry. A broad band exists below 100 cm^{-1} which consists of a main recognized mode at 90 cm^{-1}, Γ_3(E) mode of transverse symmetry. The crystallized structure transitions from a combination of multiple peaks depending on the distribution of various tetrahedra to a precise peak and broad band. As the annealing temperature increases, the main peak intensity (120 cm^{-1}) increases with continuous reorganization in the broad band. This occurs due to the possibility of change in bond lengths upon varying thermal budget, due to coexistence of various similar crystal structures in GeTe [230]. On analyzing the peak characteristics at 120 cm^{-1}, the peak position red shifts along with a distinct decrease in FWHM indicating better crystallinity and increase in grain size, Fig. 4.19. Some rearrangement around the Raman band at 90 cm^{-1} can be spotted but no striking changes are observed in the Raman spectra. A small bump appears at 300cm^{-1} indicating formation of tetrahedral $GeGe_4$ structure formation but is not conclusive. In some samples, the c-Ge-Ge peak was observed even at 200°C. Then around 400°C, c-GeTe is believed to stabilize from the rhombohedral phase to a cubic NaCl structure. This transition is caused by the softening of the zone centre transverse optic phonon mode [207].

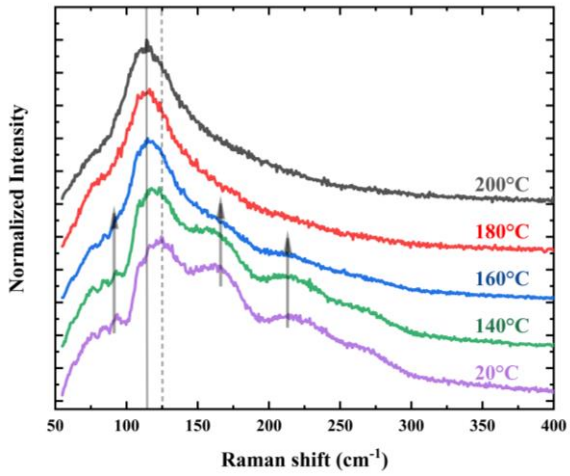

Fig. 4.20. Evolution of Raman spectrum with in-situ analysis, the acquisitions are performed at the indicated temperatures. Arrows indicate the disappearance of the vibrations upon phase transition.

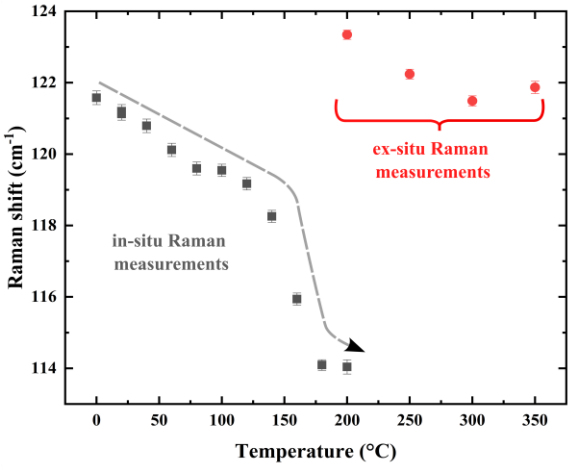

Fig. 4.21. In-situ analysis of Raman shift with increasing temperature (black). Raman shift obtained from fit of the Raman spectra of ex-situ annealed samples presented in red.

In-situ Raman spectroscopy measurements corroborated the swift crystallization of GeTe, presented in Fig. 4.20. These measurements were performed using a heating stage as presented in Chapter 2. As temperature of amorphous phase increases, the population of $GeTe_4$ tetrahedra increases on the expense of other structures like $GeTeGe_3$, $GeTe_3Ge$ and $GeTe_2Ge_2$ facilitating the transformation to a distorted octahedral coordination in the crystalline phase. This implies strengthening of the peak at 120 cm^{-1} in a-GeTe as observed by the immediate disappearance of other vibrational modes above 160°C, presented in Fig. 4.20. The peak appears as a broad band, accompanied by a gradual red shift of Ge-Te vibrations up to the crystallization temperature followed by an abrupt drop. Upon cooling the sample, the position of the peak returns to its

original position as indicated by ex-situ measurements (in red) presented in Fig. 4.21. The change in Raman shift from 122 cm^{-1} to 114 cm^{-1} implies the change of local structure/ bonds distribution upon crystallization into some meta-stable crystallized phase. Upon cooling, the Raman spectrum reveals its relaxation into stable rhombohedral structure with a sharp peak at 120 cm^{-1}.

4.4.3 In-situ XRD characterization

Fig. 4.22 and 4.23 present the heating ramp and cooling ramp for GeTe, respectively. Note: the crystallization temperatures recorded in in-situ XRD analysis are higher than ones observed during Raman analysis. An offset of 30°C is considered to align the XRD results with Raman analysis. The spectra are presented as received after recording.

Heating – GeTe

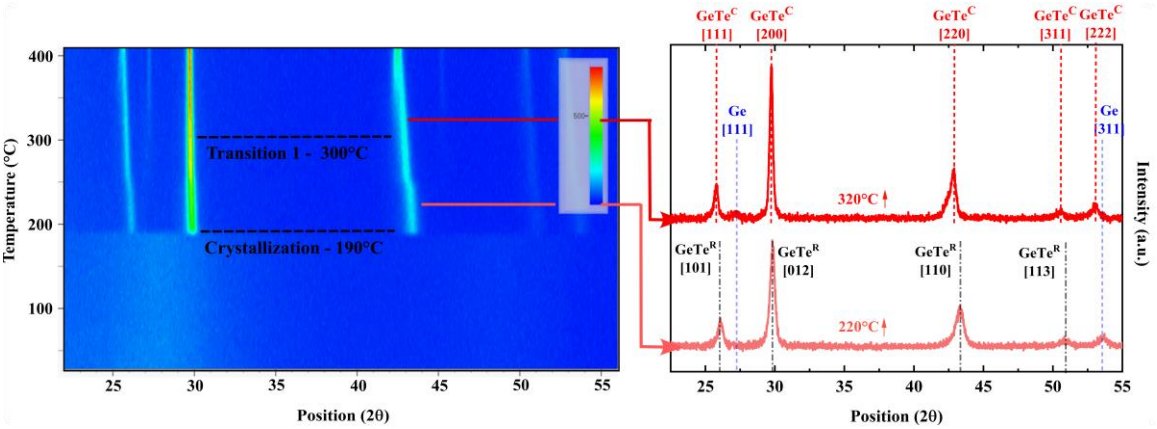

Fig. 4.22. Left: XRD map for in-situ annealing of GeTe during the heating ramp, Right: XRD patterns at 220 and 320°C annealing temperature extracted from the XRD map. PDF card information: c-Ge (04-016-2396), rhombohedral GeTe - $GeTe^R$ (01-080-8422), cubic GeTe – $GeTe^C$ (04-006-1927)

Cooling – GeTe

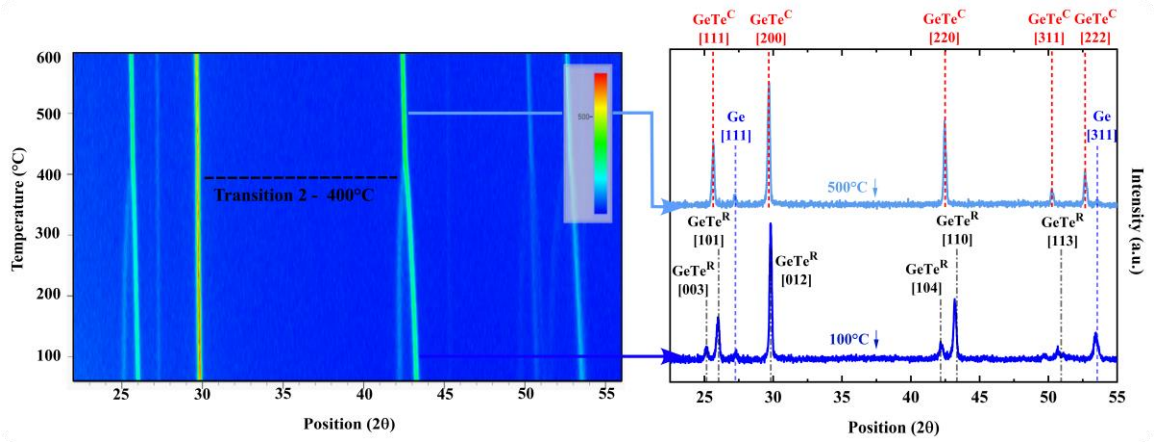

Fig. 4.23. Left: XRD map for in-situ annealing of GeTe during the cooling ramp, Right: XRD patterns at 220 and 320°C annealing temperature extracted from the XRD map. PDF card information: c-Ge (04-016-2396), rhombohedral GeTe - $GeTe^R$ (01-076-7106), cubic GeTe – $GeTe^C$ (04-006-1927)

Temperature-position (2θ) map presented in Fig. 4.22 shows the amorphous phase stability up to 190°C. Then the material crystallizes into a Rhombohedral phase (Space group – R3m). The line cut at 220°C shows the peaks identified for the rhombohedral structure. On further heating the material begins to undergo the next phase transition from α-GeTe to β-GeTe around 300°C. The peak associated to $\theta \sim 29.8$ appears to be similar for both the geometries related to indexation of 012 for rhombohedral and 200 for cubic phase. In-depth Rietveld analysis states that this peak could belong to C1m1 space group which is formed during this α-GeTe to β-GeTe transition 200. Further, the peak at ~43.09 has a signature of the rhombohedral indexation but drags towards the cubic 220 direction at 42.5° in the XRD map. This occurs due to a continuous decrease in distortion angle of the rhombohedral structure which is completed at the critical temperature of 423 °C [228]. It is also suggested that the structure of GeTe could comprise of P1 and R3m space groups at room temperature which transitions to a combination of C1m1 and R3m crystal structures at intermediate temperatures before transitioning into a cubic structure at higher temperature [230]. Weak Ge peaks can be observed indicating presence of crystalline cubic Ge structure in the GeTe matrix.

The transition to meta-stable cubic is complete at higher temperature of 500°C, as the diffractogram presents narrower peaks belonging to the cubic structure (Fd-3m space group), as presented in Fig. 4.23. During the down ramp, at 400°C a transition back to rhombohedral phase is observed with the peaks of cubic symmetry 111 and 220 splitting into 003, 101 and 104, 110 of the rhombohedral geometry, respectively. So, the para-electric/ stable-cubic phase is only possible at higher temperature > 400°C and during cooling the material return to the rhombohedral phase (or a combination of structures) at low temperature. This corroborated by the line-cut at 100°C presented in Fig. 4.23.

Summarizing the investigation and understanding of crystallization of GeTe:

- The crystallization as observed from in-situ Raman and XRD is 160°C with transition to a Rhombohedral phase. The rhombohedral phase is characterized by space groups R3m and P1, as it is difficult to distinguish between them. These structures have 3 short and 3 long bonds.
- The Bragg peak at 43° assigned for R3m space group appears to have a slope. This can be explained by the transition from rhombohedral to meta-stable cubic with an intermediate structure emerging due to decrease in the rhombohedral distortion angle. It is argued that R3m space group persists throughout the temperature range but our observations suggest otherwise.
- From a perspective of bonding arrangement, the transition is viewed as: Rhombohedral - R3m (*three short and long bonds*) to monoclinic - Cm (*two short, two intermediate and two long bonds*) to Cubic - Fd3m (*six identical bonds*), Fig. 4.24 [230]. In our observations, the structure belonging to space group Cm this is evidenced by broadening of the Bragg peak present at 42.5°.
- The presence of cubic peak is confirmed from the line cut at 500°C (Fig. 4.23), and this meta-stable phase transitions back to rhombohedral phase upon cooling.

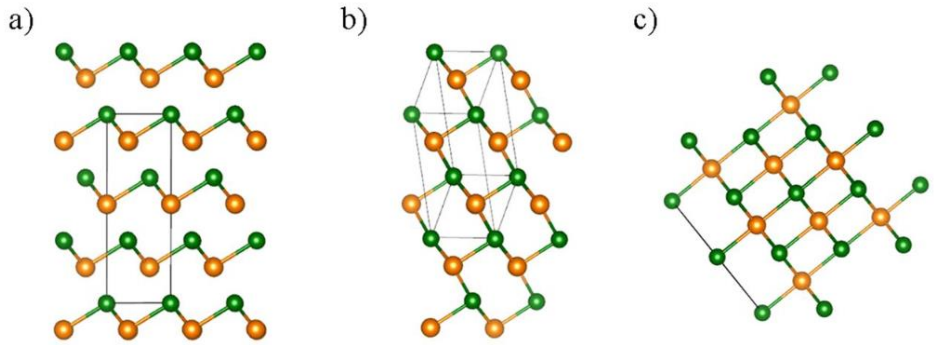

Fig. 4.24. Atomic images of a) R3m or P1, b) Cm and c) Fm3m structures, the material transitions from R3m to Cm to Fm3m upon annealing [230]

4.5 Conclusion

This chapter summarized the vibrational and structural properties originating from elemental - Ge, Sb, Te and pseudo-binary GeTe-Sb_2Te_3 alloys. These characteristics became the building blocks to understand crystallization dynamics and phase transitions for complex Ge-rich GST alloys.

- Ge-rich GST and N-doping

The crystallization riddle was decoded with *in-situ* XRD and Raman observations supporting the scenario of crystallization occurring with simultaneous crystallization of Ge and GST phases. It is worth noting two important things: 1. Ge content does influence these crystallization dynamics, so our observations could be true for Ge > 45%, 2. The studies agreeing on simultaneous crystallization Ge and GST were in-situ XRD, Raman studies, on the contrary the studies suggesting Ge crystallization preceding GST crystallization were in-situ synchrotron XRD studies. Even though the heating rates were similar in some cases the high sensitivities and intensities from in-situ synchrotron offers a better understanding. The general agreement is that Ge phase segregation begins in amorphous phase (Raman intensity changes) with local changes around Ge-Ge and Ge-Te motifs, whereas Sb-Te is unaffected. Once, Ge is flushed out of the GST matrix crystallization occurs. Apart from the differences of mechanism on onset of crystallization, Ge and GST grains crystallize and undergo growth due to Ostwald ripening as the annealing temperature increases. Generally, GST grains are larger than Ge grains. The transition of GST phase from cubic to trigonal is dependent on N-doping.

The effect of N-doping is clear from these observations. In the amorphous phase, it primarily bonds with Ge, affecting the intensity of a-Ge Raman bands. Crystallization is retarded as it slows down the atomic migration of Ge atoms, delaying the flushing out of Ge from a GST matrix. Next, N-doping prohibited the transition of GGSTN from cubic to trigonal phase and lowered its melting point. The grain size of GST and Ge grains is smaller than in GGSTN on comparison with GGST. This happens as N is segregated around the grain boundaries, slowing down the grain growth.

From the perspective of a PCM cell, as repeatedly pointed out, the BEOL fabrication temperature is crucial. For GST-225, at this temperature transitioned to trigonal phase which was detrimental to the cell as it introduced voids and an uneven surface. Ge-enrichment increased the

crystallization temperature but led to Ge segregation and also initial transition to trigonal phase was observed around 400°C. Introduction of Nitrogen slowed down the Ge segregation phenomena, avoided formation of trigonal phase and maintained a better homogenized composition profile. These developments further advance the practicality of using this alloy for embedded memories.

The study shows a complete structure profile of the as-deposited material from room temperature to 600°C, the possible cycle of changes in a working PCM cell except melting. A key highlight for the advancement of Raman thermometry – the structural changes observed in in-situ XRD investigation align with observation from Raman spectroscopy, identifying the GST phase and the crystallinity of the material based on Ge peak characteristics. Further vouching for Raman thermometry to be a simultaneous structural and thermal characterization technique.

- GeTe

The crystallization dynamics of GeTe has been extensively investigated and is an understood phenomenon. The amorphous phase (distorted octahedral structure) transitions to rhombohedral upon crystallization. This structure transitions through another structure – Cm, before its paramagnetic transformation to a stable cubic structure. During the cooling cycle, the material switches back from stable cubic to rhombohedral structure at the critical temperature of 400°C. There is a debate about the presence of stable cubic structure, but our results do evidence the structural transitions. Raman spectra gives an in depth understanding of the presence of various GeTe tetrahedral combination which differs for different deposition technique.

GeTe is being investigated for its application in radio-frequency switches. During the operation of this switch, it traverses via these different structures. The resistivity measurements presented do not present data above 400°C. It would be interesting to see the effect of the transitions on the transport properties of the material and device.

Chapter 5

Thermal conductivity – Raman thermometry

Thermal conductivity of ternary GST alloys is a key parameter which influences the programming current requirements and thermal crosstalk between neighboring cells. In chapter 2, a comprehensive review of alloys along the pseudo-binary GeTe-Sb_2Te_3 line is presented with a key focus on GST-225 and the influence of doping this flagship alloy. Over the years, development targeted towards high temperature data retention for embedded memories implement Ge-rich GST-225 and its variants. The crystallization of this alloy has been a complex story. Recent developments give a comprehensive understanding of the crystallization dynamics, phase segregation and the beneficial influence of N-doping. Regarding its thermal properties, much investigation is not undertaken apart from a single report.

In this chapter, we present the thermal conductivity results of Ge-rich GST alloys characterized by Raman thermometry. This technique is presented in the view of a simultaneous structural plus thermal characterization technique which is crucial and beneficial for phase change materials. As this is the first time Raman thermometry is applied to ternary GeSbTe alloys, the viability of the technique as a thermal characterization for ternary alloys is analyzed. As it's a technique based on vibrational properties of a material, we present the key considerations and improvement of the technique over trial and error. Then thermal conductivity results of GGST and GGSTN are presented with critical discussion. We end the chapter by portraying the versatility of the technique and issues faced for different alloys like GeTe.

5.1 Raman thermometry

This technique has been extensively used for unary (Si, Ge, Graphene) or binary (MoS_2, GaAs, SiC, Sb_2Te_3) systems successfully. For a single thin film or a suspended layer, it is possible to theoretically extract the thermal conductivity by solving the heat conduction equation. In case of materials used in electronics like GaAs or SiC, Raman thermometry is usually implemented to extract a temperature map of the device. For systems with multiple thin films, it is not possible to find a theoretical solution so finite element modeling is implemented. In Chapter 2, a detailed introduction is provided for the experimental and finite element modelling aspect of the technique. For experimental part, the two key parameters to extract are:

1. Temperature calibration, $\frac{d\omega}{dT}$
2. Power calibration as a function of temperature, $\frac{d\omega}{dP_{abs}}$

The ratio of these 2 quantities gives the thermal conductance of the material ($\boldsymbol{G_{TH}}$). For modelling, the experimental system is replicated and the thermal conductance of the material is extracted as a function of the thermal conductivity of the material which is an unknown parameter. For experimental analysis of data, Lorentzian peak fitting is a crucial aspect to deduce the parameters required for further analysis. For example, peak fitting parameters like number of peaks required to fit the data set can influence the peak position. In this section, the materials studied and key considerations observed for the experimental analysis of GeSbTe system are presented.

5.1.1 Materials under study

As discussed in Chapter 2, the thickness of the GeSbTe alloys and capping layer was decided to maximize the absorbance of laser in the material. The thickness of the samples used in simulations was input from thickness measurements from TEM analysis. Following is the list of samples studied.

Material	**Stack**	**Thickness (nm)**
Ge-rich GeSbTe (GGST)	SiN / GGST / Si	45 / 200 / substrate
Ge-rich GeSbTe N-doped (GGSTN)	SiN / GGSTN / Si	45 / 200 / substrate
Ge-rich GeSbTe N-doped (GGSTN)	TiN / GGSTN / Si	10 / 200 / substrate
GeTe	SiN / GeTe / Si	15 / 200 / substrate
GST-447	SiN / GST-447 / Si	45 / 200 / substrate
GST-447	SiN / TiN / GST-447 / SiN / SiO_2 / Si	20 / 23 / 56 / 75 / 28 / substrate

Table 5.1 List of materials under study, the sequence of materials in the stack are ordered from top to substrate.

To present the viability of the technique, SiN and TiN were selected as the capping layer. Both the materials are a part of the PCM cell, so the influence of the capping layers on the properties of GGST would be interesting.

5.1.2 Influence of peak fitting

The recorded data from a Raman spectrometer is first treated by subtracting baseline using the basic straight-line technique. For every acquisition, the acquisition time is decided to optimize the signal to noise ratio. The magnitude of noise of the setup ranges from 40-60 counts, so a satisfactory ratio of at least 10 is maintained. Post baseline subtraction, the peaks are identified and fitted. As presented in Chapter 3, the amorphous and crystalline phases of GeSbTe system consists of various vibrational modes. The complexity of GeSbTe alloys is due to the presence of Ge-Te, Sb-Te and Te-Te vibrational modes arising from different structural configurations in a narrow range of 100 – 200 cm^{-1}. To elaborate, the Ge-Te modes – 100 cm^{-1}, 130 cm^{-1} and Sb-Te mode at 154 cm^{-1} are not well defined due to their proximity. Also, the number of vibrational modes possible in an alloy and the ones required for fitting can differ to obtain a quality fit.

Fig. 5.1 presents a Raman spectrum of annealed crystalline GGSTN (c-GGSTN) recorded at 25°C. The spectrum is fitted with 4 peaks (GeTe – 100 cm^{-1}, SbTe – 154 cm^{-1}, GeTe – 225 cm^{-1}, GeGe – 299 cm^{-1}) and 5 peaks (additional at 280 cm^{-1}). Peaks are the expected number of vibrational modes possible, whereas 5 peaks were required to acquire a better quality (R^2) fit. Although the quality of fit does not visually have a significant impact on the peak positions of the most intense modes – SbTe and GeGe. This is investigated by comparing the peak positions as a function of temperature, as presented in Fig. 5.2. The peak fitting parameter has a minor influence on the peak positions. Further, upon fitting of temperature dependent Raman shift behavior resulted in almost no impact on the calibration coefficient, which is the key quantity for thermometry. This indicates that peak fitting does not have a major influence, and this was studied for all material in both the phases.

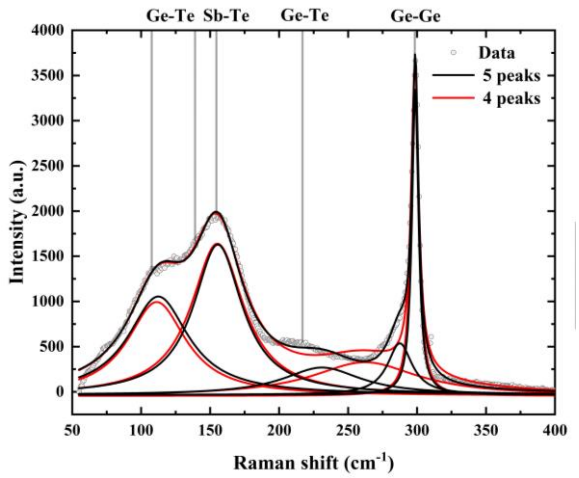

Fig. 5.1. Raman spectrum of c-GGSTN (grey circles) is fitted with 4 peaks (red) and 5 peaks (black) Lorentzian fitting procedure highlighting the difference in the fitted curve.

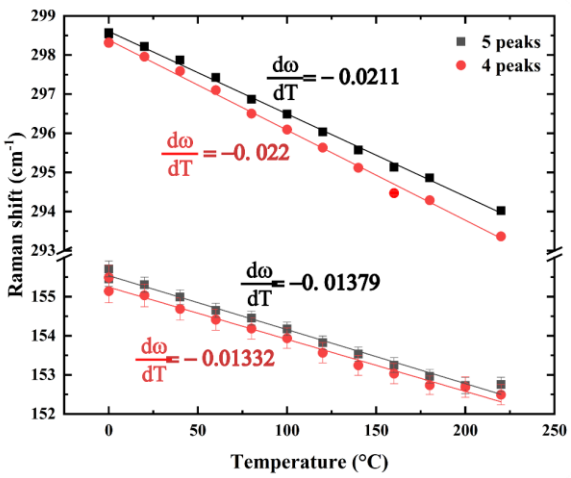

Fig. 5.2. Temperature calibration curve (calibration coefficients indicated) for 4 peaks (red) and 5 peaks (black) Lorentzian fitting procedure for SbTe (@ 154 cm^{-1}) and c-Ge (@ 299cm^{-1}) vibrational modes.

5.1.3 Reliability of the technique

This technique is quite sensitive to input laser power – as it can alter the material locally and influence the vibration modes of the material. This could result in influencing the peak position or disappearance of modes due to structural rearrangement. In order to check this effect and reliability of the technique, the material was studied using different power ranges and multiple measurements were performed to obtain statistics on the measurement. Fig. 5.3 presents multiple power measurements performed on as-deposited amorphous-GGST (a-GGST) at 25°C. These measurements were performed on different samples cleaved from the same wafer. Sb-Te mode being the most intense in the amorphous phase is chosen as the thermometer. A difference in the position of Sb-Te is observed, which could rise from the calibration of spectrometer. The power range of 0.5 mW to 4 mW was tested, and as observed did not locally influence the peak position. A consistent red-shift of Raman shift was observed in agreement with the behavior of vibrational modes upon increasing the input heating. The power calibration coefficient extracted from fitting Raman shift vs Power absorbed curve in a range of -0.67 to -0.8 $cm^{-1}mW^{-1}$. Table 5.2 lists the thermal conductance of the material showing the consistency of the results with G_{TH} lying in a narrow range. Upon converting these thermal conductance values lie in narrow range of 0.2 – 0.22 $Wm^{-1}K^{-1}$.

Careful considerations - For power calibration performed at higher temperatures (>300°C) for higher laser power (>2.5 mW) affected the peak position as the laser power led to local crystallization of the amorphous material. In case of condensation on the window, it is recommended to use a cleaner window as it can impact the laser power. The condensation did not impact the peak positions but influenced the signal to noise ratio.

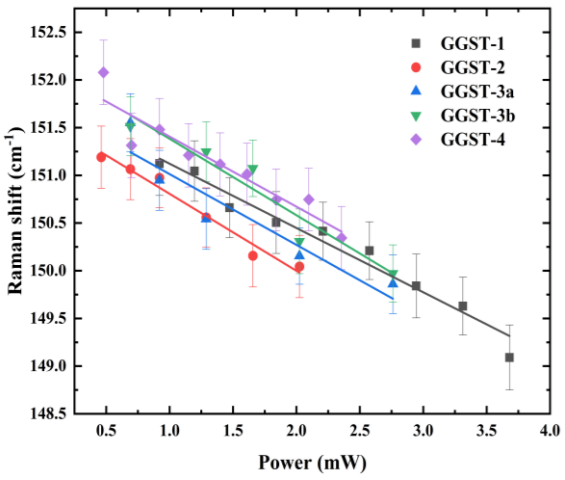

Fig. 5.3 Power calibration measurements performed on different samples of as-deposited a-GGST presented with their respective linear fits.

Sample	$\frac{d\omega}{dP_{abs}}\left[\frac{cm^{-1}}{mW}\right]$	$G_{TH}\frac{dP_{abs}}{dT}\left[\frac{\mu W}{K}\right]$
GGST-1	-0.673 ± 0.048	26.71416 ± 2.93
GGST-2	-0.807 ± 0.067	22.30207 ± 2.63
GGST-3a	-0.742 ± 0.15	24.25549 ± 5.43
GGST-3b	-0.801 ± 0.13	22.45789 ± 4.12
GGST-4	-0.734 ± 0.097	24.49313 ± 3.82

Table 5.2 Power calibration coefficients of the measurements presented in Fig. 5.3 with the experimental thermal conductance.

5.1.4 Amorphous phase stability

Ge-rich GST alloys were primarily targeted due to its amorphous phase stability. For both GGST and GGSTN, the material showed high temperature stability up to 320°C and 360°C, respectively. This is beneficial when targeting embedded memories at the back end of the line as it should sustain the solder reflow temperature to preserve the code integrity. According to the JEDEC

standard, the reflow conditions are set 260°C for 2 mins which is feasible for GGST alloys due to its high crystallization temperature. This ensures the integrity of code during the soldering process during assembly and robustness over the lifetime of the device. In-situ XRD and Raman measurements supported the structural stability of the material. In case of Raman analysis, rearrangement of vibrations associated with Ge-Te structural units was observed.as the vibrational properties of a material are sensitive to temperature. The crystallization theory for GGST suggests that before the onset of crystallization, phase segregation of Ge atoms occurs in the uniform Ge-Sb-Te matrix.

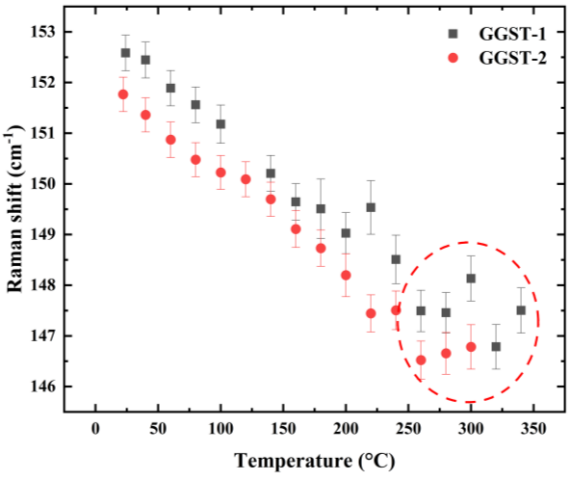

Fig. 5.4 In-situ temperature change in Raman shift (SbTe mode) of as-deposited a-GGST performed on 2 different samples from 25°C to 340°C)

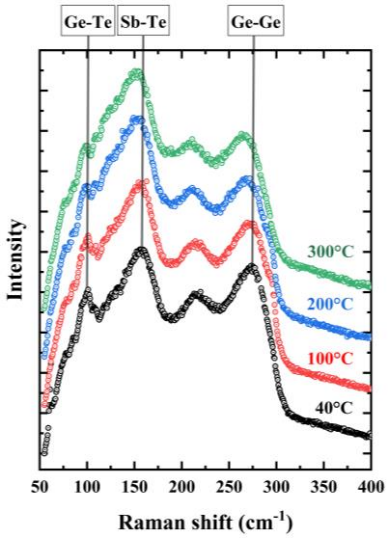

Fig 5.5 Evolution of Raman spectrum of as-deposited a-GGST at 40°C, 100°C, 200°C and 300°C showing the instability of GeTe modes.

Fig. 5.4 presents the influence of temperature on Raman shift of Sb-Te vibrations for as-deposited (amorphous) GGST obtained after extracting the peak positions. For consistency of the method, the experiment was repeated twice on different samples cleaved from the same wafer. Upto 250°C the calibration curve follows a linear trend, and post 250°C this trend discontinues (marked by the red dotted circle). This occurs due to the peak fitting procedure rather than a physical phenomenon. From 25°C to 250°C, the spectra are fitted with 5 peaks (GeTe – 100 cm^{-1}, GeTe – 130 cm^{-1}, SbTe – 154 cm^{-1}, GeTe – 225 cm^{-1}, GeGe – 275 cm^{-1}). The spectra presented are raw data and not normalized. Increasing annealing temperature causes a red shift in the vibrational modes, with Sb-Te mode being the most sensitive. In case of intensity, the Sb-Te mode is not affected but vibrational modes associated with Ge-Te and Ge-Ge suffer from a loss of intensity and widening of FWHM. As presented in Fig. 5.5, the Ge-Te intense peak present at 100 cm^{-1} loses intensity and significantly disappears at 300°C. This results in the spectra post 250°C fitted with 4 peaks and not 5 peaks, affecting the fitting procedure and an uncertainty in evaluating the precise peak position of Sb-Te. Note that the Sb-Te peak does red shift after 250 cm^{-1} but the inability to consistently fit the spectrum with the same parameters leads to this uncertainty. This results in difficulty for thermal characterization of amorphous GGST and GGSTN at higher temperature (>250°C). As a general rule, by analyzing he temperature dependence of vibrational modes and parametrizing the number of peaks selected for fitting the spectrum the working temperature range for characterization can be decided.

5.1.5 High temperature measurement – crystalline phase

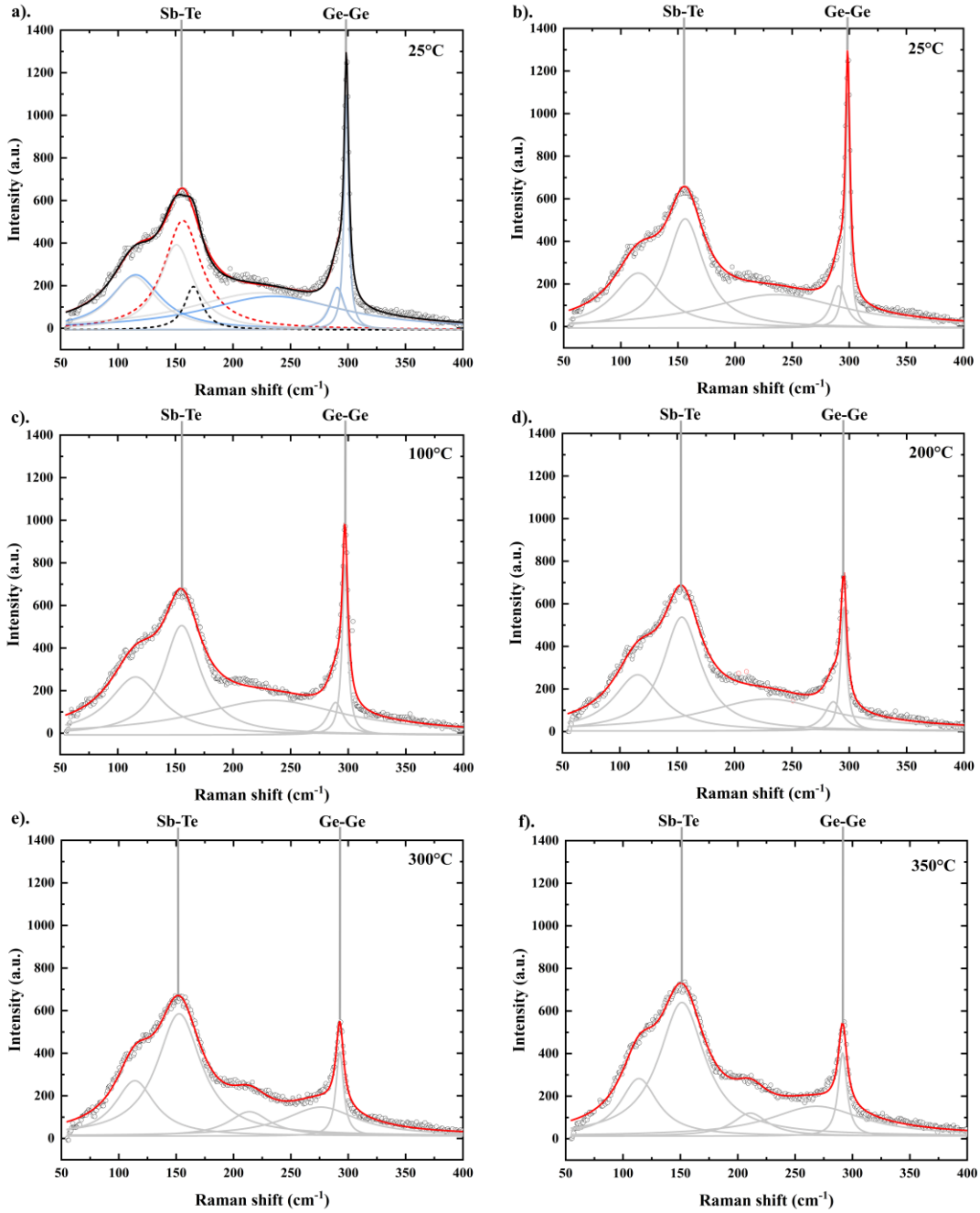

Fig. 5.7. Raman spectrum of c-GGSTN highlighting the behavior of SbTe and GeGe vibrational modes a) Comparison of peak fitting procedures 5 peaks (red) and 6 peaks (blue) – SbTe peak loses its intensity for the 6 peak fitting procedure as highlighted by black dotted line whereas 5 peak fitting preserves the original intensity of SbTe mode during fitting, Next graphs present the Raman spectrum evolution with temperature and influence on peak fitting b) 25°C, c) 100°C, d) 200°C, e) 300°C and f) 350°C

In amorphous phase of GGST alloys, the vibrational modes are present in close proximity due to the complex structural units resulting in convolution of the peaks. Similar is the case for annealed crystalline phase with minor rearrangement of Ge-Te and Sb-Te units. The spectrum is similar in intensity for crystalline displaying broad bands due to presence of vacancies. In addition, crystallization of GGST results in phase segregation of Ge atoms in a tetrahedral $GeGe_4$ units which produces a peak at 299 cm^{-1} in the Raman spectrum. This peak is isolated from the overall spectra and acts as an isolated thermometer for the crystalline phase.

Fig. 5.7 presents the in-situ temperature evolution of Raman spectrum of c-GGSTN annealed at 400°C for 30 mins. The spectrum (a) recorded at room temperature was fitted with 5 (GeTe – 100 cm^{-1}, SbTe – 154 cm^{-1}, GeTe – 225 cm^{-1}, GeGe – 299 cm^{-1}) and 6 peaks (an additional peak at 140 cm^{-1}). The 6 peak fitting resulted in better R^2 but the Sb-Te peak fit was shown as a minor peak (black dotted line) compared to peak fitting (Sb-Te – Red dotted line). Peak fitting can result in a better fit but the characteristics of the respective vibrational modes can be compromised. Spectra 5.7 (b-f) show the temperature evolution of GGSTN with the most intense Ge-Ge vibrational mode broadening and decreasing in intensity significantly. On contrary to the amorphous spectra, the vibrational modes of Ge-Te and Sb-Te, associated to the GST phase of the material show stability over the entire temperature up to 350°C (maximum temperature limit of setup). The same peak fitting procedure could be followed for all the spectra over the entire temperature range. The stability of the crystalline phase and c-Ge peak makes the crystalline phase relatively easier to characterize by Raman thermometry.

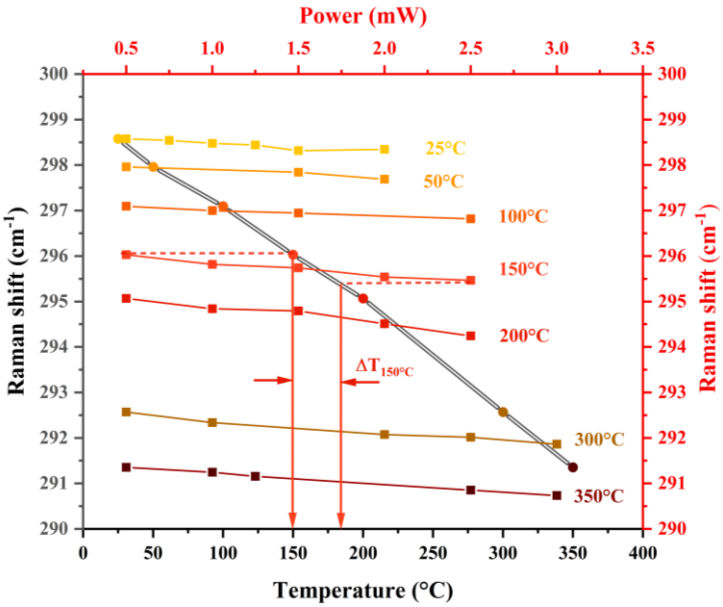

Fig. 5.8. Temperature calibration plot (black axes) with data points connected by double black lines and power calibration plot (red axes) where the colored data points are connected by colored lines (color gradient representing the respective temperature). The power calibration colored data points at 0.5mW align with the temperature calibration data points along the black line. A representative example of local temperature rise caused by a 2.5mW input power for an in-situ measurement performed at 150°C

A complete set of data required to extract the thermal properties by Raman thermometry are presented in Fig. 5.8 for annealed crystalline GGSTN. Here, the colors represent the

measurements performed at a particular temperature. A double connected black line shows the temperature calibration curve and linear fit of this data set gives the calibration coefficient. The data set connected by colored lines represent data extracted by varying power at a particular temperature and similarly its fit gives the power calibration at a particular temperature. For example, during in-situ Raman measurements at 150°C, input power of 2.5 mW results in a 30°C local temperature rise in the material. The power values used in evaluation of thermal conductivity were kept in narrow range in order to not be influenced if the thermal conductivity of the material is temperature dependent. Further, this result justifies the possibility of characterizing GGST alloys by Raman thermometry up to 350°C. For the results presented in the next section, the results were mapped in a similar way to extract the thermal conductivity of the materials.

Some critical considerations for high temperature measurements are as follows: 1). Condensation can influence the Raman spectrum by introducing noise and reducing the intensity of the spectrum. This occurred at temperature above 250°C. The signal to noise ratio changed significantly and affected the peak positions as more number of peaks were required to fit the spectrum. Before each step of in-situ measurements at a specific temperature, care was taken to avoid condensation on the transparent window. 2). For calculation of absorbed power, the absorption coefficient plays a key role. The absorption coefficient is considered independent of temperature as the refractive index of SiN [231], TiN [232] and GST alloys [233] show temperature independence in their respective phases. This was further confirmed by reflectometry measurements.

5.1.6 Revisiting input parameters and modelling assumptions

Finite element modelling was performed in COMSOL Multiphysics version 6.0.

- Laser beam profiles:

The Gaussian profiles of the laser were defined for both 50x and 100x long distance objective with their respective beam waist. For 100x,

$$P_{abs}(r)^{100x} = P_{in}\,A\left(\mu\, exp\left(-\frac{r^2}{R_{w1}^2}\right) + (1-\mu) exp\left(-\frac{r^2}{R_{w2}^2}\right)\right) \qquad \textit{Eq 5.1}$$

where μ = 0.55, R_{w1}= 0.56 μm, R_{w2} = 8.9 μm. To recap, 2 beam waists are defined as the laser profile originating from the 100x objective resulted as a contribution (μ) of 2 Gaussian beam waists. For 50x,

$$P_{abs}(r)^{50x} = P_{in}\,A\;\; exp\left(-\frac{r^2}{R_{w1}^2}\right) \qquad \textit{Eq 5.2}$$

where R_{w1}= 1.5 μm. The absorbance of the material was input as recorded by the reflectometry measurements.

- Material properties

The thermal conductivity of GST ($\boldsymbol{k}_{\mathbf{GST}}$) is parametrized and the thermal conductance is extracted as a function of $\boldsymbol{k}_{\mathbf{GST}}$. Temperature dependent thermal properties are defined for the materials

and interfaces. These properties are defined for the relevant thicknesses as SiN and TiN show thickness dependence. For thermal boundary resistance, the values are identified for SiN-GST-225, TiN-GGST as available in literature. The temperature dependent thermal properties of other materials are defined as follows:

Material	Properties	Units	Reference
Si	149*(300/T)^1.65	$Wm^{-1}K^{-1}$	
SiN	1.0e-1 + 40.1e-4*T	$Wm^{-1}K^{-1}$	[234]
TiN	(-5.34*10^-6)*(T^2)+(1.15*10^-2)*T+5	$Wm^{-1}K^{-1}$	[235]
TBR (SiN-GGST)	50	$m^2K(GW)^{-1}$	[127]
TBR (TiN-GGST)	2.7173*T + 1.1e-8	$m^2K(GW)^{-1}$	[236]

Table 5.3 Thermal properties of materials in the stack as presented in Table 5.1

- Heat transfer: Boundary conditions

All boundaries of the sample are maintained at constant temperature (stage temperature), except at the top of the sample where the laser incident. The sample size was considered large enough to not thermally impact the local influence of laser at its incident spot. The laser Gaussian beam was defined on a plane of size ($5 * R_w$) larger than the beam waist to account for the influence of the entire Gaussian beam profile. Thermal boundary resistance was defined between the thin films as a thermally thick approximation. Convection heat transfer conditions were defined for surface with a coefficient of 10 $Wm^{-2}K^{-1}$. A physics-controlled mesh sequence was defined for the system with a smallest element size of 0.05µm.

The study was parametrized as a function of the thermal conductivity of chalcogenide material ($\boldsymbol{k_{GST}}$). As an output, the local hotspot temperature was evaluated (as discussed in Chapter 3 - 3.2.3) and thermal conductance ($\mathbf{G_{TH}}$) was calculated as a function of the $\boldsymbol{k_{GST}}$. With the thermal conductance known experimentally, the thermal conductivity was extracted.

5.2 Thermal conductivity measurements

Table 5.4 lists the materials studied by Raman thermometry with the absorbance of laser at 473 nm. The calibration coefficients listed for the materials were selected based on the most intense and sensitive mode present for the material. For amorphous GGST/GGSTN, the vibrations of the Sb-Te bond were selected as a thermometer. The Ge-Te vibrational modes were not quite sensitive to temperature. Their temperature dependent behavior was impacted as the structural evolution of GST results in local changes around Ge atoms [100]. This also reflected in the Raman spectrum as presented in Fig. 5.3. The materials GGST and GGSTN were annealed at 400°C for 30 mins as it is sufficient to crystallize the material completely. Also, it would help from a comparison aspect as these conditions have been widely studied for structural investigation [105], [219], [221], [222]. For these annealed crystalline phases of GGST/GGSTN, Sb-Te and Ge-Ge related vibrations were most sensitive showing high temperature structural stability. The Ge-Ge mode was implemented for evaluation of thermal properties due to the characteristic sharp

peak and low error on determining the peak position. The calibration coefficients of GGST and GGSTN are different suggesting the influence of N-doping in the structural arrangement, especially for the crystalline annealed phase. In case of GeTe, the respective vibrations as listed in the table were most sensitive to temperature.

Material *Stack*	**Phase** (conditions)	**Absorbance** A = (1-R)	**Calibration coefficient** $\frac{d\omega}{dT}$ $\left[\frac{cm^{-1}}{K}\right]$
Ge-rich GST *SiN/ GGST/ Si*	As-deposited Amorphous	0.92	Sb-Te = - 0.018
	Annealed – crystalline 400°C, 30 mins	0.88	Sb-Te = - 0.025 Ge-Ge = - 0.018
Ge-rich GST N-doping *SiN/ GGSTN/ Si*	As-deposited Amorphous	0.92	SbTe = - 0.016
	Annealed – crystalline 400°C, 30 mins	0.88	Sb-Te = - 0.013 Ge-Ge = - 0.022
Ge-rich GST N-doping *TiN/ GGSTN/ Si*	Annealed – crystalline 400°C, 10 mins	0.76	Sb-Te = - 0.011 Ge-Ge = - 0.020
GeTe *SiN/ GGSTN/ Si*	As-deposited Amorphous	0.8	Ge-Te (A2) = - 0.025 Ge-Te (A3) = - 0.023
	Annealed – crystalline 300°C, 10 mins	0.65	Ge-Te = - 0.068
GST-447 *SiN / TiN / GST-447 / SiN / SiO_2 / Si*	As-deposited – Crystallized	0.3	Sb-Te = - 0.020

Table 5.4 Information of stacks, phase and annealing conditions investigated, Absorbance calculated from the reflectometer and calibration coefficients of the respective samples extracted by performing in-situ temperature dependent Raman acquisitions. Thermometers (vibrational modes identified based on its sensitivity and linear behavior)

5.2.1 GGST and GGSTN

- **Amorphous phase**

Fig. 5.9. displays the thermal conductivity of GGST and GGSTN measured from room temperature to 200°C. Study at higher temperature was not possible due to local structural changes in these alloys abnormally affecting the position of the vibrational modes. The thermal conductivity lies between 0.25-0.35 $Wm^{-1}K^{-1}$ in agreement with a prior measurement for GGST [127]. The values are similar to the amorphous phase thermal conductivity of most PCMs exhibiting very low thermal conductivity [119]. In amorphous materials, the thermal transport is dictated by the vibrational component as the contribution due to electronic transport is almost negligible. For these amorphous solids, a lower limit of thermal conductivity, $k_{min,lattice}$ is obtained from the

Cahill-Pohl model where the thermal transport is assumed as a random walk of energy between neighboring oscillators. This model is valid above the Debye temperature of the material defined as

$$k_{ph,min} = \frac{1}{2}\left(\frac{\pi}{6}\right)^{1/3} K_b n^{2/3}(v_l + 2v_t) \qquad \textit{Eq 5.3}$$

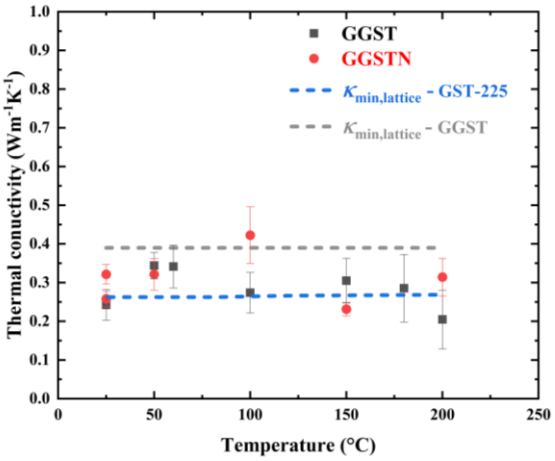

Fig. 5.9. Measured thermal conductivity as a function of temperature for GGST and GGSTN (both capped with SiN). Dashed lines present the min theoretical limit for lattice (phonon) contribution calculated using equation 5.3 for GST-225 and GGST parameters. The experimental values and minimum thermal conductivity law agree well. The longitudinal and transverse sound velocities are input for GST-225 [113] are 2250 m/s, 1350 m/sand GGST [236] are 3600 m/s and 2530 m/s, respectively.

Where n is atomic density (3.09 x 10^{28} m^{-3} [113]), υ_l and υ_t are the longitudinal and transverse sound velocities. As shown in Fig. 4.9, the two limits are assigned to the speed of sound calculated for GST-225 [113] and GGST [236], respectively. The Debye temperature calculated for GST alloys lie well below the room temperature [113], [119], except for one report suggesting it to be at 310 K [114]. The heat capacity of GST as calculated by the Debye model shows no temperature dependence, further not contributing to any fluctuations [114], [124]. The mean free path of phonons is extremely small (~ 5.2-7.6 Å) and constant with temperature, indicating no thickness dependence of thermal conductivity. Overall, good agreement for the thermal conductivity as extracted from Raman thermometry is found with literature and theoretical lower limit calculations.

- **Crystalline phase**

The crystalline phase thermal conductivity study was conducted on pre-annealed samples as discussed in this section. Note – as Raman thermometry is a steady state technique, dynamic evaluation of thermal conductivity from amorphous to crystalline is not possible, as in the case of other widely used techniques. Fig. 5.10 displays the thermal conductivity of the of GGST (capping SiN) and GGSTN (capping SiN and TiN). The measured thermal conductivity value of GGST at room temperature is 1.02 $Wm^{-1}K^{-1}$, higher than GGSTN at 0.8 $Wm^{-1}K^{-1}$. This could be associated with the effect of N-doping. Upon structural examination of these annealed sampled,

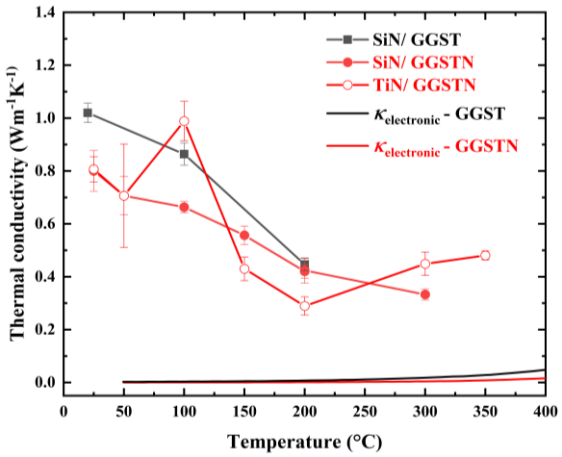

Fig. 5.10. Measured thermal conductivity as a function of temperature for c-GGST (capped with SiN) and c-GGST (capped with SiN and TiN) annealed at 400°C for 30 mins. The electronic contribution is calculated using the Wiedemann-Franz law by using the resistivity data presented for the respective thin films (shown in Fig. 4.4). The contribution of electronic conductivity to the total thermal conductivity is negligible to affect the temperature dependence.

the XRD pattern of GGST shows sharp features of cubic Ge with trigonal and cubic GST phases as shown in Fig. 5.11. Whereas, for the same annealing conditions GGSTN shows broad features with presence of only cubic Ge and GST phases. This suggests that in GGST the sharper peaks indicate growth of the initially small grains whereas the in GGSTN the grain size remains smaller. Evaluation of Ge grain size (peak Ge [111]) results in 28.96 and 7.35 nm for GGST and GGSTN, respectively. So, N-doping affects the crystallization as it bonds primarily to Ge and controls the nature of growth of crystals. Further, it restricts the formation of a ordered trigonal structure in GGSTN as is the case for GGST. Also, the thermal budget provided for GGSTN is not sufficient to obtain a material of higher crystallinity.

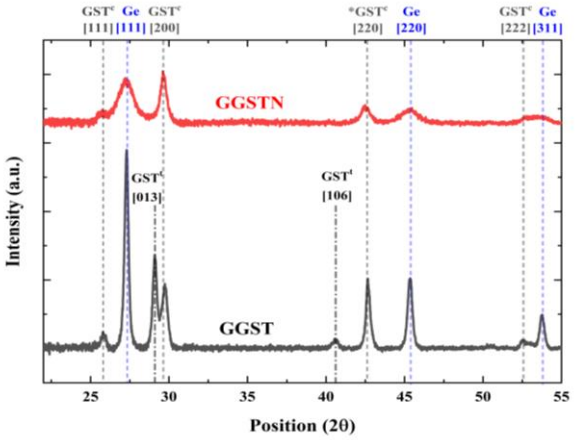

Fig. 5.11 Evolution for GGST and GGSTN for same annealing conditions – 400°C for 30 mins. Impact of annealing conditions is evident with sharp peaks and presence of trigonal GST (GST^T) in GGST whereas only cubic-GST phases are present in GGSTN.

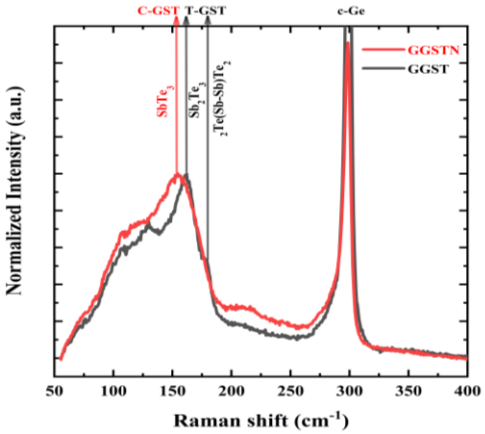

Fig 5.12 Raman spectrum of GGST is characterized by sharper peaks and presence of Sb_2Te_3 vibrations signifying trigonal GST phase whereas GGSTN has broader peaks for similar annealing conditions.

Similar conclusions can be drawn from the Raman spectrum presented in Fig. 5.12 where the peak characteristics are broader for GGSTN. The Sb-Te peak characteristics indicate difference in structure of GGST and GGSTN. GGST has one sharp peak at 162 cm^{-1} and a shoulder at 175 cm^{-1} whereas GGSTN has a rather broad peak at 154 cm^{-1} as presented in Fig.5.12. The presence of trigonal structural motifs and larger grain size contribute to higher thermal conductivity of GGST. For GST alloys, trigonal structural features result in higher thermal conductivity rather than metastable cubic phase [113] and in general for polycrystalline material grains size evidently affects the thermal conductivity [237].

TEM analysis of these samples further corroborates to this explanation. Fig. 5.13 (a) and (b) presents the BF-TEM image of the cross section of GGST and GGSTN, respectively. The whiter areas are associated with Ge-poor areas and dark gray as Ge-rich areas, whereas the complete black spots in the matrix are associated with voids. Complete Ge segregation can be observed in GGST as compared to GGSTN. This also supports the theory of expulsion of Ge from a Ge-rich matrix to reach a stoichiometric GST preceding crystallization.

a.

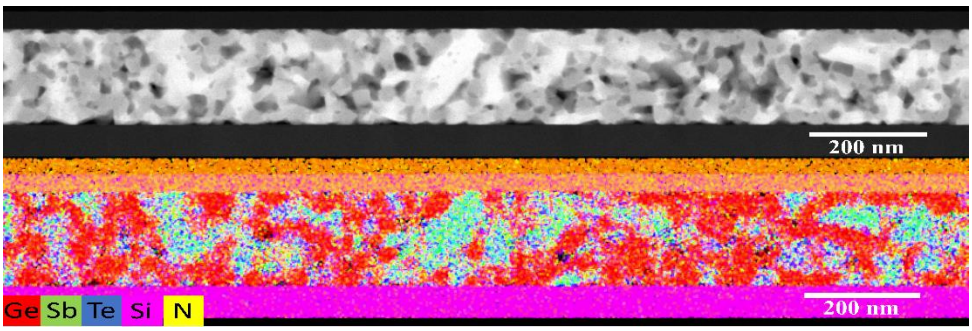

b.

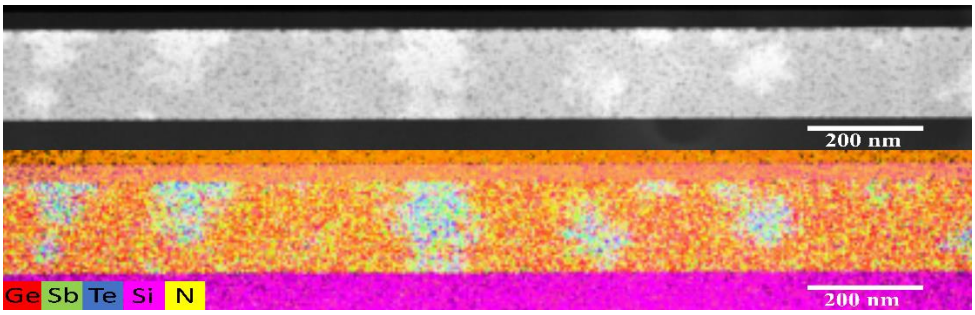

Fig. 5.13 Bright-field (BF)-TEM image (top) and chemical mapping (bottom) for a) GGST and b) GGSTN, respectively. Whiter areas are Ge poor and grey areas are Ge-rich, whereas black areas represent voids. GGST shows clear phase segregation of Ge and GST phases (Ge-poor) with presence of voids agreeing with presence of trigonal phase. The phase segregation in GGSTN is not as inhomogeneous as in GGST.

Ge grains can be identified by the clear crystal planes and EDX map in Fig. 5.14 (a). The area marked as “2” is associated with the GST grains or some presence of amorphous features can be debated as clear crystal planes are not visible. Area “3” indicated presence of voids, rightly so as voids contribute to a crystalline GST structure. For GGSTN, partial Ge segregation with overall presence of N is observed in a rather uniform GST matrix. The contrast between bright and dark areas is lower as compared to GGST. The Ge grains appear to smaller as growth is retarded due to N-doping. The EDX map in Fig. 5.14 (b) show uniform dispersion of Ge, Sb, Te elements with small grains of the size of scale of image dispersed uniformly for GGSTN. This concludes that in

GGST large Ge and GST grains can be observed whereas in GGSTN smaller grains are present with lesser segregation of Ge atoms as an effect of N-doping.

Next, as the temperature increases the decreasing trend of κ for GGST and GGSTN is analogous to the behavior of highly crystalline solids. For temperatures above the one tenth of the Debye temperature, $T_D = \hbar \upsilon_s (6\pi n_a)^{1/3}/k_B$, the κ decreases with increasing temperature due to onset of three phonon Umklapp scattering process [238]. For GST alloys, the Debye temperature is estimated to be 255 K for GST-124 [119] and 220 K for GST-225 [123]. Estimating the Debye temperature of GGST for sound velocities v_l = 3600 m/s and v_t = 2530 m/s [236], results in T_D as 174K. This behavior of the alloys with temperature is reversible as the higher room temperature conductivity is attained on cooling back to room temperature. The contribution to thermal conductivity from its phonon and electron

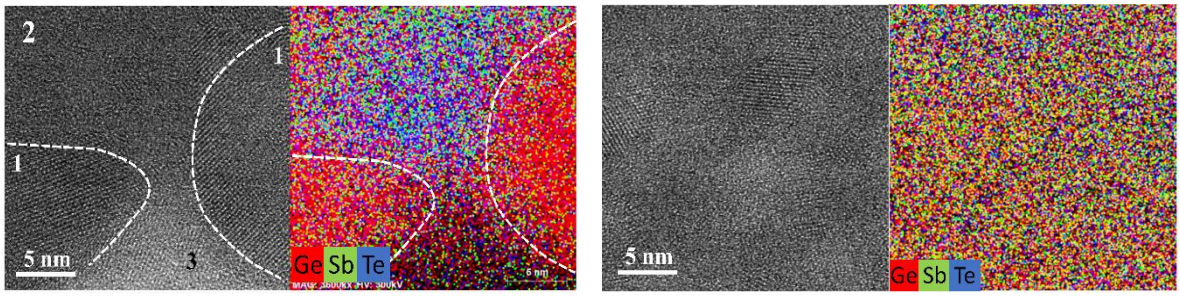

Fig. 5.14 High resolution (HR)-TEM (left) images and chemical mapping images (right) for a) GGST and b) GGSTN. For GGST, areas marked "1" and "2" show Ge and GST grains and "3" represents voids or presence of amorphous areas as no clear plane orientation can be spotted. GGSTN, shows quite homogenous Ge, Sb, Te elemental distribution with crystal planes orientation of grains. Grain size as big as the scale of the image.

components are further analyzed. Assuming that GGST behaves as a metal in its crystalline state, the electronic contribution is calculated by the Wiedemann-Franz law by using the resistivity data of the materials. The continuous lines shown in Fig. 5.10 show that the electronic contribution towards resistivity is quite low. Considering the entire range of Lorenz number from 1.5 to 2.44 x 10^{-8} WΩK^{-2}, the electronic contribution at room temperature is negligible whereas at higher temperature is in the range of 2-5%. This hints that the major contribution arises from the lattice contribution, making the decreasing thermal conductivity behavior due to phonon scattering processes a valid explanation.

It is evident that N-doping affects the thermal conductivity by controlling the crystallization and nucleation-growth kinetics. It would be interesting to see the effect of increased annealing temperature on the thermal conductivity of GGSTN.

5.2.2 GGSTN as a function of annealing temperature

GGSTN was annealed at 380°C, 400°C for 30 mins and 450°C for 10 mins to understand the effect of annealing temperature on thermal conductivity. As 360-370°C is the onset temperature for crystallization 380°C was chosen and 400°C as a benchmark for comparison. Due to delamination of SiN capping film the highest temperature conditions were limited to 450°C for 10 mins. A higher annealing temperature evidently resulted in a structure of better crystallinity. This conclusion is based on the difference in shift of Ge peak between 380°C/400°C and 450°C

annealed sample, as shown in Fig. 5.15. The position of Ge peak at 299.5 cm^{-1} for the 450°C GGSTN sample and 400°C annealed GGST sample is similar, indicating similarity in characteristics of cubic Ge crystalline grains. On the contrary, the Sb-Te peak for GGSTN-450°C sample is positioned at 154 cm^{-1} and does not undergo transition like in GGST. This also confirms that N-doping prohibits the transition to a trigonal GST phase.

Fig. 5.16 presents the room temperature thermal conductivity of GSTN as a function of annealing conditions. Analogous to the structural observations from Raman spectra, the thermal conductivity of the GGSTN increased with increased annealing temperature. The thermal conductivity increased to 0.87 $Wm^{-1}K^{-1}$ but didn't reach to the values of GGST. A higher annealing temperature might further increase the thermal conductivity. As N primarily bonds with Ge, it impedes the migration and segregation of Ge-atoms which occurs swiftly in GGST. This retards the crystallization process and further nucleation and growth dynamics of Ge and GST grains. To refresh on a key point, the annealing conditions around 400°C were chosen as it is the maximum thermal budget endured by the BEOL during fabrication of embedded PCM. This means that the entire PM bit line is crystallized under these conditions. At the next step of forming operation of a virgin PCM cell, the process of amorphous dome formation if performed. To summarize, the entire PM line made of GGST/GGSTN is crystallized at the BEOL fabrication conditions and during PCM cell operation the dome near the heater contact transition between amorphous and crystalline phase. So, a combination of material and annealing conditions leads to a stable GGST structure.

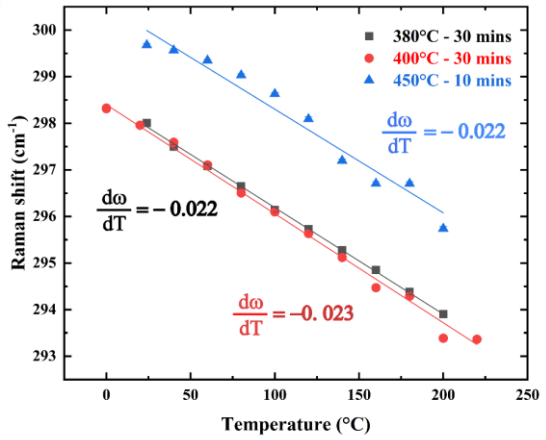

Fig. 5.15. Impact of different annealing conditions on GGSTN observed with its effect on the calibration coefficient and position of c-Ge peak at 299 cm-1

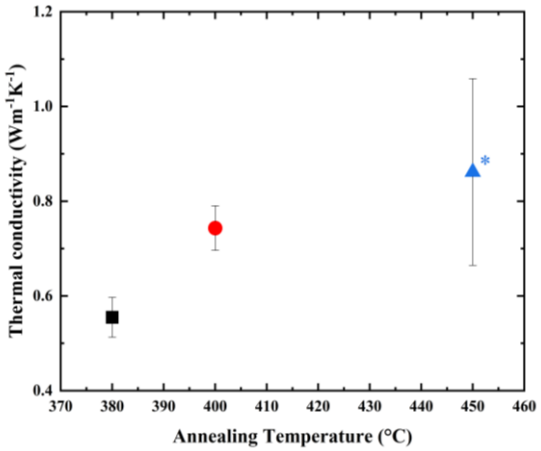

Fig. 5.16. Evolution of GGSTN room temperature thermal conductivity as a function of annealing temperature

Trigonal phase is formed in crystallized GGST at 400°C which leads to formation of voids as observed in the TEM images and supported by observations of Luong et al at higher temperatures [222]. Formation of these voids in GGST could be detrimental for operation of a PCM cell, whereas this does not occur in GGSTN as transition to trigonal phase is restricted. Also, a lower thermal conductivity can reduce the thermal crosstalk between adjacent PCM cell which is observed for GGSTN.

5.2.3 Discussion – Thermal conductivity of GST-225 and Ge-rich GST alloys

Observations concerning the decreasing thermal conductivity trend of GGST differs from the behavior observed for GST based alloys. In general, GST alloys undergo 2 transitions from amorphous to cubic to trigonal phase. For context, an example of GST-225 is discussed. The amorphous phase thermal conductivity aligns well with the thermal conductivity model by Cahill and Pohl. For in-situ annealing measurements, upon crystallization of GST-225 the thermal conductivity of cubic phase increases two-fold and for trigonal phase increases by a factor of 8. The lower thermal conductivity of cubic phase is associated with the low electronic contribution to thermal transport due to localization effects. The low value might be due to phonon scattering [119] and presence of vacancies [113]. Cubic to trigonal transition results in a highly ordered structure and increased electronic contribution resulting in the higher thermal conductivity value.

Thermal cycling of crystalline cubic phases of GST-225 [114], [119] and GST-124 [119] shows a glass-like (dk/dT >0) temperature dependence of thermal conductivity, similar to the amorphous nature. The majority contribution to thermal conductivity is from lattice, which can be understood as a combined effect of a) the Umklapp process, b) scattering by impurities and lattice defects, and c) scattering by grain boundaries. Analysis of these effects in a modified Debye model suggested the increasing thermal conductivity behavior is due to reduction of point defect scattering [119]. In case of trigonal phase, the thermal conductivity seems to be constant with temperature. The lattice contribution decreases with thermal conductivity due Umkalpp scattering processes (inverse T dependence). This decrease is compensated by the increasing electronic contribution maintaining almost constant thermal conductivity.

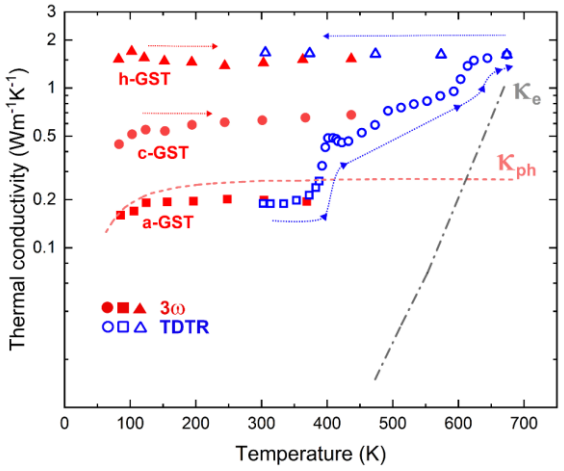

Fig. 5.17 Evolution of thermal conductivity of GST-225 as a function of temperature. Data in blue represents transition of as-deposited material through phase transitions [113], and in red presents data of thermal cycling for pre-annealed samples [114]. Dash and dot-dash lines present the lattice and electronic contribution

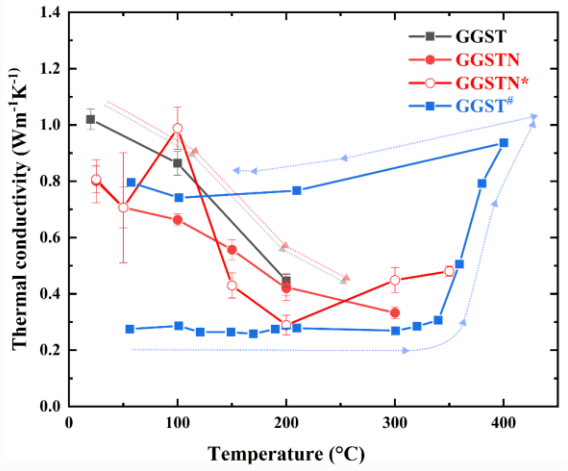

Fig. 5.18 Comparison of thermal conductivity evolution with temperature for GGST (/SiN), GGSTN (/SiN), GGSTN* (/TiN) measured using Raman thermometry and GGST# (/Pt) measured using Pulsed Photo thermal Radiometry (PTR) [127] in blue. The brackets indicate the capping layers.

In context of GGST and GGSTN, the room temperature values presented by Raman thermometry are in good agreement with one report for Ge-rich GST available in literature. The measurements

were performed in-situ on an as-deposited amorphous sample from 50° to 400°C and cooling back to 50°C. The cooling behavior of thermal conductivity shows almost constant thermal conductivity with a small drop. Our data is extracted from in-situ measurements of a pre-annealed (crystallized) sample. Contrary to the behavior of GST alloys, the decreasing thermal conductivity might seem unusual. But the low electronic contribution which does not influence the thermal transport and temperature dependent behavior of lattice contribution could corroborate to this trend. The crystallinity of the material is confirmed by XRD, whereas TEM images do confirm presence of voids and grain boundaries in GGST and GGSTN. GGST has larger grains and GGSTN has smaller grains which explains the difference in the thermal conductivity. Umklapp scattering process being a temperature dependent phonon scattering process could have a major influence on the thermal conductivity. Summing up on the lattice contributions, the decrease in thermal conductivity could occur in Ge-rich GST alloys. Further detailed analysis and theoretical models would be essential to support these findings.

Some inconsistencies might arise from Raman thermometry, but they have been cross checked with literature. Components like absorbance of the laser power in stack could have a considerable influence on the extraction of thermal conductivity. Temperature dependent reports of refractive index of GST alloys, SiN and TiN do not show critical temperature dependence to have a considerable impact on the thermal conductivity. Next, the temperature dependence of thermal conductivities of SiN, TiN and Si was considered during computation by FEM. Influence of different TBR values between interfaces resulted in a change of thermal conductivity in the range of 2-5% which does not have a major influence. The technique was proven with different capping layers SiN and TiN showing similar results for thermal conductivity. 100x and 50x objective lenses were implemented to check the consistency of the results as the input power profile varies. Summing up on all factors, Raman thermometry is successfully implemented for thermal conductivity extraction of GGST alloys.

5.2.4 GeTe

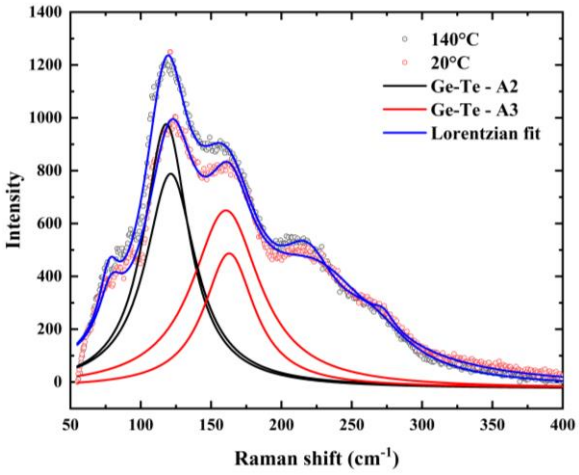

Fig. 5.19 Comparison of Rama spectra for a-GeTe at 20°C and 140°C. The two most intense modes are highlighted with Lorentzian fitting.

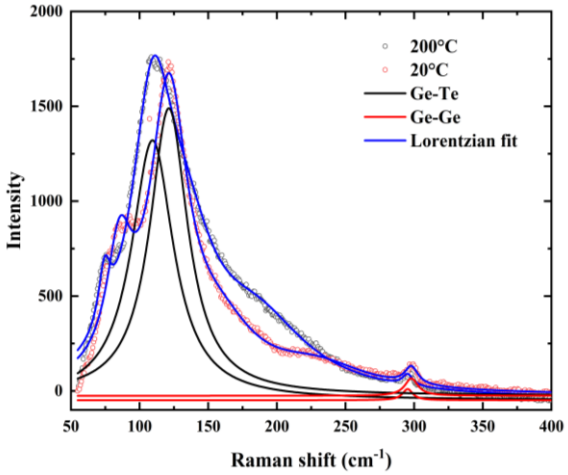

Fig. 5.20 Comparison of Raman spectra for c-GeTe (annealed at 300°C) at 20°C and 200°C. The most intense modes and c-Ge contribution are highlighted with Lorentzian fitting.

Structural analysis from Raman spectroscopy reveals that GeTe spectrum consists of at least 5 modes associated with different structural units and vibrations. In-situ XRD examination gave a comprehensive insight into the structural component of GeTe upon crystallization as it transitioned from amorphous to rhombohedral to cubic crystalline structure with the possible existence of an intermediate crystalline structure. The higher temperature crystalline structures are metastable and appear only under influence of temperature or pressure [230]. The room

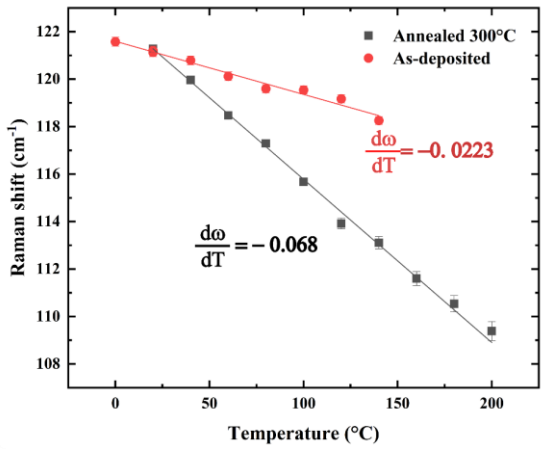

Fig. 5.21 Temperature calibration curve of as-deposited a-GeTe and annealed c-GeTe presented as Raman shift vs temperature. Significant different in the sensitivity of the bonds is evident from the calibration coefficients

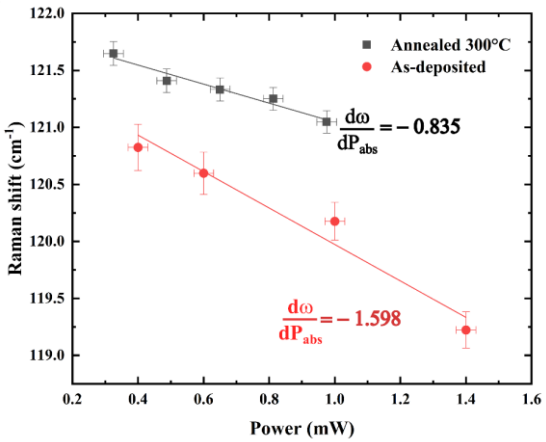

Fig. 5.22 Power calibration curve of as-deposited a-GeTe and annealed c-GeTe presented as Raman shift vs Power absorbed. The coefficients are indicated for the respective phases.

temperature structure is always associated with its rhombohedral phase. For Raman thermometry the amorphous (as-deposited) and crystalline (annealed at 300°C) samples were studied. Fig. 5.19 shows the as –recorded Raman spectrum of amorphous GeTe at 20°C and 140°C with the 2 most intense vibrational modes highlighted. The vibrational mode A2 grows more intense compared to A3, with both showing temperature sensitivity. The A2 mode was selected as a thermometer due to its superior peak characteristics and sensitivity as presented by its calibration coefficient in Fig. 5.21. Fig. 5.20 presents the crystalline Raman spectrum at 20°C and 200°C. The Raman spectrum simplified upon crystallization with rearrangement of Ge-Te structural units in a rhombohedral geometry and minor presence of tetrahedral Ge observed at 299 cm^{-1}. The c-GeTe Raman mode at 120 cm^{-1} shows greater sensitivity to temperature than its amorphous counterpart as is evident from the Fig. 5.21. Power dependent Raman shift measurements at room temperature measurements are presented in Fig. 5.22. The ratio of the temperature and power calibration extracted from their respective calibration curves yield the room temperature thermal conductance of the material.

For amorphous and crystalline phase, the thermal conductance values of 13.9 μWK^{-1} and 8.4 μWK^{-1} are associated with 0.15 and 1.15 $Wm^{-1}K^{-1}$ thermal conductivity respectively. The amorphous thermal conductivity values agree with literature values of 0.19 $Wm^{-1}K^{-1}$ [119]. Whereas, crystalline thermal conductivity values appear to be lower than the expected values of 2.2 $Wm^{-1}K^{-1}$ [119] and 3 $Wm^{-1}K^{-1}$ [239] as reported. From multiple measurements, temperature calibration results remained consistent and power dependent measurements showed high inconsistency. The behavior of Raman modes with increasing power input did not follow a

specific trend and the presented measurements were an exceptional case, especially for crystalline measurements. This stems from the sensitivity of GeTe material (bonds) to increasing input power. In the Raman spectrum, 6 Ge-Te vibrational modes are present in a range of 100 to 180 cm^{-1}. Influence of temperature or power leads to minor local structural changes which might affect the fitting procedure. It has been documented that corner and edge-sharing $GeTe_{4-n}Ge_n$ (n=0) modes (111 and 162 cm^{-1}) increase in intensity at the expense off corner and edge-sharing $GeTe_{4-n}Ge_n$ (n=1,2) modes (127 and 162 cm^{-1}) on influence of temperature. These modes are present in quite close which affects the identification of precise peak position. Also, the it is reported that the room temperature GeTe structure transitions from R3m to Cm to Fm3m structure upon application of pressure or temperature [230]. These different structures have different bond and angle distributions which can affect the sensitivity of the vibrational mode. Though it is unusual that in our case the temperature response is different from power response of the material which needs to be further investigated. In GST materials, most of the structural reorganization does occur around Ge-Te units which showed fluctuations in GGST study, too. It could be concluded with further analysis that Ge-Te vibrations are not reliable to perform thermometry experiments.

5.3 Conclusion

- Raman thermometry

This technique shows potential to be a simultaneous structural and thermal characterization technique. For PMs, it is crucial to monitor the temperature dependent phase during thermal characterization. Raman thermometry provides this insight while making it possible to observe structural changes like – rearrangement around GeTe motifs, Ge segregation, peak characteristics giving an insight into the crystallinity of the material. Key parameters for feasibility of the technique: consistent calibration of the Raman spectrometer, precise control over power and temperature, optimized signal to noise ratio by choice of acquisition time and averaging parameters to have consistent measurements. Data analysis is quite straightforward but the influence of fitting parameters should be checked on the calibration coefficients. The fit must preserve the original intensities of the vibrations. Thermal boundary resistance was considered during analysis by FEM but the technique was not very sensitive. It yielded a difference of 2% in the thermal conductivity values for a system with no TBR and with TBR of 50 $m^2K(GW)^{-1}$.

Consistency of the technique was justified by multiple measurements for the same material in different sample configurations. The crystalline GGSTN thin film stack was investigated with different capping layers – SiN and TiN. The results in both cases were similar, showing the viability of the technique for different stacks – transparent (SiN) and non-transparent (TiN). The technique is highly material dependent and might not work for other material, like in the case of GeTe. A new material should be checked rigorously by performing a few temperature and power dependent acquisitions to identify the sensitive vibrational modes and their reliability. To give some time metrics, the temperature dependent thermal conductivity of a material could be extracted in 3-4 days.

- Ge-rich GST and N-doping

The amorphous phase thermal conductivity aligns well with the minimum thermal conductivity model and, the general expectation of thermal conductivity of GST based alloys. The crystalline phase thermal conductivity showed behavior contrasting the temperature independence

behavior of GST based alloys observed so far. The behavior observed for GGST/ GGSTN aligns well with the temperature dependent decrease of thermal conductivity in crystalline solids due to phonon scattering processes. It is possible for GGST as the electronic contribution is low and the lattice component is the majority contributor to thermal conductivity. For other GST alloys, mainly GST-225, extensive analysis shows that lattice contribution does show temperature dependence but is compensated with the increasing electronic contribution owing to the superior electrical conductivity. This electrical conductivity is hampered in the case of GGST due to Ge doping by 2-3 orders of magnitude. Structural investigation (Raman, XRD and TEM) shows the material to be completely crystalline confirming the phase of the material. Apart from the presented results, only one measurement for GGST is available in literature so further analysis is required to understand this behavior. N-doping leads to a decrease in the thermal conductivity and also affects the grain size and segregation as evident from the TEM analysis.

The next step would be to understand the effect of this temperature dependent thermal conductivity on the operation of PCM cell and cross-talk, by electro-thermal simulations.

Conclusions and Perspectives

The last 20 years have witnessed the evolution of phase change memories as a viable storage class memory. Its capability to serve as a standalone and embedded memory help curtail the diverging trends of logic and memory in the hierarchy. PCMs performance metrics in terms of scalability ($4F^2$), endurance (> 10^8 cycles), quick access (~100 ns) and low programming power perfectly fits in the hierarchy between Flash and DRAM. Device and materials engineering played a key role in realization of PCM as a product entering the market. The two routes of stand-alone and embedded memory application evolved parallelly.

Stand-alone research focused on device architecture to increase the memory density, whereas embedded efforts were dedicated towards extensive materials engineering. The novel cross point architecture proved the impressive scalability of PCM with ovonic threshold switches powering the device. Intel displayed the maturity of PCM with its 3D X-Point product and recently, SK-Hynix prototyped a 4-deck cross-point structure displaying stacking of PCM. Further innovation on the memory density front continues to make it on par with 3D NAND from a cost perspective.

Embedded research has been equally successful due to the simplicity of BEOL integration and low voltage operation. The key requirements for embedded memories are: 1) Endure thermal budget of 400°C for 30 mins back-end of line process, and after fabrication of memory, 2) to be compliant with manufacturing soldering step (2 mins at 260°C) to ensure preservation of programmed information. To satisfy these criterions required extensive materials engineering, as the conventional phase-change materials (pseudo binary GeTe-Sb_2Te_3) exhibited poor high temperature properties. Materials engineering was aimed towards increasing the crystallization temperature, thermal stability and reliability to improve the following characteristics:

1. High temperature integration
2. Amorphous thermal stability
3. Data retention benchmark – 10 years at 165°C (Stand-alone benchmark -10 years at 105°C)

Two key materials engineering pathways made this possible – Ge or Sb enrichment and doping with N or C. This sufficed the high temperature stability of the material with on-par performance metrics required for embedded memory application. Ge-rich GST alloys were successful in fulfilling the challenging automotive requirements and were implemented in automotive microcontroller units due to its excellent data retention, high cyclability and reduced power consumption. However, a lot of doubts arise as the intrinsic material properties like crystallization mechanism, structural evolution, phase segregation and thermal properties are not completely understood. Furthermore, the PCM cell utilizes only 1-2% of the injected power to program the cell and a high percentage of heat is dissipated in the surroundings. Then as the devices scale, thermal cross-talk creates an issue for data retention in the neighboring cell. So, it is critical to understand the heat dissipation pathways and thermal cross talk behavior of the cell by simulating the electro-thermal behavior of the cell. For this, knowledge of thermal

conductivity plays a vital role in contributing to this optimization of PCM cell. Thermal characterization of the newly developed alloys did not keep up the same pace, contrary to the pace of materials development.

To contribute towards the further understanding of newly developed materials, this work focuses on the thermal and structural characterization of Ge-rich GST alloys and GeTe. The aim is to develop Raman thermometry as a simultaneous thermal and structural characterization technique for efficient and reliable extraction of thermal conductivity of the ternary alloys. The underlying reason is two-fold: 1. Understand thermal conductivity as it plays a key role in optimizing the programming current and 2. To address the need to complement thermal characterization by structural investigation for phase change materials, so to develop a method which can perform both functions, simultaneously. As abundantly made clear in Chapter 2 (2.1), the thermal conductivity of GST-225 has been well understood but for Ge-rich GST much data doesn't exist apart from a singular report. The thermal conductivity of most alloys along the GeTe-Sb_2Te_3 pseudo-binary line exhibit similar behavior as GST-225. Amorphous to cubic to trigonal transition, increases the thermal conductivity by 2x and 7x, respectively. Amorphous and cubic phases show glass-like thermal conductivity and trigonal shows metallic behavior. Majority contribution towards thermal conductivity in amorphous and cubic phase is from the lattice part. Whereas, trigonal phase electronic contribution is majority due to its superior electrical conductivity. The lattice contribution to trigonal thermal conductivity decreases as temperature increase due to phonon scattering processes but is compensated by the increasing electrical conductivity. This maintains constant thermal conductivity, showing no temperature dependence.

The techniques used for thermal characterization of GeSbTe alloys – 3 thermoreflectance and photo-thermal radiometry are well established but all suffer from some drawbacks. All the techniques require device fabrication. The deposition of metallic layers hinders with high temperature characterization due to cross diffusion. PPTR has evolved as the preferred choice amongst these techniques. In addition, these techniques require complementary physiochemical characterization for validity of the results. In this aspect, Raman thermometry can address the characterization needs of phase and temperature dependent extraction of thermal conductivity. This technique has been highly successful for materials like Si, Ge, GaN, SiC, Graphene, MoS_2 but has never been implemented to the GeSbTe ternary family.

The materials involved, Ge-rich GST and Ge-rich N-doped were provided from STMicroelectronics who are extensively developing embedded PCM for automotive applications. GeTe was provided by CEA-Leti to contribute towards their development of phase change material-based radio frequency switches for 5G communication. Chapter 4 presented extensive structural characterization to understand the phase transitions and structural arrangement of the alloys by in-situ XRD and Raman spectroscopy. Chapter 5 presented a complete thermal characterization of these materials by Raman thermometry and complemented with XRD and EDX-TEM analysis.

In Chapter 4, Raman spectroscopy (4.2.1) and *In-situ* XRD (4.2.3) complemented well to provide an in-depth structural analysis. Raman spectroscopy revealed the possible structural units contributing to as-deposited (amorphous) Ge-rich GST alloys. There was a clear presence of 3 structural units: Ge-Te, Sb-Te and Ge-Ge. Sb-Te vibrations were the strongest due to its high polarizability, followed by the presence of Ge-Ge vibrations confirming the excess nature of Ge.

As-deposited Ge-rich GST N-doped showed similar features as the un-doped alloy with some alterations. The presence of N-doping was easily detected as it affected the Ge-Ge and Ge-Te vibrations. As N primarily bonds with Ge, the intensity of these peaks related to tetrahedral Ge decreased but the Ge-Te vibrations in the distorted octahedral units remained unaffected. This gives an insight of the nature of bonding of Ge-N bonding. *In-situ* Raman experiments by cycling the material from RT up to crystallization temperature presented impressive thermal stability of the amorphous phase. Transition of amorphous to crystalline was witnessed by the appearance of crystalline Ge peak at 299 cm^{-1} in Raman spectroscopy. N-doping delayed the crystallization of Ge-rich GST N-doped by 40°C. The key features observed in the spectra were:

1. Impressive thermal stability of Sb-Te modes up to a higher temperature for both alloys. Ge-Te modes undergo reorganization witnessed by minor changes in position and intensity. Overall, the amorphous phase shows thermal stability up until its crystallization temperature of 320°C for GGST and 360°C for GGSTN making it viable for high-temperature data retention applications.
2. Upon crystallization Sb-Te modes behaved differently in GGST and GGSTN. Sb-Te mode in GGST showed a transition to Sb_2Te_3 vibrations which can be related to a transition from cubic-like to trigonal-line symmetry with the peak characteristics getting sharper. Whereas in the N-doped alloy, Sb-Te mode did not achieve this transition and showed presence at 154 cm^{-1} related to vibrations in pyramidal $SbTe_3$ units (cubic-like). This indicates that N-doping suppresses the cubic to trigonal transition in Ge-rich GST N-doped alloy.

In-situ XRD characterization (RT to 600°C, back to RT) contributed towards this understanding substantially by identifying the crystalline phases precisely and evolution of crystallite size as a function of temperature. The link between Raman and *in-situ* XRD characterization was strong, corroborating towards the strong structural insight provided by Raman. The multi-step crystallization phenomena observed is as follows:

1. Ge and GST crystallize at the same temperature upon onset of crystallization. Ge grain sizes are smaller than GST.
2. GGST undergoes 2 crystalline phase transitions from cubic to trigonal and back to cubic. Whereas GGSTN crystallizes to cubic phase and is stable after that.
3. Effect of N-doping - delays crystallization, inhibits transition of GGSTN to the trigonal phase and controls grain size as it segregates primarily at the grain boundaries. Also, GGSTN melted at 580°C whereas GGST was stable up to 600°C which could be an effect of N-doping.

This analysis corroborates towards the existing understanding of crystallization mechanism in Ge-rich alloys (4.3). The unusual transition of Ge-rich GST from cubic to trigonal and back to cubic needs further understanding. TEM-EDX analysis further sheds light on distribution of the elements, the microstructure and crystal orientation of the phases. It is clear that Ge phase segregates and a separate GST phase is formed. The trigonal phase of GGST shows large grain size and leads to formation of voids, similar to GST-225. Whereas, in the N-doped material avoids trigonal transition, has smaller grains and better uniformity than Ge-rich GST. From an application point of view, GGSTN is a suitable material for the reliability of PCM and BEOL integration, due to these factors.

For GeTe investigation (4.4), Raman spectra for amorphous phase revealed the complex nature of Ge-Te structural arrangement with convolution of peaks in a short range. The phase transition

showed the transition from multiple Ge-Te vibrations to 2 key vibrations. *In-situ* XRD investigations provided beautiful insight into the crystallization and further gradual phase transition in GeTe from rhombohedral to monoclinic to cubic.

In Chapter 5, we extract the thermal conductivity of these alloys and try to comprehend the structural and doping effects. Raman thermometry proved to be a successful technique for extraction of thermal properties of Ge-rich GST and Ge-rich GST N-doped. The key advantages over the other techniques are, no need to microfabrication and can be capped by materials of choice. We presented results with SiN and TiN capping, which are the materials implemented in a PCM cell around GST. This avoids the problem of inter-diffusion of capping material in GST and considers the interfaces as of the actual PCM cell. The reliability of the technique was tested by performing multiple measurements. Influence of data fitting parameters were checked to prove the reliability of the results. Temperature power dependence of Sb-Te mode for amorphous phase and Ge-Ge mode for crystalline phase exhibited sensitivity to temperature and were used as thermometers to extract the thermal conductivity of the materials. Incase of GeTe, it was not possible to reliably extract the thermal conductivity due to the unreliable sensitivity of Ge-Te vibrations to temperature and power.

The temperature dependent amorphous phase thermal conductivity of GGST and GGSTN lies between 0.25 to 0.35 $Wm^{-1}K^{-1}$ and is constant with temperature. This value is similar to most GST alloys and in accordance with the lower limit of thermal conductivity model by Cahill-Pohl. The characterization of amorphous phase in GGST and GGSTN was limited to 250°C. Above this temperature, rearrangement of GeTe units affected the extraction of precise peak positions of Sb-Te vibrations and impacted the linearity of its calibration curve.

For crystalline phase, the technique was successful up to higher temperatures (~350°C) as Ge peak is precise and isolated from the rest of the spectra. The crystalline phases exhibited room temperature thermal conductivity of 1.02 and 0.8 $Wm^{-1}K^{-1}$, for Ge-rich GST and Ge-rich GST N-doped, respectively. N-doping lowered the thermal conductivity of Ge-rich GST. The value for both materials are much lower than that of GST-225 and aids the low power operation goal of PCM. On the contrary to amorphous phase, crystalline phase thermal conductivity decreases with temperature. The electronic contribution to thermal conductivity lies in the range of 2-5%. So, the lattice contribution plays a key role in dictating the thermal conductivity behavior of crystalline GGST. The decreasing trend is due to onset of Umklapp scattering processes which are commonly observed in crystalline solids. For GST-225, electronic contribution compensated the decreasing lattice contribution yielding a constant thermal conductivity, which is not the case for Ge-rich GST alloys. The decreasing thermal conductivity might be beneficial for PCM cell operation and cross-talk. It would be interesting to see the effect of the decreasing thermal conductivity on operation of PCM cell by electro thermal simulations.

In addition, the room temperature thermal conductivity was extracted as a function of annealing temperature. The Ge-rich GST N-doped samples were annealed at 380°C, 400°C and 450°C. The thermal conductivity of Ge-rich GST N-doped increased with increasing annealing temperature. From a structural point of view, a higher thermal budget improves the crystallinity of Ge-rich GST N-doped (similar to Ge-rich GST), thus increasing its thermal conductivity. This sheds light into the importance of knowing the exact BEOL temperature conditions in order to know the precise thermal properties.

Some challenges and disadvantages were faced during Raman thermometry characterization. SiN as a capping layer limited the characterization temperature as it cracked and delaminated upwards of 400°C. In case of TiN, a very thin (10nm) capping layer was deposited to optimize the Raman intensity. This resulted in cracking of TiN thin film upwards of 450°C. This could be due mismatch in thermal expansion coefficients as TiN also crystallizes around 400°C. The microscopic images of TiN revealed weird circular pattern of nucleation like sites. To further improve this technique, it would be beneficial to find an appropriate material and annealing conditions to avoid cracking of the capping material. Amorphous Si or carbon could be the potential solutions.

Overall, the technique provided reliable preliminary results. With the design of experiments, it was possible to extract the thermal properties of the material in a duration of 3-4 days. The added benefit of the technique was the precise observation of structural changes in the Raman spectra, and especially for the amorphous phase. The thesis presents the feasibility of the Raman thermometry as a thermal characterization technique. It can be improved by automation of the experimental setup for power measurements, acquisitions and by upgrading to two-laser Raman thermometry. An ultra-low frequency module could be installed to investigate the material imprint for wavenumbers lower than 100cm^{-1}. Absorbance of the laser in the material has a direct effect on the value of extracted thermal conductivity. It would be beneficial to evaluate the absorbance of the material as a function of temperature for the reliability of the technique. Next, Thermal boundary resistance has a significant impact on the operation of PCM. Designing experiments for samples with various thicknesses and capping layers could be studied to evaluate the thermal boundary resistance. Coupling of Raman thermometry (steady technique) with techniques like thermoreflectance (transient technique) can complement each other to extract reliable thermal properties. An interesting aspect of thermal characterization of phase change materials would be to design experiments for extracting thermal properties of microscopic melt materials. This would complete the domain of thermal properties required to optimize PCM.

To conclude, Raman thermometry shows potential for applicability as thermal – structural characterization for GeSbTe alloys or other ternary alloys. By thorough experimental analysis and identification of reliable vibrations, thermal conductivity can be easily extracted. Currently, other phase change materials like GeSeTe, Sb-rich GST, GeSbSe and their doped versions are being investigated for high temperature stability and low power applications. It would be interesting to extend the scope of Raman thermometry to other ternary families. With regards to Ge-rich GST alloys, structural investigation shows suitability of the material for high temperature applications and applicability in devices.

Phase change materials have been crucial to the development of non-volatile memory and neuro-inspired computing technologies. Development of efficient thermal and structural characterization techniques would go long way in its future realizations.

References

[1] G. E. Moore, “Cramming more components onto integrated circuits, Reprinted from Electronics, volume 38, number 8, April 19, 1965, pp.114 ff.,” *IEEE Solid-State Circuits Society Newsletter*, vol. 11, no. 3, pp. 33–35, Sep. 2006, doi: 10.1109/N-SSC.2006.4785860.

[2] R. H. Dennard, F. H. Gaensslen, H.-N. Yu, V. L. Rideout, E. Bassous, and A. R. LeBlanc, “Design of ion-implanted MOSFET’s with very small physical dimensions,” *IEEE Journal of Solid-State Circuits*, vol. 9, no. 5, pp. 256–268, Oct. 1974, doi: 10.1109/JSSC.1974.1050511.

[3] “232-Layer NAND Flash Memory.” Accessed: Sep. 20, 2023. [Online]. Available: https://www.micron.com/products/nand-flash/232-layer-nand

[4] “Historical Memory Prices 1957+.” Accessed: Sep. 20, 2023. [Online]. Available: https://jcmit.net/memoryprice.htm

[5] “Historical cost of computer memory and storage,” Our World in Data. Accessed: Sep. 20, 2023. [Online]. Available: https://ourworldindata.org/grapher/historical-cost-of-computer-memory-and-storage

[6] I. T. AG, “Energy Efficiency | Making Green Energy Happen - Infineon Technologies.” Accessed: Sep. 20, 2023. [Online]. Available: https://www.infineon.com/cms/en/about-infineon/energy-efficiency-technologies/

[7] “Smart Watch.” Accessed: Sep. 20, 2023. [Online]. Available: https://www.nxp.com/applications/mobile/wearables/smart-watch:SMARTWATCH

[8] “Information and communications technology,” *Wikipedia*. Sep. 11, 2023. Accessed: Sep. 20, 2023. [Online]. Available: https://en.wikipedia.org/w/index.php?title=Information_and_communications_technology&oldid=1174901357

[9] Y. Sun, N. B. Agostini, S. Dong, and D. Kaeli, “Summarizing CPU and GPU Design Trends with Product Data.” arXiv, Jul. 13, 2020. Accessed: Sep. 18, 2023. [Online]. Available: http://arxiv.org/abs/1911.11313

[10] M. Graef, “More Than Moore White Paper,” in *2021 IEEE International Roadmap for Devices and Systems Outbriefs*, Nov. 2021, pp. 1–47. doi: 10.1109/IRDS54852.2021.00013.

[11] “INTERNATIONAL ROADMAP FOR DEVICES AND SYSTEMS™ 2021 UPDATE MORE MOORE.” Accessed: Feb. 22, 2023. [Online]. Available: https://web.archive.org/web/20221212213659/https://irds.ieee.org/images/files/pdf/2021/2021IRDS_MM.pdf

[12] T. Endoh, H. Koike, S. Ikeda, T. Hanyu, and H. Ohno, “An Overview of Nonvolatile Emerging Memories— Spintronics for Working Memories,” *IEEE Journal on Emerging and Selected Topics in Circuits and Systems*, vol. 6, no. 2, pp. 109–119, Jun. 2016, doi: 10.1109/JETCAS.2016.2547704.

[13] E. Liu, “Materials and Designs of Magnetic Tunnel Junctions with Perpendicular Magnetic Anisotropy for High-Density Memory Applications,” *IIOimport*, Nov. 2018, Accessed: Sep. 23, 2023. [Online]. Available: https://imec-publications.be/handle/20.500.12860/31203

[14] H.-Y. Cheng, F. Carta, W.-C. Chien, H.-L. Lung, and M. J. BrightSky, “3D cross-point phase-change memory for storage-class memory,” *J. Phys. D: Appl. Phys.*, vol. 52, no. 47, p. 473002, Sep. 2019, doi: 10.1088/1361-6463/ab39a0.

[15] J. Yi *et al.*, “The chalcogenide-based memory technology continues: beyond 20nm 4-deck 256Gb cross-point memory,” in *2023 IEEE Symposium on VLSI Technology and Circuits (VLSI Technology and Circuits)*, Jun. 2023, pp. 1–2. doi: 10.23919/VLSITechnologyandCir57934.2023.10185210.

[16] F. Arnaud *et al.*, “High Density Embedded PCM Cell in 28nm FDSOI Technology for Automotive Micro-Controller Applications,” in *2020 IEEE International Electron Devices Meeting (IEDM)*, Dec. 2020, p. 24.2.1-24.2.4. doi: 10.1109/IEDM13553.2020.9371934.

[17] S. R. Ovshinsky, “Reversible Electrical Switching Phenomena in Disordered Structures,” *Phys. Rev. Lett.*, vol. 21, no. 20, pp. 1450–1453, Nov. 1968, doi: 10.1103/PhysRevLett.21.1450.

[18] S. Lai, “Current status of the phase change memory and its future,” in *IEEE International Electron Devices Meeting 2003*, Dec. 2003, p. 10.1.1-10.1.4. doi: 10.1109/IEDM.2003.1269271.

[19] R. G. Neale, D. L. Nelson, and G. E. Moore, “Nonvolatile and reprogrammable, the read-mostly memory is here,” *Electronics*, vol. 43, no. 20, pp. 56–60, 1970.

[20] S. Lai and T. Lowrey, “OUM - A 180 nm nonvolatile memory cell element technology for stand alone and embedded applications,” in *International Electron Devices Meeting. Technical Digest (Cat. No.01CH37224)*, Dec. 2001, p. 36.5.1-36.5.4. doi: 10.1109/IEDM.2001.979636.

[21] “Intel 3D XPoint Memory Die Removed from Intel Optane™ PCM (Phase Change Memory).” Accessed: Mar. 20, 2023. [Online]. Available: https://www.techinsights.com/blog/intel-3d-xpoint-memory-die-removed-intel-optanetm-pcm-phase-change-memory

[22] D. Min *et al.*, “18nm FDSOI Technology Platform embedding PCM & Innovative Continuous-Active Construct Enhancing Performance for Leading-Edge MCU Applications,” in *2021 IEEE International Electron Devices Meeting (IEDM)*, Dec. 2021, p. 13.1.1-13.1.4. doi: 10.1109/IEDM19574.2021.9720542.

[23] N. Yamada, E. Ohno, K. Nishiuchi, N. Akahira, and M. Takao, “Rapid-phase transitions of GeTe-Sb2Te3 pseudobinary amorphous thin films for an optical disk memory,” *Journal of Applied Physics*, vol. 69, no. 5, pp. 2849–2856, Mar. 1991, doi: 10.1063/1.348620.

[24] A. Athmanathan, “Multi-level cell phase-change memory-modeling and reliability framework,” PhD Thesis, Ph. D. Dissertation. EPFL, 2016.

[25] A. Pirovano, A. L. Lacaita, A. Benvenuti, F. Pellizzer, and R. Bez, “Electronic switching in phase-change memories,” *IEEE Transactions on Electron Devices*, vol. 51, no. 3, pp. 452–459, Mar. 2004, doi: 10.1109/TED.2003.823243.

[26] D. Ielmini and Y. Zhang, “Analytical model for subthreshold conduction and threshold switching in chalcogenide-based memory devices,” *Journal of Applied Physics*, vol. 102, no. 5, p. 054517, Sep. 2007, doi: 10.1063/1.2773688.

[27] A. Faraclas, N. Williams, A. Gokirmak, and H. Silva, "Modeling of Set and Reset Operations of Phase-Change Memory Cells," *IEEE Electron Device Letters*, vol. 32, no. 12, pp. 1737–1739, Dec. 2011, doi: 10.1109/LED.2011.2168374.

[28] A. Athmanathan, D. Krebs, A. Sebastian, M. Le Gallo, H. Pozidis, and E. Eleftheriou, "A finite-element thermoelectric model for phase-change memory devices," in *2015 International Conference on Simulation of Semiconductor Processes and Devices (SISPAD)*, Sep. 2015, pp. 289–292. doi: 10.1109/SISPAD.2015.7292316.

[29] G. W. Burr *et al.*, "Phase change memory technology," *Journal of Vacuum Science & Technology B, Nanotechnology and Microelectronics: Materials, Processing, Measurement, and Phenomena*, vol. 28, no. 2, pp. 223–262, Mar. 2010, doi: 10.1116/1.3301579.

[30] M. Boniardi and A. Redaelli, "Phase Change Memory: Device scaling and challenges for material engineering in the GeSbTe compound system," *Microelectronic Engineering*, vol. 137, pp. 1–4, Apr. 2015, doi: 10.1016/j.mee.2014.09.021.

[31] A. L. Lacaita and A. Redaelli, "The race of phase change memories to nanoscale storage and applications," *Microelectronic Engineering*, vol. 109, pp. 351–356, Sep. 2013, doi: 10.1016/j.mee.2013.02.105.

[32] D. Ielmini and A. L. Lacaita, "Phase change materials in non-volatile storage," *Materials Today*, vol. 14, no. 12, pp. 600–607, Dec. 2011, doi: 10.1016/S1369-7021(11)70301-7.

[33] G. Navarro *et al.*, "Phase-Change Memory: Performance, Roles and Challenges," in *2018 IEEE International Memory Workshop (IMW)*, May 2018, pp. 1–4. doi: 10.1109/IMW.2018.8388845.

[34] H.-S. P. Wong *et al.*, "Phase Change Memory," *Proceedings of the IEEE*, vol. 98, no. 12, pp. 2201–2227, Dec. 2010, doi: 10.1109/JPROC.2010.2070050.

[35] A. Pirovano, A. L. Lacaita, A. Benvenuti, F. Pellizzer, S. Hudgens, and R. Bez, "Scaling analysis of phase-change memory technology," in *IEEE International Electron Devices Meeting 2003*, Dec. 2003, p. 29.6.1-29.6.4. doi: 10.1109/IEDM.2003.1269376.

[36] Y. H. Ha *et al.*, "An edge contact type cell for Phase Change RAM featuring very low power consumption," in *2003 Symposium on VLSI Technology. Digest of Technical Papers (IEEE Cat. No.03CH37407)*, Jun. 2003, pp. 175–176. doi: 10.1109/VLSIT.2003.1221142.

[37] A. Pirovano *et al.*, "Self-aligned µTrench phase-change memory cell architecture for 90nm technology and beyond," in *ESSDERC 2007 - 37th European Solid State Device Research Conference*, Sep. 2007, pp. 222–225. doi: 10.1109/ESSDERC.2007.4430918.

[38] G. Servalli, "A 45nm generation Phase Change Memory technology," in *2009 IEEE International Electron Devices Meeting (IEDM)*, Dec. 2009, pp. 1–4. doi: 10.1109/IEDM.2009.5424409.

[39] S. J. Ahn *et al.*, "Highly reliable 50nm contact cell technology for 256Mb PRAM," in *Digest of Technical Papers. 2005 Symposium on VLSI Technology, 2005.*, Jun. 2005, pp. 98–99. doi: 10.1109/.2005.1469227.

[40] D. H. Im *et al.*, "A unified 7.5nm dash-type confined cell for high performance PRAM device," in *2008 IEEE International Electron Devices Meeting*, Dec. 2008, pp. 1–4. doi: 10.1109/IEDM.2008.4796654.

[41] M. Boniardi *et al.*, "Optimization metrics for Phase Change Memory (PCM) cell architectures," in *2014 IEEE International Electron Devices Meeting*, Dec. 2014, p. 29.1.1-29.1.4. doi: 10.1109/IEDM.2014.7047131.

[42] G. Atwood and R. Bez, "90nm Phase Change Technology with μTrench and Lance Cell Elements," in *2007 International Symposium on VLSI Technology, Systems and Applications (VLSI-TSA)*, Apr. 2007, pp. 1–2. doi: 10.1109/VTSA.2007.378938.

[43] R. Annunziata, F. Arnaud, F. Disegni, A. Maurelli, and P. Zuliani, "Phase change memory for automotive grade embedded NVM applications," *J. Phys. D: Appl. Phys.*, vol. 53, no. 19, p. 193002, Mar. 2020, doi: 10.1088/1361-6463/ab71aa.

[44] I. S. Kim *et al.*, "High performance PRAM cell scalable to sub-20nm technology with below 4F2 cell size, extendable to DRAM applications," in *2010 Symposium on VLSI Technology*, Jun. 2010, pp. 203–204. doi: 10.1109/VLSIT.2010.5556228.

[45] W. Kim *et al.*, "ALD-based confined PCM with a metallic liner toward unlimited endurance," in *2016 IEEE International Electron Devices Meeting (IEDM)*, Dec. 2016, p. 4.2.1-4.2.4. doi: 10.1109/IEDM.2016.7838343.

[46] O. Weber *et al.*, "A New BJT Selector for sub-0.02μm2 High Density Embedded PCM Memory in FDSOI CMOS Technology," in *2021 Symposium on VLSI Technology*, Jun. 2021, pp. 1–2.

[47] S. M. Sadeghipour, L. Pileggi, and M. Asheghi, "Phase change random access memory, thermal analysis," in *Thermal and Thermomechanical Proceedings 10th Intersociety Conference on Phenomena in Electronics Systems, 2006. ITHERM 2006.*, May 2006, pp. 660–665. doi: 10.1109/ITHERM.2006.1645408.

[48] S. W. Fong, C. M. Neumann, and H.-S. P. Wong, "Phase-Change Memory—Towards a Storage-Class Memory," *IEEE Transactions on Electron Devices*, vol. 64, no. 11, pp. 4374–4385, Nov. 2017, doi: 10.1109/TED.2017.2746342.

[49] J. Y. Wu *et al.*, "A low power phase change memory using thermally confined TaN/TiN bottom electrode," in *2011 International Electron Devices Meeting*, Dec. 2011, p. 3.2.1-3.2.4. doi: 10.1109/IEDM.2011.6131479.

[50] A. Sood *et al.*, "Thermal characterization of nanostructured superlattices of TiN/TaN: Applications as electrodes in Phase Change Memory," in *Fourteenth Intersociety Conference on Thermal and Thermomechanical Phenomena in Electronic Systems (ITherm)*, May 2014, pp. 765–770. doi: 10.1109/ITHERM.2014.6892358.

[51] A. Chandra, P. Oldiges, C.-T. Chen, T. M. Philip, P. Adusumilli, and M. BrightSky, "Impact of heater configuration on Reset characteristics of PCM Mushroom cell," in *2019 IEEE Albany Nanotechnology Symposium (ANS)*, Nov. 2019, pp. 1–6. doi: 10.1109/ANS47466.2019.8963741.

[52] S. W. Fong *et al.*, "Thermal conductivity measurement of amorphous dielectric multilayers for phase-change memory power reduction," *Journal of Applied Physics*, vol. 120, no. 1, p. 015103, Jul. 2016, doi: 10.1063/1.4955165.

[53] C. De Camaret *et al.*, "Enhanced Thermal Confinement in Phase-Change Memory Targeting Current Reduction," in *ESSDERC 2022 - IEEE 52nd European Solid-State Device Research Conference (ESSDERC)*, Sep. 2022, pp. 233–236. doi: 10.1109/ESSDERC55479.2022.9947190.

[54] C. Kim *et al.*, "Fullerene thermal insulation for phase change memory," *Appl. Phys. Lett.*, vol. 92, no. 1, p. 013109, Jan. 2008, doi: 10.1063/1.2830002.

[55] S. Harnsoongnoen and C. Sa-ngiamsak, "Confined-chalcogenide phase-change memory with thin metal oxide interlayer for low reset current operation," in *2009 6th International Conference on Electrical Engineering/Electronics, Computer, Telecommunications and Information Technology*, May 2009, pp. 440–443. doi: 10.1109/ECTICON.2009.5137043.

[56] A. De Proft *et al.*, "Carbon-Based Liner for RESET Current Reduction in Self-Heating Phase-Change Memory Cells," *IEEE Transactions on Electron Devices*, vol. 67, no. 10, pp. 4228–4233, Oct. 2020, doi: 10.1109/TED.2020.3016625.

[57] J. P. Reifenberg, D. L. Kencke, and K. E. Goodson, "The Impact of Thermal Boundary Resistance in Phase-Change Memory Devices," *IEEE Electron Device Letters*, vol. 29, no. 10, pp. 1112–1114, Oct. 2008, doi: 10.1109/LED.2008.2003012.

[58] J. P. Reifenberg *et al.*, "Thickness and stoichiometry dependence of the thermal conductivity of GeSbTe films," *Appl. Phys. Lett.*, vol. 91, no. 11, p. 111904, Sep. 2007, doi: 10.1063/1.2784169.

[59] C. M. Neumann, K. L. Okabe, E. Yalon, R. W. Grady, H.-S. P. Wong, and E. Pop, "Engineering thermal and electrical interface properties of phase change memory with monolayer MoS_2," *Appl. Phys. Lett.*, vol. 114, no. 8, p. 082103, Feb. 2019, doi: 10.1063/1.5080959.

[60] H. Y. Cheng *et al.*, "A high performance phase change memory with fast switching speed and high temperature retention by engineering the GexSbyTez phase change material," in *2011 International Electron Devices Meeting*, Dec. 2011, p. 3.4.1-3.4.4. doi: 10.1109/IEDM.2011.6131481.

[61] G. Navarro *et al.*, "Multilayer Deposition in Phase-Change Memory for Best Endurance Performance and Reduced Bit Error Rate," in *2022 IEEE International Memory Workshop (IMW)*, May 2022, pp. 1–4. doi: 10.1109/IMW52921.2022.9779285.

[62] C. D. Wright, M. Armand, and M. M. Aziz, "Terabit-per-square-inch data storage using phase-change media and scanning electrical nanoprobes," *IEEE Transactions on Nanotechnology*, vol. 5, no. 1, pp. 50–61, Jan. 2006, doi: 10.1109/TNANO.2005.861400.

[63] F. Arnaud *et al.*, "High Density Embedded PCM Cell in 28nm FDSOI Technology for Automotive Micro-Controller Applications," in *2020 IEEE International Electron Devices Meeting (IEDM)*, Dec. 2020, p. 24.2.1-24.2.4. doi: 10.1109/IEDM13553.2020.9371934.

[64] L. Sun *et al.*, "Ab initio molecular dynamics and materials design for embedded phase-change memory," *npj Comput Mater*, vol. 7, no. 1, Art. no. 1, Feb. 2021, doi: 10.1038/s41524-021-00496-7.

[65] N. Yamada, E. Ohno, N. Akahira, K. Nishiuchi, K. Nagata, and M. Takao, "High Speed Overwritable Phase Change Optical Disk Material," *Jpn. J. Appl. Phys.*, vol. 26, no. S4, p. 61, Jan. 1987, doi: 10.7567/JJAPS.26S4.61.

[66] T. Matsunaga, Y. Umetani, and N. Yamada, "Structural study of a Ag 3.4 In 3.7 Sb 76.4 Te 16.5 quadruple compound utilized for phase-change optical disks," *Phys. Rev. B*, vol. 64, no. 18, p. 184116, Oct. 2001, doi: 10.1103/PhysRevB.64.184116.

[67] O. G. Karpinsky, L. E. Shelimova, M. A. Kretova, and J.-P. Fleurial, "An X-ray study of the mixed-layered compounds of (GeTe)n (Sb2Te3)m homologous series," *Journal of Alloys and Compounds*, vol. 268, no. 1, pp. 112–117, Mar. 1998, doi: 10.1016/S0925-8388(97)00625-7.

[68] T. Matsunaga *et al.*, "Single Structure Widely Distributed in a GeTe–Sb2Te3 Pseudobinary System: A Rock Salt Structure is Retained by Intrinsically Containing an Enormous Number

of Vacancies within its Crystal," *Inorg. Chem.*, vol. 45, no. 5, pp. 2235–2241, Mar. 2006, doi: 10.1021/ic051677w.

[69] T. Matsunaga, N. Yamada, and Y. Kubota, "Structures of stable and metastable Ge2Sb2Te5, an intermetallic compound in GeTe–Sb2Te3 pseudobinary systems," *Acta Cryst B*, vol. 60, no. 6, Art. no. 6, Dec. 2004, doi: 10.1107/S0108768104022906.

[70] T. Nonaka, G. Ohbayashi, Y. Toriumi, Y. Mori, and H. Hashimoto, "Crystal structure of GeTe and Ge2Sb2Te5 meta-stable phase," *Thin Solid Films*, vol. 370, no. 1, pp. 258–261, Jul. 2000, doi: 10.1016/S0040-6090(99)01090-1.

[71] T. Matsunaga and N. Yamada, "A Study of Highly Symmetrical Crystal Structures, Commonly Seen in High-Speed Phase-Change Materials, Using Synchrotron Radiation," *Jpn. J. Appl. Phys.*, vol. 41, no. 3S, p. 1674, Mar. 2002, doi: 10.1143/JJAP.41.1674.

[72] T. Matsunaga *et al.*, "Structural characteristics of GeTe-rich GeTe–Sb2Te3 pseudobinary metastable crystals," *Journal of Applied Physics*, vol. 103, no. 9, p. 093511, May 2008, doi: 10.1063/1.2901187.

[73] M. Wuttig and N. Yamada, "Phase-change materials for rewriteable data storage," *Nature Mater*, vol. 6, no. 11, Art. no. 11, Nov. 2007, doi: 10.1038/nmat2009.

[74] J. Akola and R. O. Jones, "Structural phase transitions on the nanoscale: The crucial pattern in the phase-change materials Ge 2 Sb 2 Te 5 and GeTe," *Phys. Rev. B*, vol. 76, no. 23, p. 235201, Dec. 2007, doi: 10.1103/PhysRevB.76.235201.

[75] R. Zallen, "Models of amorphous solids," *Journal of Non-Crystalline Solids*, vol. 75, no. 1, pp. 3–14, Oct. 1985, doi: 10.1016/0022-3093(85)90196-6.

[76] A. V. Kolobov, P. Fons, A. I. Frenkel, A. L. Ankudinov, J. Tominaga, and T. Uruga, "Understanding the phase-change mechanism of rewritable optical media," *Nature Mater*, vol. 3, no. 10, Art. no. 10, Oct. 2004, doi: 10.1038/nmat1215.

[77] D. A. Baker, M. A. Paesler, G. Lucovsky, S. C. Agarwal, and P. C. Taylor, "Application of Bond Constraint Theory to the Switchable Optical Memory Material $Ge_2Sb_2Te_5$," *Phys. Rev. Lett.*, vol. 96, no. 25, p. 255501, Jun. 2006, doi: 10.1103/PhysRevLett.96.255501.

[78] A. Hirata, T. Ichitsubo, P. F. Guan, T. Fujita, and M. W. Chen, "Distortion of Local Atomic Structures in Amorphous Ge-Sb-Te Phase Change Materials," *Phys. Rev. Lett.*, vol. 120, no. 20, p. 205502, May 2018, doi: 10.1103/PhysRevLett.120.205502.

[79] S. Kohara *et al.*, "Structural basis for the fast phase change of $Ge_2Sb_2Te_5$: Ring statistics analogy between the crystal and amorphous states," *Appl. Phys. Lett.*, vol. 89, no. 20, p. 201910, Nov. 2006, doi: 10.1063/1.2387870.

[80] S. Caravati, M. Bernasconi, T. D. Kühne, M. Krack, and M. Parrinello, "Coexistence of tetrahedral- and octahedral-like sites in amorphous phase change materials," *Appl. Phys. Lett.*, vol. 91, no. 17, p. 171906, Oct. 2007, doi: 10.1063/1.2801626.

[81] G. C. Sosso, S. Caravati, R. Mazzarello, and M. Bernasconi, "Raman spectra of cubic and amorphous Ge2Sb2Te5 from first principles," *Phys. Rev. B*, vol. 83, no. 13, p. 134201, Apr. 2011, doi: 10.1103/PhysRevB.83.134201.

[82] S. Caravati, M. Bernasconi, T. D. Kühne, M. Krack, and M. Parrinello, "First principles study of crystalline and amorphous $Ge_2Sb_2Te_5$ and the effects of stoichiometric defects," *J. Phys.: Condens. Matter*, vol. 22, no. 39, pp. 399801–399801, Oct. 2010, doi: 10.1088/0953-8984/22/39/399801.

[83] G. C. Sosso, S. Caravati, C. Gatti, S. Assoni, and M. Bernasconi, "Vibrational properties of hexagonal Ge $_2$ Sb $_2$ Te $_5$ from first principles," *J. Phys.: Condens. Matter*, vol. 21, no. 24, p. 245401, Jun. 2009, doi: 10.1088/0953-8984/21/24/245401.

[84] C. Steimer *et al.*, "Characteristic Ordering in Liquid Phase-Change Materials," *Advanced Materials*, vol. 20, no. 23, pp. 4535–4540, 2008, doi: 10.1002/adma.200700016.

[85] M. Wuttig, D. Lüsebrink, D. Wamwangi, W. Wełnic, M. Gilleßen, and R. Dronskowski, "The role of vacancies and local distortions in the design of new phase-change materials," *Nature Mater*, vol. 6, no. 2, Art. no. 2, Feb. 2007, doi: 10.1038/nmat1807.

[86] B. Huang and J. Robertson, "Bonding origin of optical contrast in phase-change memory materials," *Phys. Rev. B*, vol. 81, no. 8, p. 081204, Feb. 2010, doi: 10.1103/PhysRevB.81.081204.

[87] M. Xu, Y. Q. Cheng, H. W. Sheng, and E. Ma, "Nature of Atomic Bonding and Atomic Structure in the Phase-Change Ge $_2$ Sb $_2$ Te $_5$ Glass," *Phys. Rev. Lett.*, vol. 103, no. 19, p. 195502, Nov. 2009, doi: 10.1103/PhysRevLett.103.195502.

[88] W. Wełnic, S. Botti, L. Reining, and M. Wuttig, "Origin of the Optical Contrast in Phase-Change Materials," *Phys. Rev. Lett.*, vol. 98, no. 23, p. 236403, Jun. 2007, doi: 10.1103/PhysRevLett.98.236403.

[89] H.-Y. Cheng, S. Raoux, and J. L. Jordan-Sweet, "Crystallization properties of materials along the pseudo-binary line between GeTe and Sb," *Journal of Applied Physics*, vol. 115, no. 9, p. 093101, Mar. 2014, doi: 10.1063/1.4867045.

[90] Y. Gu, T. Zhang, Z. Song, Y. Liu, B. Liu, and S. Feng, "Characterization of the properties for phase-change material GeSb," *Appl. Phys. A*, vol. 99, no. 1, pp. 205–209, Apr. 2010, doi: 10.1007/s00339-009-5498-2.

[91] G. Navarro *et al.*, "Highly Sb-Rich Ge-Sb-Te Engineering in 4Kb Phase-Change Memory for High Speed and High Material Stability Under Cycling," in *2019 IEEE 11th International Memory Workshop (IMW)*, May 2019, pp. 1–4. doi: 10.1109/IMW.2019.8739656.

[92] H.-Y. Cheng, S. Raoux, and Y.-C. Chen, "The impact of film thickness and melt-quenched phase on the phase transition characteristics of Ge $_2$ Sb $_2$ Te $_5$," *Journal of Applied Physics*, vol. 107, no. 7, p. 074308, Apr. 2010, doi: 10.1063/1.3357379.

[93] M. Tomelleri *et al.*, "Overcoming the Thermal Stability Limit of Chalcogenide Phase-Change Materials for High-Temperature Applications in GeSe1−xTex Thin Films," *physica status solidi (RRL) – Rapid Research Letters*, vol. 15, no. 3, p. 2000451, 2021, doi: 10.1002/pssr.202000451.

[94] H. Y. Cheng *et al.*, "Novel fast-switching and high-data retention phase-change memory based on new Ga-Sb-Ge material," in *2015 IEEE International Electron Devices Meeting (IEDM)*, Dec. 2015, p. 3.5.1-3.5.4. doi: 10.1109/IEDM.2015.7409620.

[95] Q. Hubert *et al.*, "Lowering the Reset Current and Power Consumption of Phase-Change Memories with Carbon-Doped Ge2Sb2Te5," in *2012 4th IEEE International Memory Workshop*, May 2012, pp. 1–4. doi: 10.1109/IMW.2012.6213683.

[96] H. S. H. Seo, T.-H. J. T.-H. Jeong, J.-W. P. J.-W. Park, C. Y. C. Yeon, S.-J. K. S.-J. Kim, and S.-Y. K. S.-Y. Kim, "Investigation of Crystallization Behavior of Sputter-Deposited Nitrogen-Doped Amorphous Ge2Sb2Te5 Thin Films," *Jpn. J. Appl. Phys.*, vol. 39, no. 2S, p. 745, Feb. 2000, doi: 10.1143/JJAP.39.745.

[97] N. Matsuzaki *et al.*, "Oxygen-doped gesbte phase-change memory cells featuring 1.5 V/100-/spl mu/A standard 0.13/spl mu/m CMOS operations," in *IEEE InternationalElectron Devices Meeting, 2005. IEDM Technical Digest.*, Dec. 2005, pp. 738–741. doi: 10.1109/IEDM.2005.1609459.

[98] Y. Jiang *et al.*, "Silicon doping effect on the crystallization behavior of Ge2Sb2Te5 film," *physica status solidi (a)*, vol. 210, no. 10, pp. 2231–2237, 2013, doi: 10.1002/pssa.201228840.

[99] H. Horii *et al.*, "A novel cell technology using N-doped GeSbTe films for phase change RAM," in *2003 Symposium on VLSI Technology. Digest of Technical Papers (IEEE Cat. No.03CH37407)*, Jun. 2003, pp. 177–178. doi: 10.1109/VLSIT.2003.1221143.

[100] E. Cho, Y. Youn, and S. Han, "Enhanced amorphous stability of carbon-doped Ge2Sb2Te5: Ab Initio investigation," *Appl. Phys. Lett.*, vol. 99, no. 18, p. 183501, Oct. 2011, doi: 10.1063/1.3657139.

[101] Q. Hubert *et al.*, "Lowering the Reset Current and Power Consumption of Phase-Change Memories with Carbon-Doped Ge2Sb2Te5," in *2012 4th IEEE International Memory Workshop*, May 2012, pp. 1–4. doi: 10.1109/IMW.2012.6213683.

[102] G. Navarro *et al.*, "Trade-off between SET and data retention performance thanks to innovative materials for phase-change memory," in *2013 IEEE International Electron Devices Meeting*, Dec. 2013, p. 21.5.1-21.5.4. doi: 10.1109/IEDM.2013.6724678.

[103] M. A. Luong *et al.*, "Impact of Nitrogen on the Crystallization and Microstructure of Ge-Rich GeSbTe Alloys," *physica status solidi (RRL) – Rapid Research Letters*, vol. 15, no. 3, p. 2000443, 2021, doi: 10.1002/pssr.202000443.

[104] E. Rahier *et al.*, "Crystallization of Ge-Rich GeSbTe Alloys: The Riddle Is Solved," *ACS Appl. Electron. Mater.*, vol. 4, no. 6, pp. 2682–2688, Jun. 2022, doi: 10.1021/acsaelm.2c00038.

[105] M. Agati, M. Vallet, S. Joulié, D. Benoit, and A. Claverie, "Chemical phase segregation during the crystallization of Ge-rich GeSbTe alloys," *J. Mater. Chem. C*, vol. 7, no. 28, pp. 8720–8729, 2019, doi: 10.1039/C9TC02302J.

[106] P. Zuliani *et al.*, "Overcoming Temperature Limitations in Phase Change Memories With Optimized GexSbyTez," *IEEE Transactions on Electron Devices*, vol. 60, no. 12, pp. 4020–4026, Dec. 2013, doi: 10.1109/TED.2013.2285403.

[107] A. Redaelli, E. Petroni, and R. Annunziata, "Material and process engineering challenges in Ge-rich GST for embedded PCM," *Materials Science in Semiconductor Processing*, vol. 137, p. 106184, Jan. 2022, doi: 10.1016/j.mssp.2021.106184.

[108] E. Palumbo, P. Zuliani, M. Borghi, and R. Annunziata, "Forming operation in Ge-rich GexSbyTez phase change memories," *Solid-State Electronics*, vol. 133, pp. 38–44, Jul. 2017, doi: 10.1016/j.sse.2017.03.016.

[109] H. Y. Cheng *et al.*, "A thermally robust phase change memory by engineering the Ge/N concentration in (Ge, N)xSbyTe z phase change material," in *2012 International Electron Devices Meeting*, Dec. 2012, p. 31.1.1-31.1.4. doi: 10.1109/IEDM.2012.6479141.

[110] J. Lee *et al.*, "Decoupled thermal resistances of phase change material and their impact on PCM devices," in *2010 12th IEEE Intersociety Conference on Thermal and Thermomechanical Phenomena in Electronic Systems*, Jun. 2010, pp. 1–6. doi: 10.1109/ITHERM.2010.5501412.

[111] U. Russo, D. Ielmini, A. Redaelli, and A. L. Lacaita, "Modeling of Programming and Read Performance in Phase-Change Memories—Part II: Program Disturb and Mixed-Scaling Approach," *IEEE Transactions on Electron Devices*, vol. 55, no. 2, pp. 515–522, Feb. 2008, doi: 10.1109/TED.2007.913573.

[112] T. Siegrist *et al.*, "Disorder-induced localization in crystalline phase-change materials," *Nature Mater*, vol. 10, no. 3, Art. no. 3, Mar. 2011, doi: 10.1038/nmat2934.

[113] H.-K. Lyeo *et al.*, "Thermal conductivity of phase-change material Ge2Sb2Te5," *Appl. Phys. Lett.*, vol. 89, no. 15, p. 151904, Oct. 2006.

[114] Q. Li, O. Levit, E. Yalon, and B. Sun, "Temperature-dependent thermal conductivity of $Ge_2Sb_2Te_5$ polymorphs from 80 to 500 K," *Journal of Applied Physics*, vol. 133, no. 13, p. 135105, Apr. 2023, doi: 10.1063/5.0142536.

[115] A. Furlan, D. Grochla, Q. D'Acremont, G. Pernot, S. Dilhaire, and A. Ludwig, "Influence of Substrate Temperature and Film Thickness on Thermal, Electrical, and Structural Properties of HPPMS and DC Magnetron Sputtered Ge Thin Films," *Advanced Engineering Materials*, vol. 19, no. 5, p. 1600854, 2017, doi: 10.1002/adem.201600854.

[116] T. Zhan *et al.*, "Thermal conductivity of sputtered amorphous Ge films," *AIP Advances*, vol. 4, no. 2, p. 027126, Feb. 2014, doi: 10.1063/1.4867122.

[117] S. Shamoto *et al.*, "Large displacement of germanium atoms in crystalline Ge2Sb2Te5," *Applied Physics Letters*, vol. 86, no. 8, p. 081904, Feb. 2005, doi: 10.1063/1.1861976.

[118] D. G. Cahill and R. O. Pohl, "Lattice Vibrations and Heat Transport in Crystals and Glasses," *Annual Review of Physical Chemistry*, vol. 39, no. 1, pp. 93–121, 1988, doi: 10.1146/annurev.pc.39.100188.000521.

[119] K. S. Siegert *et al.*, "Impact of vacancy ordering on thermal transport in crystalline phase-change materials," *Rep. Prog. Phys.*, vol. 78, no. 1, p. 013001, Dec. 2014, doi: 10.1088/0034-4885/78/1/013001.

[120] D. Campi, L. Paulatto, G. Fugallo, F. Mauri, and M. Bernasconi, "First-principles calculation of lattice thermal conductivity in crystalline phase change materials: GeTe, Sb 2 Te 3 , and Ge 2 Sb 2 Te 5," *Phys. Rev. B*, vol. 95, no. 2, p. 024311, Jan. 2017, doi: 10.1103/PhysRevB.95.024311.

[121] J. Lee *et al.*, "Thermal conductivity anisotropy and grain structure in $Ge_2Sb_2Te_5$ films," *Journal of Applied Physics*, vol. 109, no. 8, p. 084902, Apr. 2011, doi: 10.1063/1.3573505.

[122] M. Kuwahara *et al.*, "Temperature Dependence of the Thermal Properties of Optical Memory Materials," *Jpn. J. Appl. Phys.*, vol. 46, no. 6S, p. 3909, Jun. 2007, doi: 10.1143/JJAP.46.3909.

[123] J. Lee, E. Bozorg-Grayeli, S. Kim, M. Asheghi, H.-S. Philip Wong, and K. E. Goodson, "Phonon and electron transport through $Ge_2Sb_2Te_5$ films and interfaces bounded by metals," *Appl. Phys. Lett.*, vol. 102, no. 19, p. 191911, May 2013, doi: 10.1063/1.4807141.

[124] P. Zalden *et al.*, "Specific Heat of $(GeTe)_x(Sb_2Te_3)_{1-x}$ Phase-Change Materials: The Impact of Disorder and Anharmonicity," *Chem. Mater.*, vol. 26, no. 7, pp. 2307–2312, Apr. 2014, doi: 10.1021/cm500175j.

[125] J. Yang, "Theory of Thermal Conductivity," in *Thermal Conductivity: Theory, Properties, and Applications*, T. M. Tritt, Ed., in Physics of Solids and Liquids. , Boston, MA: Springer US, 2004, pp. 1–20. doi: 10.1007/0-387-26017-X_1.

[126] J.-L. Battaglia *et al.*, "Temperature-dependent thermal characterization of Ge2Sb2Te5 and related interfaces by the photothermal radiometry technique," *J. Phys.: Conf. Ser.*, vol. 214, no. 1, p. 012102, Mar. 2010, doi: 10.1088/1742-6596/214/1/012102.

[127] A. Kusiak *et al.*, "Temperature-Dependent Thermal Conductivity and Interfacial Resistance of Ge-Rich Ge2Sb2Te5 Films and Multilayers," *physica status solidi (RRL) – Rapid Research Letters*, vol. 16, no. 4, p. 2100507, 2022, doi: 10.1002/pssr.202100507.

[128] E. A. Scott *et al.*, "Thermal conductivity of $(Ge_2Sb_2Te_5)_{1-x}C_x$ phase change films," *Journal of Applied Physics*, vol. 128, no. 15, p. 155106, Oct. 2020, doi: 10.1063/5.0023476.

[129] Y.-H. Huang and T.-E. Hsieh, "Effective thermal parameters of chalcogenide thin films and simulation of phase-change memory," *International Journal of Thermal Sciences*, vol. 87, pp. 207–214, Jan. 2015, doi: 10.1016/j.ijthermalsci.2014.08.004.

[130] E.-K. Kim, S.-I. Kwun, S.-M. Lee, H. Seo, and J.-G. Yoon, "Thermal boundary resistance at Ge2Sb2Te5/ZnS:SiO2 interface," *Appl. Phys. Lett.*, vol. 76, no. 26, pp. 3864–3866, Jun. 2000, doi: 10.1063/1.126852.

[131] V. Giraud *et al.*, "Thermal characterization and analysis of phase change random access memory," *Journal of Applied Physics*, vol. 98, no. 1, p. 013520, Jul. 2005, doi: 10.1063/1.1944910.

[132] T.-Y. Lee *et al.*, "Low thermal conductivity in Ge2Sb2Te5–SiOx for phase change memory devices," *Appl. Phys. Lett.*, vol. 94, no. 24, p. 243103, Jun. 2009, doi: 10.1063/1.3155202.

[133] W. P. Risk, C. T. Rettner, and S. Raoux, "In situ 3ω techniques for measuring thermal conductivity of phase-change materials," *Rev. Sci. Instrum.*, vol. 79, no. 2, p. 026108, 2008, doi: 10.1063/1.2841802.

[134] J. Lee *et al.*, "Measurement of anisotropy in the thermal conductivity of Ge2Sb2Te5 films," in *2009 10th Annual Non-Volatile Memory Technology Symposium (NVMTS)*, Oct. 2009, pp. 52–57. doi: 10.1109/NVMT.2009.5429777.

[135] R. Fallica *et al.*, "Thermal and Electrical Characterization of Materials for Phase-Change Memory Cells," *J. Chem. Eng. Data*, vol. 54, no. 6, pp. 1698–1701, Jun. 2009, doi: 10.1021/je800770s.

[136] M. Kuwahara *et al.*, "Measurements of Temperature Dependence of Optical and Thermal Properties of Optical Disk Materials," *Jpn. J. Appl. Phys.*, vol. 45, no. 2S, p. 1419, Feb. 2006, doi: 10.1143/JJAP.45.1419.

[137] E. Bozorg-Grayeli, J. P. Reifenberg, K. W. Chang, M. Panzer, and K. E. Goodson, "Thermal conductivity and boundary resistance measurements of GeSbTe and electrode materials using nanosecond thermoreflectance," in *2010 12th IEEE Intersociety Conference on Thermal and Thermomechanical Phenomena in Electronic Systems*, Jun. 2010, pp. 1–7. doi: 10.1109/ITHERM.2010.5501263.

[138] C. C. Tan *et al.*, "Thermal conductivity measurements of nitrogen-doped Ge2Sb2Te5," in *2011 11th Annual Non-Volatile Memory Technology Symposium Proceeding*, Nov. 2011, pp. 1–4. doi: 10.1109/NVMTS.2011.6137080.

[139] P. Guo *et al.*, "Tungsten-doped Ge2Sb2Te5 phase change material for high-speed optical switching devices," *Appl. Phys. Lett.*, vol. 116, no. 13, p. 131901, Mar. 2020, doi: 10.1063/1.5142552.

[140] B. J. Kooi, W. M. G. Groot, and J. Th. M. De Hosson, "In situ transmission electron microscopy study of the crystallization of Ge2Sb2Te5," *Journal of Applied Physics*, vol. 95, no. 3, pp. 924–932, Feb. 2004, doi: 10.1063/1.1636259.

[141] I. I. Petrov and R. M. Imamov, "ZG Pinsker Electron-diffraction determination of structures of Ge2Sb2Te5 and GeSb4Te7 Soviet Physics Crystallography," *Ussr*, vol. 13, no. 3, p. 339, 1968.

[142] T. H. Jeong, M. R. Kim, H. Seo, J. W. Park, and C. Yeon, "Crystal Structure and Microstructure of Nitrogen-Doped Ge2Sb2Te5 Thin Film," *Jpn. J. Appl. Phys.*, vol. 39, no. 5R, p. 2775, May 2000, doi: 10.1143/JJAP.39.2775.

[143] S. Privitera, E. Rimini, C. Bongiorno, R. Zonca, A. Pirovano, and R. Bez, "Crystallization and phase separation in Ge2+xSb2Te5 thin films," *Journal of Applied Physics*, vol. 94, no. 7, pp. 4409–4413, Oct. 2003, doi: 10.1063/1.1604458.

[144] D. T. Yimam *et al.*, "Phase Separation in Ge-Rich GeSbTe at Different Length Scales: Melt-Quenched Bulk versus Annealed Thin Films," *Nanomaterials*, vol. 12, no. 10, Art. no. 10, Jan. 2022, doi: 10.3390/nano12101717.

[145] A. Redaelli *et al.*, "Improving Ge-rich GST ePCM reliability through BEOL engineering," in *ESSDERC 2021 - IEEE 51st European Solid-State Device Research Conference (ESSDERC)*, Sep. 2021, pp. 231–234. doi: 10.1109/ESSDERC53440.2021.9631807.

[146] M. A. Luong, N. Cherkashin, B. Pecassou, C. Sabbione, F. Mazen, and A. Claverie, "Effect of Nitrogen Doping on the Crystallization Kinetics of Ge2Sb2Te5," *Nanomaterials*, vol. 11, no. 7, Art. no. 7, Jul. 2021, doi: 10.3390/nano11071729.

[147] O. Thomas, C. Mocuta, M. Putero, M.-I. Richard, P. Boivin, and F. Arnaud, "Crystallization behavior of N -doped Ge-rich GST thin films and nanostructures: An in-situ synchrotron X-ray diffraction study," *Microelectronic Engineering*, vol. 244–246, p. 111573, May 2021, doi: 10.1016/j.mee.2021.111573.

[148] M. Baldo *et al.*, "Modeling Environment for Ge-rich GST Phase Change Memory Cells," in *2022 IEEE International Memory Workshop (IMW)*, May 2022, pp. 1–4. doi: 10.1109/IMW52921.2022.9779290.

[149] E. Bozorg-Grayeli, J. P. Reifenberg, M. Asheghi, and K. E. Goodson, "Annual Review of Heat Transfer, Vol. 16 (2013)," *ANNUAL REVIEW OF HEAT TRANSFER*.

[150] C. Peng and M. Mansuripur, "Measurement of the thermal conductivity of erasable phase-change optical recording media," *Appl. Opt., AO*, vol. 39, no. 14, pp. 2347–2352, May 2000, doi: 10.1364/AO.39.002347.

[151] W. P. Risk, C. T. Rettner, and S. Raoux, "Thermal conductivities and phase transition temperatures of various phase-change materials measured by the 3ω method," *Appl. Phys. Lett.*, vol. 94, no. 10, p. 101906, Mar. 2009, doi: 10.1063/1.3097353.

[152] S. Shin, H. K. Kim, J. Song, D. J. Choi, and H. H. Cho, "Phase-dependent thermal conductivity of Ge1Sb4Te7 and N:Ge1Sb4Te7 for phase change memory applications," *Journal of Applied Physics*, vol. 107, no. 3, p. 033518, Feb. 2010, doi: 10.1063/1.3294694.

[153] S. Sandell, E. Chávez-Ángel, A. E. Sachat, J. He, C. M. S. Torres, and J. Maire, "Thermoreflectance techniques and Raman thermometry for thermal property characterization of nanostructures," *Journal of Applied Physics*, vol. 128, no. 13, p. 131101, Oct. 2020, doi: 10.1063/5.0020239.

[154] J. Reifenberg, "Thermal Phenomena in Phase Change Memory". https://purl.stanford.edu/mq070mn5002

[155] D. Zhao, X. Qian, X. Gu, S. A. Jajja, and R. Yang, "Measurement Techniques for Thermal Conductivity and Interfacial Thermal Conductance of Bulk and Thin Film Materials," *Journal of Electronic Packaging*, vol. 138, no. 4, p. 040802, Dec. 2016, doi: 10.1115/1.4034605.

[156] J.-L. Battaglia, A. Kusiak, and K. Ghosh, "The use of photothermal techniques for thermal conductivity and thermal boundary resistance measurements of phase-change chalcogenides alloys," *Journal of Applied Physics*, vol. 129, no. 5, p. 055106, Feb. 2021, doi: 10.1063/5.0020983.

[157] J.-L. Battaglia *et al.*, "Thermal resistance at Al-Ge $_2$ Sb $_2$ Te $_5$ interface," *Appl. Phys. Lett.*, vol. 102, no. 18, p. 181907, May 2013, doi: 10.1063/1.4803923.

[158] J.-L. Battaglia *et al.*, "Thermal characterization of the SiO2-Ge2Sb2Te5 interface from room temperature up to 400°C," *Journal of Applied Physics*, vol. 107, no. 4, p. 044314, Feb. 2010, doi: 10.1063/1.3284084.

[159] J.-L. Battaglia *et al.*, "The periodic pulse photothermal radiometry technique within the front face configuration," *Measurement*, vol. 158, p. 107691, Jul. 2020, doi: 10.1016/j.measurement.2020.107691.

[160] K. Ghosh, A. Kusiak, P. Noé, M.-C. Cyrille, and J.-L. Battaglia, "Thermal conductivity of amorphous and crystalline GeTe thin film at high temperature: Experimental and theoretical study," *Phys. Rev. B*, vol. 101, no. 21, p. 214305, Jun. 2020, doi: 10.1103/PhysRevB.101.214305.

[161] J.-L. Battaglia *et al.*, "Evolution of thermal conductivity of In3Sbβ Teγ thin films up to 550 °C," *physica status solidi (RRL) – Rapid Research Letters*, vol. 10, no. 7, pp. 544–548, 2016, doi: 10.1002/pssr.201600109.

[162] T. R. Hart, R. L. Aggarwal, and B. Lax, "Temperature Dependence of Raman Scattering in Silicon," *Phys. Rev. B*, vol. 1, no. 2, pp. 638–642, Jan. 1970, doi: 10.1103/PhysRevB.1.638.

[163] T. Beechem, S. Graham, S. P. Kearney, L. M. Phinney, and J. R. Serrano, "Invited Article: Simultaneous mapping of temperature and stress in microdevices using micro-Raman spectroscopy," *Review of Scientific Instruments*, vol. 78, no. 6, p. 061301, Jun. 2007, doi: 10.1063/1.2738946.

[164] T. Batten, A. Manoi, M. J. Uren, T. Martin, and M. Kuball, "Temperature analysis of AlGaN/GaN based devices using photoluminescence spectroscopy: Challenges and comparison to Raman thermography," *Journal of Applied Physics*, vol. 107, no. 7, p. 074502, Apr. 2010, doi: 10.1063/1.3359651.

[165] A. Sarua *et al.*, "Thermal Boundary Resistance Between GaN and Substrate in AlGaN/GaN Electronic Devices," *IEEE Transactions on Electron Devices*, vol. 54, no. 12, pp. 3152–3158, Dec. 2007, doi: 10.1109/TED.2007.908874.

[166] M. Kuball and J. W. Pomeroy, "A Review of Raman Thermography for Electronic and Opto-Electronic Device Measurement With Submicron Spatial and Nanosecond Temporal Resolution," *IEEE Transactions on Device and Materials Reliability*, vol. 16, no. 4, pp. 667–684, Dec. 2016, doi: 10.1109/TDMR.2016.2617458.

[167] I. Calizo, A. A. Balandin, W. Bao, F. Miao, and C. N. Lau, "Temperature Dependence of the Raman Spectra of Graphene and Graphene Multilayers," *Nano Lett.*, vol. 7, no. 9, pp. 2645–2649, Sep. 2007, doi: 10.1021/nl071033g.

[168] E. Yalon *et al.*, "Temperature-Dependent Thermal Boundary Conductance of Monolayer MoS2 by Raman Thermometry," *ACS Appl. Mater. Interfaces*, vol. 9, no. 49, pp. 43013–43020, Dec. 2017, doi: 10.1021/acsami.7b11641.

[169] Y. Kim *et al.*, "Temperature dependence of Raman-active optical phonons in Bi2Se3 and Sb2Te3," *Appl. Phys. Lett.*, vol. 100, no. 7, p. 071907, Feb. 2012, doi: 10.1063/1.3685465.

[170] V. Zani, D. Pedron, R. Pilot, and R. Signorini, "Contactless Temperature Sensing at the Microscale Based on Titanium Dioxide Raman Thermometry," *Biosensors*, vol. 11, no. 4, Art. no. 4, Apr. 2021, doi: 10.3390/bios11040102.

[171] M. P. Singh, M. Mandal, K. Sethupathi, M. S. R. Rao, and P. K. Nayak, "Study of Thermometry in Two-Dimensional Sb2Te3 from Temperature-Dependent Raman Spectroscopy," *Nanoscale Research Letters*, vol. 16, no. 1, p. 22, Feb. 2021, doi: 10.1186/s11671-020-03463-1.

[172] C. Kittel and D. F. Holcomb, "Introduction to Solid State Physics," *American Journal of Physics*, vol. 35, no. 6, pp. 547–548, Jun. 1967, doi: 10.1119/1.1974177.

[173] P. R. N. Childs, J. R. Greenwood, and C. A. Long, "Review of temperature measurement," *Review of Scientific Instruments*, vol. 71, no. 8, pp. 2959–2978, Aug. 2000, doi: 10.1063/1.1305516.

[174] S. Xu, A. Fan, H. Wang, X. Zhang, and X. Wang, "Raman-based Nanoscale Thermal Transport Characterization: A Critical Review," *International Journal of Heat and Mass Transfer*, vol. 154, p. 119751, Jun. 2020, doi: 10.1016/j.ijheatmasstransfer.2020.119751.

[175] D. Tuschel, "Raman Thermometry," *Spectroscopy E-Books*, vol. e4, no. 2, Dec. 2016, Accessed: Jul. 16, 2023. [Online]. Available: https://www.spectroscopyonline.com/view/raman-thermometry-1

[176] M. Balkanski, R. F. Wallis, and E. Haro, "Anharmonic effects in light scattering due to optical phonons in silicon," *Phys. Rev. B*, vol. 28, no. 4, pp. 1928–1934, Aug. 1983, doi: 10.1103/PhysRevB.28.1928.

[177] R. Tubino, L. Piseri, and G. Zerbi, "Lattice Dynamics and Spectroscopic Properties by a Valence Force Potential of Diamondlike Crystals: C, Si, Ge, and Sn," *The Journal of Chemical Physics*, vol. 56, no. 3, pp. 1022–1039, Feb. 1972, doi: 10.1063/1.1677264.

[178] B. Pivac, K. Furić, D. Desnica, A. Borghesi, and A. Sassella, "Raman line profile in polycrystalline silicon," *Journal of Applied Physics*, vol. 86, no. 8, pp. 4383–4386, Oct. 1999, doi: 10.1063/1.371374.

[179] E. Yalon *et al.*, "Spatially Resolved Thermometry of Resistive Memory Devices," *Sci Rep*, vol. 7, no. 1, Art. no. 1, Nov. 2017, doi: 10.1038/s41598-017-14498-3.

[180] B. Stoib *et al.*, "Spatially resolved determination of thermal conductivity by Raman spectroscopy," *Semicond. Sci. Technol.*, vol. 29, no. 12, p. 124005, Nov. 2014, doi: 10.1088/0268-1242/29/12/124005.

[181] S. J. Byrnes, "Multilayer optical calculations," Mar. 2016, doi: 10.48550/arXiv.1603.02720.

[182] J. Jaramillo-Fernandez, E. Chavez-Angel, and C. M. Sotomayor-Torres, "Raman thermometry analysis: Modelling assumptions revisited," *Applied Thermal Engineering*, vol. 130, pp. 1175–1181, Feb. 2018, doi: 10.1016/j.applthermaleng.2017.11.033.

[183] "Conduction of Heat in Solids | Physics Today | AIP Publishing." Accessed: Jul. 17, 2023. [Online]. Available: https://pubs.aip.org/physicstoday/article-abstract/15/11/74/422531/Conduction-of-Heat-in-Solids

[184] M. Lax, "Temperature rise induced by a laser beam," *Journal of Applied Physics*, vol. 48, no. 9, pp. 3919–3924, Sep. 1977, doi: 10.1063/1.324265.

[185] H. Malekpour and A. A. Balandin, "Raman-based technique for measuring thermal conductivity of graphene and related materials," *Journal of Raman Spectroscopy*, vol. 49, no. 1, pp. 106–120, 2018, doi: 10.1002/jrs.5230.

[186] S. Didenko, "Artificially induced anisotropy of thermal conductivity in 2D Si phononic membranes," These de doctorat, Université de Lille (2018-2021), 2019. Accessed: Jul. 17, 2023. [Online]. Available: https://www.theses.fr/2019LILUI048

[187] M. Jafari and M. Rais-Zadeh, "An ultra-high contrast optical modulator with 30 dB isolation at 1.55 μm with 25 THz bandwidth," in *Photonic Fiber and Crystal Devices: Advances in Materials and Innovations in Device Applications XI*, SPIE, Aug. 2017, pp. 155–162. doi: 10.1117/12.2278918.

[188] W. H. P. Pernice and H. Bhaskaran, "Photonic non-volatile memories using phase change materials," *Appl. Phys. Lett.*, vol. 101, no. 17, p. 171101, Oct. 2012, doi: 10.1063/1.4758996.

[189] E. Gemo *et al.*, "Simple technique for determining the refractive index of phase-change materials using near-infrared reflectometry," *Opt. Mater. Express*, vol. 10, no. 7, p. 1675, Jul. 2020, doi: 10.1364/OME.395353.

[190] D. N. Wright, E. S. Marstein, A. Rognmo, and A. Holt, "Plasma-enhanced chemical vapour-deposited silicon nitride films; The effect of annealing on optical properties and etch rates," *Solar Energy Materials and Solar Cells*, vol. 92, no. 9, pp. 1091–1098, Sep. 2008, doi: 10.1016/j.solmat.2008.03.013.

[191] R. Annunziata *et al.*, "Phase Change Memory technology for embedded non volatile memory applications for 90nm and beyond," in *2009 IEEE International Electron Devices Meeting (IEDM)*, Dec. 2009, pp. 1–4. doi: 10.1109/IEDM.2009.5424413.

[192] P. Kazimierski, J. Tyczkowski, M. Kozanecki, Y. Hatanaka, and T. Aoki, "Transition from Amorphous Semiconductor to Amorphous Insulator in Hydrogenated Carbon−Germanium Films Investigated by Raman Spectroscopy," *Chem. Mater.*, vol. 14, no. 11, pp. 4694–4701, Nov. 2002, doi: 10.1021/cm020428s.

[193] A. R. Zanatta, I. Chambouleyron, and P. V. Santos, "Study of structural changes in amorphous germanium–nitrogen alloys by optical techniques," *Journal of Applied Physics*, vol. 79, no. 1, pp. 433–438, Jan. 1996, doi: 10.1063/1.360849.

[194] Z. Cheng *et al.*, "Antimony thin films demonstrate programmable optical nonlinearity," *Science Advances*, vol. 7, no. 1, p. eabd7097, Jan. 2021, doi: 10.1126/sciadv.abd7097.

[195] J. S. Lannin, "Raman scattering properties of amorphous As and Sb," *Phys. Rev. B*, vol. 15, no. 8, pp. 3863–3871, Apr. 1977, doi: 10.1103/PhysRevB.15.3863.

[196] J. Fortner, R. Q. Yu, and J. S. Lannin, "Near-surface Raman scattering in germanium clusters and ultrathin amorphous films," *Phys. Rev. B*, vol. 42, no. 12, pp. 7610–7613, Oct. 1990, doi: 10.1103/PhysRevB.42.7610.

[197] W. K. Choi, V. Ng, S. P. Ng, H. H. Thio, Z. X. Shen, and W. S. Li, "Raman characterization of germanium nanocrystals in amorphous silicon oxide films synthesized by rapid thermal

annealing," *Journal of Applied Physics*, vol. 86, no. 3, pp. 1398–1403, Aug. 1999, doi: 10.1063/1.370901.

[198] M. H. Brodsky, R. J. Gambino, J. E. Smith Jr., and Y. Yacoby, "The Raman Spectrum of Amorphous Tellurium," *physica status solidi (b)*, vol. 52, no. 2, pp. 609–614, 1972, doi: 10.1002/pssb.2220520229.

[199] L. Bo, S. Zhi-Tang, Z. Ting, F. Song-Lin, and C. Bomy, "Raman spectra and XPS studies of phase changes in Ge $_2$ Sb $_2$ Te $_5$ films," *Chinese Phys.*, vol. 13, no. 11, pp. 1947–1950, Nov. 2004, doi: 10.1088/1009-1963/13/11/033.

[200] I. Watanabe, S. Noguchi, T. Shiizu, Study on local structure in amorphous Sb-S films by Raman scattering, J. Non Cryst. Solids 58 (1983) 35, doi: 10.1016/j.jnoncrysol.2023.122461

[201] S. Caravati, M. Bernasconi, and M. Parrinello, "First-principles study of liquid and amorphous Sb_2Te_3," *Phys. Rev. B*, vol. 81, no. 1, p. 014201, Jan. 2010, doi: 10.1103/PhysRevB.81.014201.

[202] G. C. Sosso, S. Caravati, and M. Bernasconi, "Vibrational properties of crystalline Sb2Te3 from first principles," *J. Phys.: Condens. Matter*, vol. 21, no. 9, p. 095410, Feb. 2009, doi: 10.1088/0953-8984/21/9/095410.

[203] P. Němec, V. Nazabal, A. Moreac, J. Gutwirth, L. Beneš, and M. Frumar, "Amorphous and crystallized Ge–Sb–Te thin films deposited by pulsed laser: Local structure using Raman scattering spectroscopy," *Materials Chemistry and Physics*, vol. 136, no. 2, pp. 935–941, Oct. 2012, doi: 10.1016/j.matchemphys.2012.08.024.

[204] L. Prazakova *et al.*, "Temperature driven structural evolution of Ge-rich GeSbTe alloys and role of N-doping," *Journal of Applied Physics*, vol. 128, no. 21, p. 215102, Dec. 2020, doi: 10.1063/5.0027734.

[205] K. L. Chopra and S. K. Bahl, "Amorphous versus Crystalline GeTe Films. I. Growth and Structural Behavior," *Journal of Applied Physics*, vol. 40, no. 10, pp. 4171–4178, Sep. 1969, doi: 10.1063/1.1657161.

[206] S. K. Bahl and K. L. Chopra, "Amorphous Versus Crystalline GeTe Films. II. Optical Properties," *Journal of Applied Physics*, vol. 40, no. 12, pp. 4940–4947, Nov. 1969, doi: 10.1063/1.1657318.

[207] E. F. Steigmeier and G. Harbeke, "Soft phonon mode and ferroelectricity in GeTe," *Solid State Communications*, vol. 8, no. 16, pp. 1275–1279, Aug. 1970, doi: 10.1016/0038-1098(70)90619-8.

[208] A. V. Kolobov, J. Tominaga, P. Fons, and T. Uruga, "Local structure of crystallized GeTe films," *Appl. Phys. Lett.*, vol. 82, no. 3, pp. 382–384, Jan. 2003, doi: 10.1063/1.1539926.

[209] A. V. Kolobov, P. Fons, J. Tominaga, A. L. Ankudinov, S. N. Yannopoulos, and K. S. Andrikopoulos, "Crystallization-induced short-range order changes in amorphous GeTe," *J. Phys.: Condens. Matter*, vol. 16, no. 44, p. S5103, Oct. 2004, doi: 10.1088/0953-8984/16/44/008.

[210] K. S. Andrikopoulos, S. N. Yannopoulos, G. A. Voyiatzis, A. V. Kolobov, M. Ribes, and J. Tominaga, "Raman scattering study of the a-GeTe structure and possible mechanism for the amorphous to crystal transition," *J. Phys.: Condens. Matter*, vol. 18, no. 3, pp. 965–979, Jan. 2006, doi: 10.1088/0953-8984/18/3/014.

[211] R. Mazzarello, S. Caravati, S. Angioletti-Uberti, M. Bernasconi, and M. Parrinello, "Signature of Tetrahedral Ge in the Raman Spectrum of Amorphous Phase-Change Materials," *Phys. Rev. Lett.*, vol. 104, no. 8, p. 085503, Feb. 2010, doi: 10.1103/PhysRevLett.104.085503.

[212] M. Bouška *et al.*, "Pulsed laser deposited GeTe-rich GeTe-Sb2Te3 thin films," *Sci Rep*, vol. 6, no. 1, Art. no. 1, May 2016, doi: 10.1038/srep26552.

[213] V. Bragaglia *et al.*, "Far-Infrared and Raman Spectroscopy Investigation of Phonon Modes in Amorphous and Crystalline Epitaxial GeTe-Sb2Te3 Alloys," *Sci Rep*, vol. 6, no. 1, Art. no. 1, Jun. 2016, doi: 10.1038/srep28560.

[214] S. Kozyukhin, M. Veres, H. P. Nguyen, A. Ingram, and V. Kudoyarova, "Structural Changes in Doped Ge2Sb2Te5 Thin Films Studied by Raman Spectroscopy," *Physics Procedia*, vol. 44, pp. 82–90, Jan. 2013, doi: 10.1016/j.phpro.2013.04.011.

[215] K. S. Andrikopoulos, S. N. Yannopoulos, A. V. Kolobov, P. Fons, and J. Tominaga, "Raman scattering study of GeTe and Ge2Sb2Te5 phase-change materials," *Journal of Physics and Chemistry of Solids*, vol. 68, no. 5, pp. 1074–1078, May 2007, doi: 10.1016/j.jpcs.2007.02.027.

[216] R. De Bastiani *et al.*, "Crystallization of ion amorphized Ge2Sb2Te5 thin films in presence of cubic or hexagonal phase," *Journal of Applied Physics*, vol. 107, no. 11, p. 113521, Jun. 2010, doi: 10.1063/1.3437636.

[217] E. Rahier *et al.*, "Multistep Crystallization of Ge-Rich GST Unveiled by In Situ synchrotron X-ray diffraction and (scanning) transmission electron microscopy," *physica status solidi (RRL) – Rapid Research Letters*, vol. 17, no. 8, p. 2200450, 2023, doi: 10.1002/pssr.202200450.

[218] M. A. Luong *et al.*, "Impact of Nitrogen on the Crystallization and Microstructure of Ge-Rich GeSbTe Alloys," *physica status solidi (RRL) – Rapid Research Letters*, vol. 15, no. 3, p. 2000443, 2021, doi: 10.1002/pssr.202000443.

[219] M. Agati, F. Renaud, D. Benoit, and A. Claverie, "In-situ transmission electron microscopy studies of the crystallization of N-doped Ge-rich GeSbTe materials," *MRS Communications*, vol. 8, no. 3, pp. 1145–1152, Sep. 2018, doi: 10.1557/mrc.2018.168.

[220] S. M. S. Privitera *et al.*, "Atomic diffusion in laser irradiated Ge rich GeSbTe thin films for phase change memory applications," *J. Phys. D: Appl. Phys.*, vol. 51, no. 14, p. 145103, Mar. 2018, doi: 10.1088/1361-6463/aab1d0.

[221] S. M. S. Privitera *et al.*, "Crystallization properties of melt-quenched Ge-rich GeSbTe thin films for phase change memory applications," *Journal of Applied Physics*, vol. 128, no. 15, p. 155105, Oct. 2020, doi: 10.1063/5.0023696.

[222] M. A. Luong *et al.*, "On Some Unique Specificities of Ge-Rich GeSbTe Phase-Change Material Alloys for Nonvolatile Embedded-Memory Applications," *physica status solidi (RRL) – Rapid Research Letters*, vol. 15, no. 3, p. 2000471, 2021, doi: 10.1002/pssr.202000471.

[223] L. Prazakova *et al.*, "The effect of Ge content on structural evolution of Ge-rich GeSbTe alloys at increasing temperature," *Materialia*, vol. 21, p. 101345, Mar. 2022, doi: 10.1016/j.mtla.2022.101345.

[224] P. Zuliani *et al.*, "Overcoming Temperature Limitations in Phase Change Memories With Optimized $Ge_xSb_yTe_z$," *IEEE Transactions on Electron Devices*, vol. 60, no. 12, pp. 4020–4026, Dec. 2013, doi: 10.1109/TED.2013.2285403.

[225] V. Sousa *et al.*, "Operation fundamentals in 12Mb Phase Change Memory based on innovative Ge-rich GST materials featuring high reliability performance," in *2015 Symposium on VLSI Technology (VLSI Technology)*, Jun. 2015, pp. T98–T99. doi: 10.1109/VLSIT.2015.7223708.

[226] P. Zuliani, E. Palumbo, M. Borghi, G. Dalla Libera, and R. Annunziata, "Engineering of chalcogenide materials for embedded applications of Phase Change Memory," *Solid-State Electronics*, vol. 111, pp. 27–31, Sep. 2015, doi: 10.1016/j.sse.2015.04.009.

[227] O. Abou El Kheir, D. Dragoni, and M. Bernasconi, "Density functional simulations of decomposition pathways of Ge-rich GeSbTe alloys for phase change memories," *Phys. Rev. Materials*, vol. 5, no. 9, p. 095004, Sep. 2021, doi: 10.1103/PhysRevMaterials.5.095004.

[228] T. Chattopadhyay, J. X. Boucherle, and H. G. vonSchnering, "Neutron diffraction study on the structural phase transition in GeTe," *J. Phys. C: Solid State Phys.*, vol. 20, no. 10, p. 1431, Apr. 1987, doi: 10.1088/0022-3719/20/10/012.

[229] R. De Bastiani *et al.*, "Ion-irradiation-induced selective bond rearrangements in amorphous GeTe thin films," *Phys. Rev. B*, vol. 80, no. 24, p. 245205, Dec. 2009, doi: 10.1103/PhysRevB.80.245205.

[230] K. Jeong *et al.*, "Evolution of crystal structures in GeTe during phase transition," *Sci Rep*, vol. 7, no. 1, Art. no. 1, Apr. 2017, doi: 10.1038/s41598-017-01154-z.

[231] A. Erven, R. Bosch, A. W. Weeber, and M. Bijker, "Effects of Different Firing Profiles on Layer Characteristics and Passivation Properties of Industrial ETP Deposited Silicon Nitride Films," vol. 20, Jan. 2004.

[232] A. Banerjee *et al.*, "Optical properties of refractory metal based thin films," *Opt. Mater. Express*, vol. 8, no. 8, p. 2072, Aug. 2018, doi: 10.1364/OME.8.002072.

[233] H. J. Kim, J. Sohn, N. Hong, C. Williams, and W. Humphreys, "PCM-net: a refractive index database of chalcogenide phase change materials for tunable nanophotonic device modelling," *J. Phys. Photonics*, vol. 3, no. 2, p. 024008, Apr. 2021, doi: 10.1088/2515-7647/abeb55.

[234] A. L. Serra *et al.*, "Optimization of 3ω Method for Phase-Change Materials Thermal Conductivity Measurement at High Temperature," in *2019 IEEE 32nd International Conference on Microelectronic Test Structures (ICMTS)*, Mar. 2019, pp. 76–79. doi: 10.1109/ICMTS.2019.8730993.

[235] E. Bozorg-Grayeli, J. P. Reifenberg, M. A. Panzer, J. A. Rowlette, and K. E. Goodson, "Temperature-Dependent Thermal Properties of Phase-Change Memory Electrode Materials," *IEEE Electron Device Letters*, vol. 32, no. 9, pp. 1281–1283, Sep. 2011, doi: 10.1109/LED.2011.2158796.

[236] C. Chassain *et al.*, "Thermal characterization of Ge-rich GST/TiN thin multilayers for phase change memories," *Journal of Applied Physics*, vol. 133, no. 22, p. 225102, Jun. 2023, doi: 10.1063/5.0152049.

[237] H. Dong, B. Wen, and R. Melnik, "Relative importance of grain boundaries and size effects in thermal conductivity of nanocrystalline materials," *Sci Rep*, vol. 4, no. 1, Art. no. 1, Nov. 2014, doi: 10.1038/srep07037.

[238] T. M. Tritt, Ed., *Thermal Conductivity*. in Physics of Solids and Liquids. Springer US, 2004. doi: 10.1007/b136496.

[239] A. Kusiak, J.-L. Battaglia, P. Noé, V. Sousa, and F. Fillot, "Thermal conductivity of carbon doped GeTe thin films in amorphous and crystalline state measured by modulated photo thermal radiometry," *J. Phys.: Conf. Ser.*, vol. 745, no. 3, p. 032104, Sep. 2016, doi: 10.1088/1742-6596/745/3/032104.